Nanoelectrochemistry in Room Temperature Ionic Liquids



Eden E. L. Tanner

St John's College

University of Oxford

A thesis submitted for the degree of

Doctor of Philosophy

Trinity 2016

Abstract

The work presented in this thesis concerns the use of Room Temperature Ionic Liquids in nanoelectrochemistry. This thesis is presented in Parts, with the Introduction being presented in Part I, the General Experimental Section in Part II, the Results and Discussion being presented in Part III and IV, and the Conclusions in Part V.
Part III is concerned with the critical comparison of electron transfer theories in RTILs - namely Butler-Volmer (BV), Symmetric Marcus-Hush (SMH), and Asymmetric Marcus Hush (AMH) theories and contains three chapters.

Chapter 1 examines the one electron reduction of oxygen in 1-butyl-1-methylpyrrolinidium *bis*(trifluoromethylsulfonyl)imide ([Bmpyrr][NTf_2]). Experimental voltammetry is presented, and modelled using BV and SMH kinetics. Butler-Volmer theory consistently provided experimental parameters with a higher level of certainty than SMH theory. A value of solvent reorganisation energy for oxygen reduction in ionic liquids was inferred for the first time as 0.4 $\pm$ 0.1 eV, which is attributable to inner-sphere reorganisation with a negligible contribution from solvent reorganisation.

Chapter 2 reports the voltammetry for the reduction of 2-nitrotoluene at a gold microdisc electrode in two ionic liquids: trihexyltetradecylphosphonium *tris*(pentafluoroethyl)trifluorophosphate ([$P_{14,6,6,6}$][FAP]) and 1-ethyl-3-methylimidazolium *bis*(trifluoromethylsulfonyl)imide ([Emim]

[NTf_2]). The reduction of nitrocyclopentane (NCP) and 1-nitrobutane (BuN) is investigated using voltammetry at a gold microdisc electrode in [$P_{14,6,6,6}$][FAP]. Simulated voltammograms, generated through the use of Butler-Volmer theory and Symmetric Marcus-Hush theory, are compared to experimental data, with both theories parameterizing the data similarly well. An experimental value for the Marcusian parameter, λ, was also determined in all cases. For the reduction of 2-nitrotoluene, this was 0.5

$\pm$ 0.1 eV in both solvents, whilst for NCP and BuN in $[P_{14,6,6,6}][FAP]$, it was 2 $\pm$ 0.1 eV and 5 $\pm$ 0.1 eV respectively. This is attributed to the localization of charge on the nitro group, and the increased interaction with the environment, resulting in a larger reorganization energy.

Chapter 3 extends the previous work by applying AMH theory for the first time in ionic solvents to model the voltammetric reduction of oxygen in $[Bmpyrr][NTf_2]$, and 2-nitrotoluene, nitrocyclopentane, and 1-nitrobutane in $[P_{14,6,6,6}][FAP]$, on a gold microdisc electrode. AMH theory was able to parameterize the experimental data similarly well to Butler-Volmer and Symmetric Marcus-Hush theories, and in the case of reduction of oxygen, AMH was superior to SMH theory. An asymmetry parameter, γ, was estimated for all systems as -0.4 for the reduction of oxygen, and -0.05, 0.25, and 0 $\pm$ 0.05 for the reductions of 2-NT, NCP and BuN respectively, which suggests equal force constants of reactants and products in the case of 2-NT and BuN, and unequal force constants for oxygen and NCP, where the force constants of the oxidised species are greater than the reduced species in the case of oxygen, and less than the reduced species in the case of NCP.

Part IV is concerned with analysis of the electrochemistry of silver nanoparticles in RTILs, and contains three chapters.
Chapter 4 details the stochastic oxidation of individual nanoparticles (NPs) from a nanoparticle modified electrode, observed for the first time in a RTIL. A polyethylene glycol (PEG) capping agent on a silver nanoparticle is examined in 1-butyl-3-methylimidazolium tetrafluoroborate ([Bmim]-$[BF_4]$). Both the successful transfer of Ag NPs, and an in situ modification in a RTIL of the electrode with an ensemble of nanoparticles is demonstrated. From this ensemble of adsorbed nanoparticles on the electrode surface, single nanoparticle stripping was observed, and this resulted in spikes of current that allowed accurate electrochemically sizing of the NP, as evidenced by Transmission Electron Microscopy (TEM). A polymer-gated mechanism is proposed to explain the observed stochastic behaviour, whereby an activation of the NP occurs, involving an equilibrium between unwrapping and rewrapping of the PEG capping agent, followed by oxidation of the silver core.

Chapter 5 reports the observation of nano-impacts for the first time in a RTIL with the oxidation of silver nanoparticles in [Bmim][BF_4]. The addition of chloride facilitates the oxidation of the silver nanoparticles to silver chloride, which is observed as spikes in the current that correspond to single nanoparticles occurring via 'nano-impacts', whereby random diffusion ('Brownian motion') brings particles to within electron tunnelling distance of an electrode.

Chapter 6 reports a change in mechanism of oxidation of Ag NPs with the molecular weight of the PEG capping agent. Characterisation of the modified nanoparticles is undertaken using Dynamic Light Scattering and UV-Vis Spectroscopy. Electrochemical analyses reveal that the oxidation of 6000 molecular weight (MW) PEG is consistent with a polymer-gated mechanism, whilst for 2000 MW PEG the polymer does not hinder the oxidation. The 10,000 MW PEG Ag NP are rendered almost electrochemically inactive. This chapter demonstrates the ability to alter and better understand the electron transfer mechanism in a RTIL by systematically altering the capping agent.

Overall, this thesis uses theories of electron transfer and the oxidation of Ag NPs to gain insight into redox processes in RTILs at a nano-scale, and reports on the detection of NPs in ionic solvents for the first time.

Acknowledgements

My first thank you must go to Professor Richard Compton, whose support and guidance has been essential in the production of the thesis and in my continual growth as an academic, scientist, and individual. Your solid belief in me has made even seemingly-rough seas seem quiet.

The second thank you must go to Dr Christopher Batchelor-McAuley who not only designed the system that made the second half of this thesis possible, but has taught me an absolutely incredible amount. Moving from student to colleague will be an absolute pleasure, and I would definitely not be in the position I am now without your guidance and support.

To my collaborators in the Compton Group - especially Dr Eddy Barnes - thank you for all of your assistance with programming, and for coming to my rescue whilst learning/fighting LaTeX. To other members of the Compton Group - Tom, Ivana, Shaltiel, Patty, Her Shuang, Rita, Enno, Stan, Dia, Crystal - thanks for making the lab such a great place to work.

I would not be here without the financial support of the Clarendon Fund, the Department of Chemistry, and St John's College. I am so grateful for your assistance, and I hope I've been, and will continue to be, a trustworthy ambassador.

To the wonderful folk of St John's MCR - your companionship, solidarity, and energy has kept me afloat. To the Queen of Organised Fun, Mikayla, and the Biochem coffee-break saviours Ellie and Olivier - thank you. I thoroughly enjoyed my time on the committee and as President, and it taught me skills I never thought I would take away from a DPhil! To Kat, you are wonderful at the job, and may nobody tell you otherwise!

Similarly, my time working for students with Oxford University Students' Union has provided a lot of opportunities for strength and growth, and I feel grateful to all those who work - especially behind the scenes - to fight for students at this University.

To the other extraordinary people I have had the pleasure of meeting in Oxford - crossing paths with you has changed me, and I continually learn and grow from

you. Even though I don't have space to acknowledge all of the people I have met who have helped me grow, thank you all for sharing your lives with me, and being an unwavering support system. To Anna - coming to Oxford was worth it just for the opportunity to know and love you. To Megan and Mitch - your pursuit of kindness, love, and strength below grey skies fuels me. To Chiara and Aditya - thank you for embracing me so fully in your wonderful lives and home. Thank you for countless cups of tea, and letting me get to know your brilliant selves up close. To Flora Sheldon - your stream of postcards glued my life together - thanks for letting me escape to you (and then Cambridge) when life got tough. To Flora Kennedy McConnell - the trip to California with you will stay with me forever, and helped me picture a future beyond this place. To Joanna, the path we have walked together has made me a better friend and colleague. I am so impressed by you.

To the Jones' - it has been such a pleasure to get to know you and Charlie - thank you for sharing him with us!

To my family and friends in Australia - although physically far away, your support has meant a lot. To Madison and Michael, Harry, and Lawson. You are all such incredible humans, and your growing into yourselves has been a pleasure to watch, even if from a distance. To PJ and Grandpa Chris - thank you for being so constantly supportive. To my dear Dad, whose worry about whether I'm getting enough vitamins and warmth has spanned my three years here - at least at this point I can say - yes, the thesis is finally finished. To my Mum, who is dearly missed, although you will not be here to see me be Dr Tanner, I am who I am because of you.

Lastly, to James, who has given me the freedom to follow my passions, but who is always there at the end of the day with unfaltering love and support. Thanks for sticking by me even though the future is scary and involves a lot of planning.

Publications

[1] Tanner, E. E. L.; Xiong, L.; Barnes, E. O.; Compton, R. G. *J. Electroanal. Chem.* **2014**, *727*, 59–68.

[2] Tanner, E. E. L.; Barnes, E. O.; Goodrich, P.; Hardacre, C.; Compton, R. G. *J. Phys. Chem. C* **2015**, *119*, 3634–3647.

[3] Tanner, E. E. L.; Barnes, E. O.; Tickell, C. B.; Goodrich, P.; Hardacre, C.; Compton, R. G. *J. Phys. Chem. C* **2015**, *119*, 7360–7370.

[4] Tanner, E. E. L.; Tschulik, K.; Tahany, R.; Jurkschat, K.; Batchelor-McAuley, C.; Compton, R. G. *J. Phys. Chem. C* **2015**, *119*, 18808–18815.

[5] Tanner, E. E. L.; Batchelor-McAuley, C.; Compton, R. G. *J. Phys. Chem. C* **2016**, *120*, 1959–1965.

[6] Tanner, E. E. L.; Batchelor-McAuley, C.; Compton, R. G. *Chem. Eur. J.* **2016**, *22*, 5976–5981.

Table of Symbols

Symbol	Description	Units
A	Electrode area	m^2
C_{dl}	Double layer capacitance	$\mu F\ cm^{-2}$
J	Flux	$mol\ s^{-1}\ m^{-2}$
n	Number of electrons	Unitless
$n^{'}$	Number of electrons in rate determining step	Unitless
x	Distance travelled	m
k_B	Boltzmann's constant = 1.38×10^{-23}	$m^2\ kg\ s^{-2}\ K^{-1}$
η	Viscosity	cP
κ	Conductivity	$mS\ cm^{-1}$
ρ	Density	$g\ cm^{-3}$
v	Volume	m^3
Q	Charge	C
N_A	Avogadro's constant = 6.022×10^{23}	mol^{-1}
M_R	Molar mass	$gm\ mol^{-1}$
r_D	Radius of diffusing species	m
D_∞	Hypothetical diffusion coefficient at infinite temperature	$m^2\ s^{-1}$
ω	Pre-exponential factor	Unitless
E_a	Activation energy of diffusion	$kJ\ mol^{-1}$
ϕ	Lattice saturation parameter	Unitless
$E^{\ominus}$	Standard electrode potential	V
Γ	Activity coefficient	Unitless

k_a	Heterogeneous rate constant of species A	m s^{-1}
k_b	Heterogeneous rate constant of species B	m s^{-1}
α	Transfer coefficient	Unitless
$\Delta G^{\ddagger}$	Gibbs free energy of activation	kJ
$\Delta G^{\ominus}$	Standard Gibbs free energy	kJ
γ	Asymmetry factor	Unitless
λ	Overall reorganisation energy	eV
λ_i	Molecular reorganisation energy	eV
λ_o	Solvent reorganisation energy	eV
C_{A}	Concentration of species A	mol m^{-3}
C_{A}^{*}	Bulk solution concentration of species A	mol m^{-3}
C_{A}^{0}	Electrode surface concentration of species A	mol m^{-3}
D_{A}	Diffusion coefficient of species A	m^2 s^{-1}
D_{B}	Diffusion coefficient of species B	m^2 s^{-1}
E	Applied potential	V
$E_f^{\ominus}$	Formal potential	V
F	Faraday constant = 96485	C mol^{-1}
I	Current	A
i_c	Capacitative current	A
k^0	Standard electrochemical rate constant	m s^{-1}
$k_{\mathrm{red/ox}}$	Reduction/oxidation rate constant	m s^{-1}
ν	Scan rate	V s^{-1}

R	Gas constant = 8.314	J K^{-1} mol^{-1}
R	Radial coordinate	m
r	Radius of electrode	m
T	Temperature	K
t	Time	s
z	z coordinate	m
N	Number of features	Unitless
C_{NP}	Bulk nanoparticle concentration	mol m^{-3}
r_{NP}	Radius of the nanoparticle	m

Contents

I Introduction **1**

0.1 Fundamental Electrochemistry . . . 2
0.1.1 The Electrode-Solution Interface . . . 2
0.1.1.1 The Structure of The Interfacial Region . . . 2
0.1.1.2 Faradaic and Non-Faradaic Currents . . . 4
0.1.2 Mass Transport . . . 5
0.1.2.1 Diffusion . . . 5
0.1.2.2 The Diffusion Coefficient . . . 6
0.1.3 Heterogenous Electron Transfer . . . 7
0.1.3.1 Electrochemical Equilibria . . . 7
0.1.3.2 Butler-Volmer Theory . . . 9
0.1.3.3 Marcus-Hush Theories . . . 10
0.1.4 Practical Considerations - Working Electrodes . . . 12
0.1.5 Voltammetric Techniques . . . 13
0.1.5.1 Chronoamperometry . . . 13
0.1.5.2 Cyclic Voltammetry on a Macroelectrode . . . 16
0.1.5.3 Reversible voltammetry . . . 17
0.1.5.4 Quasi-reversible voltammetry . . . 18
0.1.5.5 Irreversible voltammetry . . . 19
0.1.5.6 Cyclic Voltammetry on a Microelectrode . . . 19
0.2 Room Temperature Ionic Liquids . . . 21
0.2.1 What are Room Temperature Ionic Liquids? . . . 21
0.2.2 Why Ionic Liquids? . . . 23
0.2.3 Properties of RTILs . . . 23
0.2.3.1 Viscosity . . . 23
0.2.3.2 Density . . . 25
0.2.3.3 Conductivity . . . 25
0.2.3.4 Electrochemical Window . . . 26

0.2.4 Synthesis . . . 27
0.2.5 Common Impurities and Their Effects on Reaction Outcomes 28
0.2.5.1 Water . . . 28
0.2.5.2 Halides . . . 29
0.2.5.3 Dissolved Gases . . . 29
0.2.6 Fundamental Electrochemistry in Room Temperature Ionic Liquids . . . 31
0.2.6.1 Voltammetry in RTILs . . . 31
0.2.6.2 Double Layer Capacitance . . . 34
0.3 Metallic Nanoparticles . . . 40
0.3.1 What are nanoparticles? . . . 40
0.3.1.1 Capping Agents . . . 41
0.3.2 Non-Electrochemical Characterisation of NPs . . . 43
0.3.2.1 Transmission Electron Microscopy . . . 43
0.3.2.2 Scanning Electron Microscopy . . . 45
0.3.2.3 Dynamic Light Scattering . . . 45
0.3.2.4 UV-Vis Spectroscopy . . . 47
0.3.3 Electrochemical Characterisation of NPs . . . 50
0.3.3.1 Stripping Voltammetry . . . 50
0.3.3.2 Nano-impacts . . . 51

II General Experimental Details 66
0.4 Chemical Reagents . . . 67
0.4.1 Commercially Available Reagents . . . 67
0.4.2 Room Temperature Ionic Liquids . . . 67
0.5 Electrodes . . . 67
0.6 Potentiostats . . . 70
0.7 Glovebox and Experimental Apparatus . . . 71

III A Comparison of Electron Transfer Theories in RTIL 74
0.8 Introduction . . . 75
0.9 Theory . . . 82
0.9.1 Chronoamperometry . . . 83
0.9.1.1 The Shoup and Szabo equation . . . 83
0.9.1.2 Simulation of chronoamperometry . . . 85

0.9.2 Cyclic voltammetry . . . 87
0.9.2.1 Applied potential . . . 87
0.9.2.2 Butler-Volmer kinetics . . . 88
0.9.2.3 Symmetric Marcus-Hush kinetics . . . 88
0.9.2.4 Asymmetric Marcus-Hush Theory . . . 90
0.9.3 Calculation of the current . . . 92
0.9.4 Numerical methods . . . 92
0.9.5 Error . . . 94
0.9.5.1 Chronoamperometry . . . 94
0.9.5.2 Cyclic voltammetry . . . 94
0.10 Experimental . . . 95

1 A Comparative Study of Butler-Volmer and Symmetric Marcus-Hush Theories: Oxygen Reduction 101

2 A Comparative Study of Butler-Volmer and Symmetric Marcus-Hush Theories: Nitro groups 112
2.1 Reduction of 2-nitrotoluene in $[P_{14,6,6,6}][FAP]$ and $[Emim][NTf_2]$ . . . 113
2.1.1 Reduction of 2-nitrotoluene in $[P_{14,6,6,6}][FAP]$ . . . 114
2.1.2 Reduction of 2-nitrotoluene in $[Emim][NTf_2]$ . . . 119
2.1.3 Comparison of reduction of 2-nitrotoluene in $[P_{14,6,6,6}][FAP]$ and $[Emim][NTf_2]$ . . . 123
2.2 Reduction of nitrocyclopentane and 1-nitrobutane in $[P_{14,6,6,6}][FAP]$. 124
2.2.1 Nitrocyclopentane in $[P_{14,6,6,6}][FAP]$ . . . 124
2.2.2 Reduction of 1-nitrobutane in $[P_{14,6,6,6}][FAP]$ . . . 128
2.2.3 Discussion of the reduction of nitrocyclopentane and 1-nitrobutane in $[P_{14,6,6,6}][FAP]$ . . . 131

3 The Application of Asymmetric Marcus-Hush Theory to Voltammetry in Room Temperature Ionic Liquids 135
3.1 Reduction of Oxygen in $[Bmpyrr][NTf_2]$ . . . 135
3.2 Reduction of Nitro Compounds in $[P_{14,6,6,6}][FAP]$ . . . 139
3.2.1 Reduction of 2-nitrotoluene in $[P_{14,6,6,6}][FAP]$ . . . 139
3.2.2 Reduction of Nitrocyclopentane in $[P_{14,6,6,6}][FAP]$ . . . 142
3.2.3 Reduction of 1-Nitrobutane in $[P_{14,6,6,6}][FAP]$ . . . 145
3.3 Part III Conclusions . . . 148

IV Silver Nanoparticle Oxidation in Room Temperature Ionic Liquids 151

3.4 Introduction . . . 152
3.5 Experimental . . . 156
3.5.1 Nanoparticle Modification and Sample Preparation . . . 156
3.5.2 TEM . . . 157
3.5.3 Dynamic Light Scattering . . . 158
3.5.4 UV-Vis Spectroscopy . . . 159
3.5.5 Transfer into Glovebox and Experimental Assembly . . . 159
3.5.6 Electrochemical Apparatus . . . 159

4 Polymer Gated Single Nanoparticle Oxidation 165

4.1 Sizing . . . 166
4.2 Reactivity Towards Oxidative Dissolution . . . 166
4.3 Reactivity Differences in Ionic Liquids . . . 170
4.3.1 Transfer into Ionic Liquid . . . 172
4.3.2 In-situ Modification . . . 173
4.4 Time Dependency . . . 175
4.5 Potential Dependency . . . 178
4.6 Sizing of nanoparticles . . . 179
4.7 Proposed Mechanism for Stochastic Stripping . . . 181
4.8 Conclusions . . . 183

5 Nano-impacts in Room Temperature Ionic Liquids - the role of chloride 186

5.1 Silver Stripping . . . 187
5.2 Time Dependency . . . 189
5.3 Chloride Concentration Effects . . . 191
5.4 Electrochemical Sizing . . . 192
5.5 Mechanism . . . 196
5.6 Conclusions . . . 198

6 Capping Agent Controlled Electron Transfer Dynamics 201

6.1 Modification of nanoparticles . . . 202
6.1.1 Dynamic Light Scattering . . . 203
6.1.2 UV-Vis Spectrometry . . . 204
6.2 Electrochemistry . . . 205

6.2.1 Electrochemical Sizing 206
6.2.2 Time Dependency and Frequency 207
6.3 Mechanism 209
6.4 Conclusions 213
6.5 Part IV Conclusions 213

V Conclusions **217**

A Derivation of the Butler-Volmer Equation **221**

Part I

Introduction

0.1 Fundamental Electrochemistry

Electrochemistry is a discipline that is concerned with the interrelation of electrical and chemical effects, in particular the chemical changes that occur as a result of passing current through a medium (an electrolyte, an ionic conductor) and an electrode (an electronic conductor). This thesis' focus is on dynamic electrochemistry, whereby a potential difference (ΔV) is applied between a metallic electrode and the electrolyte, and the current (I), and subsequent chemical effects on the reactant molecule in solution phase, are monitored with respect to the applied potential. The composition of the interface between electrode and electrolyte as electron transfer is occurring, as well as other fundamental concepts integral to understanding the subsequent work, are described in this section. A more comprehensive introduction to Electrochemistry can be found in seminal text books.[1,2]

0.1.1 The Electrode-Solution Interface

0.1.1.1 The Structure of The Interfacial Region

As a potential difference is applied between an electrode and the solution, the electrode, depending on the potential applied, is either rich in or deficient in electrons relative to the media surrounding it. This results in a charge separation across the interface, and the charged electrolyte molecules and ions seek to reorient themselves to correct for this and maintain electroneutrality. Charged molecules realign themselves into an energetically stable arrangement, whereby ions of the opposite charge to the electrode are usually attracted, whilst similarly charged ions are repelled. This creates an electrical field gradient forms from the electrode surface out to the bulk solution, so called the 'double-layer'. A number of models have been proposed to explain the electrode-solution interface and the structure of the double layer. Helmholtz[3,4] coined the term in the 1850s, with a model visualising the interface as a row of equal-but-

oppositely charged ions forming a layer adjacent to the electrode, constrained by the 'Outer Helmholtz Plane' (OHP). This model was then improved by Gouy[5] and Chapman,[6] who conceived of the ions as point charges, and suggested that the potential dropped approximately exponentially over a 'diffuse layer', out to the bulk solution. Stern[7] incorporated both models, with improvements, to describe the double layer as consisting of an OHP with ions of opposite (but not equal) charge with a diffuse layer comprised of spheres of realistic dimensions rather than point charges. Stern's model proposes a linear potential drop between the electrode (ϕ_m) and the OHP (ϕ_{OHP}), followed by an exponential decrease to the bulk solution (ϕ_s). This model is illustrated in a schematic in Figure 1.

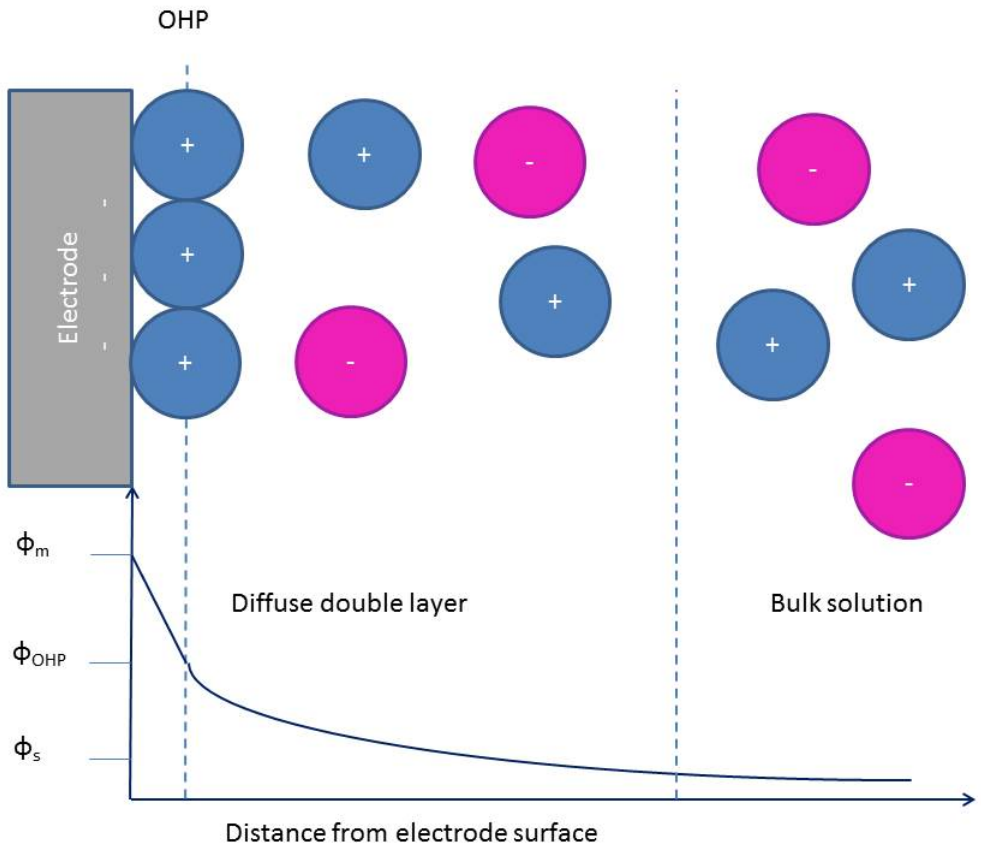


Figure 1: A diagram showing the Stern model of the double layer.

0.1.1.2 Faradaic and Non-Faradaic Currents

The current measured as a result of the potential difference held between the electrode and the electrolyte is comprised of two types of processes; Faradaic and Non-Faradaic. The former, named after Sir Michael Faraday,[8] involves the transfer of electrons between the electrode and the species in solution. The species can either lose (oxidation) or gain (reduction) electrons to/from the electrode, depending on the potential applied. Faraday's 1st Law states that the amount of material electrolysed is proportional to the amount of charge passed. The Faraday constant, F, of 96485 C, is an expression of the amount of charge passed per mole of electrons, and is the product of the Avogadro number (6.022×10^{23}) and the charge on one electron (1.6×10^{-19} C). Assuming only one electrochemical process is occurring, and assuming a single electron is transferred, a Faraday of charge is passed per mole of reactant. The second process, known as non-Faradaic, refers to the contributions of changes in the interfacial structure, resulting in charge and discharge of currents. This current is also referred to as the capacitative current, and is described by:

$$i_c = AC_{dl}\frac{dE}{dt} = AC_{dl}\nu \tag{1}$$

where A is the electrode area, C_{dl} is the double layer capacitance, $\frac{dE}{dt}$ is the rate of potential change with time, and ν is the scan rate, which is a parameter used to describe the rate of change of the potential with time. Capacitative currents have a particular effect when the scan rate is high, often distorting the signal when the non-Faradaic currents make a significant contribution to the overall measured current. As will be discussed below, the magnitude of Faradaic current is controlled by the rate of mass transport of the reactant to and from the electrode and the rate of electron transfer at the interface.*

*It is worth noting that "follow-up chemistry" is also a factor, but it will not be discussed in detail in this Introduction.

0.1.2 Mass Transport

Mass Transport is responsible for the movement of species to and from the electrode surface, and is controlled by three main processes: Diffusion, Migration, and Convection. Since neither migration (because, as will be discussed in the coming section, the ionic solvent used throughout this thesis negates these effects, *vide infra*, see section 0.2.6.1) or convection, due to the set up of our electrochemical cells, contribute significantly, only the role of diffusion will be discussed.

0.1.2.1 Diffusion

Diffusion occurs when a concentration gradient forms, as species move from an area of high concentration to an area of low concentration, such as when a reactant is depleted at the electrode surface. The observed flux (J) is related to the measured current (I / Amps) observed by:

$$I = -nFAJ \tag{2}$$

where n is the number of electrons exchanged, F is the Faraday constant, A is the area of the electrode, and J is the flux (mol s^{-1} m^{-2}).

Fick's first law[9] describes the diffusive flux in one dimension to a planar electrode:

$$J_A = -D_A \frac{\partial C_A}{\partial x} \tag{3}$$

where J is the flux of species A (mol s^{-1} m^{-2}), D_A is the diffusion coefficient of species A (m^2 s^{-1}), C_A is the concentration of species A (mol m^{-3}), and x is the distance travelled (m).

Fick's second law, which is derived from the first, describes the concentration

dependence of a species over time, t (in one dimension):

$$\frac{\partial C_A}{\partial t} = D_A \frac{\partial^2 C_A}{\partial x^2} \tag{4}$$

In three-dimensions, this becomes:

$$\frac{\partial C_A}{\partial t} = D_A \nabla^2 C_A \tag{5}$$

where ∇^2 is the Laplacian operator, and the form of this operator is defined depending on electrode geometry.

For three dimension Cartesian coordinates, the Laplacian operator is:

$$\nabla^2 = \frac{\partial^2}{\partial x^2} + \frac{\partial^2}{\partial y^2} + \frac{\partial^2}{\partial z^2} \tag{6}$$

For a cylindrical geometry, such as will be used throughout this thesis, the following mass transport equation must be solved:

$$\frac{\partial C_\mathrm{A}}{\partial t} = D_\mathrm{A} \left(\frac{\partial^2 C_\mathrm{A}}{\partial r^2} + \frac{1}{r} \frac{\partial C_\mathrm{A}}{\partial r} + \frac{\partial^2 C_\mathrm{A}}{\partial z^2} \right) \tag{7}$$

where C_A is the concentration of species A (mol m^{-3}), t (s) is time, D_A (m^2 s^{-1}) is the diffusion coefficient of species A, and r and z (m) are the spatial coordinates.

0.1.2.2 The Diffusion Coefficient

The diffusion coefficient, D, is given by the Einstein equation:[10]

$$D = \frac{(\delta x)^2}{2\delta t} \tag{8}$$

where δt is the time the species takes to diffuse a mean square distance ($(\delta x)^2$). The diffusion coefficient is dependent on the size of the species, the viscosity of the

medium, and the temperature.

Hydrodynamic theory relates the diffusion coefficient to the inverse of the viscosity through the Stokes-Einstein[10,11] equation:

$$D = \frac{k_B T}{6\eta\pi r_D} \tag{9}$$

where k_B is the Boltzmann constant, T is the temperature, η is the viscosity, and r_D is the hydrodynamic radius of the diffusing species. The Stokes-Einstein relation only holds true for spherical macroparticles in a solvent with a sufficiently low Reynolds number (which is the ratio of inertial forces to viscous forces) and may differ in different solvents.

The relationship between the diffusion coefficient and the temperature is described by the Arrhenius equation:

$$D = D_\infty e^{\frac{-E_a}{RT}} \tag{10}$$

where D_∞ is the hypothetical diffusion coefficient at infinite temperature, E_a is the activation energy of diffusion, and R is the universal gas constant (8.314 J K^{-1} mol^{-1}).

0.1.3 Heterogenous Electron Transfer

Having considered the processes by which an electroactive material travels to the electrode surface, the Faradaic processes that occurs once it reaches its destination will now be discussed.

0.1.3.1 Electrochemical Equilibria

Consider a one-electron transfer:

$$A + e^- \leftrightharpoons B \tag{11}$$

where B is the reduced form of A. If the electrode is held at a sufficiently negative potential relative to the solution, the forward reaction will be thermodynamically favourable, as electrons pass from the electrode to the solution and convert species A to species B. If a sufficiently positive potential is applied, the reverse will occur, with the transfer of electrons from species B to the electrode becoming more thermodynamically favourable.

At equilibrium, the flow of electrons, which manifests itself as a measurable current (in a closed circuit environment), will be net zero, as the rate of electron transfer in each direction is equal. The Nernst[2] equation quantifies this:

$$E = E_f^{\ominus} + \frac{RT}{F} ln \frac{[A]}{[B]} \tag{12}$$

where $[A]$ and $[B]$ are concentrations of the reactant and product, and $E_f^{\ominus}$ is the formal potential at which no current will flow if A and B are present in equal amounts.

The formal potential is used in non-ideal conditions, and modifies the standard electrode potential ($E^{\ominus}$) to account for variations in pH, temperature, and difference in activity coefficients, Γ (where the standard potential reports values at 1 atm, 298K, [A] at 1 mol dm^{-3}, pH at 0):

$$E_f^{\ominus} = E^{\ominus} + \frac{2.303RT}{F} log \frac{[\Gamma_A]}{[\Gamma_B]} \tag{13}$$

Γ is a constant that modifies the concentration, $[X]$, to account for any deviations from ideality, and the resultant property, the activity, a, is an expression of effective concentration:

$$a = [X]\Gamma \tag{14}$$

In dilute solutions, where the activity coefficients are approaching 1, concentrations are used in lieu of activities, as in Equation 12.

A reference electrode is necessary to close the circuit, and each potential is given

in reference to this electrode, where a known electrochemical reaction is maintained at equilibrium. Where the system is not at equilibrium, it can be described by a number of other electron transfer theories, detailed below.

0.1.3.2 Butler-Volmer Theory

Butler-Volmer theory[12,13] relates the flux (J) with heterogenous rate constants for each species:

$$J = k_a C_A^0 - k_b C_B^0 \tag{15}$$

where C^0 is the concentration of the electroactive species at the electrode surface.

The rate constants, k_a and k_b, are given by:

$$k_{\mathrm{a}} = k^0 \exp\left[\frac{-\alpha F\left(E - E_f^{\ominus}\right)}{RT}\right] \tag{16}$$

$$k_{\mathrm{b}} = k^0 \exp\left[\frac{\beta F\left(E - E_f^{\ominus}\right)}{RT}\right] \tag{17}$$

where k^0 is the standard electrochemical rate constant, α is the transfer coefficient (where $\alpha + \beta = 1$), E is the cell potential, and $E_f^{\ominus}$ is the formal cell potential. E - $E_f^{\ominus}$ is the overpotential, which is defined as the additional potential, above what is thermodynamically necessary, needed to drive the reaction.[2]

The transfer coefficient is a phenomenological way of describing the transition state, and, for a reduction, takes a value <0.5 if it is more reactant-like, and >0.5 if it is more product-like.[14,15]

Although Butler-Volmer theory has been shown to accurately parameterise experimental data,[16–18] the use of the empirical transfer coefficient means that it does not add any significant microscopic insight to electrochemical processes. At increas-

ing overpotentials, Butler-Volmer theory also predicts an infinitely-increasing current, which is not supported by physical observations.

0.1.3.3 Marcus-Hush Theories

Marcus-Hush Theory[19,20] is a microscopic theory of electron transfer that relates the heterogeneous rate constant, k^0, to the reaction Gibbs energy, $\Delta G^{\ominus}$. In place of a phenomenological rate constant, Marcus-Hush theory uses reorganisation energy, λ.

$$\Delta G^{\ddagger} = \frac{\lambda}{4}\left(1 + \frac{\Delta G^{\ominus}}{\lambda}\right)^2 \tag{18}$$

$$k^0 = \omega \exp\left[\frac{-\Delta G^{\ddagger}}{RT}\right] \tag{19}$$

where $\Delta G^{\ddagger}$ is the Gibbs free energy of activation, $\Delta G^{\ominus}$ is the standard Gibbs free energy, λ is the reorganisation energy (defined below), k^0 is the standard electrochemical rate constant, and ω is a pre-exponential factor. Figure 2 shows two overlapping potential energy curves, belonging to a reactant and a product respectively. This diagram relates real normal modes, describing intramolecular vibrations, to a 1-D coordinate that represents the reaction pathway, known as the reaction coordinate. The point at which the parabolae overlap in this diagram represents the transition state, ‡. The reorganisation energy, λ, is the energy of the reactant at the reaction coordinate where the product is at its lowest energy. It is comprised of two contributions:

$$\lambda = \lambda_i + \lambda_o \tag{20}$$

where λ_i is the energy required from the inner-sphere, or molecular, reorganisation, due to changes in bond length and angle, and λ_o is the outer, or solvent, reorganisation energy, and stems from solvent molecules reorienting around the newly-formed

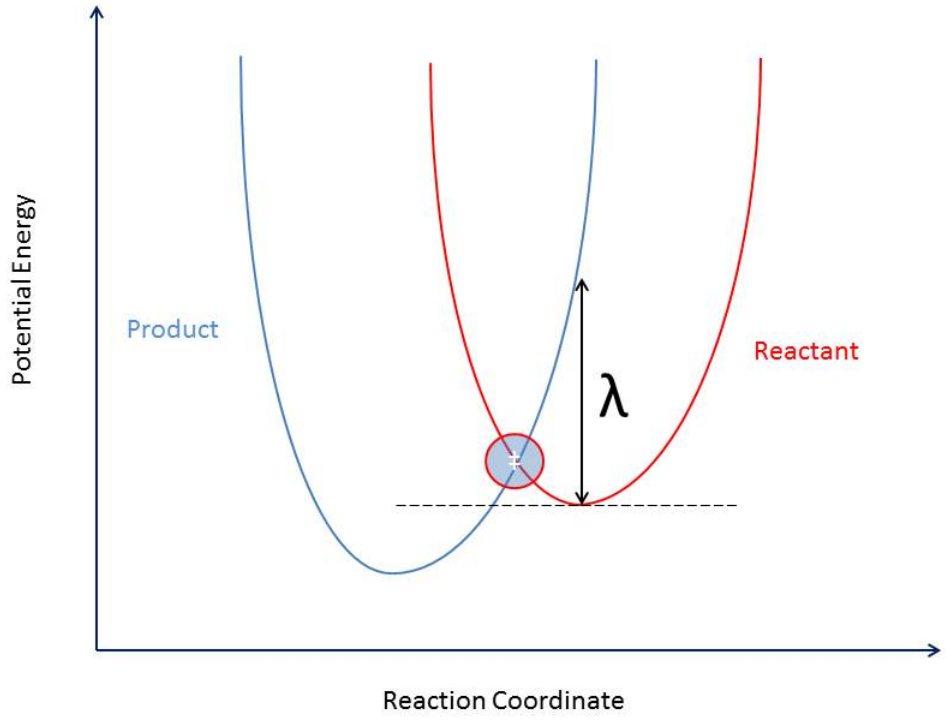


Figure 2: Potential energy curves - the transition state (‡) is the point at which they meet.

product.

The magnitude of the standard electrochemical rate constant is determined by the difference between the reaction coordinates of the ground states of the reactant and product curves, whereby a bigger difference results in a higher energy transition state and a slower electrochemical rate.

Marcus-Hush theory has two forms — Symmetric Marcus-Hush theory (SMH), where the curvature of the potential energy parabolae are equal, and Asymmetric Marcus-Hush theory (AMH), where an asymmetry parameter, γ, is introduced to relax this requirement. Fuller details are given in Part III, 0.9.2.

The asymmetry parameter, γ, which describes the curvature of the reactant and product parabolae relative to one another, has recently been reconciled with the

transfer coefficient (α) from Butler-Volmer (B-V) theory with the following relationship:[21,22]

$$\alpha\left(E_f^{\ominus}\right) = \frac{1}{2} + \gamma\left(\frac{1}{4} - \frac{1.267}{\Lambda + 3.353}\right) \tag{21}$$

where Λ is the dimensionless reorganisation energy ($\frac{F}{RT}\lambda$). From this relationship, we can infer the relative symmetry of the force constants, which describe the intramolecular vibrations and interactions with the solvent, to be set individually for the reactants and the products, of the reactants (the oxidised species) and the products (the reduced species). Where α is less than 0.5, the force constants of the reduced species are larger than those of the oxidised species ($f_s^{Ox} < f_s^{Red}$), and γ takes a value less than 0 to reflect this. Where α is greater than 0.5, the force constants of the oxidised species are larger than those of the reduced species ($f_s^{Ox} > f_s^{Red}$), and γ takes a value greater than 0.

0.1.4 Practical Considerations - Working Electrodes

The working electrodes used throughout this thesis have a disc geometry. Disc electrodes are commonly used because of their ease of manufacture and some simplification of mass transport equations that their symmetry offers.[1] At a particular experimental timescale, two diffusion regimes are observed to disc electrodes, with larger electrodes experiencing linear diffusion, whilst smaller electrodes, because of edge effects, show convergent diffusion (see Figure 3). At conventional scan rates with sufficiently fast mass transport, convergent diffusion dominates at so-called microelectrodes, where the disc radius is <50 μm.

This altered diffusion regime will have an affect on the observed voltammetric output, which is covered in the coming section.

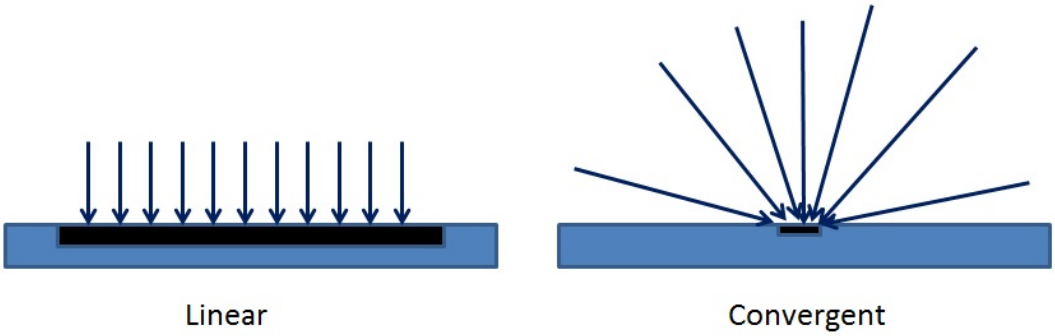


Figure 3: Two diffusion regimes - on a large electrode relative to mass transport, linear, or planar diffusion occurs, whereas on a smaller electrode, convergent diffusion occurs.

0.1.5 Voltammetric Techniques

This subsection details the electrochemical methods used throughout this thesis. Both chronoamperometry and cyclic voltammetry use the application of a potential and the measurement of the resultant current to extract information from the electrochemical system.

0.1.5.1 Chronoamperometry

The first technique, chronoamperometry, involves holding the potential at a set value for a given period of time whilst recording the current, jumping from E_0 to E_1 or from open-circuit potential to E_1 (Figure 4 a).[2]

The resultant plot of current vs time is called a chronoamperogram. Figure 4 b) shows the initially large current fall with time as species A is depleted at the electrode. Where linear diffusion dominates, the diffusion limited current (i_d) approaches zero with time, and is described by the Cottrell equation:[23]

$$i_d = \frac{nFAD_A^{0.5}C}{\sqrt{\pi t}} \tag{22}$$

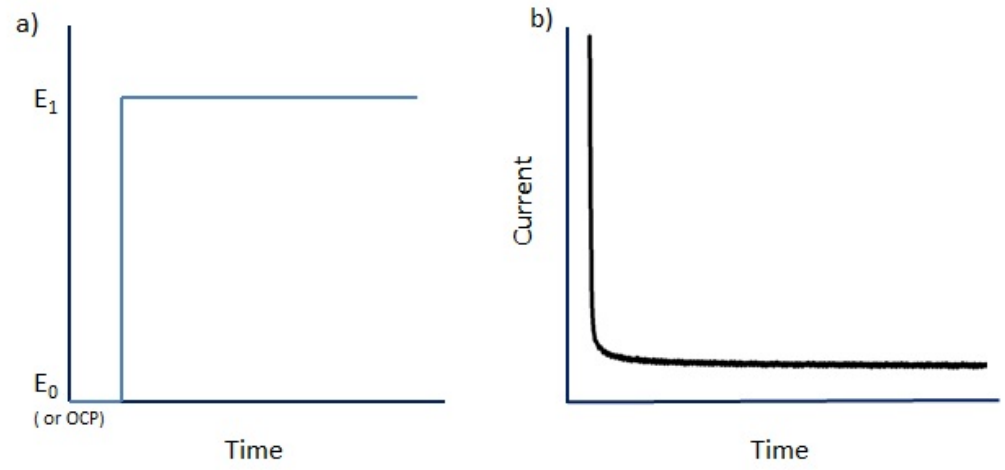


Figure 4: A schematic showing a) the potential sequence with time and b) a typical oxidative chronoamperogram.

where n is the number of electrons (as $A + ne^- \rightarrow B$), F is Faraday's constant, A is the area of the electrode, D is the diffusion coefficient of the electroactive species, C is the concentration of the electroactive species, and t is the time. The Cottrell equation is only valid in systems where three boundary conditions are upheld: the first is that only species A is present in solution at $t = 0$, the second that the surrounding solution is large enough such that concentration of A is at its bulk value sufficiently far from the electrode, and the third is that the concentration of A at the electrode surface is zero immediately after the potential step.

For a convergent diffusion regime, the current decays not to zero, but to a limiting current, as given by Equation 23, and is best described by:

$$i_{iss} = -4nFD_ACr \tag{23}$$

where r is the electrode radius. At very short times, the Cottrell Equation can be applied, but in order to take into account the full range of dimesnionless time (τ), as described below, an expression derived by Shoup and Szabo must be used:[24]

$$I = 4nFD_ACAr f(\tau) \tag{24}$$

$$f(\tau) = 0.7854 + 0.4432\tau^{-0.5} + 0.2146 \exp\left(-0.3912\tau^{-0.5}\right) \tag{25}$$

$$\tau = \frac{D_A}{r^2}t \tag{26}$$

where n is the number of moles of electrons transferred per mole of reactant, D_A is the diffusion coefficient, C is the bulk concentration, F is the Faraday constant, t is time, and r is the radius of the electrode. Fitting experimental data with this expression allows the determination of the concentration and diffusion coefficient (providing n and r are known) with an error of 0.6%.[24]

A double-step chronoamperogram, whereby the potential is jumped from an initial potential, E_0, to a different potential, E_1, then back to the original potential (see Figure 5), can be used to monitor a reactant's initial electron transfer as well as its return to original form, and is useful for deriving the respective diffusion coefficients of each process.

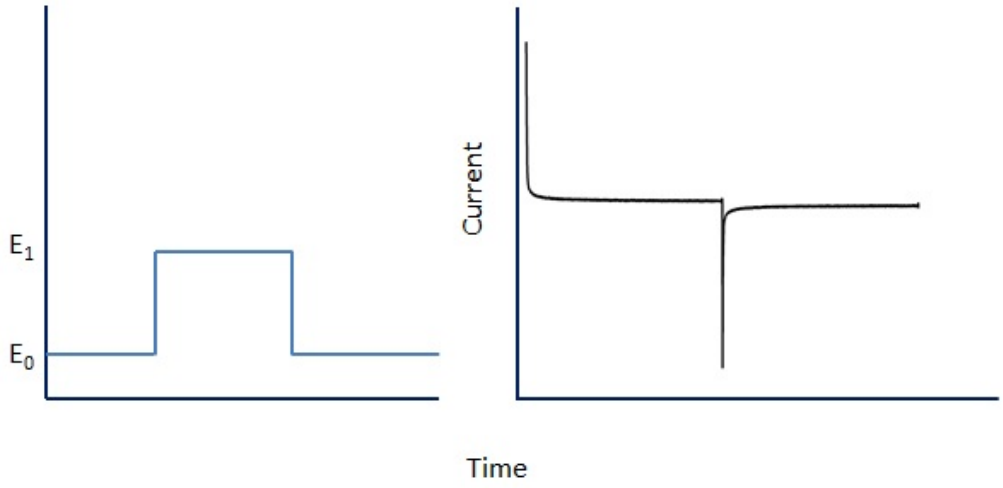


Figure 5: A schematic showing a) the potential sequence with time of b) a typical double-step chronoamperogram.

For the first step, the above Shoup and Szabo expression is used to extract the concentration and diffusion coefficient, but for second step, no such analytical expression exists, and so numerical simulation must be performed.[25] Knowing the number of electrons being transferred, this methodology allows the deduction of both the concentration and the diffusion coefficients of species A and the diffusion coefficient of species B. Chronoamperometry is also used in Chapters 4 – 6 to detect individual nanoparticles as they undergo oxidation at the electrode surface. This results in a sharp increase in current, which can be integrated to provide the charge, and therefore the size of the nanoparticle.

0.1.5.2 Cyclic Voltammetry on a Macroelectrode

The second technique is Cyclic Voltammetry (CV), where the potential is varied linearly with time, and then returned to its original potential (see Figure 6).[1] The rate at which the potential is varied is called the scan rate (ν). The output of this

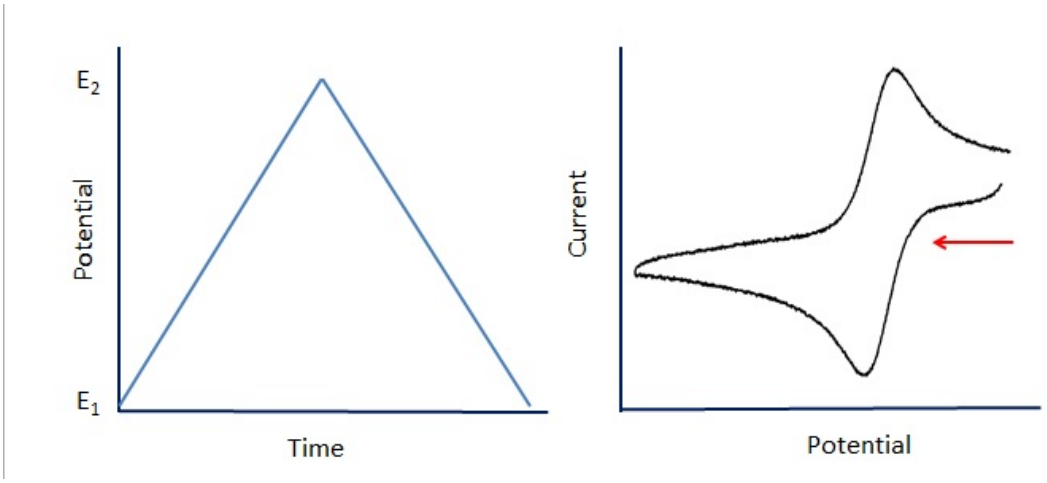


Figure 6: A schematic showing the potential sequence with time for a CV, and the resultant plot.

process is a current, I, vs potential, V, plot, termed a CV. The shape of the cyclic voltammogram is heavily influenced by the mass transport, and the size of the working electrode, which results in very different voltammetry on macro and micro electrodes.

First, the voltammetry on a macroelectrode will be considered. The shape of the voltammetry on a macroelectrode can be understood as a balance between electron transfer and diffusion.[1] As the potential is swept from E_1 to E_2, the current increases approximately exponentially as species A undergoes electron transfer, until it reaches the point at which the mass transport is limiting as species A is depleted, resulting in a peak at the maximum current. The thick diffusion layer now present then results in a slow falling off of the current.

The shape of the observed voltammetry is governed by the magnitude of the heterogeneous rate constant, k^0, and the scan rate. In some instances, this may place restrictions on the parameters which may be extracted. Three cases are discussed below.

0.1.5.3 Reversible voltammetry

If k^0 is large, defined by Matsuda and Ayabe[26] if $k^0 \geq 0.3\ \nu^{0.5}$ cm s^{-1}, then "reversible" electrode kinetics will be observed. In this limit, at the electrode surface $A + e^- \leftrightharpoons B$ is at equilibrium, meaning that the Nernst Equation applies. Therefore, the resultant voltammogram is insensitive to the value of k^0, the wave-shape and the peak separation are fixed ($\Delta \mathrm{E}_p = 59$ mV). This means an actual value of k^0 cannot be extracted, *via* simulation or any other means. All that can be said is that k^0 is above a certain value. Simulated examples of this kind of voltammetry are shown in Figure 7 (circles and line 1). At the reversible limit, the peak current can be described by the Randles-Sevčik equation:[27,28]

$$i_p = (2.69 \times 10^5) n^{1.5} A D_A^{0.5} \nu^{0.5} C \tag{27}$$

where n is the number of electrons, A is the area of the electrode, D_A is the diffusion coefficient, ν is the scan rate, and C is the bulk concentration.

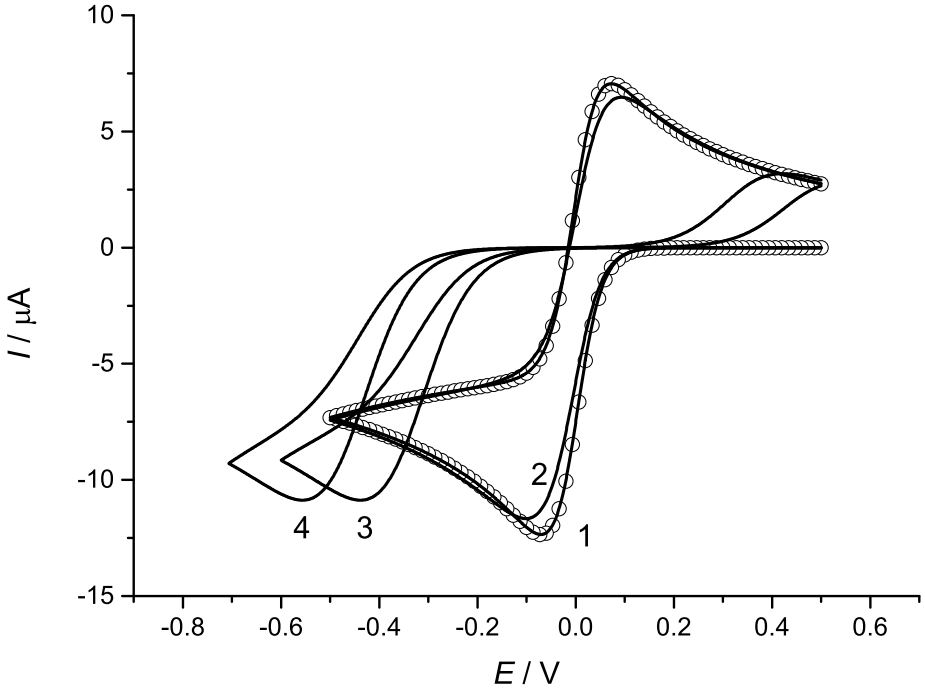


Figure 7: Simulated voltammograms showing the effect of changing the value of k^0 on a macroelectrode. Simulated using the Butler-Volmer model with $r_e = 1$ mm, $D_{\mathrm{A}} = 1 \times 10^{-5}$ cm^2 s^{-1}, $C^*_{\mathrm{A}} = 1$ mM, $\alpha = 0.5$, $E^{\ominus}_{\mathrm{f}} = 0$ V and a fast rate constant of $k^0 = 10$ cm s^{-1} (circles), 1 cm s^{-1} (line 1), 0.01 cm s^{-1} (line 2), 1×10^{-5} cm s^{-1} (line 3) and 1×10^{-6} cm s^{-1} (line 4).

0.1.5.4 Quasi-reversible voltammetry

If k^0 is intermediate in value, defined[26] as $0.3\ \nu^{0.5} > k^0 > 2 \times 10^{-5}\nu^{0.5}$ cm s^{-1} then both the wave-shape and peak separation are sensitive to it. The forward and (if present) reverse peaks become more separated for smaller values of k^0, and the waves become less steep with a smaller peak height. If both peaks are present, then both the peak separation and waveshape can be used while fitting experimental data to simulations to deduce a value of k^0. If the back peak is absent, then the waveshape alone can be used. An example of quasireversible voltammetry is shown in Figure 7 (line 2).

0.1.5.5 Irreversible voltammetry

In the limit of small k^0, where $k^0 \leq 2 \times 10^{-5}\nu^{0.5}$ cm s^{-1},[26] the waveshape once again becomes insensitive to the the value of k^0, but peak separation continues to increase as k^0 decreases. If then a forward and reverse peak are both observed, k^0 can be determined from the peak separations. If, however, a back peak is not observed (either because it falls outside the potential window or because of a homogeneous reaction trapping the species which would be involved in the formation of this peak) then all we have is a wave-shape, which is insufficient to establish a value for k^0. Instead, all which may be reported for a reduction is a composite parameter $k^0\exp\left(\frac{\alpha E_f^{\ominus} F}{RT}\right)$. Changing k^0 in a simulation will simply move the voltammetric wave to more negative potentials for smaller k^0, and vice versa. The original response can then be recovered by changing $E_f^{\ominus}$ appropriately. Simulated voltammograms exemplifying this are shown in Figure 7 (lines 3 and 4). The peak current, i_p, is described by the irreversible Randles-Sevčik equation:

$$i_p = (2.99 \times 10^5)n(n^{'} + \alpha)^{0.5} A D_A^{0.5} \nu^{0.5} C \tag{28}$$

where n is the number of electrons transferred overall, n$^{'}$ is the number of electrons transferred in the rate determining step, α is the transfer coefficient, A is the area of the electrode, D is the diffusion coefficient, ν is the scan rate, and C is the bulk concentration.

0.1.5.6 Cyclic Voltammetry on a Microelectrode

The altered, convergent, diffusion regime experienced on a microelectrode means that, providing the rate of mass transport is sufficiently fast, the electroactive species is being constantly delivered to the electrode surface, and the current reaches a steady state. As shown in Figure 8, this results, at modest voltage scan rates, in the loss of

the peaks observed when using a macroelectrode.

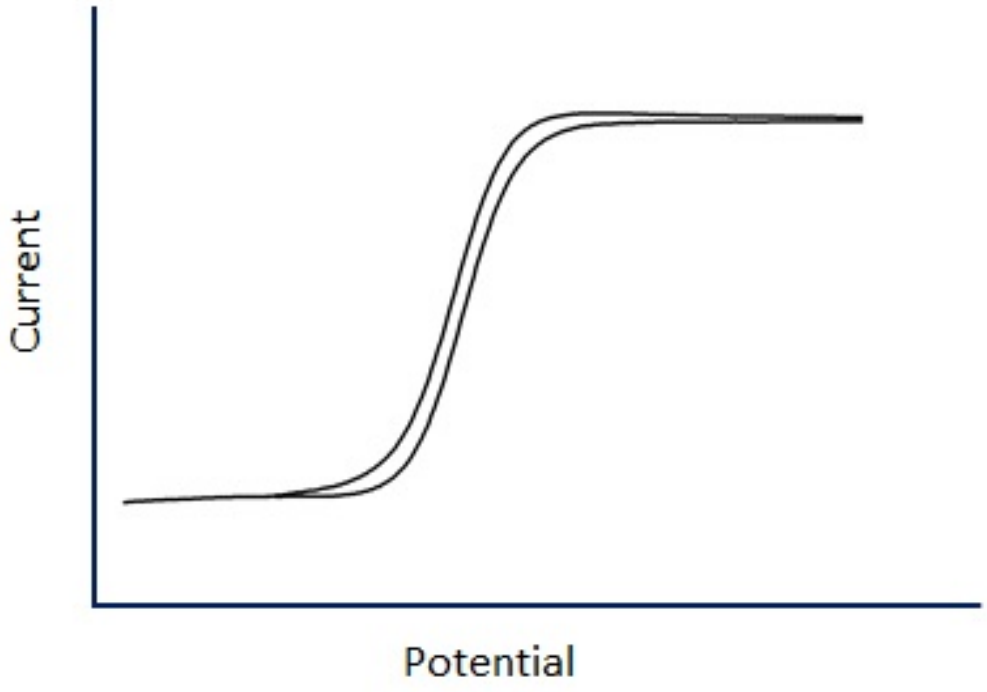


Figure 8: A typical CV performed on 10 μM metallic microelectrode.

The steady-state current is the related to the radius of the electrode by:

$$i_{iss} = -4nFD_ACr \tag{29}$$

Planar diffusion begins to once again affect the shape of the voltammogram in cases of sufficiently high scan rates or very slow diffusion, such as in particularly viscous solvents, such as Room Temperature Ionic Liquids, which will be introduced in the coming section.

0.2 Room Temperature Ionic Liquids

All of the experiments contained within this thesis were conducted in Room Temperature Ionic Liquids (RTILs), and this section acts as an introduction to this class of solvents, their properties, and the voltammetry that has been reported.

0.2.1 What are Room Temperature Ionic Liquids?

RTILs are salts with melting points below room temperature.[29] They typically consist of asymmetric, bulky cations, and inorganic anions.[30] The high coulombic forces between the cations and anions lower their melting points, resulting in inherently conductive liquids for use as solvents in a vast range of applications, such as batteries, fuel cells, and as synthetic solvents.

Typical cations include the imidazolium, pyrrolidinium, tetraalkylphosphonium, tetraalkylammonium and pyridinium salts. Anions include simple halides, such as chloride and bromide (these are often solid at room temperature), tetrafluoroborates, and *bis*(trifluoromethylsulfonyl)imides. A selection of different anions and cations is shown in Figure 9.

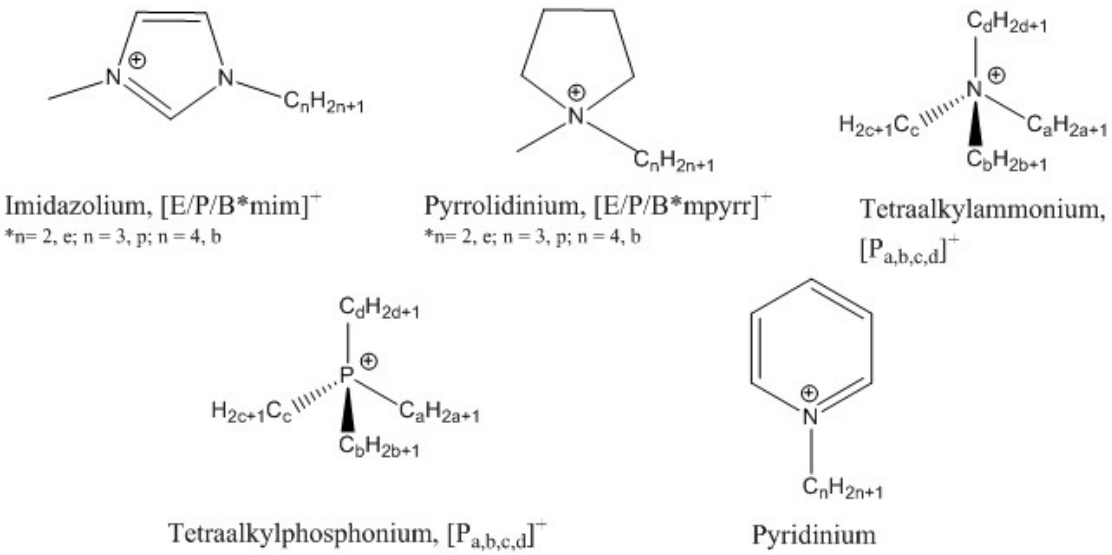


Figure 9: Structures of commonly used cations and anions that make up RTILs, along with the abbreviations used.

Any combination of anion and cation forms an ionic liquid, and as will be discussed in the coming subsection, this tuneability is one of the characteristics that make RTILs interesting solvents.

0.2.2 Why Ionic Liquids?

Along with their inherent conductivity, RTILs have a number of other favourable properties that make them interesting solvents, such as low volatility, and negligible vapour pressure,[31] recyclability,[32] and the ability to tailor a number of physiochemical properties to the desired application by careful selection of the cation and anion.[33] An in-depth exploration of the various properties will be covered in the next subsection. RTILs are currently used commercially for a number of applications, most commonly in fuel cells,[34] light-emitting cells,[35,36] solar cells,[37] lithium batteries,[38] and as electrochemical sensors.[39] They have a special appeal as electrochemical electrolytes as their relative stability means that they provide a very wide electrochemical window within which to explore previously inaccessible electrochemical processes.[40]

0.2.3 Properties of RTILs

The physical properties of each RTIL can vary greatly depending on the components chosen. Below are the major properties to be considered: viscosity, density, conductivity, and electrochemical window. These values for a range of commonly used RTILs and conventional solvents are summarised in Table 2.

0.2.3.1 Viscosity

RTILs tend to possess viscosities of one-to-two magnitudes above that of conventional solvents, and this has ramifications for the mass transport of electroactive species during electrochemical experiments. The viscosities of RTILs are primarily due to hydrogen bonding and van der Waals (vdW) forces, as an increase in vdW forces results in more energy being required for molecular movement.[29,51,52] As can be seen in Table 2, the effect of the cation on the viscosity of a RTIL is related to the number of alkyl substituents, whereby an [Emim] based RTIL is less viscous than a [Bmim] based RTIL, for example, which is consistent with increased vdW forces. The anion

Ionic Liquid	Viscosity (η, cP)	Density (ρ, g cm^{-3})	Conductivity (κ, mS cm^{-1})	Electrochemical Window (EW, V)
[Emim][NTf_2]	34[33]	1.53[41]	8.8[33]	4.3[40]
[Bmim][NTf_2]	52[33]	1.44[41]	3.9[33]	4.8[40]
[Omim][NTf_2]	74[42]	1.33[41]	-	5.0[40]
[Bdmim][NTf_2]	105[43]	1.42[41]	2.0[44]	5.2[40]
[Bmim][BF_4]	112[43]	1.21[45]	1.7[45]	4.7[40]
[Bmpyrr][NTf_2]	89[43]	1.4[41]	2.2[46]	5.2[40]
[$N_{6,2,2,2}$][NTf_2]	167[47]	1.27[47]	0.67[48]	5.4[40]
[$P_{14,6,6,6}$][NTf_2]	450[49]	1.07[41]	-	5.0[40]
[$P_{14,6,6,6}$][FAP]	464[41]	1.18[41]	-	5.6[40]
Acetonitrile	0.34[50]	0.79[50]	7.6[50]	5.0[2]
N, N-Dimethylformamide	0.92[50]	0.94[50]	4.0[50]	4.3[2]
Dimethylsulfoxide	1.99[50]	1.10[50]	2.7[50]	4.4[2]

Table 2: Literature values for viscosity (η, cP), density (ρ, g cm^{-3}), conductivity (κ, mS cm^{-1}), and electrochemical window (EW, V) on a platinum electrode in a range of RTILs and molecular solvents at 293 K. The values measured in molecular solvents contain 0.1M TBAP.

plays a greater role in determining the viscosity of the solvent, with anions possessing greater numbers of fluoride anions ($[BF_4]^-$ or $[FAP]^-$, for example) being much more viscous than weakly coordinating anions ($[NTf_2]^-$, for example). This is due both to the strong H—F interactions between the anions and the cations in the former case, and the delocalised negative charge in the latter case. Both temperature and the introduction of co-solvents can affect the viscosity dramatically, with a 20% change over 5 K observed around room temperature in a range of imidazolium-based RTILs.[53]

0.2.3.2 Density

The density can be an important solvent property where mass-sensitive applications are concerned, such as in batteries or fuel cells. In general terms, RTILs are denser than other organic solvents and water. As noted in the third column of Table 2, the density of RTILs tends to lie between 1 — 1.6 g cm^{-3}. With respect to the imidazolium cation, the addition of alkyl substituents decreases the density, due to the lower density of the CH_2 group relative to the imidazolium ring.[54,55] Similarly to the cation, the greater the alkyl chain length in the anion, the smaller the reported density. The addition of fluorine also results in an increased observed density. The general trend with respect to the anions is:

$$[BF_4]^- < [OTf]^- < [PF_6]^- < [NTf_2]^- < [FAP]^- \tag{30}$$

Densities of RTILs decrease approximately linearly with increasing temperature, as occurs with many other materials.[42,56,57]

0.2.3.3 Conductivity

Conductivity is a critical property when using RTILs as solvents in electrochemistry. Because RTILs are composed entirely of ions, one might expect their conductivity

to be very high. This is not what is observed (see column four of Table 2). This is primarily due to their high viscosities, and large components, because the ability for the charge carriers to freely move through solution is hindered. This therefore results in a similar conductivity to what is observed using a conventional aprotic solvent with added supporting electrolyte (such as tetrabutylammonium perchlorate). Generally, the conductivity of a RTIL is inversely proportional to its viscosity,[58] as can be seen with the [Emim] and [Bmim] imidazolium RTILs, with viscosities of 34 and 52 cP respectively, and conductivities of 8.8 and 3.9 mS cm^{-1}.[58] The structure of the cation also has affect on the ionic liquid's viscosity, with a planar cationic core,[40] as is observed in the case of the imidazolium cation, favouring greater conductivity, and bulkier cores, such as the ammonium or phosphonium cations, demonstrating lower conductivity. Conductivity increases with temperature, as the viscosity decreases, allowing greater mobility of the ions.[59]

0.2.3.4 Electrochemical Window

The electrochemical window refers to the potentials at which the solvent does not undergo oxidation or reduction, and is defined by the potential difference of the anodic and cathodic decomposition potentials.[60] It is specific to the experimental conditions, including the working electrode material, the scan rate, temperature, and other impurities in the solvent, such as water (the impact of water and other impurities will be discussed in detail in a later subsection). Ionic liquids possess much larger electrochemical windows than aqueous solvents,[2] and slightly larger windows than non-aqueous solvents, as shown in Table 2. The imidazolium cation is the most vulnerable to reduction, due to the presence of the C2 proton which is fairly easily removed, whilst the ammonium, phosphonium, and pyrrolinidinium cations show greater stability. This is confirmed by analysing the electrochemical window of the substituted imidazolium, which shows an increase in electrochemical window of 0.4V.

The general trend for stability is:

$$[Cmim]^+ < [Cmpyrr]^+ < [N_{a,b,c,d}]^+ < [P_{a,b,c,d}]^+ \tag{31}$$

The oxidative limit is largely controlled by the anion, with the FAP anion displaying the greatest stability, and halides displaying the least. The anions follow this order in terms of stability, where X is a halide:

$$[FAP]^- > [NTf_2]^- > [BF_4]^- > [PF_6]^- > X^- \tag{32}$$

0.2.4 Synthesis

The simplest, and most commonly used, synthesis of RTILs, shown in Figure 10, involves the alkylation of a methylimidazole or amine followed by a salt metathesis performed with the desired anion.

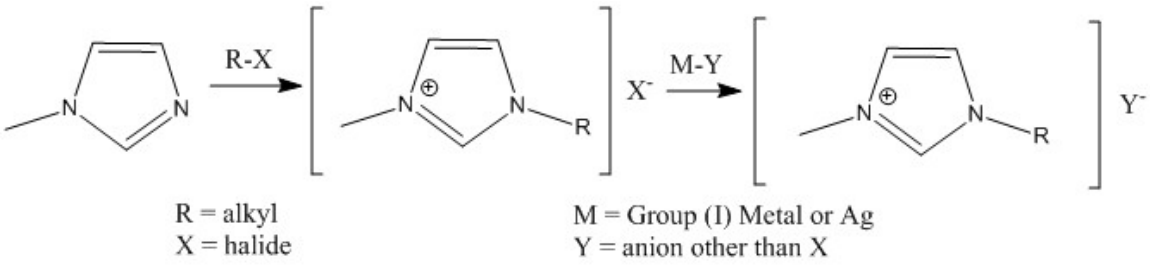


Figure 10: Synthesis of an imidazolium-based RTIL.[33] Pyrrolindium, tetraalkylammonium, tetraalkylphosphosium based ILs are also synthesised using similar methods.[46,49,61,62]

This two step synthesis is the source of at least two of the most common impurities reported in RTILs: imidazole or amine contamination and halides. Any unreacted methylimidazole proves difficult to remove in the later stages, since common purification techniques, such as column chronomatography, prove to be much more difficult with RTILs than other synthetic products, especially as typically used sorbents are

known to contaminate ionic liquids.[63] The second step, whereby an alkali metal or a silver salt is mixed with the intermediate product to yield the desired anion, is prone to result in halide impurities. The standard test for removal of halide impurities is the silver nitrate test, which results in a detection limit of 1.3×10^{-5} mol L^{-1}.[64]

0.2.5 Common Impurities and Their Effects on Reaction Outcomes

The three most common impurities in RTILs are water, halides, and dissolved gases, such as oxygen. The effect of each of these on the properties of the RTIL will be explored in detail below.

0.2.5.1 Water

Water tends to be the most ubiquitous impurity present in RTILs, and great care must be taken to ensure its removal because, as evidenced below, water content can have a big affect on the physiochemical properties of the RTIL. Some RTILs are more hydrophilic than others, and this means a higher baseline of water will be present even with the use of high vaccuum. Table 3 summarises the relative amounts of water present in a range of RTILs under different conditions to illustrate this, with water content being quantified using Karl Fischer Titration.[40,65] Table 3 also demonstrates the huge effect water has on the size of the electrochemical window.

The addition of water also has a dramatic effect on the viscosity, and as a result, conductivity and diffusivity of species within the RTIL. When 0.19% water is added to [Bmim][PF_6], for example, its viscosity decreases by 17%, whilst a 1% addition of water to [Emim] and [Bmim][NTf_2] results in a 30% decrease in viscosity.[66] Water impurities can also have a significant effect on the diffusion of electroactive species through a RTIL. In the presence of *ca.* 5% water in [Bmim][PF_6], the diffusion coefficient of N, N, N', N'-tetramethylphenylenediamine (TMPD) nearly doubles. An

order of magnitude increase has also been reported for the diffusion of methylviologen.[67] For these reasons, exposing the sample of RTIL to high vacuum before use is critically important.

0.2.5.2 Halides

As detailed earlier, the synthetic process by which RTILs are prepared is prone to the introduction of halide salts. The presence of halides in imidazolium-based RTILs has been reported to dramatically increase the viscosity of the solvent.[68] In addition to this, the easily-oxidised halides shorten the electrochemical window, and have been reported to decrease the anodic limit by up to 0.9 V on gold electrodes due to the oxidation of gold surface chloride.[69] Along with the above affects, halides have been documented to affect synthetic reaction outcomes. Gallo *et al.*[70] reported that halide impurities significantly affected the rate of nickel catalysed Michael reactions, with ytterbium and iron catalysis experiencing a complete suppression. Chloride, even in trace amounts, has been shown to poison catalysts in other contexts,[71] including hydrogenation.[72,73] Halides have also been known to participate in reactions as ligands, reactants, or nucleophiles.[74]

0.2.5.3 Dissolved Gases

The final impurity to be detailed is potential interference of atmospheric gases. The removal of oxygen in particular is a challenging but necessary preparative step before electrochemical analyses are undertaken. If oxygen reduction is not the target reaction, the process can obscure the desired electrochemical process, or even react with the desired electroactive species. Atmospheric oxygen is generally moist, which amplifies its impacts (as detailed above). Wet oxygen in the presence of a proton source undergoes an irreversible electron transfer to superoxide, then hydrogen peroxide, followed by water,[75] obscuring the entire reductive region past - 0.5 V vs Ag.

Ionic Liquid	Atmospheric/ppm	Vacuum-dried/ppm	Wet/ppm	Electrochemical Window/V, dry	Electrochemical Window/V, wet
[Emim][NTf_2]	3385	105	19,940	4.3	2.6
[Bmim][NTf_2]	491	144	5680	4.8	2.8
[Bdmim][NTf_2]	504	295	9868	5.0	2.9
[Bmim][I]	11,349	1050	Miscible	2.2	1.6
[Bmim][BF_4]	5083	119	Miscible	4.7	2.0
[Bmpyrr][NTf_2]	406	133	11,407	5.2	2.0
[$N_{6,2,2,2}$][NTf_2]	1150	167	8200	5.4	2.2
[$P_{14,6,6,6}$][FAP]	328	-	-	5.6	1.8

Table 3: Literature values for water content of atmospheric, vacuum-dried, and wet RTILs, plus the electrochemical windows of dry and wet RTILs.[40]

Other gases, such as carbon dioxide,[76] which has a high solubility in RTILs, and argon,[77] have been documented to affect the diffusion coefficient of the electroactive species. It is for this reason that experiments are put under high vacuum before use, and where possible (excluding the experiments undertaken with oxygen), thoroughly degassed with Argon, and introduced into a glove box, prior to the recording of any voltammetry.

0.2.6 Fundamental Electrochemistry in Room Temperature Ionic Liquids

This section briefly summarises the existing literature of electrochemical studies undertaken in RTILs. This takes two parts - first, consideration of the voltammetry and affect of RTILs on the waveshapes and diffusion coefficients, and second the structure of the double layer.

0.2.6.1 Voltammetry in RTILs

RTILs, once they have been carefully prepared as detailed in the previous subsection, can be used as solvents in electrochemical experiments without any additional difficulties compared with molecular solvents. Their intrinsic conductivity, as detailed above, simplifies the experimental set-up as it means that no supporting electrolyte is necessary, in contrast with molecular solvents, and ensures that mass transport effects due to migration can be neglected. Once dried, their large electrochemical windows can facilitate the measurement of redox reactions that occur at high potentials, either positively or negatively, that may not be possible to capture in aqueous solvents. However, their large viscosities mean that interpretation of the voltammetry must be approached with caution. In particular, the use of RTILs can result in a one to two order of magnitude decrease in the diffusion coefficients of the electroactive species of interest. This has implications on the measurement of a steady-state current:

$$i_{ss} = 4nFD_ACr \tag{33}$$

In order to measure a full steady-state current, the following inequality must be adhered to:[1]

$$\nu << \frac{RTD_A}{nFr^2} \tag{34}$$

Using a D of 1×10^{-11} m^2 s^{-1} and an electrode of radius 5μM, scan rates of <10 mV s^{-1} need to be employed to accurately measure a steady-state current. At higher scan rates, the voltammogram will tend to become peak-shaped and a true steady-state current will not be measured. Chronoamperometry is the technique of choice in this thesis to measure diffusion coefficients and concentrations experimentally, as detailed in the 'Voltammetric Techniques' section above. With a known radius and number of electrons transferred, the Shoup-Szabo[24] equation can be fitted to experimental data to calculate both D and C with 0.6% error.

The other outcome of using RTILs as solvents in electrochemical experiments is that ions tend to move much more slowly through solution than their neutral counterparts. Consider oxygen, which is analysed in detail in Chapters 1 and 3, with a diffusion coefficient of 1.5×10^{-10} m^2 s^{-1} in $[N_{6,2,2,2}][NTf_2]$.[78]

At scan rates of 10 - 500 mV s^{-1} on electrodes < 50 μM, the voltammetry of the reduction of oxygen to superoxide (see Figure 11) is steady-state in nature as a result of convergent diffusion to the electrode surface. The charged superoxide has a diffusion coefficient of 4.7×10^{-12} m^2 s^{-1} in this ionic liquid, which induces planar diffusion to the electrode, and the resulting voltammetry shows a transient response. Along with different diffusion regimes being present in one voltammogram, this work emphasises that the commonly-held assumption of equal diffusion coefficients, often made in molecular solvents, cannot be made when using ionic solvents.

One benefit of slow diffusion in RTILs is that microelectrodes can be used to

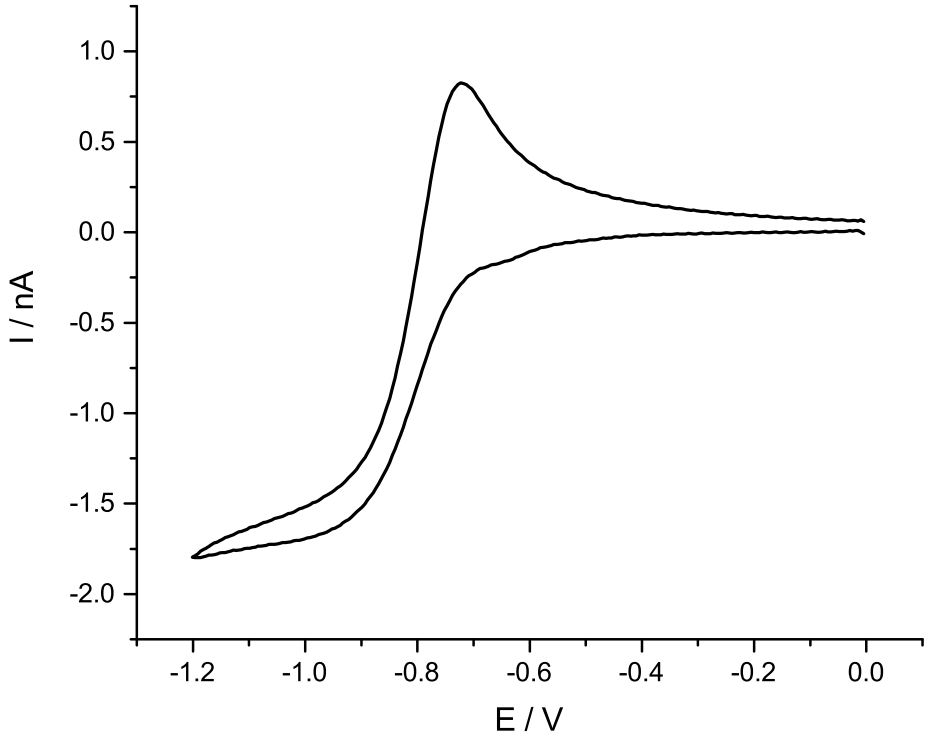


Figure 11: The electroreduction of oxygen to superoxide in $[N_{6,2,2,2}][NTf_2]$ on a micro gold electrode (5μM in radius) at 200 mV s^{-1}.

analyse approximate planar diffusion,[†] and provide information for mechanistic and kinetic studies. In reality, simulation is needed as the diffusion regime is a mixture of linear and convergent. The consideration of the affect of ionic solvents on the electron transfer kinetics, and in particular the electrochemical rate constant, k^0, has been undertaken in the literature by Hapiot,[79] Bond,[80] Doherty,[81] and Compton.[82–84] The magnitude of k^0 in RTILs and their relationship with Marcus theory will be discussed in full in the Introduction to Part III.

The high current density and low ohmic drop are other benefits conferred with the use of microelectrodes. In addition to this, the low currents produced mean that a two electrode system can be employed, with a silver wire being used as a counter electrode and a pseudo-reference electrode. This set-up greatly reduces the volume of ionic liquid required to construct an electrochemical cell, which along with minimising waste allows drying, degassing, and saturating solutions to occur on a much shorter timescale. As such, almost all of the work is carried out on metallic microelectrodes in this thesis.

The other consideration is taking care to ensure that the analyte has replenished itself at the electrode surface between scans, otherwise there will be disparities in the actual and measured concentration. In less viscous solvents, one can achieve this by leaving the system at rest for 2 -3 minutes between scans. However, provisions for ensuring this is the case in the more viscous RTILs involve leaving the experimental set-up at open circuit potential for at least 15 minutes between scans.

0.2.6.2 Double Layer Capacitance

Consideration of the structure of the double layer at the electrode-solvent interface is vital, especially as the variation of the double layer with potential can affect electrode processes. Its effect is most dramatic when low Faradaic currents are present, for

[†]Although note that rarely is pure planar diffusion observed.

example where the analyte is in low concentrations, and the charging current is the dominant contribution to the measured current.[2]

The structure of the double layer in RTILs cannot be explained by the diffuse double layer model proposed by Stern[7] introduced earlier in the Introduction. It is an active field of research and as such, many questions are still unanswered. The following subsection briefly summarises the present work, from simulation to experiment-based studies, to give a representative view of the current consensus of the structure of the double layer in RTILs.

Mean-field theories are often the first port of call to describe complex statistical-mechanical systems, and can act reference points for more sophisticated theories. In 2007, Kornyshev[85] employed a mean field theory of a double layer at a flat interface, using simple principles of the lattice gas model. This yielded a lattice-saturation parameter, ϕ, where 1 - ϕ describes the portion of free volume available. This value varies between RTILs, but in most cases is equal to or above 0.5.[86] As ϕ approaches 1, an effect known as lattice saturation, or crowding, occurs, as the component ions become very tightly packed.[87] The value of ϕ affects the shape of the capacitance-voltage plot,[‡] with a value $>1/3$ resulting in a bell-shaped curve, and $\phi < 1/3$ resulting in a camel-shaped curve (see Figure 2 of reference[85]). This analysis is also capable of a crude modification that takes into account asymmetry of ion sizes. However, mean-field theories fail to take into account strong Coulomb correlations,[88] which are particularly important in an ionic solvent, and this results in an overestimation of capacitance at small electrode potentials.

Next, direct simulations were used to model the behaviour of the double layer. First, simple, or coarse grain, models, will be considered, followed by molecular models. Coarse grain models, which considered spherical particles in dense liquid-like assemblies,[89,90] showed first that the capacitance takes a bell shape as a function

[‡]Note that a typical Gouy-Chapman capacitance-voltage plot takes a U shape.[86]

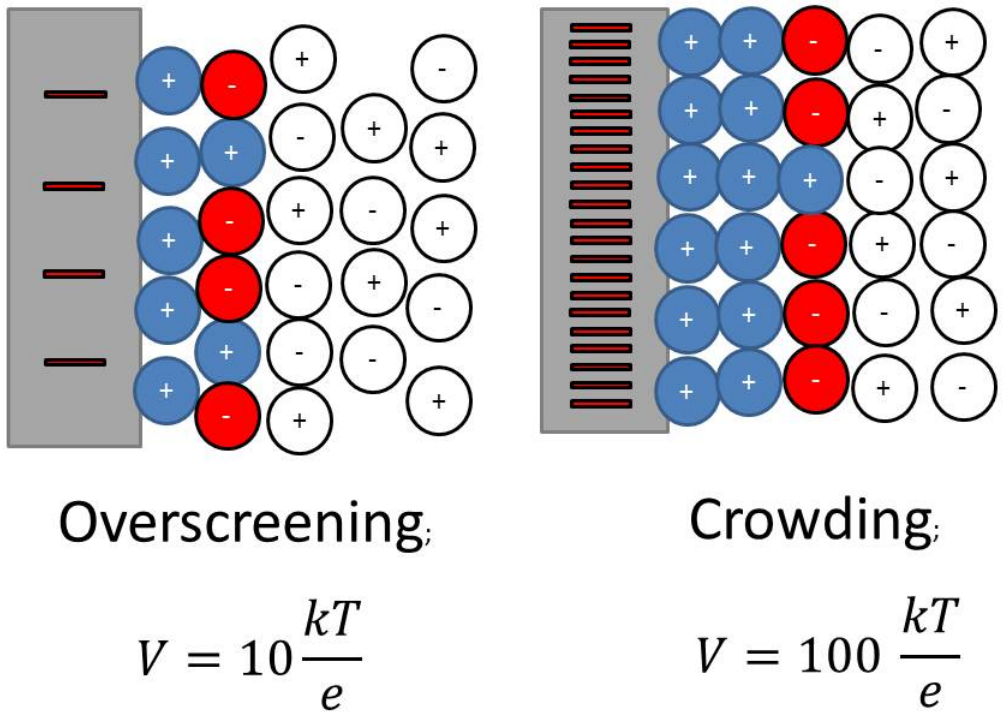


Figure 12: The structure of the double layer. At a moderate voltage, counterions overscreen the charge on the electrode, and a layer of coions overcompensates until electroneutrality is reached. At a high voltage, the counterions form two monolayers, and the third layer consists of an excess of coions.

of potential, secondly, that at small electrode potentials, a substantial overscreening effect occurs as the double layer takes on an oscillating structure, where anions and cations alternate in layers, and thirdly, that at large electrode polarisations, this effect is replaced by lattice saturation. The term overscreening refers to the phenomenon of a monolayer of counterions, which exceed the charge on the electrode, being followed by a layer in which the oppositely charged particles overcompensate, and so on until electroneutrality is reached, as shown in Figure 12.[88,91]

This overscreening behaviour corrects the erroneously high capacitance at low electrode potentials seen using mean-field theory, and is consistent with experimental

observations. Bazant *et al.*[91] developed a phenomenological Gibbs energy function to describe a propensity for oscillating profiles in the charge and potential distribution at the interface. This theory covers both the overscreening and crowding regimes through essentially one parameter, and despite being phenomenological, was able to accurately reproduce the work of Federov and Kornyshev.[89] Demery *et al.*[92,93] have also reported a Coulomb gas model that has obtained an exact solution of the double layer at an electrode in RTILs, albeit under one dimensional conditions, which enables with some certainty to state that the overscreening is as a result of Coulomb correlations.

Fully atomistic models, using realistic force fields representing interionic interactions, were then employed to get a more refined picture of the molecular structure of RTILs in the double layer. Feng *et al.*[94] studied the individual double layers composed of [Bmim][NO_3]. As the electrode was held at a positive potential, a large increase in the density of anions was observed adjacent to the electrode, followed by a layer of cations, with a partial overlap occurring due to the cations being much larger than the anions, with several layers being observed overall. The opposite occurs when the electrode is held at a negative potential. The [Bmim] cation is persistently adsorbed at the electrode surface, even when the electrode is held at a slightly positive potential, due to increased van der Waals interaction between the cation and the electrode, which is much less apparent with the anions. Lynden-Bell *et al.*[95] corroborated the above findings, as well as reporting that at low negative electrode potentials, the cations orient parallel to the electrode surface, whereas at high potentials, they orient perpendicularly to maximise the density of ions in the first layer.

Experimentally, the magnitude of the capacitance in [Bmim][PF_6] has been measured by electrochemical impedance spectroscopy as 6—7 μF cm^{-2},[96] however serious doubts have been cast on the validity of the method, with Wang and Pilon reporting on its intrinsic limitations to estimate capacitance.[97] Beyond a precise value for ca-

pacitance, other properties of the double layer have been determined experimentally. Mezger *et al.*[98,99] used high energy X-ray reflectivity data to show unambiguous oscillating overscreening patterns of charge distribution, whilst Yamamoto *et al.*[100] used X-ray reflectometry at different potentials to show a weakening of this effect when +/- 3 V was applied to the system. This study did not use high enough voltages to see a complete transition to overcrowding, and this phenomenon was attributed to the presence of the alkyl chain on the pyrrolidinium cation resisting lattice saturation. Atomic Force Microscopy was used to study the Au (111) interface with [Bmpyrr] and [Emim][FAP], which showed between 4 — 7 layers present, with negative electrode potentials stabilising the layering.[101] Where the length of the alkyl chain is increased such that n = 8 or 10, a bilayer structure was observed, involving full interdigitation of the alkyl chains.[102] However, Baldelli has challenged the presence of multilayers, stating that under certain charge density regimes, a single monolayer of counterions adjacent to the electrode are observed.[103] Kirchner *et al.*[104] attempted to reconcile this through the use of molecular dynamics simulations, which suggest that the multilayer can undergo structural transition to a monolayer, and the point at which this occurs is decided by the balance of surface-counterion attraction and ion-ion steric repulsion.

Observations of increased capacitance with temperature have been documented by several reports,[105–109] however, other studies show conflicting, and in some cases, opposite results.[110,111] It remains unclear if a generalised relationship of capacitance with temperature can be stated for all RTILs, and looks to be dependent on electrode material.

As discussed above, the composition of the double layer in RTILs is still very much under consideration, although the effects of crowding and overscreening necessarily distinguish RTILs from dilute electrolytes. Where necessary, the capacitative component of the experimental voltammetry in this thesis has been subtracted prior

to analysis to minimise its effect.

0.3 Metallic Nanoparticles

Part IV is concerned with the dynamics of silver nanoparticles (Ag NPs) in RTILs. The following section details the growing interest in nanomaterials, what analysis techniques are currently used, and the limitations of aqueous solvents in characterising and understanding microscopic interactions of nanoparticles with their environments.

0.3.1 What are nanoparticles?

Nanoparticles are defined by IUPAC as clusters of atoms that have at least one dimension between 1 — 100 nm.[112] They are of interest due to the fact that they often possess properties that deviate from bulk material of the same atomic structure. Many metallic nanoparticles have special optical properties due to the existence of plasmonic resonances (which will be explained in more detail in Section 0.3.3.3).[113,114] As Ag NPs decrease in size to subnano (<2 nm), the energy continuum found in bulk metal breaks down, leading to fluorescent properties that are not found in bulk silver.[115] NPs also possess a much larger surface-to-volume ratio than larger particles, increasing the percentage of atoms on the surface, and this can affect the outcomes of reactions in which they are a substrate or a catalyst.

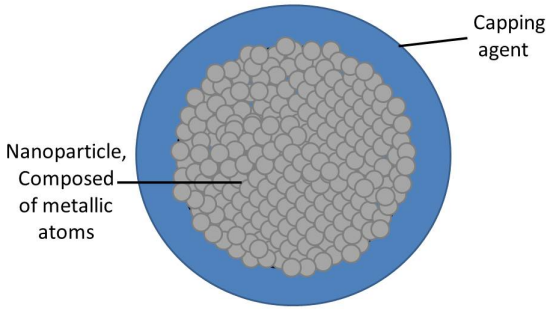


Figure 13: A silver nanoparticle, made up of a large number of silver atoms, and partially stabilised by a capping agent.

Typically, metallic nanoparticles use a capping agent is to stabilise the constituent atoms, which can also affect their properties.

0.3.1.1 Capping Agents

The stability of a metallic NP is governed largely by the choice of capping agent,[116] which is added to prevent aggregation and agglomeration of the nanoparticles. One of the other advantages of this capping agent control is that it provides the opportunity to customise the NP for an application. A selection of common capping agents are shown in Figure 14 and include citrate, polyethylene glycol (PEG), polyvinylpyrrolidone (PVP), and branched polyethylenimine (BPEI).

Capping agents can work to stabilise the silver core in four ways.[117,118] The first is electrostatic stabilisation, whereby the NP is stabilised by charged molecules that repel other NPs in solution, preventing aggregation. The second is steric stabilisation, which works by attaching a sterically bulky molecule to the surface of the nanoparticle. Thirdly, a NP can be stabilised by hydration, where a layer of water coats the surface.[119] Lastly, depletion stabilisation,[120] sees free polymers in solution stabilise the NPs by surrounding them and creating a repulsive field. Citrate capping agents are an example of electrostatic stabilisation, whilst polyethylene glycol (PEG) stabilise the NP sterically. Citrate capped NPs are frequently used for a variety of applications, whilst PEG modification is particularly valued in contexts with high ionic strength. Specifically, PEG capped NPs have been used in medical applications, where their use has been proposed to allow for the targeted delivery of drugs.[121] Although it is known that alteration of the capping agent can dramatically affect the nanoparticle - size, shape, and interaction with the solvent - effects of the capping agent on microscopic solution dynamics are still not well understood and will be explored in Chapter 6 of the thesis.

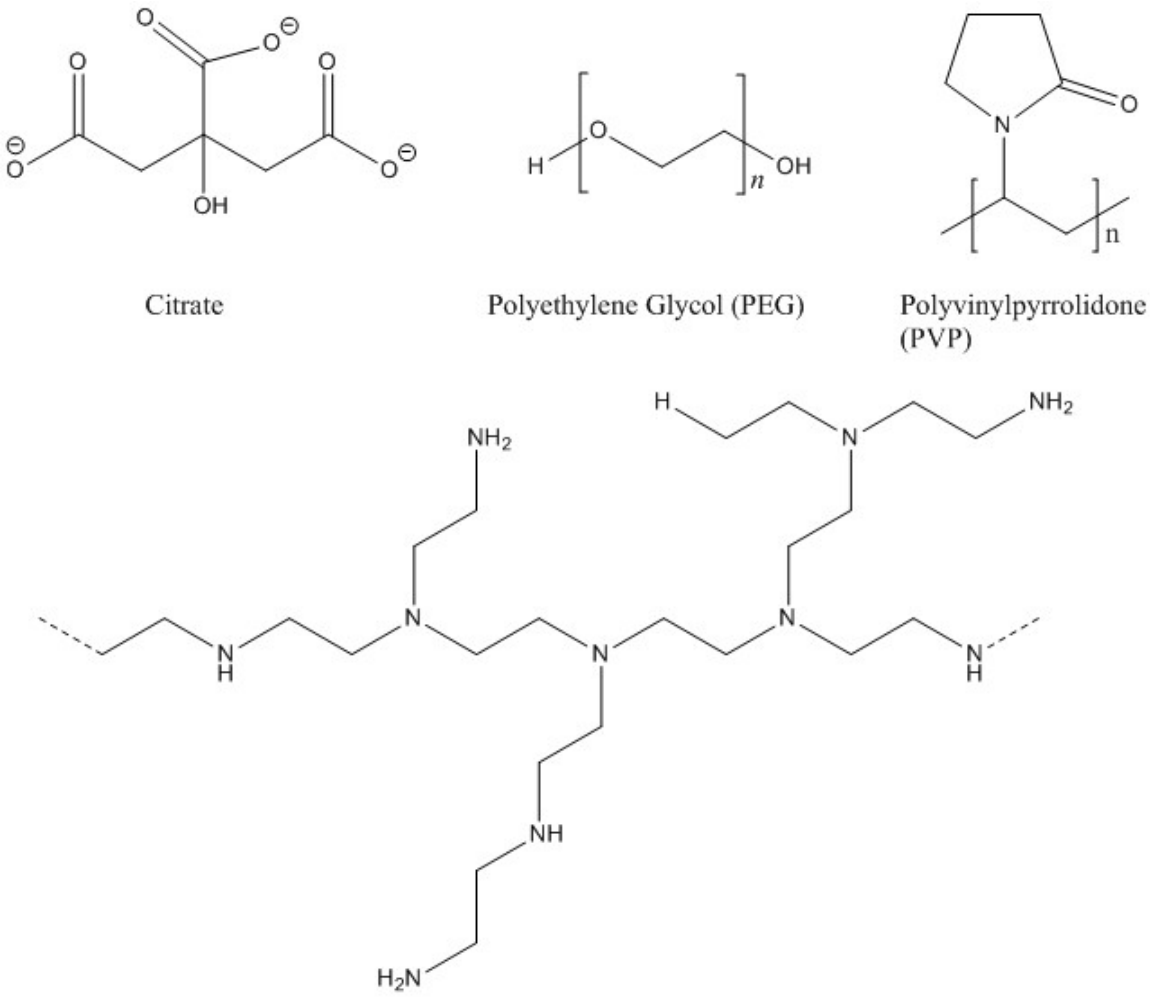


Figure 14: Capping agents used to stabilise NPs: citrate, polyethylene glycol (PEG), Polyvinylpyrrolidone (PVP) and Branched Polyethylenimine (BPEI).

0.3.2 Non-Electrochemical Characterisation of NPs

A range of non-electrochemical methods are used to detect and characterise nanoparticles, including nanoparticle tracking analysis (NTA),[122,123] Inductively Coupled Plasma-Mass Spectrometry (ICP-MS),[124] Atomic Force Microscopy (AFM),[125,126] Scanning Electron Microscopy (SEM),[127] Transmission Electron Microscopy (TEM),[123] Dynamic Light Scatting (DLS),[122,128] and UV-Vis Spectroscopy.[113] The latter four techniques will be explored in more detail below, as these are the techniques used throughout this thesis.

0.3.2.1 Transmission Electron Microscopy

Transmission Electron Microscopy (TEM) is used to quantify the size and concentration of nanoparticles. This is achieved through the analysis of images that are generated by passing electrons through a sample. Figure 15 is a schematic showing the process by which this occurs. An electron beam is directed through magnetic lenses, and is imaged after interacting with a sample (which must be ultrathin and dry). TEM works analogously to a light microscope, but as the electrons are at a much smaller wavelength than that of light, significantly better resolution can be obtained, revealing structures down to 1 nm.

As the electron beam is focused by the magnetic lenses and enters the sample, depending on the density of the sample, some electrons are scattered, whilst the unscattered electrons hit a fluorescent screen, producing a shadow image, with varying intensities of light depending on the degree of scattering. Estimates of concentration of samples can be made through counting the number of NPs in the sample chamber and extrapolating to the bulk solution. The way in which TEM works (through capturing images) means that it is a useful technique for deducing nanoparticle shape. However, one of the primary disadvantages of TEM as a technique is that the nanoparticles must be dried prior to sampling, and this can often result in aggregation, and so

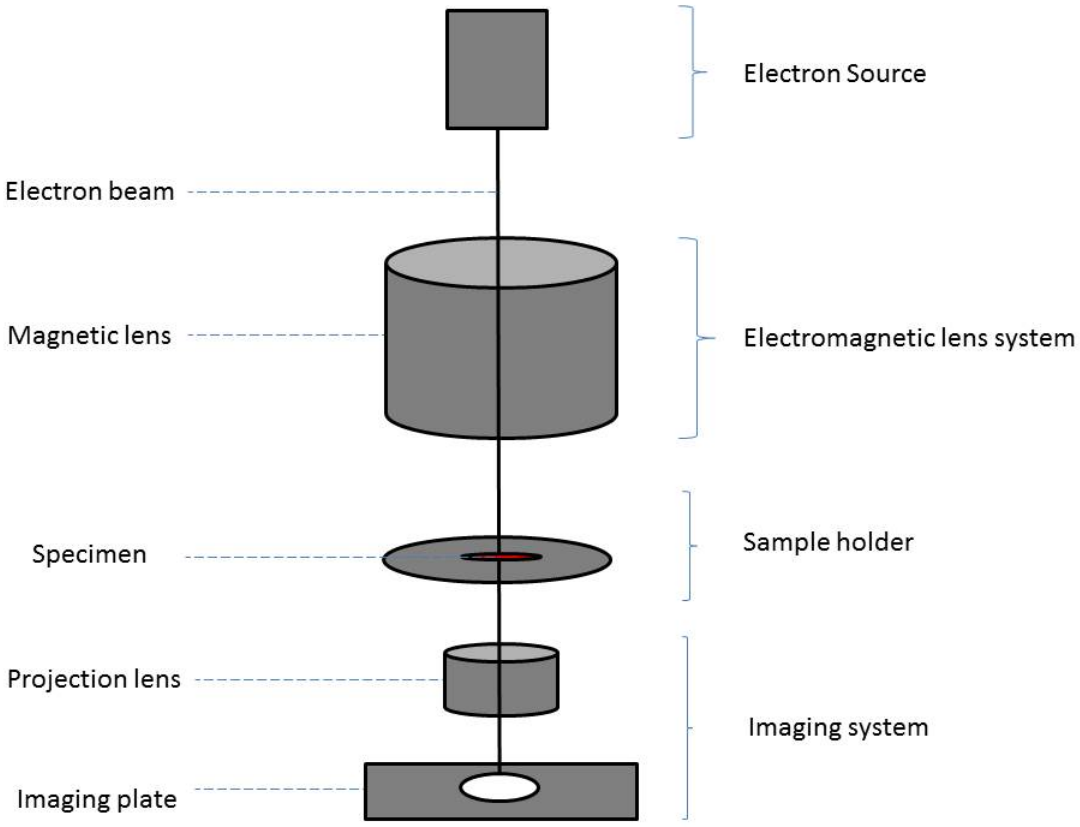


Figure 15: A schematic of a Transmission Electron Microscope, used to measure the core size of nanoparticles.[129]

TEM is not a useful technique for deducing the composition of the solution. The aggregation of the NPs as they are dried can also have implications for the ability to accurately measure the concentration.[130] TEM is also only capable of sizing the core of the nanoparticle, as the molecular weight of the capping agents is usually too low to allow proper contrast. Another similar microscopic technique for measuring the size of the core of the nanoparticle is Scanning Electron Microscopy, detailed below.

0.3.2.2 Scanning Electron Microscopy

Scanning Electron Microscopy (SEM) is also able to measure the size and concentration of nanoparticles through analysing the images that are produced. Whilst TEM measures the electrons that pass through a sample, SEM detects the electrons that scatter from the sample as the electron beam makes contact. Once again a map is produced showing areas of higher and lower density, which provides an image of the NPs. Concentration is calculated by averaging out the numbers of NPs per image. Figure 15 is a schematic showing the process by which this occurs, whereby an electron beam is focused on the sample using magnetic lenses, and the scattered electrons are measured by detectors.[131]

SEM has similar advantages to TEM, such as deducing nanoparticle shape, needing a dry sample, and only measuring the size of the core of the nanoparticle. To achieve an accurate measurement of the whole nanoparticle, another technique, DLS, must be employed.

0.3.2.3 Dynamic Light Scattering

Dynamic Light Scattering (DLS) is capable of analysing nanoparticles in solution, which addresses the concerns of aggregation affecting the analysis, and it gives an accurate measurement of the nanoparticles' hydrodynamic radius. DLS works by irradiating a solution containing nanoparticles with a laser at a wavelength much

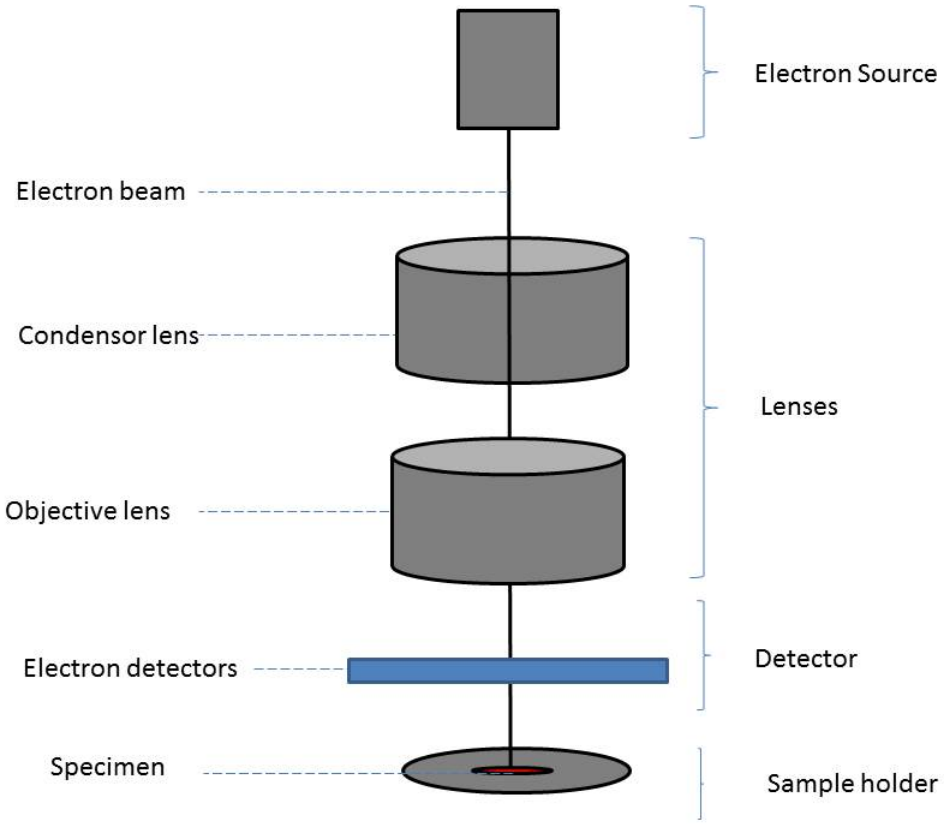


Figure 16: A schematic of a Scanning Electron Microscope, used to measure the core size of nanoparticles.[129]

larger than that of the particles, and measuring the resultant Rayleigh scattering.[132] Figure 17 shows the laser, attenuated to a fixed power, travelling to the sample, and the detector capturing the scattering pattern. An image is generated showing dark areas where the scattered light from the particles is out of phase (destructive) and brighter areas where the light is in phase (constructive). This map is then used to calculate the diffusion coefficient of the particles, which can then be converted into a radius *via* the Stokes-Einstein relation:[1,10]

$$D = \frac{k_B T}{6\eta\pi r_D} \tag{35}$$

where k_B is the Boltzmann constant, T is the temperature, η is the viscosity, and r_D is the hydrodynamic radius of the diffusing species.

A key outcome of the Stokes-Einstein relation is that small particles should diffuse faster than larger ones, and the fluctuations in the light scattering reflect this.

The Rayleigh approximation[133] provides that the measured intensity is proportional to the diameter of the particle to the sixth power. This means that, for example, a 100nm particle will scatter one million times more light than a 10nm particle, and can lead to overrepresentation of larger particles in the analysis. The sample used for analysis needs to be monodispersed and transparent, and contain spherical particles, which restricts this analysis to more ideal solutions, where these conditions are met and the characteristics of the sample can be input prior to analysis.

0.3.2.4 UV-Vis Spectroscopy

UV-Vis Spectroscopy uses the wavelength at which the maximum absorbance occurs to identify the nanoparticle material and the size of the nanoparticle. UV-Vis Spectroscopy operates by passing a beam of light through a sample, and the absorbance of certain wavelengths of light are then recorded. Silver nanoparticles have charac-

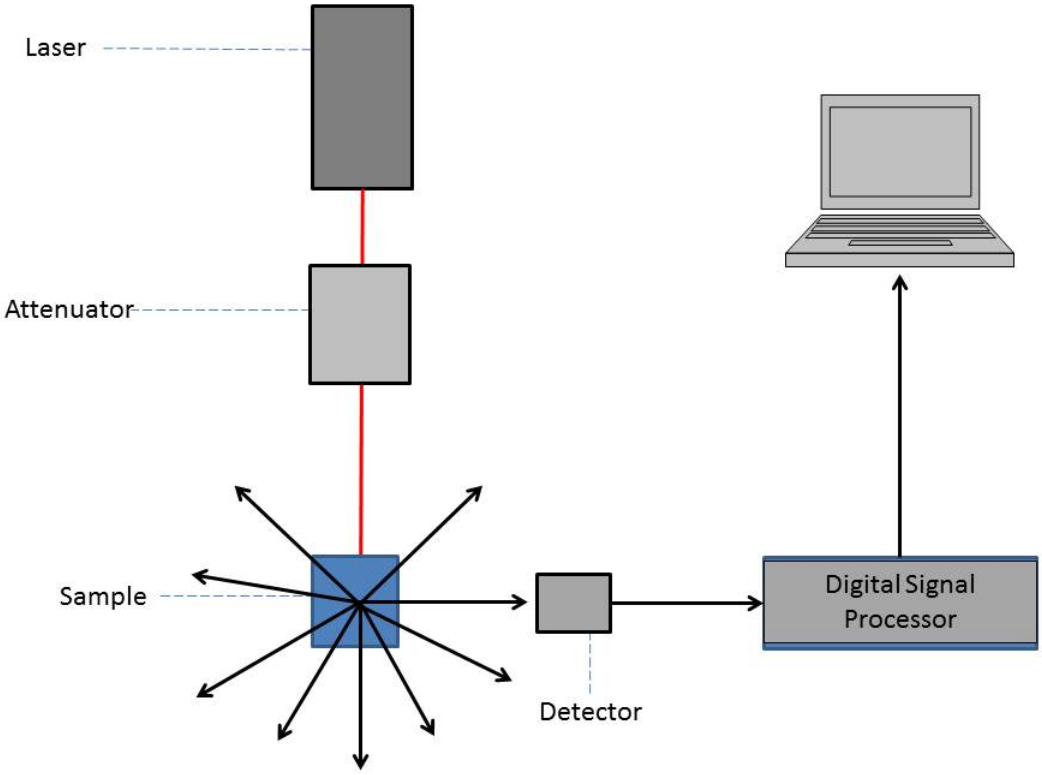


Figure 17: A schematic of Dynamic Light Scattering apparatus - used to measure the hydrodynamic radius of nanoparticles in solution.

teristic absorbances because of the presence of a surface plasmon resonance.[134] The d electrons present in the silver atoms are able to move freely through the nanoparticle, and oscillate in the conduction band. Because the mean free path of silver is *ca.* 50nm, any scattering from particles smaller than this is surface-based. When light, at a wavelength much larger than the size of the NPs, in resonance with the surface oscillation comes into contact with it, it causes the electrons to oscillate. A standing oscillation is created when the light passes through the nanoparticle and causes the electron density to be polarised to one surface, and oscillates in resonance with the light's frequency, as shown in Figure 18.[135]

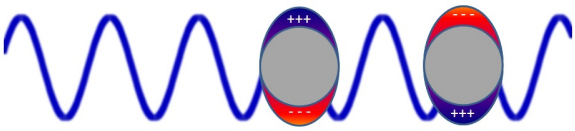


Figure 18: A schematic showing an incoming wave of light, in resonance with the NP, causing the electrons in the metal to oscillate.

Figure 19 shows a typical output of this technique for silver nanoparticles, which show maximum absorbances around 400nm.

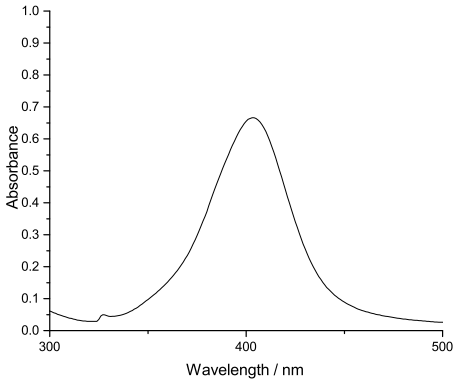


Figure 19: A typical surface plasmon resonance peak of a *ca.* 20nm diameter silver nanoparticle.

Haiss *et al.*[113] report the sizing of gold nanoparticles larger than 25 nm by estab-

lishing a theoretical relationship between the diameter of the NPs and the wavelength at which they exhibit maximum absorbance (see Equation 10[113]). Sizing of silver nanoparticles using UV-Vis by fitting with Mie theory (which describes the scattering of an electromagnetic wave by a sphere) has also been reported.[136] This technique can be used to identify both the nanoparticle material, the size of the nanoparticle, and the concentration, as the maximum wavelength and absorbance shift with these properties. However, it does not allow monitoring of individual nanoparticles, and so must be used in conjunction with other techniques.

0.3.3 Electrochemical Characterisation of NPs

This subsection will briefly cover the two electrochemical techniques currently used to analyse nanoparticles in molecular solvents that will be extended to use in RTILs throughout this thesis — stripping voltammetry and nano-impacts.

0.3.3.1 Stripping Voltammetry

This technique involves modifying the surface of an electrode with a droplet of solution containing nanoparticles. The solvent is then allowed to evaporate, leaving behind the nanoparticles immobilised on the electrode surface. This process is referred to as dropcasting. The modified electrode is then immersed in an electrochemical cell, and a measurement is recorded, often a CV, to determine the potential at which the nanoparticles are dissolved from the surface. This process is undertaken to fingerprint the nanoparticles. Stripping voltammetry has been successfully used to characterise molybdenum,[137] nickel,[138] platinum,[139] copper oxide,[140] gold,[141–143] and silver[144–146] nanoparticles. In the case of the silver and platinum nanoparticles, size-dependent voltammetry was observed.[139,144] Non-metallic nanoparticles, composed of polymers,[147] indigo,[148,149] and fullerenes[150] have also been characterised using this technique.

However, as with other techniques where solvent removal is required, this technique is prone to structural changes.[151] Cloake *et al.*[152] report the incomplete stripping of the nanoparticles as a result of their agglomeration, which leads this technique to have significant drawbacks for precisely characterising nanoparticles. In addition to this, Toh *et al.*[153] investigated NPs capped with a range of molecules, including citrate, BPEI, and PEG, and concluded that regardless of the capping material, incomplete stripping of the immobilised nanoparticles was observed, making this technique very unreliable for quantitative nanoparticle characterisation.

0.3.3.2 Nano-impacts

Given the drawbacks of stripping voltammetry for characterising NPs, another electrochemical technique was developed to detect and characterise NPs in solution — 'nano-impacts'. This technique sees the nanoparticle arrive from the bulk solution to the electrode surface *via* Brownian motion. When the nanoparticle arrives at an electrode that is held at a sufficient potential for an electron transfer to occur, it exchanges an electron with the electrode. This then generates a 'spike' in the time current transient. Figure 20 shows the oxidation of a metal nanoparticle.

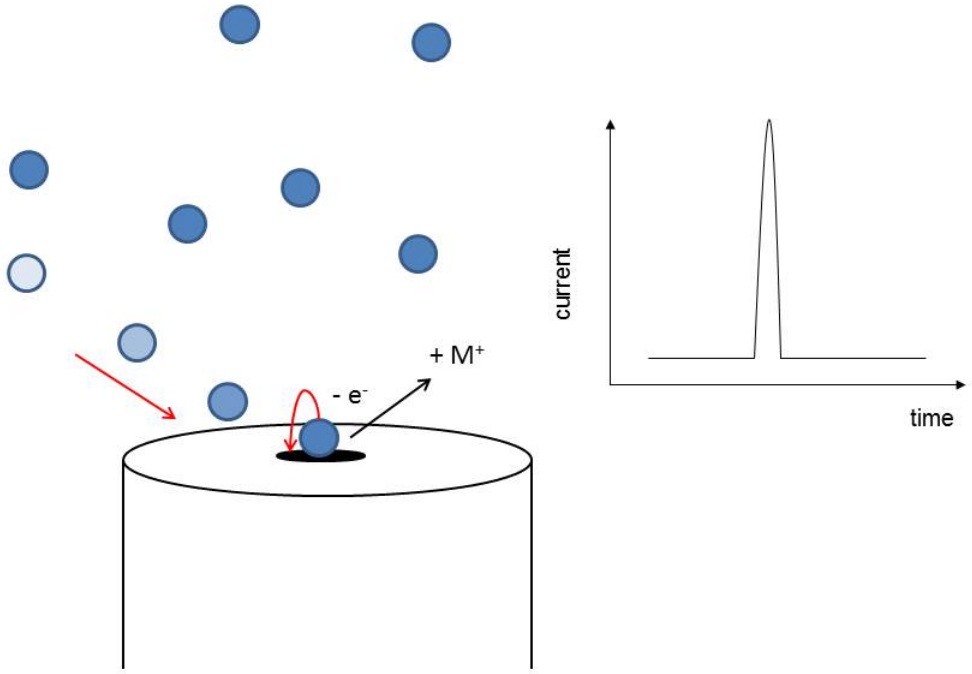


Figure 20: An oxidative impact, and the resultant current response from the oxidation of one nanoparticle.

The area under the spike in the current can then be measured, and converted into a nanoparticle radius (assuming the particle is spherical):

$$\frac{\frac{Area}{F} \times M_R}{\rho} = v \tag{36}$$

$$radius = \sqrt[3]{\frac{v}{\frac{4}{3}\pi}} \tag{37}$$

where F is the Faraday constant, M_R is the molar mass, ρ is the density and v is the volume of the nanoparticle.

The nano-impact methodology has been used successfully to directly measure properties of individual metal nanoparticles, including silver,[154] gold,[155] and nickel.[154] A full review of the use of nano-impacts is conducted in the Introduction to Part IV.

A recent publication by Toh *et al.*[153] observed reactivity differences of NPs in water, but were no new insight about the *dynamics* of the different capping agents in that aqueous medium was gained. To examine the effect of the capping agent on the particle-solution dynamics, extending existing approaches to examine NPs in an entirely different, high-ionic strength solvent such as RTILs is highly advantageous. The ability to study the fundamental properties of individual nanoparticles in ionic environments will be invaluable for the advancement of the combined use of RTILs and nanoparticles in both electroanalysis and catalysis.

References

[1] Compton, R. G.; Banks, C. E. *Understanding Voltammetry*, 2nd ed.; Imperial College Press: London, 2011.

[2] Bard, A. J.; Faulkner, L. R. *Electrochemical Methods: Fundamentals and Applications*, 2nd ed.; John Wiley and Sons: New York, USA, 2001.

[3] Helmholtz, H. v. *Annal. Phys.* **1853**, *165*, 211–233.

[4] Helmholtz, H. V. *Annal. Phys.* **1879**, *243*, 337–382.

[5] Gouy, M. *J. Phys. Theor. Appl.* **1910**, *9*, 457–468.

[6] Chapman, D. L. *Philos. Mag.* **1913**, *25*, 475–481.

[7] Stern, O. *Z. Elktrochem. Angew. P.* **1924**, *30*, 508–516.

[8] Faraday, M. *Experimental Researches in Electricity*; Bernard Quaritch: London, UK, 1839.

[9] Fick, A. *Annal. Phys. Chem.* **1855**, *94*, 59 – 86.

[10] Einstein, A. *Ann. Phys.* **1905**, *322*, 549–560.

[11] Compton, R. G.; Laborda, E.; Ward, K. R. *Understanding Voltammetry: Simulation of Electrode Processes*; Imperial College Press: London, 2014.

[12] Butler, J. A. V. *Trans. Faraday Soc.* **1924**, *19*, 729–733.

[13] Erdey-Gruz, T and Volmer, M, *Z. Physik. Chem.* **1930**, *150*, 203–213.

[14] Guidelli, R.; Compton, R. G.; Feliu, J. M.; Gileadi, E.; Lipkowski, J.; Schmickler, W.; Trasatti, S. *Pure Appl. Chem.* **2014**, *86*, 245–258.

[15] Guidelli, R.; Compton, R. G.; Feliu, J. M.; Gileadi, E.; Lipkowski, J.; Schmickler, W.; Trasatti, S. *Pure Appl. Chem.* **2014**, *86*, 259–262.

[16] Henstridge, M. C.; Wang, Y.; Limon-Petersen, J. G.; Laborda, E.; Compton, R. G. *Chem. Phys. Let.* **2011**, *517*, 29–35.

[17] Suwatchara, D.; Rees, N. V.; Henstridge, M. C.; Laborda, E.; Compton, R. G. *J. Electroanal. Chem.* **2012**, *665*, 38–44.

[18] Suwatchara, D.; Henstridge, M. C.; Rees, N. V.; Compton, R. G. *J. Phys. Chem. C* **2011**, *115*, 14876–14882.

[19] Marcus, R. A. *J. Chem. Phys.* **1956**, *24*, 966–978.

[20] Hush, N. S. *J. Phys. Chem.* **1958**, *28*, 962–972.

[21] Laborda, E.; Henstridge, M. C.; Batchelor-McAuley, C.; Compton, R. G. *Chem. Soc. Rev.* **2013**, *42*, 4894–905.

[22] Henstridge, M. C.; Laborda, E.; Wang, Y.; Suwatchara, D.; Rees, N.; Molina, A.; Martínez-Ortiz, F.; Compton, R. G. *J. Electroanal. Chem.* **2012**, *672*, 45–52.

[23] Cottrell, F. *Z.Phys.Chem.(Leipzig)* **1903**, *42*, 385.

[24] Shoup, D.; Szabo, A. *J. Electroanal. Chem.* **1982**, *140*, 237–245.

[25] Klymenko, O. V.; Evans, R. G.; Hardacre, C.; Svir, I. B.; Compton, R. G. *J. Electroanal. Chem.* **2004**, *571*, 211–221.

[26] Matsuda, H.; Ayabe, Y. *Ber. Bunsenges. Phys. Chem.* **1955**, *59*, 494–503.

[27] Randles, J. E. B. *Trans. Faraday Soc.* **1948**, *44*, 327–338.

[28] Ševčik, A. *Collect. Czech. Chem. Commun.* **1948**, *13*, 349–377.

[29] Wasserscheid, P.; Keim, W. *Angew. Chem. Int. Ed.* **2000**, *39*, 3772–3789.

[30] Hussey, C. L. *Pure Appl. Chem* **1988**, *60*, 1763–1772.

[31] Deetlefs, M.; Seddon, K. R. *Chim. Oggi Chem. Today* **2006**, *24*, 16–23.

[32] Kore, R.; Srivastava, R. *J. Mol. Catal. A: Chem.* **2011**, *345*, 117–126.

[33] Bonhote, P.; Dias, A. P.; Papageorgiou, N.; Kalyanasundaram, K.; Gratzel, M. *Inorg. Chem.* **1996**, *35*, 1168–1178.

[34] de Souza, R. F.; Padilha, J. C.; Gonalves, R. S.; Dupont, J. *Electrochem. Commun.* **2003**, *5*, 728 – 731.

[35] Yang, C.; Sun, Q.; Qiao, J.; Li, Y. *J. Phys. Chem. B* **2003**, *107*, 12981–12988.

[36] Shao, Y.; Bazan, G.; Heeger, A. *Adv. Mat.* **2007**, *19*, 365–370.

[37] Kawano, R.; Watanabe, M. *Chem. Commun.* **2005**, 2107–2109.

[38] Xu, K. *Chem. Rev.* **2004**, *104*, 4303–4418.

[39] Buzzeo, M. C.; Hardacre, C.; Compton, R. G. *Anal. Chem.* **2004**, *76*, 4583–4588.

[40] O'Mahony, A. M.; Silvester, D. S.; Aldous, L.; Hardacre, C.; Compton, R. G. *J. Chem. Eng. Data* **2008**, *53*, 2884–2891.

[41] Silvester, D. S. Electrochemical Studies in Room Temperature Ionic Liquids. Ph.D. thesis, University of Oxford, 2008.

[42] Dzyuba, S. V.; Bartsch, R. A. *Chem. Phys. Chem.* **2002**, *3*, 161–166.

[43] Okoturo, O. O.; VanderNoot, T. J. *J. Electroanal. Chem.* **2004**, *568*, 167–181.

[44] Wang, Y.; Zaghib, K.; Guerfi, A.; Bazito, F. F.; Torresi, R. M.; Dahn, J. *Electrochim. Acta* **2007**, *52*, 6346 – 6352.

[45] Seddon, K. R.; Stark, A.; Torres, M.-J. *Clean Solvents*; 2002; Chapter 5, pp 34–49.

[46] MacFarlane, D. R.; Meakin, P.; Sun, J.; Amini, N.; Forsyth, M. *J. Phys. Chem. B* **1999**, *103*, 4164–4170.

[47] Sun, J.; Forsyth, M.; MacFarlane, D. R. *J. Phys. Chem. B* **1998**, *102*, 8858–8864.

[48] MacFarlane, D.; Sun, J.; Golding, J.; Meakin, P.; Forsyth, M. *Electrochim. Acta* **2000**, *45*, 1271 – 1278.

[49] Del Sesto, R. E.; Corley, C.; Robertson, A.; Wilkes, J. S. *J. Organomet. Chem.* **2005**, *690*, 2536–2542.

[50] Lide, D. R., Ed. *Handbook of Chemistry and Physics*, 76th ed.; CRC Press: Boca Raton, USA, 1996.

[51] Xu, W.; Wang, L.-M.; Nieman, R. A.; Angell, C. A. *J. Phys. Chem. B* **2003**, *107*, 11749–11756.

[52] Endres, F.; Zein El Abedin, S. *Phys. Chem. Chem. Phys.* **2006**, *8*, 2101–2116.

[53] McEwen, A. B.; Ngo, H. L.; LeCompte, K.; Goldman, J. L. *J. Electrochem. Soc.* **1999**, *146*, 1687–1695.

[54] Jacquemin, J.; Husson, P.; Padua, A. A. H.; Majer, V. *Green Chem.* **2006**, *8*, 172–180.

[55] Wilkes, J. S. *J. Mol. Catal. A: Chem.* **2004**, *214*, 11 – 17.

[56] Gu, Z.; ; Brennecke, J. F. *J. Chem. Eng. Data* **2002**, *47*, 339–345.

[57] Fredlake, C. P.; Crosthwaite, J. M.; Hert, D. G.; Aki, S. N. V. K.; Brennecke, J. F. *J. Chem. Eng. Data* **2004**, *49*, 954–964.

[58] Tsuzuki, S.; Tokuda, H.; Hayamizu, K.; Watanabe, M. *J. Phys. Chem. B* **2005**, *109*, 16474–16481.

[59] MacFarlane, D.; Sun, J.; Golding, J.; Meakin, P.; Forsyth, M. *Electrochim. Acta* **2000**, *45*, 1271 – 1278.

[60] Wilkes, J. S.; Levisky, J. A.; Wilson, R. A.; Hussey, C. L. *Inorg. Chem.* **1982**, *21*, 1263–1264.

[61] Golding, J.; Forsyth, S.; MacFarlane, D. R.; Forsyth, M.; Deacon, G. B. *Green Chem.* **2002**, *4*, 223–229.

[62] MacFarlane, D. R.; Forsyth, S. A.; Golding, J.; Deacon, G. B. *Green Chem.* **2002**, *4*, 444–448.

[63] Clare, B. R.; Bayley, P. M.; Best, A. S.; Forsyth, M.; MacFarlane, D. R. *Chem. Commun.* **2008**, 2689–2691.

[64] McIntosh, A. J.; Griffith, J.; Grsvik, J. In *Application, Purification, and Recovery of Ionic Liquids*; Kuzmina, O., Hallett, J. P., Eds.; Elsevier: Amsterdam, 2016; pp 59 – 99.

[65] Fischer, K. *Angew. Chem.* **1935**, *48*, 394–396.

[66] Widegren, J. A.; Laesecke, A.; Magee, J. W. *Chem. Comm.* **2005**, 1610–1612.

[67] Schröder, U.; Wadhawan, J. D.; Compton, R. G.; Marken, F.; Suarez, P. A. Z.; Consorti, C. S.; de Souza, R. F.; Dupont, J. *New J. Chem.* **2000**, *24*, 1009–1015.

[68] Seddon, K.; Stark, A.; Torres, M.-J. *Pure Appl. Chem.* **2000**, *72*, 2275–2287.

[69] Aldous, L.; Silvester, D. S.; Villagran, C.; Pitner, W. R.; Compton, R. G.; Cristina Lagunas, M.; Hardacre, C. *New J. Chem.* **2006**, *30*, 1576–1583.

[70] Gallo, V.; Mastrorilli, P.; Nobile, C. F.; Romanazzi, G.; Suranna, G. P. *J. Chem. Soc., Dalton Trans.* **2002**, 4339–4342.

[71] Scammells, P. J.; Scott, J. L.; Singer, R. D. *Aus. J. Chem.* **2005**, *58*, 155–169.

[72] Suarez, P. A.; Dullius, J. E.; Einloft, S.; de Souza, R. F.; Dupont, J. *Inorg. Chim. Acta* **1997**, *255*, 207–209.

[73] Dyson, P. J.; Ellis, D. J.; Welton, T.; Parker, D. G. *Chem. Commun.* **1999**, 25–26.

[74] Peter Wasserscheid, T. W. In *Ionic Liquids in Synthesis*; Peter Wasserscheid, T. W., Ed.; Wiley-VCH: Weinheim, 2003; Chapter 53.

[75] Silvester, D.; Compton, R. G. *Z. Phys. Chem.* **2006**, *220*, 1247–1274.

[76] Barrosse-Antle, L. E.; Hardacre, C.; Compton, R. G. *J. Phys. Chem. B* **2009**, *113*, 2805–2809.

[77] Barrosse-Antle, L. E.; Aldous, L.; Hardacre, C.; Bond, A. M.; Compton, R. G. *J. Phys. Chem. C* **2009**, *113*, 7750–7754.

[78] Buzzeo, M. C.; Klymenko, O. V.; Wadhawan, J. D.; Hardacre, C.; Seddon, K. R.; Compton, R. G. *J. Phys. Chem. A* **2003**, *107*, 8872–8878.

[79] Andrieux, C. P.; Hapiot, P.; Saveant, J. M. *J. Phys. Chem.* **1988**, *92*, 5987–5992.

[80] Zhang, J.; ; Bond, A. M. *J. Phys. Chem. B* **2004**, *108*, 7363–7372.

[81] Brooks, C. A.; ; Doherty, A. P. *J. Phys. Chem. B* **2005**, *109*, 6276–6279.

[82] Rogers, E. I.; Streeter, I.; Aldous, L.; Hardacre, C.; Compton, R. G. *J. Phys. Chem. C* **2008**, *112*, 10976–10981.

[83] Rogers, E. I.; Silvester, D. S.; Aldous, L.; Hardacre, C.; Compton, R. G. *J. Phys. Chem. C* **2008**, *112*, 6551–6557.

[84] Allen, G. D.; Buzzeo, M. C.; Villagrn, C.; Hardacre, C.; Compton, R. G. *J. Electroanal. Chem.* **2005**, *575*, 311 – 320.

[85] Kornyshev, A. *J. Phys. Chem. B* **2007**, *111*, 5545–5557.

[86] Fedorov, M. V.; Kornyshev, A. A. *Chem. Rev.* **2014**, *114*, 2978–3036.

[87] Georgi, N.; Kornyshev, A.; Fedorov, M. *J. Electroanal. Chem.* **2010**, *649*, 261 – 267.

[88] Levin, Y. *Rep. Prog. Phys.* **2002**, *65*, 1577.

[89] Fedorov, M.; Kornyshev, A. *Electrochim. Acta* **2008**, *53*, 6835–6840.

[90] Fedorov, M. V.; Kornyshev, A. A. *J. Phys. Chem. B* **2008**, *112*, 11868–11872.

[91] Bazant, M. Z.; Storey, B. D.; Kornyshev, A. A. *Phys. Rev. Lett.* **2011**, *106*, 046102.

[92] Démery, V.; Dean, D. S.; Hammant, T. C.; Horgan, R. R.; Podgornik, R. *J. Chem. Phys.* **2012**, *137*, 064901.

[93] Démery, V.; Dean, D. S.; Hammant, T. C.; Horgan, R. R.; Podgornik, R. *EPL* **2012**, *97*, 28004.

[94] Feng, G.; Zhang, J. S.; Qiao, R. *J. Phys. Chem. C* **2009**, *113*, 4549–4559.

[95] Lynden-Bell, R. M.; Frolov, A. I.; Fedorov, M. V. *Phys. Chem. Chem. Phys.* **2012**, *14*, 2693–2701.

[96] Gnahm, M.; Pajkossy, T.; Kolb, D. *Electrochim. Acta* **2010**, *55*, 6212 – 6217.

[97] Wang, H.; Pilon, L. *Electrochim. Acta* **2012**, *63*, 55 – 63.

[98] Mezger, M.; Schröder, H.; Reichert, H.; Schramm, S.; Okasinski, J. S.; Schöder, S.; Honkimäki, V.; Deutsch, M.; Ocko, B. M.; Ralston, J.; Rohwerder, M.; Stratmann, M.; Dosch, H. *Science* **2008**, *322*, 424–428.

[99] Mezger, M.; Schramm, S.; Schrder, H.; Reichert, H.; Deutsch, M.; De Souza, E. J.; Okasinski, J. S.; Ocko, B. M.; Honkimäki, V.; Dosch, H. *J. Chem. Phys.* **2009**, *131*.

[100] Yamamoto, R.; Morisaki, H.; Sakata, O.; Shimotani, H.; Yuan, H.; Iwasa, Y.; Kimura, T.; Wakabayashi, Y. *App. Phys. Lett.* **2012**, *101*.

[101] Hayes, R.; Borisenko, N.; Tam, M. K.; Howlett, P. C.; Endres, F.; Atkin, R. *J. Phys. Chem. C* **2011**, *115*, 6855–6863.

[102] Smith, A. M.; Lovelock, K. R. J.; Gosvami, N. N.; Licence, P.; Dolan, A.; Welton, T.; Perkin, S. *J. Phys. Chem. Lett.* **2013**, *4*, 378–382.

[103] Baldelli, S. *J. Phys. Chem. Lett.* **2013**, *4*, 244–252.

[104] Kirchner, K.; Kirchner, T.; Ivaništšev, V.; Fedorov, M. V. *Electrochim. Acta* **2013**, *110*, 762–771.

[105] Lockett, V.; Sedev, R.; Ralston, J.; Horne, M.; Rodopoulos, T. *J. Phys. Chem. C* **2008**, *112*, 7486–7495.

[106] Ivaništšev, V.; Ruzanov, A.; Lust, K.; Lust, E. *J. Electrochem. Soc.* **2013**, *160*, H368–H375.

[107] Siinor, L.; Arendi, R.; Lust, K.; Lust, E. *J. Electroanal. Chem.* **2013**, *689*, 51 – 56.

[108] Silva, F.; Gomes, C.; Figueiredo, M.; Costa, R.; Martins, A.; Pereira, C. M. *J. Electroanal. Chem.* **2008**, *622*, 153 – 160.

[109] Costa, R.; Pereira, C. M.; Silva, F. *Phys. Chem. Chem. Phys.* **2010**, *12*, 11125–11132.

[110] Vatamanu, J.; Borodin, O.; Smith, G. D. *J. Am. Chem. Soc.* **2010**, *132*, 14825–14833.

[111] Nishi, N.; Uruga, T.; Tanida, H.; Kakiuchi, T. *Langmuir* **2011**, *27*, 7531–7536.

[112] Duffus, J. H.; Nordberg, M.; Templeton, D. M. *Pure Appl. Chem.* **2007**, *79*, 1153–1344.

[113] Haiss, W.; Thanh, N. T. K.; Aveyard, J.; Fernig, D. G. *Anal. Chem.* **2007**, *79*, 4215–4221.

[114] Jain, P. K.; Huang, X.; El-Sayed, I. H.; El-Sayed, M. A. *Plasmonics* **2007**, *2*, 107–118.

[115] Diez, I.; Ras, R. H. A. *Nanoscale* **2011**, *3*, 1963–1970.

[116] Tejamaya, M.; Rmer, I.; Merrifield, R. C.; Lead, J. R. *Environ. Sci. Technol.* **2012**, *46*, 7011–7017.

[117] Kim, K. D.; Han, D. N.; Kim, H. T. *Chem. Eng. J.* **2004**, *104*, 55 – 61.

[118] Dobias, X. Q.; Rybinski, W. V. *Solid-Liquid Dispersions*; Marcel Dekker: New York, 1999; Vol. 81; pp 127–255.

[119] Firlar, E.; Çınar, S.; Kashyap, S.; Akinc, M.; Prozorov, T. *Sci Rep.* **2015**, *5*.

[120] Kim, S.; Hyun, K.; Moon, J. Y.; Clasen, C.; Ahn, K. H. *Langmuir* **2015**, *31*, 1892–1900.

[121] Zhang, Q.; Zhang, X.; Chen, T.; Wang, X.; Fu, Y.; Jin, Y.; Sun, X.; Gong, T.; Zhang, Z. *Nanoscale* **2015**, *7*, 9298–9310.

[122] Wilkinson, K. E.; Palmberg, L.; Witasp, E.; Kupczyk, M.; Feliu, N.; Gerde, P.; Seisenbaeva, G. A.; Fadeel, B.; Dahln, S.-E.; Kessler, V. G. *ACS Nano* **2011**, *5*, 5312–5324.

[123] Orefuwa, S. A.; Ravanbakhsh, M.; Neal, S. N.; King, J. B.; Mohamed, A. A. *Organometallics* **2014**, *33*, 439–442.

[124] Allabashi, R.; Stach, W.; de la Escosura-Muñiz, A.; Liste-Calleja, L.; Merkoçi, A. *J. Nanopart. Res.* **2008**, *11*, 2003–2011.

[125] Bullen, H. A.; Garrett, S. J. *Nano Lett.* **2002**, *2*, 739–745.

[126] Morita, T.; Lindsay, S. *J. Am. Chem. Soc.* **2007**, *129*, 7262–7263.

[127] Zhou, Y.-G.; Rees, N. V.; Compton, R. G. *Angew. Chem. Int. Ed.* **2011**, *50*, 4219–4221.

[128] Prapainop, K.; Witter, D. P.; Paul Wentworth, J. *J. Am. Chem. Soc.* **2012**, *134*, 4100–4103.

[129] On-Site Courses. 2011; `http://www.dsimagingllc.com/courses/`.

[130] Shang, J.; Gao, X. *Chem. Soc. Rev.* **2014**, *43*, 7267–7278.

[131] Atkins, P. W.; De Paula, D. *Atkins' Physical Chemistry*; Oxford University Press: Oxford, 2006.

[132] Pecora, R., Ed. *Dynamic Light Scattering*; Plenum Press: New York, 1985.

[133] Seinfield, J.; Pandis, S. N. *Atmospheric Chemistry and Physics*; John Wiley and Sons: NewJersey, 2006.

[134] Burda, C.; Chen, X.; Narayanand, R.; El-Sayed, M. A. *Chem. Rev.* **2005**, *105*, 1025–1102.

[135] Eustis, S.; El-Sayed, M. A. *Chem. Soc. Rev.* **2006**, *35*, 209–217.

[136] Desai, R.; Mankad, V.; Gupta, S. K.; Jha, P. K. *Nanosci. Nanotechnol. Lett.* **2012**, *4*, 30–34.

[137] Giovanni, M.; Pumera, M. *Electrochem. Commun.* **2011**, *13*, 203–204.

[138] Giovanni, M.; Ambrosi, A.; Pumera, M. *Chem. - Asian J.* **2012**, *7*, 702–706.

[139] Tang, L.; Han, B.; Persson, K.; Friesen, C.; He, T.; Sieradzki, K.; Ceder, G. *J. Am. Chem. Soc.* **2010**, *132*, 596–600.

[140] Teo, W. Z.; Ambrosi, A.; Pumera, M. *Electrochem. Commun.* **2013**, *28*, 51 – 53.

[141] Stuart, E.; Tschulik, K.; Lowinsohn, D.; Cullen, J.; Compton, R. *Sens. Actuator B-Chem.* **2014**, *195*, 223 – 229.

[142] Gillespie, A.; Jao, D.; Andriola, A.; Duda, T.; Yang, C. F.; Yu, L. *Anal. Lett.* **2012**, *45*, 1310–1320.

[143] Lakbub, J.; Pouliwe, A.; Kamasah, A.; Yang, C.; Sun, P. *Electroanal.* **2011**, *23*, 2270–2274.

[144] Giovanni, M.; Pumera, M. *Electroanal.* **2012**, *24*, 615–617.

[145] Brainina, K. Z.; Galperin, L. G.; Kiryuhina, T. Y.; Galperin, A. L.; Stozhko, N. Y.; Murzakaev, A. M.; Timoshenkova, O. R. *J. Solid State Electrochem* **2012**, *16*, 2365–2372.

[146] Cepria, G.; Cordova, W. R.; Jimenez-Lamana, J.; Laborda, F.; Castillo, J. R. *Anal. Methods* **2014**, *6*, 3072–3078.

[147] Zhou, X.-F.; Cheng, W.; Batchelor-McAuley, C.; Tschulik, K.; Compton, R. G. *Electroanalysis* **2014**, *26*, 248–253.

[148] Cheng, W.; Batchelor-McAuley, C.; Compton, R. G. *ChemElectroChem* **2014**, *1*, 714–717.

[149] Cheng, W.; Zhou, X.-F.; Compton, R. G. *Angew. Chem. Int. Ed.* **2013**, *52*, 12980–12982.

[150] Stuart, E. J. E.; Tschulik, K.; Batchelor-McAuley, C.; Compton, R. G. *ACS Nano* **2014**, *8*, 7648–7654.

[151] Toh, H. S.; Batchelor-McAuley, C.; Tschulik, K.; Uhlemann, M.; Crossley, A.; Compton, R. G. *Nanoscale* **2013**, *5*, 4884–4893.

[152] Cloake, S. J.; Toh, H. S.; Lee, P. T.; Salter, C.; Johnston, C.; Compton, R. G. *ChemistryOpen* **2015**, *4*, 22–26.

[153] Toh, H. S.; Jurkschat, K.; Compton, R. G. *Chem. Eur. J.* **2015**, *21*, 2998–3004.

[154] Stuart, E. J. E.; Zhou, Y.-G.; Rees, N. V.; Compton, R. G. *RSC Adv.* **2012**, *2*, 6879–6884.

[155] Zhou, Y.-G.; Rees, N. V.; Pillay, J.; Tshikhudo, R.; Vilakazi, S.; Compton, R. G. *Chem. Commun.* **2012**, *48*, 224–226.

Part II

General Experimental Details

Experimental details common to the thesis are described in this section - any deviations specific to Parts III and IV are shared in their preambles.

0.4 Chemical Reagents

0.4.1 Commercially Available Reagents

This section details the source, purity, and use of commercially available chemical reagents throughout this thesis, excluding RTILs, which will be discussed separately below. All of the reagents listed in Table 4 were used as received.

0.4.2 Room Temperature Ionic Liquids

Where RTILs were used in the glovebox, they were dried under a Schlenk line for *ca.* 1 week before use, with stirring, at 70 °C. In other cases, a small aliquot of RTIL was placed under a 0.2 mbar vacuum for a minimum of 24 hours prior to use, to remove water and other volatile impurities. All RTILs used in this thesis are listed in Table 5. Where the source of the RTIL is marked as 'Donated by Belfast', this RTIL was kindly donated by Professor C. Hardacre then of Queens University, Belfast.

0.5 Electrodes

In all cases, the microelectrodes were polished and calibrated before use. Each electrode was polished prior to use using a water-alumina slurry (1, 0.3, 0.05 μm, five minutes on each grade) on soft lapping pads (Buehler, Illinois).[1] Precise radii were determined through calibration of the electrode with a 2.0 mM solution of ferrocene in acetonitrile containing 0.1 M TBAP (silver wire as both a counter and quasi-reference electrode); chronoamperometry was recorded at 298 K, and assuming a diffusion coefficient of 2.3 x 10^{-9} m^2 s^{-1},[2] the data was analysed with respect to the Shoup and

Name	Abbreviation	Supplier	Purity	Chapter
Ferrocene	$Fe(C_5H_5)_2$/Fc	Aldrich	98%	All
Tetra-n-butylammonium perchlorate	TBAP	Fluka	99%	All
2-Nitrotoluene	2-NT	Aldrich	>99%	2 + 3
Nitrocyclopentane	NCP	Aldrich	99%	2 + 3
1-Nitrobutane	BuN	Aldrich	98%	2 + 3
Oxygen	O_2	BOC	99.5%	1, 3
Argon	Ar	BOC	99.5%	All
Silver Nanoparticles, 20 nm d	Ag NPs	NanoComposix	-	4 – 6
Poly(ethylene glycol) methyl ether thiol (2000 MW)	Thiolated PEG	Aldrich	98%	6
Poly(ethylene glycol) methyl ether thiol (6000 MW)	Thiolated PEG	Aldrich	98%	4 – 6
Poly(ethylene glycol) methyl ether thiol (10,000 MW)	Thiolated PEG	Aldrich	98%	6
Ultrapure water	H_2O	Millipore	Resistivity >18.2 M Ωcm at 25 °C	4 – 6

Table 4: Commercially available reagents used throughout this thesis

Name	Abbreviation	Supplier	Chapter
1-Butyl-1-methylpyrrolidinium *bis*(trifluoromethylsulfonyl)imide	[Bmpyrr][NTf_2]	Donated by Belfast	1, 3
Trihexyltetradecylphosphonium *tris*(pentafluoroethyl)trifluorophosphate	[$P_{14,6,6,6}$][FAP]	Merck	2 + 3
1-Ethyl-3-methylimidazolium *bis*(trifluoromethylsulfonyl)imide	[Emim][NTf_2]	Donated by Belfast	2 + 3
1-Butyl-3-methylimidazolium chloride	[Bmim][Cl]	Aldrich	5
1-Butyl-3-methylimidazolium tetrafluoroborate	[Bmim][BF_4]	Donated by Belfast	4 – 6

Table 5: RTILs used throughout this thesis

Material	Radius	Supplier	Chapter
Gold microelectrode	5.04 ± 0.05 μm	IJ Cambria Scientific Ltd, UK	1, 2
Gold microelectrode	5.10 ± 0.05 μm	IJ Cambria Scientific Ltd, UK	1, 3
Silver wire (CE and RE)	0.25 mm	Aldrich	All
Carbon microelectrode	4.91 ± 0.05 μm	IJ Cambria Scientific Ltd, UK	4–6
Glassy Carbon	1.5 mm	BASi	4

Table 6: Electrodes used throughout this thesis

Szabo equation[3] (Equations 38, 39, and 40, described fully in the Theory Section of Part III).

$$I = -4nFD_{\mathrm{A}}c_{\mathrm{A}}rf(\tau) \tag{38}$$

$$f(\tau) = 0.7854 + 0.4432\tau^{-0.5} + 0.2146\exp\left(-0.3912\tau^{-0.5}\right) \tag{39}$$

and

$$\tau = \frac{D_{\mathrm{A}}}{r^2}t \tag{40}$$

Table 6 details the precise radii of all electrodes used in this thesis.

In the case of the Glassy Carbon electrode, used in Chapter 4 for dropcasting experiments, it was polished prior to use with white lapping pads with diamond spray (3.0, 1.0, 0.1 μm, five minutes on each size from Kemet, Kent, UK).

0.6 Potentiostats

Chapters 1 – 3 use a μ-Autolab potentiostat (Eco-Chemie, Netherlands), whilst chapters 4 – 6 utilise a potentiostat built in-house. The latter consisted of three main sections; a stabilised potentiostat, a current amplifier circuit, and an analog-to-digital

converter within the computer interface. The computer interface utilised a National Instruments USB-6003 Data Acquisition Device (National Instruments, Berkshire, UK) which was connected through a USB to the computer. A script was written by Dr Christopher Batchelor-McAuley in Python 2.7 and run through the IDE Canopy (Enthought, Austin, TX USA) to control the Data Acquisition Device. The current at the working electrode (running to ground) was measured with a low current-amplifier LCA-4K-1G (FEMTO, Messtechnik GmbH, Germany) and the bandwidth of the output of the current amplifier was limited using a 100 Hz 2-pole passive RC filter, Linear Technology DC338A-B (Farnell, Leeds, UK). The Data Acquisition Device digitised, at a stream rate of 4kHz, the resulting analog signal, which was oversampled. A highly stabilized (1kHz bandwidth) classic adder potentiostat was used to provide potentiostatic control. To maintain control of the reference electrode, a high quality operational-amplifier LMC6001 (Farnell, Leeds, UK) with ultra low-input bias (25fA) was used. Control of the potential at the counter electrode was maintained by a high quality low-noise operational-amplifier, AD797 (Farnell, Leeds, UK).

0.7 Glovebox and Experimental Apparatus

In all cases, the samples were prepared in a plastic collar fixed on top of the working electrode, and a T-cell was used for structural stability,[4] as shown in Figure 21. The T-cell was then placed inside a temperature controlled Faraday cage.[4]

All experiments (excluding those done with oxygen) were carried out in an acrylic MBRAUN glovebox (GB-2202-P-VAC) under an inert Argon atmosphere. Before inital use, the glovebox was purged in totality a dozen times and items entering the glovebox after this initial period were transferred through the antechamber, which went through three purge and refill cycles prior to their introduction to the main chamber.

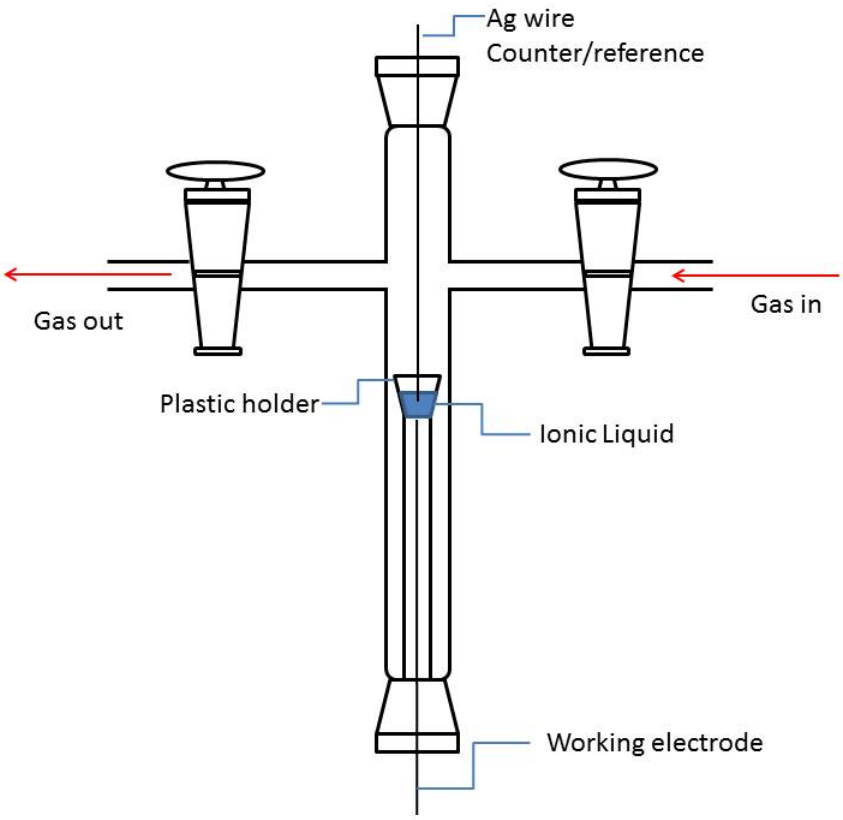


Figure 21: A schematic of the glass cell used throughout this thesis.[4] In the experiments with oxygen, the gas was pushed through the sidearms until it reached saturation.

References

[1] Cardwell, T. J.; Mocak, J.; Santos, J. H.; Bond, A. M. *Analyst* **1996**, *121*, 357.

[2] Rogers, E. I.; Silvester, D. S.; Aldous, L.; Hardacre, C.; Compton, R. G. *J. Phys.Chem. B* **2008**, *112*, 6551–6557.

[3] Shoup, D.; Szabo, A. *J. Electroanal. Chem.* **1982**, *140*, 237–245.

[4] Evans, R. G.; Klymenko, O. V.; Saddoughi, S.; Hardacre, C.; Compton, R. G. *J. Phys. Chem. B* **2004**, *108*, 7878–7886.

Part III

A Comparison of Electron Transfer Theories in RTIL

Part III examines the use of three different electron transfer theories - Butler-Volmer, Symmetric Marcus-Hush, and Asymmetric Marcus Hush - in quantitatively describing experimental voltammetry. This Part has its own introduction, followed by Theory and Experimental sections. This is followed by three chapters, the first of which covers the application of BV and SMH theories to the reduction of oxygen. The second chapter extends the application of BV and SMH theories to the reduction of a range of nitro compounds, whilst the third chapter applies AMH theory to the systems covered in the previous two chapters.

0.8 Introduction

Two theories dominate the current understanding of election transfer, Butler-Volmer and Marcus-Hush, which both consider a one-electron transfer:

$$\mathrm{A} + \mathrm{e}^- \rightleftharpoons \mathrm{B} \tag{41}$$

Butler-Volmer (B-V) theory[1,2] (Equations 42 and 43) describes the rate constant, k_{red} or k_{ox}, in terms of the standard heterogeneous rate constant, k^0, the formal potential, $E_f^{\ominus}$, and a transfer coefficient, α, which takes a value between 0 and 1 (where $\alpha + \beta = 1$) and describes whether the transition state is more product-like (α >0.5) or reactant-like (α <0.5).[3,4]

$$k_{\mathrm{red}} = k^0 \exp\left[\frac{-\alpha F\left(E - E_f^{\ominus}\right)}{RT}\right] \tag{42}$$

$$k_{\mathrm{ox}} = k^0 \exp\left[\frac{\beta F\left(E - E_f^{\ominus}\right)}{RT}\right] \tag{43}$$

An alternative electron transfer theory, Marcus-Hush theory,[5–7] relates the stan-

dard heterogeneous rate constant, k^0, to the reaction Gibbs energy, $\Delta G^{\ominus}$, and reorganisation energy, λ, where $\Delta G^{\ddagger}$ is the Gibbs energy of activation.

$$\Delta G^{\ddagger} = \frac{\lambda}{4}\left(1 + \frac{\Delta G^{\ominus}}{\lambda}\right)^2 \tag{44}$$

$$k^0 = A \exp\left[\frac{-\Delta G^{\ddagger}}{RT}\right] \tag{45}$$

The reorganisation energy, λ, has two components, inner and outer sphere reorganisation (λ_i and λ_o respectively, as shown in Equation 46).

$$\lambda = \lambda_i + \lambda_o \tag{46}$$

Marcus-Hush theory is based on a Gibbs energy plot with two intersecting parabolae; the reactants and products (Figure 22).

In Symmetric Marcus-Hush (SMH) theory, these parabolae are of equal curvature, whilst a more general case is made in Asymmetric Marcus-Hush (AMH) theory, where this requirement is relaxed.[8] The activation energy of a reduction/oxidation according to AMH theory is:

$$\frac{\Delta G^{\ddagger}_{\mathrm{red/ox}}(x)}{RT} = \frac{\Lambda}{4}\left(1 \pm \frac{\theta + x}{\Lambda}\right)^2 + \frac{\gamma}{4}\left(\frac{\theta + x}{\Lambda}\right)\left[1 - \left(\frac{\theta + x}{\Lambda}\right)^2\right] + \gamma^2\frac{\Lambda}{16} \tag{47}$$

The asymmetry parameter, γ, quantifies the difference in force constants in the inner shells of the reactants and products, and describes difference (if any) in curvature of the two parabolae:

$$\gamma = \frac{\lambda_i}{\lambda}\langle l_s \rangle = \frac{\lambda_i \sum_s k_s \left(\Delta q_s^0\right)^2 l_s}{\lambda \sum_s k_s \left(\Delta q_s^0\right)^2} \tag{48}$$

where λ_i is the inner sphere reorganization energy (as defined above), Δq_s^0 is the

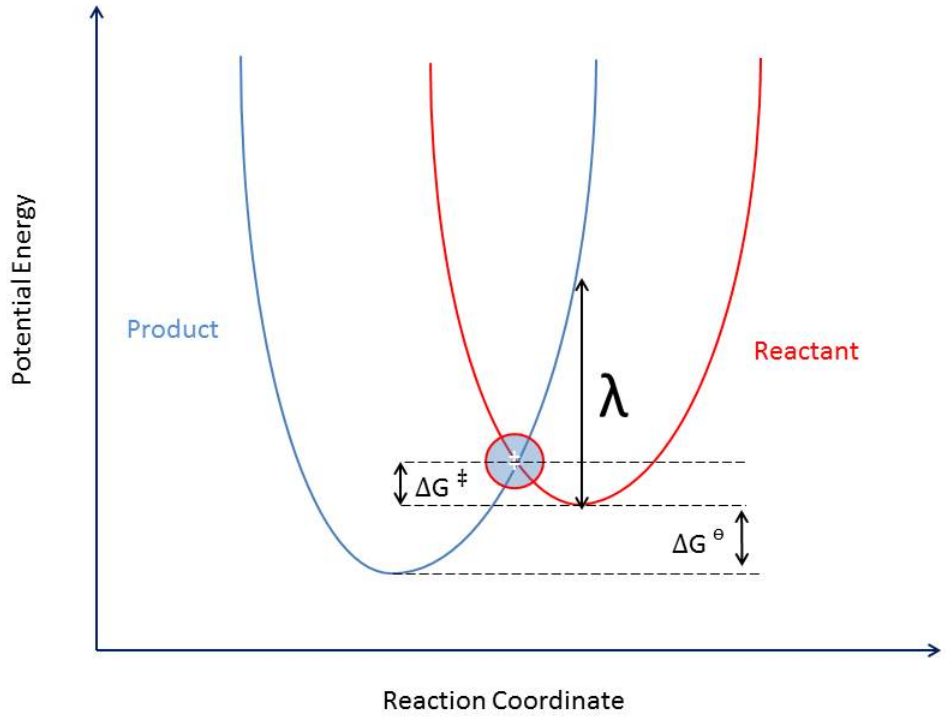


Figure 22: Schematic of the parabolic energy curves as described by Marcus-Hush theory.

difference in equilibrium values for the s-th normal mode coordinate, and k_s and l_s the symmetric and anti-symmetric combinations of the force constants, f_s^{Ox} and f_s^{Red} respectively:

$$k_s = \frac{2 f_s^{Red} f_s^{Ox}}{f_s^{Red} + f_s^{Ox}} \tag{49}$$

$$l_s = \frac{f_s^{Ox}/f_s^{Red} - 1}{f_s^{Ox}/f_s^{Red} + 1} \tag{50}$$

Both BV and MH theories in RTILs parameterise the electron transfer kinetics with k^0, and several studies[9–14] have reported slower electron transfer kinetics in RTILs than in molecular solvents. However, given, as discussed in Part I, the current

lack of knowledge of the electrode/solvent interface, it is difficult to correct for this when considering heterogeneous rate constants, and as such the below studies present an apparent rate constant. The rate constant was derived primarily through analysis of the voltammetric peak-to-peak separations, which may be unduly affected by the ohmic drop or capacitative charging, and this should also be kept in mind.

First considering the use of negative species, Lagrost *et al.*[15] analysed the reduction of substituted nitrobenzenes and aliphatic nitro-based compounds in acetonitrile, [Bmim][NTf_2], and [$N_{4,2,2,2}$][NTf_2]. When the outer-sphere process dominates, as with the nitrobenzene derivatives, the values of k^0 decreased by at least two orders of magnitude in the RTILs compared with acetonitrile. Brooks *et al.*[11] report a large decrease in k^0 for the reduction of benzaldehyde in [Bmim][NTf_2] when compared with molecular solvents. When the RTIL was changed to a pyrrolidinium cation, no such decrease was documented. This suggests that other, more complex, interactions, are contributing to the slower rate of electron transfer, such as increased $\pi - \pi$ interactions or hydrogen bonding, which are cation-specific.[11] This then leads to a higher solvent reorganisation and a slower double layer relaxation, which presents as slower electron transfer kinetics.

Considering then the behaviour of positively charged species (and the role of the anion), Fietkau *et al.*[16] examined a range of ferrocenes in [Emim][NTf_2]. This study established that k^0 took a value an order of magnitude smaller in the RTIL than in acetonitrile, and additionally that k^0 is not affected by the hydrodynamic radius of the ionic components, indicating that other factors are driving the slower kinetics. Evans *et al.*[17] report the rate constant for the oxidation of N,N-dimethyl-p-toluidine in [Bmpyrr][NT_2] as taking an order of magnitude lower value than is observed in acetonitrile. In this ionic liquid, the reduction of benzaldehyde (discussed in the previous paragraph) did not exhibit slower kinetics in the ionic solvent, suggesting that each component of the ionic liquid interacts differently with the charged species.

The lack of correlation between hydrodynamic radius and k^0 was reported consistently with work on arenes and substituted anthracenes,[18] 2,3,5,6-tetrafluoro-7,7,8,8-tetracyanoquinodimethane,[19] and phenylenediamines.[20] These studies suggest that, when considering predominately outer sphere processes, Marcus theory relating the electrochemical rate constant to the viscosity of the solvent may not be informative in RTILs due to the assumptions made about the screening response mechanisms. In molecular solvents, Marcus theory suggests that solvent molecules reorient in an applied field, whereas the component ions that make up RTILs must move relative to each other to screen the charge.[21] Therefore, consideration of non-linear solvent reorganisation is necessary. Streeter *et al.*[22] investigated the relaxation in both acetonitrile, and [Dmim][PF_6], and concluded that it takes the form of a fast subpicosecond process followed by a slower 1— 10 picosecond process, and it is the difference in the latter process between the solvents that may contribute to the slower electrochemical rate constant. Consistent with this is a report by Fawcett *et al.*,[23] which found that as the alkyl chain on an imidazolium cation increased, so too did the relaxation time, leading k^0 to take a lower value.

Overall, the kinetics of redox processes in RTILs is a still-developing field, as evidenced by the focus this thesis dedicates to this topic. The reports of electron transfer in RTILs are extremely limited, and many fail to take into account the role of the double layer, which as outlined in Part I, is a critical but underdeveloped component of considering electron transfer in RTILs.

The following paragraphs detail the varying success of the application of BV, SMH and AMH theories into examining electron transfer in non-ionic solvents. Numerical simulations were performed to fit experimental reverse scan square wave voltammetry monitoring the reduction of 2-methyl-2-nitropropane on a mercury microelectrode.[24,25] Here BV fits the experimental data well, but SMH theory is unable to quantitatively describe the reduction. Wang and coworkers[26] examined the reduction

of europium (III) in water at a mercury hemisphere electrode using differential multipulse voltammetry and square wave voltammetry. The experimental voltammetry was then fitted with numerical simulations, and reported that whilst BV theory successfully parameterised the data, SMH theory was unable to do so. Henstridge *et al.*[27] reviewed the application of SMH and BV theories to both surface bound and solution phase redox reactions in non-ionic solvents, and concluded that SMH theory has difficulty in a wide range of contexts at providing quantitative information, and that the introduction of a four-parameter model might address these concerns. AMH theory was then applied[28] to the reductions considered above, plus the reduction of cyclooctatetraene, using both experimental square wave and cyclic voltammetry.[29] AMH theory was capable of accurately fitting the experimental data in all cases, exceeding the abilities of BV theory and allowing additional physical insight into the reductions that was not possible using BV theory alone. Where reversible processes are considered, such as the one-electron oxidation of 9,10-diphenylanthracene (DPA), BV and SMH theory are equally able to parameterise the experimental data,[30] suggesting that AMH theory is particularly useful where the transfer coefficient deviates from 0.5. In circumstances where this deviation occurs, the use of AMH theory enables similarly good parameterization of the experimental voltammetry, whilst still being able to extract the additional physical insight that comes with the use of Marcus-Hush theory.[31,32]

Marcus-Hush theories have only been applied in molecular solvents, and this thesis considers their use into RTILs for the first time. As discussed in Part I, RTILs are interesting solvents to conduct electrochemical experiments in, due to a range of favourable properties, including wide electrochemical windows,[33] but insight into microscopic process in these solvents is limited. The RTILs used in this Part are 1-ethyl-3-methylimidazolium *bis*(trifluoromethylsulfonyl)imide ([Emim][NTf_2]), 1-butyl-1-methylpyrrolidinium *bis*(trifluoromethylsulfonyl)imide ([Bmpyrr][NTf_2]), 1-

trihexyltetradecylphosphonium *tris*(pentafluoroethyl)trifluorophosphate ([$P_{14,6,6,6}$][FAP]) (Figure 23).

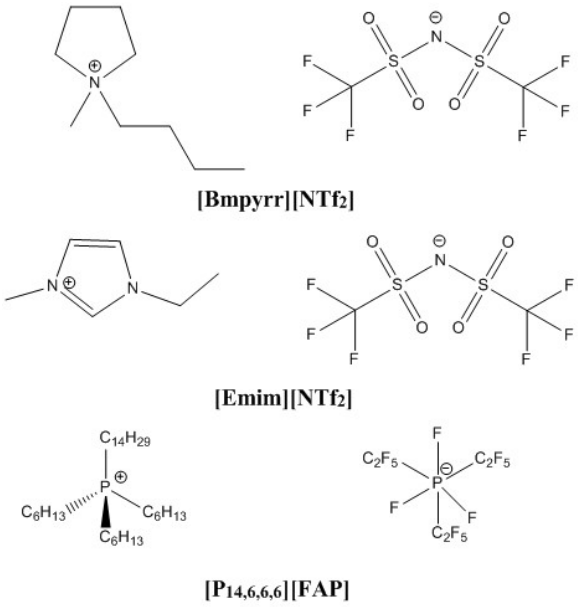


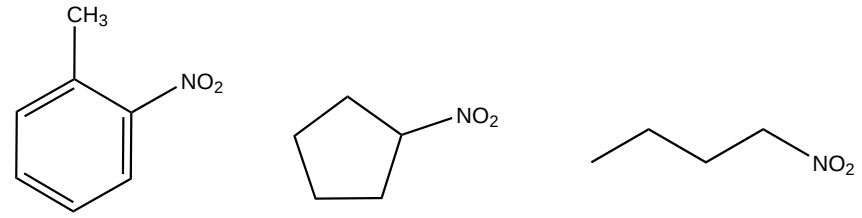
Figure 23: RTILs used in this study: 1-butyl-1-methylpyrrolidinium *bis*(trifluoromethylsulfonyl)imide ([Bmpyrr][NTf_2]), 1-ethyl-3-methylimidazolium *bis*(trifluoromethylsulfonyl)imide ([Emim][NTf_2]), and trihexyltetradecylphosphonium *tris*(pentafluoroethyl)trifluorophosphate ([$P_{14,6,6,6}$][FAP]).

This Part presents experimental voltammetry in RTILs for both the reduction of oxygen (Equation 51) and a range of nitro compounds (Figure 24, Equation 52).

$$O_2 + e^- \rightleftharpoons O_2^{\bullet -} \tag{51}$$

$$RNO_2 + e^- \rightleftharpoons [RNO_2]^{\bullet -} \tag{52}$$

This voltammetry is then critically analysed with Butler-Volmer, Symmetric Marcus-Hush and Asymmetric Marcus-Hush theories for the first time in an ionic solvent. This will allow the evaluation of the success of the electron transfer theories to parameterize data for each system in ionic liquids, and the extraction of a reorganisation energy, λ, and an asymmetry parameter, γ, thereby allowing much greater physical insight into the systems in question.



2-nitrotoluene nitrocyclopentane 1-nitrobutane

Figure 24: Nitro compounds used in this study: 2-nitrotoluene, nitrocyclopentane, and 1-nitrobutane.

0.9 Theory

All of the programs referred to below were coded by Dr Edward O. Barnes but details are included here for completeness. All electrochemical processes are modelled as a single electron reduction:

$$\mathrm{A} + \mathrm{e}^- \rightleftharpoons \mathrm{B} \tag{53}$$

Double potential step chronoamperometry and cyclic voltammetry measurements are made and simulated, in the latter case using three models for electron transfer kinetics: Butler-Volmer kinetics, Symmetric Marcus-Hush kinetics and Asymmetric Marcus-Hush kinetics. Species A is assumed to be initially present in solution. A schematic diagram of a microdisc electrode, defining the spatial coordinates used in simulations, is shown in Figure 25. In all cases, the mass transport equation is given by Fick's second law in cylindrical coordinates:

$$\frac{\partial C_\mathrm{A}}{\partial t} = D_\mathrm{A}\left(\frac{\partial^2 C_\mathrm{A}}{\partial r^2} + \frac{1}{r}\frac{\partial C_\mathrm{A}}{\partial r} + \frac{\partial^2 C_\mathrm{A}}{\partial z^2}\right) \tag{54}$$

where C_A is the concentration of species A (mol m^{-3}), t (s) is time, D_iA (m^2 s^{-1}) is the diffusion coefficient of species A, and r and z (m) are the spatial coordinates defined in Figure 25. The high ionic strength of the RTIL means that electrical migration may be neglected.[34,35] Dimensionless parameters, to remove the scaling effects of

electrode radius and concentration, are introduced to normalise the equation. These parameters are listed in Table 7, and upon their introduction the mass transport equation becomes:

$$\frac{\partial C_{\mathrm{i}}}{\partial \tau} = D_{\mathrm{i}}^{'} \left(\frac{\partial^2 C_{\mathrm{i}}}{\partial R^2} + \frac{1}{R} \frac{\partial C_{\mathrm{i}}}{\partial R} + \frac{\partial^2 C_{\mathrm{i}}}{\partial Z^2} \right) \tag{55}$$

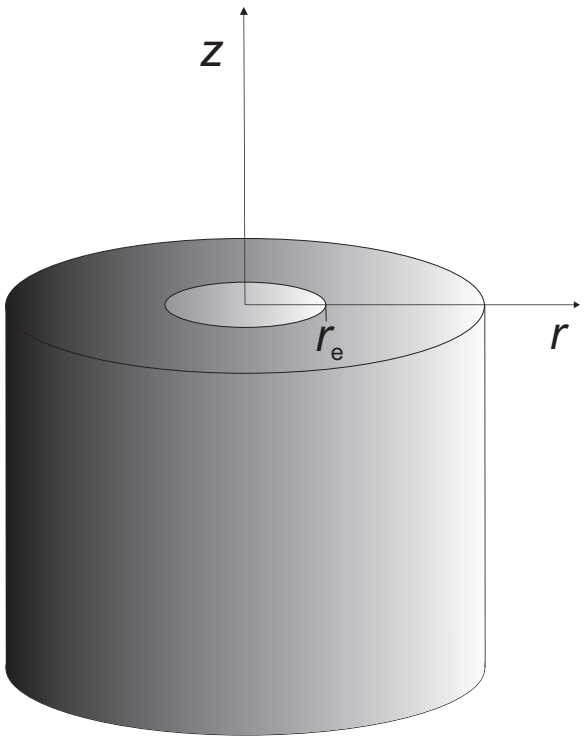


Figure 25: Schematic diagram of a microdisc electrode, defining the coordinate system used.

0.9.1 Chronoamperometry

0.9.1.1 The Shoup and Szabo equation

Single step chronoamperometry at a microdisc electrode is described to within 0.6 % error by the Shoup and Szabo equation,[36–38] where:

$$I = -4nFD_{\mathrm{A}}c_{\mathrm{A}}r_{\mathrm{e}}f(\tau) \tag{56}$$

$$f(\tau) = 0.7854 + 0.4432\tau^{-0.5} + 0.2146 \exp\left(-0.3912\tau^{-0.5}\right) \tag{57}$$

Dimensionless Parameter	Definition
Λ	$\frac{F}{RT}\lambda$
θ	$\frac{F}{RT}\left(E - E_f^{\ominus}\right)$
τ	$\frac{D_{\mathrm{A}}}{r_{\mathrm{e}}^2}t$
C_{i}	$\frac{C_{\mathrm{A}}}{C_{\mathrm{A}}^*}$
$D_{\mathrm{i}}^{'}$	$\frac{D_{\mathrm{i}}}{D_{\mathrm{A}}}$
K^0	$\frac{r_e}{D_{\mathrm{A}}}k^0$
$K_{\mathrm{red/ox}}$	$\frac{r_e}{D_{\mathrm{A}}}k_{\mathrm{red/ox}}$
R	$\frac{r}{r_e}$
Z	$\frac{z}{r_e}$

Table 7: Dimensionless parameters. Species A refers to the species initially present in solution before the experiment/simulation begins.

and

$$\tau = \frac{D_{\mathrm{A}}}{r_{\mathrm{e}}^2} t \tag{58}$$

As t $\rightarrow$ 0, the current follows the Cottrell equation, and the steady-state current is described by Equation 56.

0.9.1.2 Simulation of chronoamperometry

No such equation as the Shoup and Szabo equation exists for double potential step chronoamperometry, and hence numerical simulation is necessary.[39]

Initial conditions, at time $t < 0$, are set as:

$$C_{\mathrm{A}} = C_{\mathrm{A}}^{*} \qquad\qquad C_{\mathrm{B}} = 0 \tag{59}$$

over the whole simulation space, where C_{A}^{*} is the bulk concentration of species A. At the $r = 0$ symmetry boundary, and at the insulating surface surrounding the electrode ($r \geq r_{\mathrm{e}}$, $z = 0$), a zero flux condition is applied to both species at all times:

$$\frac{\partial C_{\mathrm{i}}}{\partial n} = 0 \tag{60}$$

where n is the appropriate spatial coordinate r or z.

The bulk solution boundaries, r_{max} and z_{max} are set at a distance $6\sqrt{D_{\mathrm{max}} t_{\mathrm{max}}}$ in both directions, where D_{max} is the largest diffusion coefficient in the system, and t_{max} is the total time of the experiment. This distance has been shown to be sufficiently far from the edge of the diffusion layer to ensure it represents the bulk solution.[40–44] At these boundaries:

$$r_{\mathrm{max}} = r_{\mathrm{e}} + 6\sqrt{D_{\mathrm{max}} t_{\mathrm{max}}} \qquad\qquad z_{\mathrm{max}} = 6\sqrt{D_{\mathrm{max}} t_{\mathrm{max}}} \tag{61}$$

concentrations are fixed at their bulk values, again at all times.

When the first potential step is applied at time $t = 0$, the boundary conditions at the electrode surface ($r \leq r_{\mathrm{e}}$, $z = 0$) become:

$$c_{\mathrm{A}} = 0 \qquad D_{\mathrm{B}} \left(\frac{\partial c_{\mathrm{B}}}{\partial z} \right) = -D_{\mathrm{A}} \left(\frac{\partial c_{\mathrm{A}}}{\partial z} \right) \tag{62}$$

At some time $t = t_{\mathrm{s}}$, the electrode is subjected to the second potential step, after which the electrode surface boundary conditions become:

$$D_{\mathrm{A}} \left(\frac{\partial C_{\mathrm{A}}}{\partial z} \right) = -D_{\mathrm{B}} \left(\frac{\partial C_{\mathrm{B}}}{\partial z} \right) \qquad c_{\mathrm{B}} = 0 \tag{63}$$

These boundary conditions are summarised, in their normalised form, in Table 8.

<table>
<tr><th colspan="3">Boundary</th><th>Condition</th></tr>
<tr><td>$\tau < 0$</td><td>All R</td><td>All Z</td><td>$C_{\mathrm{A}} = 1$, $C_{\mathrm{B}} = 0$</td></tr>
<tr><td>$0 \leq \tau < \tau_s$</td><td>$0 \leq R \leq 1$</td><td rowspan="3">$Z = 0$</td><td>$C_{\mathrm{A}} = 0$, $D'_{\mathrm{B}} \left(\frac{\partial C_{\mathrm{B}}}{\partial Z} \right) = - \left(\frac{\partial C_{\mathrm{A}}}{\partial Z} \right)$</td></tr>
<tr><td>$\tau \geq \tau_s$</td><td>$0 \leq R \leq 1$</td><td>$\left(\frac{\partial C_{\mathrm{A}}}{\partial Z} \right) = -D'_{\mathrm{B}} \left(\frac{\partial C_{\mathrm{B}}}{\partial Z} \right)$, $C_{\mathrm{B}} = 0$</td></tr>
<tr><td rowspan="4">All τ</td><td>$R > 1$</td><td>$\frac{\partial C_{\mathrm{i}}}{\partial Z} = 0$</td></tr>
<tr><td>$R = 0$</td><td rowspan="2">All Z</td><td>$\frac{\partial C_{\mathrm{i}}}{\partial R} = 0$</td></tr>
<tr><td>$R = R_{\max}$</td><td rowspan="2">$C_{\mathrm{A}} = 1$, $C_{\mathrm{B}} = 0$</td></tr>
<tr><td>All R</td><td>$Z = Z_{\max}$</td></tr>
</table>

Table 8: Dimensionless boundary conditions for double potential step chronoamperometry simulations at a microdisc electrode.

The first step of double potential step simulations may be validated by comparison to the Shoup and Szabo equation (Equations 56 to 58).

0.9.2 Cyclic voltammetry

To simulate cyclic voltammetry, the boundary conditions at the electrode surface must be changed accordingly. The flux of species A through the electrode surface as a result of its net loss *via* reduction or gain *via* oxidation is given by:

$$D_{\mathrm{A}}\left(\frac{\partial c_{\mathrm{A}}}{\partial Z}\right) = k_{\mathrm{red}}C^{0}_{\mathrm{A}} - k_{\mathrm{ox}}C^{0}_{\mathrm{B}} \tag{64}$$

where C^{0}_{A} and C^{0}_{B} are the concentrations of A and B at the electrode surface. The form of the rate constants k_{red} and k_{ox} is dependent on which model of electron transfer is being used, Butler-Volmer kinetics or Marcus-Hush kinetics.

0.9.2.1 Applied potential

In both models of electron transfer, the potential applied to the electrode requires definition. This depends on the start and vertex potentials of the scan, E_{s} (V) and E_{v} (V), and the scan rate ν (V s^{-1}):

$$E = |E_{\mathrm{s}} - E_{\mathrm{v}} - \nu t| + E_{\mathrm{v}} \tag{65}$$

which upon introduction of dimensionless parameters becomes:

$$\theta = |\theta_{\mathrm{s}} - \theta_{\mathrm{v}} - \sigma\tau| + \theta_{\mathrm{v}} \tag{66}$$

0.9.2.2 Butler-Volmer kinetics

In the Butler-Volmer model of electron transfer, the rate constants are considered to be exponentially dependent on the potential applied to the electrode:[1,2]

$$k_{\text{red}} = k^0 \exp\left[\frac{-\alpha F\left(E - E_f^{\ominus}\right)}{RT}\right] \quad (67)$$

$$k_{\text{ox}} = k^0 \exp\left[\frac{\beta F\left(E - E_f^{\ominus}\right)}{RT}\right] \quad (68)$$

where k^0 (m s^{-1}) is the standard electrochemical rate constant, α and β are the transfer coefficients ($\alpha + \beta = 1$), E (V) is the potential applied to the electrode and $E_f^{\ominus}$ (V) is the formal potential of the A/B couple. A full derivation of Equations 67 and 68 are given in the Appendix. Using the dimensionless parameters defined in Table 7, these rate constants become:

$$K_{\text{red}} = K^0 \exp\left[-\alpha\theta\right] \quad (69)$$

$$K_{\text{ox}} = K^0 \exp\left[\beta\theta\right] \quad (70)$$

These boundary conditions are summarised, in their dimensionless form, in Table 9.

Butler-Volmer theory has been extensively used in electrochemical simulation, but offers relatively less physical insight beyond an empirical knowledge of the position of the transition state (if $\alpha < 0.5$, the transition state behaves electrically more like species A, if $\alpha > 0.5$ it behaves more like species B). As noted above, asymmetric Marcus-Hush Theory makes use of an asymmetry factor, γ, which is closely linked to the Butler-Volmer α value[28,45]

0.9.2.3 Symmetric Marcus-Hush kinetics

Marcus-Hush theory is often thought to offer a more fundamental physical insight into the electron transfer process, as discussed in the Introduction. Defining the following

Boundary			Condition
$\tau < 0$	All R	All Z	$C_{\mathrm{A}} = 1$, $C_{\mathrm{B}} = 0$
$\tau \geq 0$	$R \leq 1$	$Z = 0$	$D'_{\mathrm{A}} \left(\frac{\partial C_{\mathrm{A}}}{\partial Z}\right) = K_{\mathrm{red}} C^0_{\mathrm{A}} - K_{\mathrm{ox}} C^0_{\mathrm{B}}$ $D'_{\mathrm{B}} \left(\frac{\partial C_{\mathrm{B}}}{\partial Z}\right) = -D'_{\mathrm{A}} \left(\frac{\partial C_{\mathrm{A}}}{\partial Z}\right)$
	$R > 1$		$\frac{\partial C_{\mathrm{i}}}{\partial Z} = 0$
	$R = 0$	All Z	$\frac{\partial C_{\mathrm{i}}}{\partial R} = 0$
	$R = R_{\max}$		$C_{\mathrm{A}} = 1$, $C_{\mathrm{B}} = 0$
	All R	$Z = Z_{\max}$	

Table 9: Normalised boundary conditions to simulate cyclic voltammetry at a microdisc electrode. The form of K_{red} and K_{ox} depend on the model of electron transfer being used, see text for details.

dimensionless parameters:

$$\Lambda = \frac{F}{RT}\lambda \tag{71}$$

$$x = \frac{F}{RT}(\epsilon - E) \tag{72}$$

where ϵ is the energy of one of the continuum of energy levels in the electrode, then the rate constants for reduction and oxidation in Equation 64 are given by:[46]

$$k_{\mathrm{red}} = k^0 \frac{S_{\mathrm{red}}(\theta,\, \Lambda)}{S_{\mathrm{red}}(0,\, \Lambda)} \tag{73}$$

$$k_{\mathrm{ox}} = k^0 \frac{S_{\mathrm{ox}}(\theta,\, \Lambda)}{S_{\mathrm{ox}}(0,\, \Lambda)} \tag{74}$$

where:

$$S_{\text{red/ox}} = \int_{-\infty}^{\infty} \frac{\exp\left[-\frac{\Lambda}{4}\left(1 \pm \frac{\theta+x}{\Lambda}\right)^2\right]}{1+\exp\left[\mp x\right]} \mathrm{d}x \tag{75}$$

In dimensionless parameters:

$$K_{\text{red}} = K^0 \frac{S_{\text{red}}\left(\theta,\, \Lambda\right)}{S_{\text{red}}\left(0,\, \Lambda\right)} \tag{76}$$

$$K_{\text{ox}} = K^0 \frac{S_{\text{ox}}\left(\theta,\, \Lambda\right)}{S_{\text{red}}\left(0,\, \Lambda\right)} \tag{77}$$

Table 9 again summarises the boundary conditions.

0.9.2.4 Asymmetric Marcus-Hush Theory

AMH theory enables the curvature of the reactant and product parabolae (as shown in Figure 22) to be set individually, and differently from one another. This allows differing force constants, which express the intramolecular vibrations and interactions with the solvent, to be set individually for the reactants and the products. It also relaxes the requirement that the transition state be located precisely between the reactant and product configurations. For simulations carried out in this study, the dimensionless parameters K_{red} and K_{ox} are defined using asymmetric Marcus-Hush (AMH) theory.[47] AMH theory makes use of the following dimensionless parameters:

$$\Lambda = \frac{F}{RT}\lambda \tag{78}$$

$$\theta = \frac{F}{RT}\left(E - E_{\text{f}}^{\ominus}\right) \tag{79}$$

$$x = \frac{F}{RT}\left(\epsilon - E\right) \tag{80}$$

where λ is the reorganisation energy (eV), E is the potential applied to the electrode (V), $E_{\text{f}}^{\ominus}$ is the formal potential of the A/B redox couple (V), and ϵ is the energy of one of an infinite continuum of energy levels in the metal electrode (V). Also included is γ, the unitless asymmetry factor, as discussed in the Introduction. K_{red} and K_{ox}

are then given by:

$$K_{\mathrm{red}} = K^0 \frac{S_{\mathrm{red}}(\theta, \Lambda, \gamma)}{S_{\mathrm{red}}(0, \Lambda, \gamma)} \tag{81}$$

$$K_{\mathrm{ox}} = K^0 \frac{S_{\mathrm{ox}}(\theta, \Lambda, \gamma)}{S_{\mathrm{ox}}(0, \Lambda, \gamma)} \tag{82}$$

where K^0 is the dimensionless standard heterogeneous rate constant:

$$K^0 = \frac{r_{\mathrm{e}}}{D_{\mathrm{A}}} k^0 \tag{83}$$

$S_{\mathrm{red/ox}}$ is given by:[7]

$$S_{\mathrm{red/ox}} = \int_{-\infty}^{\infty} \frac{\exp\left(\frac{\Delta G^{\ddagger}_{\mathrm{red/ox}}(x)}{RT}\right)}{1 + \exp(\mp x)} \, \mathrm{d}x \tag{84}$$

where $\pm$ or $\mp$ is used, the top sign is applied for a reduction and the bottom sign for an oxidation. $\Delta G^{\ddagger}_{\mathrm{red/ox}}(x)$ is the Gibbs activation energy for reduction or oxidation, and:

$$\frac{\Delta G^{\ddagger}_{\mathrm{red/ox}}(x)}{RT} = \frac{\Lambda}{4}\left(1 \pm \frac{\theta + x}{\Lambda}\right)^2 + \frac{\gamma}{4}\left(\frac{\theta + x}{\Lambda}\right)\left[1 - \left(\frac{\theta + x}{\Lambda}\right)^2\right] + \frac{\gamma^2}{16\Lambda} \tag{85}$$

The potential applied to the electrode as a function of time is thus defined:

$$\theta = |\theta_{\mathrm{s}} - \theta_{\mathrm{v}} - \sigma\tau| + \theta_{\mathrm{v}} \tag{86}$$

where θ_{s} and θ_{v} are the starting and vertex potentials respectively, and σ is the dimensionless scan rate:

$$\sigma = \frac{F r_{\mathrm{e}}^2}{RT D_{\mathrm{A}}} \nu \tag{87}$$

where ν is the scan rate (V s^{-1}).

0.9.3 Calculation of the current

In each experiment, the total flux of species A through the electrode is found by integrating the dimensionless flux, j, at each point over the whole electrode area:

$$j = 2\pi \int_0^1 R \left(\frac{\partial C_\mathrm{A}}{\partial Z} \right)_{z=0} \mathrm{d}R \tag{88}$$

and this dimensionless flux converted to a current using:

$$I = -nFD_\mathrm{A}c_\mathrm{A}r_\mathrm{e}j \tag{89}$$

0.9.4 Numerical methods

The mass transport equation and boundary conditions must be discretised in space and time in order to be solved numerically. For double step chronoamperometry, the same grid as used in previous simulation studies is used.[48] In this grid, an initial time point τ_0 is defined as 0. The discrete time points then increase uniformly up to some defined time τ_c, after which the grid expands:

$$\tau \leq \tau_\mathrm{c} \qquad \tau_{k+1} = \tau_k + \Delta\tau \tag{90}$$

$$\tau_\mathrm{c} < \tau < \tau_\mathrm{s} \qquad \tau_{k+1} = \tau_k + \gamma_\tau \left(\tau_k - \tau_{k-1} \right) \tag{91}$$

At τ_s, the point of the potential step, the time grid reverts to its original form and repeats itself, offset by an amount τ_s.

For cyclic voltammetry, a regular time grid is employed, where each unit of θ swept out is divided into N_θ time points.

The same form of spatial grid is employed for both chronoamperometry and cyclic voltammetry, which has been successfully employed in the past.[49] In the Z direction, the initial spatial point is defined as $Z_0 = 0$. The next spatial point is set at a distance

Δ_s away from Z_0, after which the spatial grid expands:

$$Z_0 = 0 \tag{92}$$

$$Z_1 = \Delta_s \tag{93}$$

$$Z_j = Z_j + \gamma_s (Z_j - Z_{j-1}) \tag{94}$$

In the R direction, the spatial grid has the same form, and expands away from $R = 1$ in both directions, until either the centre of the electrode ($R = 0$) or the edge of the simulation space ($R = R_{max}$) is reached. Convergence studies found the following grid parameters appropriate to return a result within 0.5% of a fully converged result. For chronoamperometry: $\Delta_\tau = 1 \times 10^{-7}$, $\tau_c = 1 \times 10^{-4}$, $\gamma_\tau = 1.0001$, $\Delta_s = 1 \times 10^{-5}$ and $\gamma_s = 1.1$. For cyclic voltammetry: $N_\theta = 1000$, $\Delta_s = 8 \times 10^{-5}$ and $\gamma_s = 1.25$.

The mass transport equation and boundary conditions were discretised using the central finite difference method[50] and solved in matrix form using the alternating direction implicit (ADI) method[51] in conjunction with the Thomas Algorithm.[52] Programs were coded in C++ by Dr Edward O Barnes and simulation carried out on a 3.0 GHz Intel(R) Core(TM)2 Duo CPU with 3.84 GB RAM. Typical run times are approximately 10 minutes for double potential step chronoamperometry, 5 minutes for Butler-Volmer cyclic voltammetry and 10 minutes for Marcus-Hush cyclic voltammetry. Simulations are validated by comparison to analytical equations such as the Shoup and Szabo equation,[36] and the Randles-Ševčík equation for cyclic voltammetric peak heights.[53]

0.9.5 Error

To quantify the percentage error between simulated and experimental data, the Mean Scaled Absolute Deviation (MSAD) is used. The MSAD value is defined as:

$$\text{MSAD} = \frac{1}{N} \sum_{N} \left| \frac{I_{\text{exp}} - I_{\text{sim}}}{I_{\text{exp}}} \right| \times 100\% \tag{95}$$

where I_{exp} and I_{sim} are experimental and simulated data points, and N is the total number of data points. This value is used to optimise the fit between simulated and experimental data for both chronoamperometry and cyclic voltammetry, as described below.

0.9.5.1 Chronoamperometry

The Shoup and Szabo equation (Equations 56 to 58) can be used to generate theoretical data for the first step of a double potential step transient. This is done for a range of values of c_{A} and D_{A} (with a known and fixed r_{e}), and each combination is compared to experimental data. Equation 95 is used to generate an MSAD value for each pair of values. This is then repeated for a smaller range of c_{A} and D_{A} around the minimum MSAD until optimal values are reached.

These optimal values are then used in the double potential step chronoamperometry program described above, and the value of D_{B} optimised to give a best fit for the second step.

0.9.5.2 Cyclic voltammetry

To generate an MSAD value for a fit between simulated and experimental cyclic voltammetry, each experimental data point is compared to a linearly extrapolated theoretical value from the two simulated data points surrounding it (since it is unlikely that an experimental data point will be at the same potential as a simulated one).

Equation 95 is again used to generate an MSAD for the fit. Parameters are then optimised by minimising the MSAD value. To avoid the MSAD value becoming misleadingly large by over-emphasising background currents, all data points in a cyclic voltammogram less than 5 % of the maximum current are neglected.

0.10 Experimental

In the case of Chapters 1 and 3, concerning oxygen reduction, 10 μ L of RTIL was placed in a plastic collar fixed on top of the working electrode, and the T-cell (as described above) was assembled, and put under vacuum (0.2 mbar) overnight, to ensure the complete removal of volatile substances, including atmospheric gases and any aqueous impurities. Oxygen was then introduced to the T-cell *via* a column of molecular sieves (activated at 200 °C overnight, 4 Å, Sigma Aldrich) at a flow rate of 200 - 300 cm^3 min^{-1} until saturation (*ca.* 30 mins). Successive cyclic voltammograms (CVs) were recorded to ensure that the RTIL was at saturation before the experimental CVs were recorded. For Chapters 2 and 3, concerning the nitro compounds, stock solutions were prepared by mixing 0.1μL of reagent with 20 μL of RTIL. A solution containing 2 μL of the aforementioned stock and 10 μL of RTIL was prepared in a plastic collar fixed on top of the working electrode, and a T-cell was used for structural stability, as described previously.[13] A wait time of minimum 15 minutes was imposed between each experiment to ensure a stable concentration of analyte at the electrode surface.

All other experimental details are described in Part II (General Experimental Details).

References

[1] Butler, J. A. V. *Trans. Faraday Soc.* **1924**, *19*, 729–733.

[2] Erdey-Gruz, T and Volmer, M, *Z. Physik. Chem.* **1930**, *150*, 203–213.

[3] Guidelli, R.; Compton, R. G.; Feliu, J. M.; Gileadi, E.; Lipkowski, J.; Schmickler, W.; Trasatti, S. *Pure Appl. Chem.* **2014**, *86*, 245–258.

[4] Guidelli, R.; Compton, R. G.; Feliu, J. M.; Gileadi, E.; Lipkowski, J.; Schmickler, W.; Trasatti, S. *Pure Appl. Chem.* **2014**, *86*, 259–262.

[5] Marcus, R. A. *J. Chem. Phys.* **1956**, *24*, 966–978.

[6] Hush, N. S. *J. Phys. Chem.* **1958**, *28*, 962–972.

[7] Zeng, Y.; Smith, R. B.; Bai, P.; Bazant, M. Z. *J. Electroanal. Chem.* **2014**, *735*, 77–83.

[8] Henstridge, M. C.; Rees, N. V.; Compton, R. G. *J. Electroanal. Chem.* **2012**, *687*, 79–83.

[9] Andrieux, C. P.; Hapiot, P.; Saveant, J. M. *J. Phys. Chem.* **1988**, *92*, 5987–5992.

[10] Zhang, J.; ; Bond, A. M. *J. Phys. Chem. B* **2004**, *108*, 7363–7372.

[11] Brooks, C. A.; ; Doherty, A. P. *J. Phys. Chem. B* **2005**, *109*, 6276–6279.

[12] Rogers, E. I.; Streeter, I.; Aldous, L.; Hardacre, C.; Compton, R. G. *J. Phys. Chem. C* **2008**, *112*, 10976–10981.

[13] Rogers, E. I.; Silvester, D. S.; Aldous, L.; Hardacre, C.; Compton, R. G. *J. Phys. Chem. B* **2008**, *112*, 6551–6557.

[14] Allen, G. D.; Buzzeo, M. C.; Villagrn, C.; Hardacre, C.; Compton, R. G. *J. Electroanal. Chem.* **2005**, *575*, 311 – 320.

[15] Lagrost, C.; Preda, L.; Volanschi, E.; Hapiot, P. *J. Electroanal. Chem.* **2005**, *585*, 1 – 7.

[16] Fietkau, N.; Clegg, A. D.; Evans, R. G.; Villagrán, C.; Hardacre, C.; Compton, R. G. *Chem. Phys. Chem.* **2006**, *7*, 1041–5.

[17] Evans, R. G.; Compton, R. G. *ChemPhysChem* **2006**, *7*, 488–496.

[18] Belding, S. R.; Rees, N. V.; Aldous, L.; Hardacre, C.; Compton, R. G. *J. Phys. Chem. C* **2008**, *112*, 1650–1657.

[19] Bano, K.; Zhang, J.; Bond, A. *J. Phys. Chem. C* **2014**, *118*, 9560–9569.

[20] Long, J. S.; Silvester, D. S.; Barnes, A. S.; Rees, N. V.; Aldous, L.; Hardacre, C.; Compton, R. G. *J. Phys. Chem. C* **2008**, *112*, 6993–7000.

[21] Lynden-Bell, R. *Electrochem. Commun.* **2007**, *9*, 1857–1861.

[22] Streeter, I.; Lynden-Bell, R. M.; Compton, R. G. *J. Phys. Chem. C* **2008**, *112*, 14538–14544.

[23] Fawcett, W. R.; Gal, A.; Misicak, D. *J. Electroanal. Chem.* **2011**, *660*, 230 – 233.

[24] Henstridge, M. C.; Wang, Y.; Limon-Petersen, J. G.; Laborda, E.; Compton, R. G. *Chem. Phys. Lett.* **2011**, *517*, 29–35.

[25] Laborda, E.; Wang, Y.; Henstridge, M. C.; Martínez-Ortiz, F.; Molina, A.; Compton, R. G. *Chem. Phys. Lett.* **2011**, *512*, 133–137.

[26] Wang, Y.; Laborda, E.; Henstridge, M. C.; Martinez-Ortiz, F.; Molina, A.; Compton, R. G. *J. Electroanal. Chem.* **2012**, *668*, 7–12.

[27] Henstridge, M. C.; Laborda, E.; Rees, N. V.; Compton, R. G. *Electrochim. Acta* **2012**, *84*, 12–20.

[28] Laborda, E.; Henstridge, M. C.; Batchelor-McAuley, C.; Compton, R. G. *Chem. Soc. Rev.* **2013**, *42*, 4894–905.

[29] Henstridge, M. C.; Laborda, E.; Wang, Y.; Suwatchara, D.; Rees, N.; Molina, A.; Martínez-Ortiz, F.; Compton, R. G. *J. Electroanal. Chem.* **2012**, *672*, 45–52.

[30] Suwatchara, D.; Henstridge, M. C.; Rees, N. V.; Compton, R. G. *J. Phys. Chem. C* **2011**, *115*, 14876–14882.

[31] Suwatchara, D.; Rees, N. V.; Henstridge, M. C.; Laborda, E.; Compton, R. G. *J. Electroanal. Chem.* **2012**, *685*, 53–62.

[32] Suwatchara, D.; Henstridge, M. C.; Rees, N. V.; Laborda, E.; Compton, R. G. *J. Electroanal. Chem.* **2012**, *677-680*, 120–126.

[33] O'Mahony, A. M.; Silvester, D. S.; Aldous, L.; Hardacre, C.; Compton, R. G. *J. Chem. Eng. Data* **2008**, *53*, 2884–2891.

[34] Dickinson, E. J. F.; Compton, R. G. *J. Phys. Chem. C* **2009**, *112*, 17585–17589.

[35] Dickinson, E. J. F.; Compton, R. G. *J. Electroanal. Chem.* **2011**, *661*, 198–212.

[36] Shoup, D.; Szabo, A. *J. Electroanal. Chem.* **1982**, *140*, 237–245.

[37] Paddon, C. A.; Silvester, D. S.; Bhatti, F. L.; Donohoe, T.; Compton, R. G. *Electroanal.* **2007**, *19*, 11–22.

[38] Xiong, L.; Aldous, L.; Henstridge, M. C.; Compton, R. G. *Anal. Methods* **2012**, *4*, 371.

[39] Klymenko, O. V.; Evans, R. G.; Hardacre, C.; Svir, I. B.; Compton, R. G. *J. Electroanal. Chem.* **2004**, *571*, 211–221.

[40] Gavaghan, D. J. *J. Electroanal. Chem.* **1997**, *420*, 147–158.

[41] Gavaghan, D. J. *J. Electroanal. Chem.* **1998**, *456*, 1–12.

[42] Gavaghan, D. J. *J. Electroanal. Chem.* **1998**, *456*, 13–23.

[43] Gavaghan, D. J. *J. Electroanal. Chem.* **1998**, *456*, 25–35.

[44] Svir, I. B.; Oleinick, A.; Compton, R. G. *Russ. J. Electrochem.* **2003**, *39*, 160–163.

[45] Laborda, E.; Henstridge, M. C.; Compton, R. G. *J. Electroanal. Chem.* **2012**, *667*, 48–53.

[46] Chidsey, C E D, *Science* **1991**, *251*, 919–922.

[47] Marcus, R. A. *J. Chem. Phys.* **1965**, *43*, 679 – 701.

[48] Barnes, E. O. and Xiong, L. and Ward, K. R. and Compton, R. G. *J. Electroanal. Chem.* **2013**, *701*, 59–68.

[49] Tanner, E. E. L.; Xiong, L.; Barnes, E. O.; Compton, R. G. *J. Electroanal. Chem.* **2014**, *727*, 59–68.

[50] Compton, R. G.; Laborda, E.; Ward, K. R. *Understanding Voltammetry: Simulation of Electrode Processes*; Imperial College Press: London, 2014.

[51] Britz, D. *Digital Simulation in Electrochemistry*; Springer-Verlag, 2005.

[52] Press, W. H., Teukolsky, S. A., Vetterling, W. T., Flannery, B. P., Eds. *Numerical Recipes: The Art of Scientific Computing*; Cambridge University Press, 2007.

[53] Compton, R. G.; Banks, C. E. *Understanding Voltammetry*, 2nd ed.; Imperial College Press: London, 2011.

Chapter 1

A Comparative Study of Butler-Volmer and Symmetric Marcus-Hush Theories: Oxygen Reduction

Interest in the electroreduction of oxygen is high due to its vital role in the development of clean energy alternatives, including fuel cells.[1–3] The reaction has been studied in a range of contexts, as varied as bioelectroreduction facilitated by enzymes[4] to carbon nanomaterials[5,6] and the newly-constructed fluorographane.[7] To improve fundamental knowledge of the system, there is a need to better understand the electron transfer kinetics underlying this process. This has therefore led to extensive studies in a variety of solvents.[8–13]

The one electron reduction is shown below in Equation 1.1. The product of the initial one-electron reduction, superoxide, is a highly nucleophilic ion that initiates

further reactions with a proton source, if one is present in solution.

$$O_2 + e^- \rightleftharpoons O_2^{\bullet -} \tag{1.1}$$

The electron transfer kinetics of the irreversible oxygen reduction have been studied in-depth in aqueous solvents[14,15] and values for the total reorganisation energy for the reduction of oxygen to superoxide have been calculated to lie between 1.26 — 4.51 eV.[16] This has been attributed to rearrangement of the polar water molecules upon formation of the charged superoxide ions. Note that *experimental* determination of this value is non-trivial in aqueous solvents, due to the reactivity of the superoxide ion.

Ionic liquids are interesting solvents in which to examine the reversible one-electron reduction of oxygen. This is largely due to the stability of the superoxide molecule in a range of ILs, which leads to quasi-reversible voltammetry.[8,12,17–19] This allows examination of the one electron reduction in a way that is not possible in aqueous solvents. The ability to record this voltammetry allows further analysis of the electron transfer kinetics, and the discovery of possible physical insights with the application of SMH theory. The structure of the IL used in this chapter, 1-butyl-1-methylpyrrolidinium
bis(trifluoromethylsulfonyl)imide ([Bmpyrr][NTf_2]), is shown in Fig. 1.1.

As outlined in the Introduction to Part III, the question of the application of Marcus theory to redox reactions undertaken in ionic liquids has not been definitively answered, but it appears to be more capable of describing inner-sphere processes.[20–22] However, as yet, the experimental ET kinetics of oxygen reduction in molecular solvents have not been studied, and the experimental applicability of Marcus-Hush theory in ionic liquids has not yet been determined, nor have any values for reorganisation energy have been established.

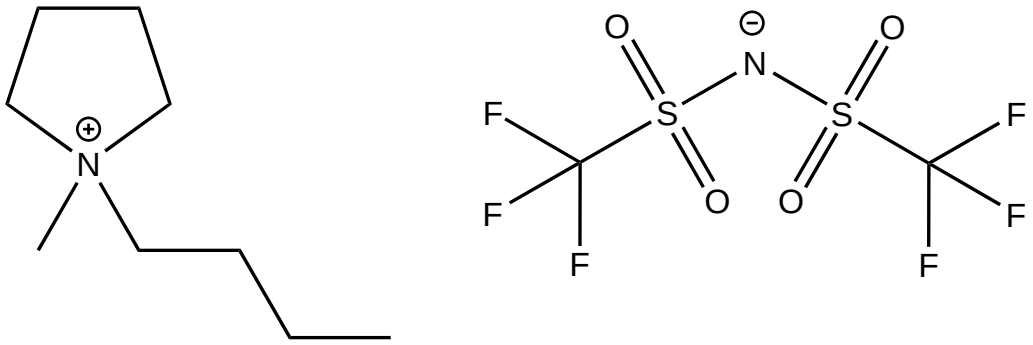


Figure 1.1: RTIL used in this chapter; 1-butyl-1-methylpyrrolodinium *bis*(trifluoromethylsulfonyl)imide ([Bmpyrr][NTf_2]).

This chapter reports the comparative outcome of the use of Butler-Volmer (BV) theory and Symmetric Marcus Hush (SMH) theory to model experimental cyclic voltammetry of the reduction of oxygen in [Bmpyrr][NTf_2] on a gold electrode. This is followed by discussion of the physical insights gained from the application of SMH and the determination of a value for solvent reorganisation energy, λ.

[Bmpyrr][NTf_2] was chosen for its relatively low viscosity (70 cP at 298 K)[23] and well characterised voltammetry for oxygen reduction.[17] Cyclic voltammetry (CV) was performed on saturated solutions of oxygen in [Bmpyrr][NTf_2] over a range of scan rates (100 — 400 mV s^{-1}). A blank CV, from -3 V — 2 V vs Ag, was recorded prior to the introduction of oxygen to ensure the ionic liquid was free from impurities, and to estimate solution capacitance for each scan rate. The capacitative current was subtracted from the experimental current to generate corrected voltammograms prior to further analysis. In all further experimental cases, the potential was swept from 0.0 V (vs Ag), a voltage at which zero Faradaic current flows, to a potential cathodic of the reduction of oxygen (-1.5 V vs Ag). At a scan rate of 200 mV s^{-1}, the oxidative peak current at -0.8 V was 1.7 nA, the limiting current was -4.4 nA, and the half peak potential was approximately -0.9 V vs silver wire (this approximation is necessary due to the use of a quasi-reference electrode). The peak corresponding to the reduction of oxygen appeared on the forward scan at -1.3 V vs Ag, whilst

the oxidative peak appeared on the reverse scan at -0.84 V vs Ag. The resultant voltammograms (Fig. 1.2, a-c) show more steady-state-like behaviour in the forward wave (corresponding to the reduction of oxygen to superoxide) than in the back wave (reoxidation of superoxide to oxygen). This difference in the shape can be explained by different types of diffusion being observed at the electrode surface (two-dimensional Fickian diffusion of oxygen as compared with one-dimensional Fickian diffusion of the much slower diffusing superoxide).[8]

Beginning with a scan rate of 200 mV s^{-1}, as it was in the middle of the range, CVs were modelled using a program described in the Theory Section that utilises Butler-Volmer kinetics.

As this is a well-reported system,[9,18,24,25] the starting point for the diffusion coefficient and the concentration of oxygen were taken from literature. Optimised values for k^0, α, c_{O_2}, D_{O_2}, $D_{O_2^{\bullet-}}$, and $E_f^{\ominus}$ (tabulated in Table 1.1) were obtained to give the "best fit", which was quantified with the calculation of a Mean Scaled Absolute Deviation (MSAD, as described in the Theory Section). These values were used across the scan rates with all values remaining constant, with the exception of $E_f^{\ominus}$, which was allowed to deviate slightly ($\pm$ 0.02 V) to account for the use of a quasi-reference electrode.[26] The optimised values and the mean MSADs across the scan rates are reported in Table 1.1.

The value of $D_{O_2^{\bullet-}}$, the diffusion coefficient of the superoxide ion, is an order of magnitude smaller than that of the diffusion coefficient for oxygen, D_{O_2}. This is as a result of the newly charged superoxide molecule's increased interaction with the ionic solvent, which reduces its movement through the solution, as predicted above. The value for the transfer coefficient, α, of 0.29, suggests an early, reactant-like transition state.[27] Another notable outcome is the small k^0, which suggests a slower electrochemical rate than seen in other ILs of comparable viscosity. Table 1.2 details transfer coefficients and rate constants for oxygen reduction in a range of ionic

Parameter	Butler-Volmer	Marcus-Hush
D_{O_2} / m^2 s^{-1}	2.05×10^{-10}	2.05×10^{-10}
$D_{O_2^{\bullet-}}$ / m^2 s^{-1}	1.80×10^{-11}	1.55×10^{-11}
C_{O_2} / mM	10	10
k^0 / cm s^{-1}	0.0023	0.0015
$E_f^{\ominus}$ / V	-0.87 ± 0.02	-0.87 ± 0.02
α	0.29	-
λ / eV	-	0.4
MSAD (average) / %	9.52	13.9

Table 1.1: Simulation Results for the reduction of oxygen in [Bmpyrr][NTf_2] on a μAu electrode.

liquids. Note that the transfer coefficients are <0.5 across the range, suggesting the early transition state provided by BV in this case is consistent.

Symmetric Marcus-Hush (SMH) theory was next used to model electrode kinetics, and the same procedure as outlined above was followed independently to establish optimal values for the parameters of concern. In this case, the transfer coefficient, α, is no longer a parameter that is taken into consideration. Instead, the reorganisation energy, λ, is used. The standard electrochemical rate constant, k^0, also takes on different values in this model. The best fit values and the mean MSAD values are outlined in Table 1.1. The similarity between the common parameters suggests that SMH theory is capable of providing a reliable measure of the reorganisation energy, λ. The experimental value for λ was determined to be 0.4 eV in this solvent, which suggests that there is a relatively little solvent reorganisation (compared with that observed in water, where λ = 1.26 — 4.51 eV[16]), and the primary contribution to the reorganisation energy is inner-sphere, or molecular, reorganisation.

Ionic Liquid	C_{O_2} / mM	D_{O_2} / m^2 s^{-1}	$D_{O_2^{\bullet-}}$ / m^2	k^0 / cm^{-1}	α
[Emim][BF_4][19]	1.1 ± 0.2	$1.7 \pm 0.2 \times 10^{-9}$	-	$0.94 \pm 0.13 \times 10^{-3}$	0.46 ± 0.02
[Pmim][BF_4][19]	0.97 ± 0.05	$1.3 \pm 0.2 \times 10^{-9}$	-	$1.5 \pm 0.4 \times 10^{-3}$	0.36 ± 0.03
[Bmim][BF_4][19]	1.1 ± 0.1	$1.2 \pm 0.1 \times 10^{-9}$	-	$0.83 \pm 0.2 \times 10^{-3}$	0.36 ± 0.02
[MOPMPip][NTf_2][13]	14.3	1.0×10^{-10}	-	-	0.18
[HMPyrr][NTf_2][13]	14.5	2.5×10^{-10}	-	-	0.13
[Emim][NTf_2][8]	3.9	8.3×10^{-10}	1.27×10^{-10}	-	-
[$N_{6,2,2,2}$][NTf_2][8]	11.6	1.48×10^{-10}	4.66×10^{-12}	-	-
[C_4dmim][NTf_2][28]	4.4	4.7×10^{-10}	7.5×10^{-11}	$0.94 \pm 0.13 \times 10^{-3}$	0.4
[$N_{6,2,2,2}$][NTf_2][28]	4.5	4.1×10^{-10}	7.3×10^{-12}	0.3×10^{-3}	0.36 ± 0.03

Table 1.2: Literature values for Butler-Volmer fitting parameters for the reduction of oxygen in various ionic liquids

Of the two electron transfer theories, the BV program is still superior in terms of its ability to parameterise the experimental data with a greater accuracy. This is evidenced by lower MSAD values and a better fit, as seen in Table 1.1 and Fig. 1.2.

This Chapter examined the ability of BV and SMH theories to quantitatively describe the reduction of oxygen at a microgold electrode in [Bmpyrr][NTf_2]. BV was the superior theory, with a lower error, but SMH theory determined a value for the reorganisation energy, λ, of 0.4 ± 0.1 eV, which corresponds to a predominately inner-sphere contribution to the overall reorganisation energy. The next chapter extends this work by comparing BV and SMH theories to the reduction of a range of nitro-compounds in RTILs.

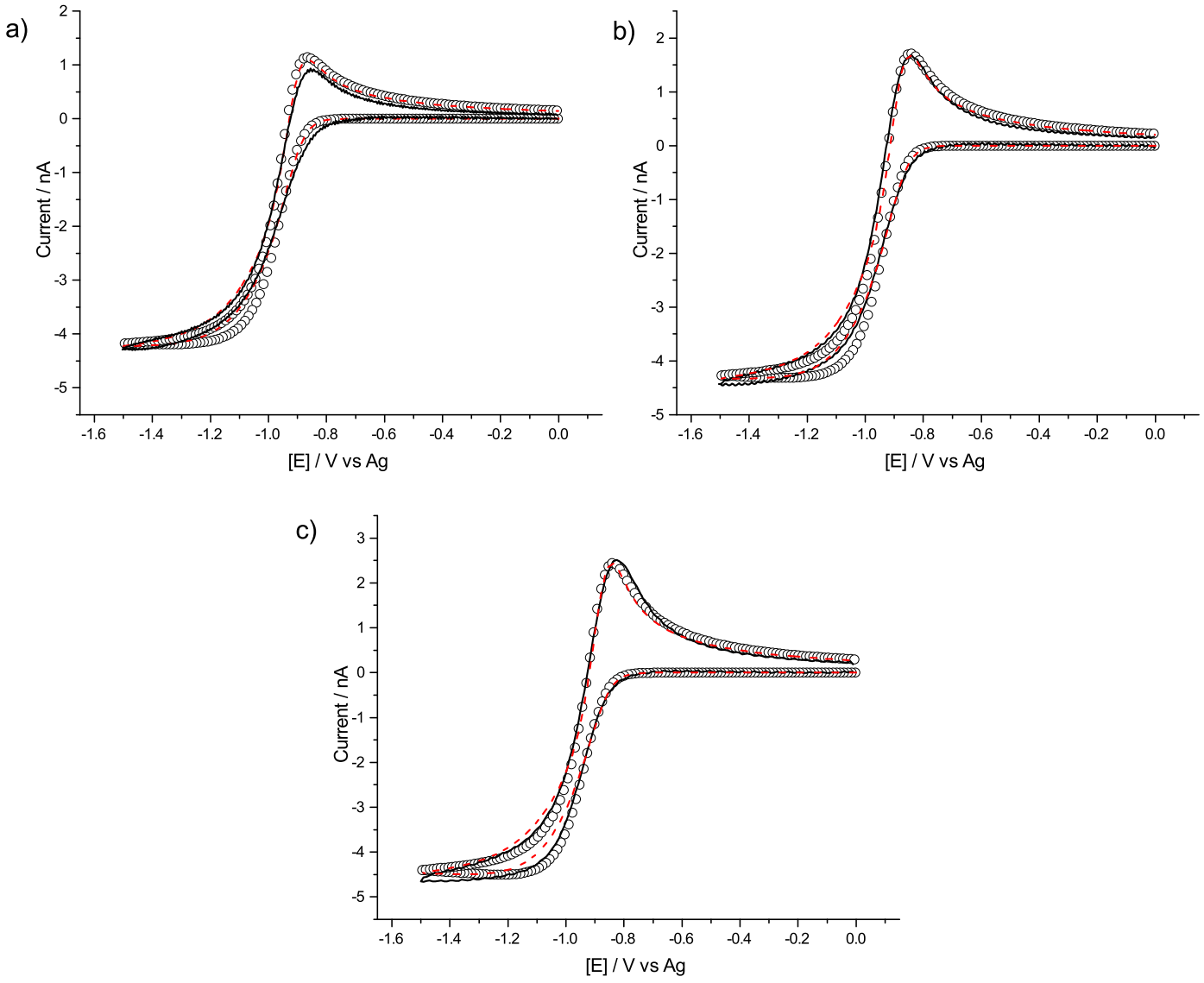


Figure 1.2: Experimental cyclic voltammetry of the reduction of oxygen in [Bmpyrr][NTf_2] on a μAu electrode (black solid line) at 298 K, compared to Butler-Volmer Theory (red dashed line), and Symmetric Marcus-Hush Theory (circles) for scan rates of (a) 100 mV s^{-1}, (b) 200 mV s^{-1}, and (c) 400 mV s^{-1}. Parameters corresponding to each simulation are detailed in Table 1.1.

References

[1] Lefèvre, M.; Proietti, E.; Jaouen, F.; Dodelet, J.-P. *Science* **2009**, *324*, 71–74.

[2] Zhang, L.; Xia, Z. *J. Phys. Chem. C* **2011**, *115*, 11170–11176.

[3] Nørskov, J. K.; Rossmeisl, J.; Logadottir, A.; Lindqvist, L.; Kitchin, J. R.; Bligaard, T.; Jónsson, H. *J. Phys. Chem. B* **2004**, *108*, 17886–17892.

[4] Holmberg, S.; Rodriguez-Delgado, M.; Milton, R.; Ornelas-Soto, N.; Minteer, S.; Parra, R.; Madou, M. *ACS Catal.* **2015**, *5*, 7507–7518.

[5] Lehmann, K.; Yurchenko, O.; Urban, G. *JPCS* **2014**, *557*.

[6] Gong, K.; Du, F.; Xia, Z.; Durstock, M.; Dai, L. *Science* **2009**, *323*, 760–764.

[7] Gusmão, R.; Sofer, Z.; Šembera, F.; Janoušek, Z.; Pumera, M. *Chem. Eur. J.* **2015**, *21*, 16474–16478.

[8] Buzzeo, M. C.; Klymenko, O. V.; Wadhawan, J. D.; Hardacre, C.; Seddon, K. R.; Compton, R. G. *J. Phys. Chem. A* **2003**, *107*, 8872 – 8878.

[9] Katayama, Y.; Sekiguchi, K.; Yamagata, M.; Miura, T. *J. Electrochem. Soc.* **2005**, *152*, E247 – E250.

[10] Zhang, L.; Li, H.; Zhang, J. *Power Sources* **2014**, *255*, 242 – 250.

[11] Wadhawan, J. D.; Welford, P. J.; McPeak, H. B.; Hahn, C. E. W.; Compton, R. G. *Sens. Actuators B* **2003**, *88*, 40 – 52.

[12] AlNashef, I. M.; Leonard, M. L.; Kittle, M. C.; Matthews, M. A.; Weidner, J. W. *Electrochem. Solid-State. Lett.* **2001**, *4*, D16 – D18.

[13] Hayyan, M.; Mjalli, F. S.; Hashim, M. A.; AlNashef, I. M.; Tan, X. M. *J. Electroanal. Chem.* **2011**, *657*, 150 – 157.

[14] Hartnig, C.; Koper, M. T. M. *J. Electroanal. Chem.* **2002**, *532*, 165 – 170.

[15] Gotti, G.; Fajerwerg, K.; Evrard, D.; Gros, P. *Int. J. Electrochem. Sci.* **2013**, *8*, 12643 – 12657.

[16] Eberson, L. *Electron Transfer Reactions in Organic Chemistry*, 1st ed.; Springer-Verlag: Heidelberg, 1987.

[17] Huang, X.; Rogers, E. I.; Hardacre, C.; Compton, R. G. *J. Phys. Chem. B* **2009**, *113*, 8953 – 8959.

[18] Evans, R. G.; Klymenko, O. V.; Saddoughi, S. A.; Hardacre, C.; Compton, R. G. *J. Phys. Chem. B* **2004**, *108*, 7878 – 7886.

[19] Zhang, D.; Okajima, T.; Matsumoto, F.; Ohsaka, T. *J. Electrochem. Soc.* **2004**, *151*, D31 – D37.

[20] Lynden-Bell, R. *J. Phys. Chem. B* **2007**, *111*, 10800–10806.

[21] Streeter, I.; Lynden-Bell, R. M.; Compton, R. G. *J. Phys. Chem. C* **2008**, *112*, 14538–14544.

[22] Fietkau, N.; Clegg, A. D.; Evans, R. G.; Villagran, C.; Hardacre, C.; Compton, R. G. *Chem. Phys. Chem.* **2006**, *7*, 1041–1045.

[23] Okoturo, O. O.; VanderNoot, T. J. *J. Electroanal. Chem.* **2004**, *568*, 167 – 181.

[24] Yuan, X.-Z.; Alzate, V.; Xie, Z.; Ivey, D. G.; Qu, W. *J. Electrochem. Soc.* **2014**, *161*, A451 – A457.

[25] Monaco, S.; Arangio, A. M.; Soavi, F.; Mastragostino, M.; Paillard, E.; Passerini, S. *Electrochim. Acta* **2012**, *83*, 94 – 104.

[26] Gritzner, J., G.; Kuta *Pure Appl. Chem.* **1984**, *56*, 461 – 466.

[27] Compton, R. G.; Banks, C. E. *Understanding Voltammetry*, 2nd ed.; World Scientific: Singapore, 2010.

[28] Rogers, E. I.; Huang, X. J.; Dickinson, E. J. F.; Hardacre, C.; Compton, R. G. *J. Phys. Chem. C* **2009**, *113*, 17811 – 17823.

Chapter 2

A Comparative Study of Butler-Volmer and Symmetric Marcus-Hush Theories: Nitro groups

The chapter outlines the outcome of experimental voltammetry and associated simulations based on Butler-Volmer (BV) theory and Symmetric Marcus-Hush (SMH) theory for the one-election reduction of 2-nitrotoluene (2-NT) in two ionic liquids, trihexyltetradecylphosphonium *tris*(pentafluoroethyl)trifluorophosphate ($[P_{14,6,6,6}][FAP]$) and 1-ethyl-3-methylimidazolium *bis*(trifluoromethylsulfonyl)imide ($[Emim][NTf_2]$), as shown in Figure 2.1, first to explore the relative success of the two models and second to compare the Marcusian parameter, λ, for the same analyte in the two solvents.

Next, two additional nitro-based compounds, nitrocyclopropane (NCP) and 1-nitrobutane (BuN) are considered in $[P_{14,6,6,6}][FAP]$ (Figure 2.2).

2-NT is aromatic, whilst both NCP and BuN are aliphatic, which allows us to

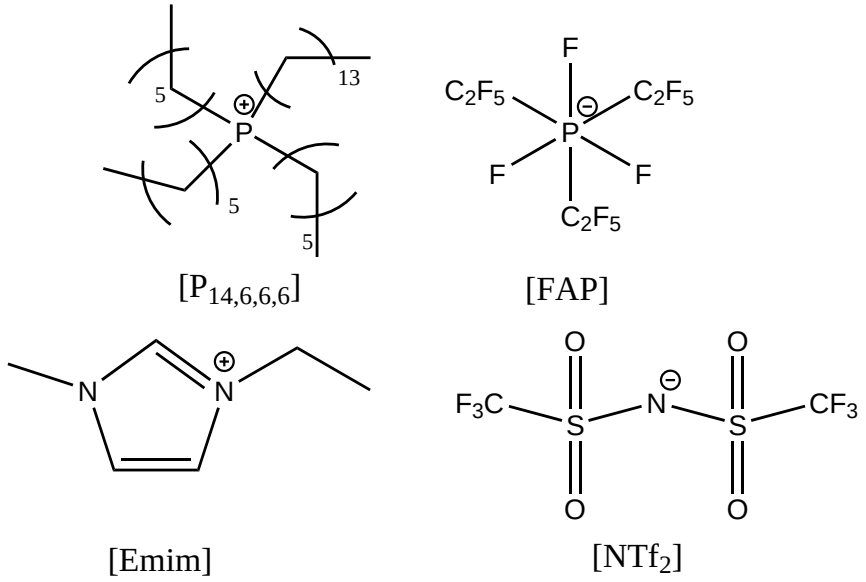


Figure 2.1: RTILs used in this study: 1-ethyl-3-methylimidazolium *bis*(trifluoromethylsulfonyl)imide ([Emim][NTf_2]) and trihexyltetradecylphosphonium *tris*(pentafluoroethyl)trifluorophosphate ([$P_{14,6,6,6}$][FAP]).

study the effects of introduction of charge onto the different classes of nitro compounds in an ionic solvent, and how this affects the respective abilities of BV theory and SMH theory to parameterise the data, as well as any change in the Marcusian parameter, λ.

2.1 Reduction of 2-nitrotoluene in [$P_{14,6,6,6}$][FAP] and [Emim][NTf_2]

This section reports the experimental cyclic voltammetry of the one electron reduction of 2-NT in the ionic liquids [$P_{14,6,6,6}$][FAP] and [Emim][NTf_2] and the comparative outcome of the use of BV theory and SMH theory to model the experimental voltammograms.

$$2-MeC_6H_4NO_2 + e^- \rightleftharpoons [2-MeC_6H_4NO_2]^{\bullet -}$$

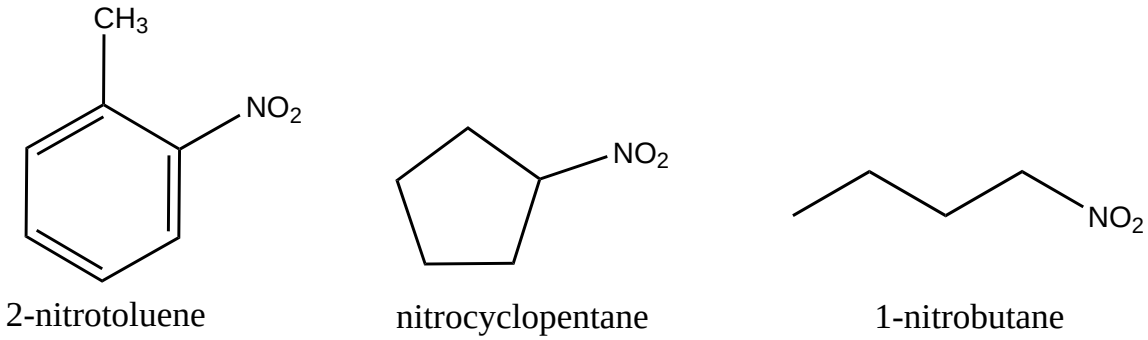


Figure 2.2: Nitro compounds used in this study: 2-nitrotoluene, nitrocyclopentane, and 1-nitrobutane.

An experimental value for solvent reorganisation energy, λ, is determined and physical insights are inferred for both RTILs.

2.1.1 Reduction of 2-nitrotoluene in $[P_{14,6,6,6}][FAP]$

The first system examined was the one electron reduction of 2-nitrotoluene (2-NT) in $[P_{14,6,6,6}]$ [FAP]. This RTIL was selected due to the disparity of sizes between the cation and anion, and its relative hydrophobicity compared with other ionic liquids.[1] Cyclic Voltammetry (CV) was performed on *ca.* 10 mM solutions of 2-NT in $[P_{14,6,6,6}][FAP]$ over a range of scan rates (100 —1000 mV s^{-1}). The potential was swept from -1.10 V vs Ag, a potential at which *ca.* zero Faradaic current flows, to a potential cathodic of the reduction of 2-NT, -1.60 V (vs Ag), then back to -1.10 V vs Ag. At a scan rate of 200 mV s^{-1}, the peak corresponding to the reduction of 2-nitrotoluene appeared on the forward scan at *ca.* -1.40 V vs Ag with a peak current of -1.0 nA, whilst the oxidative peak appeared at -1.27 V vs Ag with a peak current of 0.50 nA. The limiting current was -0.90 nA, and the half peak potential was -1.35 V vs Ag wire. All experimental cyclic voltammograms (CVs) were baseline corrected on the GPES interface prior to simulations being conducted. Representative voltammograms are shown in Figure 2.3.

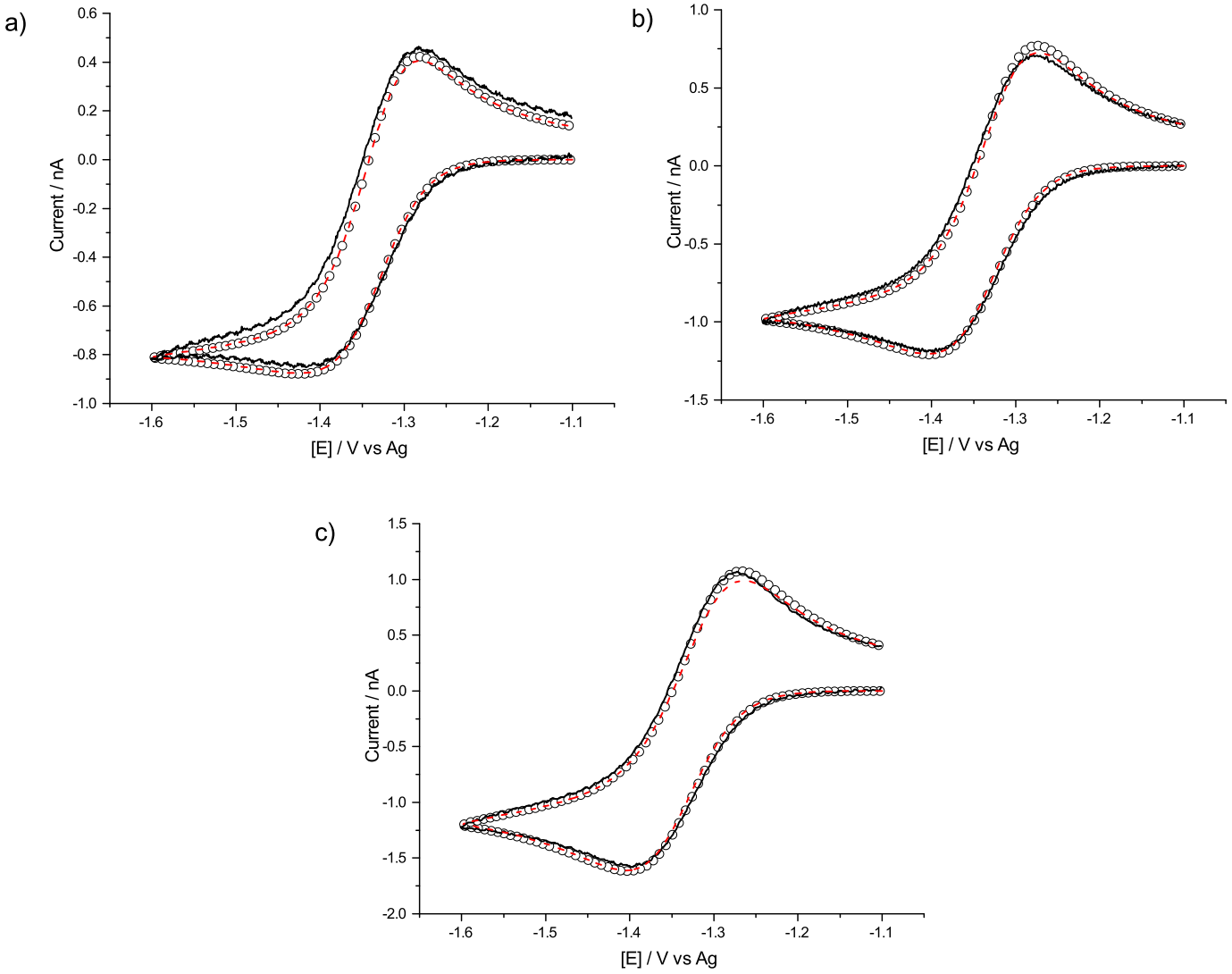


Figure 2.3: Experimental cyclic voltammetry of the reduction of 2-nitrotoluene in $[P_{14,6,6,6}][FAP]$ on a μAu electrode (black solid line) at 298 $\pm$ 1 K, compared to Butler-Volmer Theory (red dashed line), and Symmetric Marcus-Hush Theory (circles) for a scan rate of a) 100 mV s^{-1}, b) 400 mV s^{-1} and c) 1000 mV s^{-1}.

Having established the potential at which 2-NT is fully reduced, double step chronoamperometry was conducted to determine the precise concentration (C_A^*) and diffusion coefficients (D_A and D_B). This was undertaken by stepping the potential from -1.15 V vs Ag to -1.60 V vs Ag, a point at which 2-NT is fully reduced, for 2s, then back to -1.15 V vs Ag for a further 2s. Three overlaying chronoamperograms were recorded, and the analysis was carried out on the second experiment. The initial step, corresponding to the reduction, was analysed with respect to the Shoup and Szabo equation[2] (detailed in the Theory Section) to yield the bulk concentration (C_A^*) and the diffusion coefficient of 2-NT, (D_A). A fitting program (as described in the Theory Section) was used to determine the values of C_A^* and D_A of 2-NT with the lowest possible error, in this case a concentration of 16.3 $\pm$ 0.3 mM and a D_A of 2.2 $\pm$ 0.1 $\times$ 10^{-11} m^2 s^{-1}, with an error of 0.68%. A representative experimental chronoamperogram and corresponding simulation is shown in Figure 2.4.

A program described in the Theory Section was used to simulate both steps of the chronoamperogram, using the values described above for C_A^* and D_A, to obtain a starting point for D_B of 8 $\times$ 10^{-12} m^2 s^{-1}. The optimised diffusion coefficient of 2-NT, D_A, 2.2 $\times$ 10^{-11} m^2 s^{-1}, is almost an order of magnitude larger than that of the reduced species, D_B, 4.3 $\times$ 10^{-12} m^2 s^{-1}. The disparity in diffusion coefficients is likely to stem from the additional charge on the molecule, which results in an increased interaction with the ionic solvent, as has been reported previously for O_2 and $O_2^{\bullet -}$.[3] 2-NT has not been studied electrochemically in any ionic solvents, however, 2-methyl-2-nitropropane (2-MeNP) has been studied in acetonitrile, with equal diffusion coefficients of 2.7 $\times$ 10^{-9} m^2 s^{-1} measured for both the parent compound and reduced anion.[4,5] In moving to an ionic solvent, the slower diffusion is expected due to the increased viscosity of the solvent when compared with a molecular solvent.

CVs were first modelled with a program utilising BV kinetics (as described in the Theory Section). Taking the values of C_A^*, D_A and D_B from the chronoamperograms,

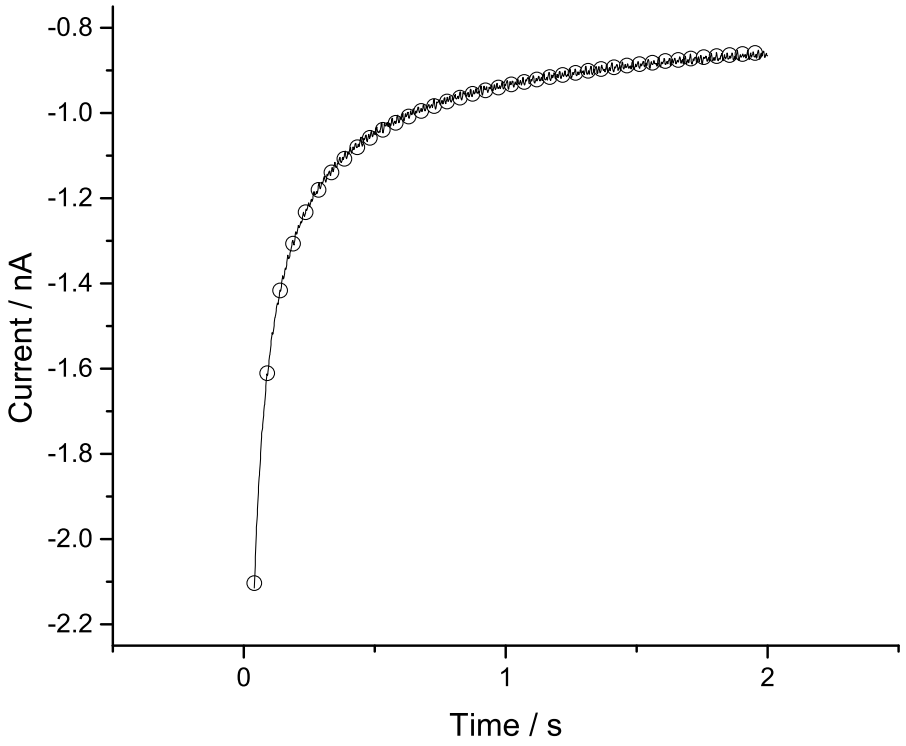


Figure 2.4: Representative experimental chronoamperometry of the reduction of 2-nitrotoluene in $[P_{14,6,6,6}][FAP]$ on a μAu electrode (solid line) compared with fitting obtained using the Shoup-Szabo analysis (circles).

optimised values for the remaining parameters (that is, the formal potential, $E_f^{\ominus}$, the transfer coefficient, α, and the heterogeneous rate constant, k^0) were obtained, with the fit quantified by calculation of the Mean-Scaled Absolute Deviation (MSAD, as described in the Theory Section). The parameters were kept constant across all scan rates, excepting the formal potential, which was allowed to deviate slightly (±0.003 V) to account for the use of pseudo-reference electrode. The optimised values and mean MSADs, averaged across all scan rates, are listed in Table 2.1.

Parameters	Butler-Volmer	Symmetric Marcus-Hush
D_A / m^2 s^{-1}	$2.2 \pm 0.1 \times 10^{-11}$	$2.2 \pm 0.1 \times 10^{-11}$
D_B / m^2 s^{-1}	$4.3 \pm 0.1 \times 10^{-12}$	$4.3 \pm 0.1 \times 10^{-12}$
Concentration / mM	16.3 ± 0.3	16.3 ± 0.3
k^0 / cm s^{-1}	0.0014 ± 0.0005	0.0014 ± 0.0005
$E_f^{\ominus}$ / V	-1.305 ± 0.003	-1.305 ± 0.003
α	0.5 ± 0.05	-
λ / eV	-	0.5 ± 0.1
MSAD (average) / %	8.89	7.92

Table 2.1: Simulation Results for the reduction of 2-nitrotoluene in $[P_{14,6,6,6}][FAP]$ on a μAu electrode

Given the quasi-reversible nature of the voltammetry, the peak separation and wave-shape are sensitive to k^0, and it is therefore possible to determine k^0 by fitting the simulations to this experimental feature, as described in Part I.

The value for the transfer coefficient, α, of 0.50 ± 0.05 suggests a transition state symmetrically located between reactant and product. The value for k^0 for the reduction of 2-NT in $[P_{14,6,6,6}][FAP]$, of $1.4 \pm 0.5 \times 10^{-3}$ cm s^{-1}, is of the same order of

magnitude as the analogous nitro compound in acetonitrile discussed above.

The CVs were then modelled with a program utilising Symmetric Marcus-Hush kinetics (described in the Theory Section). Once again, the values for D_A, D_B, and C_A^* were taken from the chronoamperograms, and the other parameters ($E_f^{\ominus}$ and k^0) were established independently by finding the combination of values with the lowest possible error, as quantified by calculation of the MSAD (described in the Theory Section). In the case of SMH theory, a value for the reorganisation energy, λ, was determined. Figure 2.3 shows the experimental CVs with generated voltammograms from both BV and SMH theories. The values for all of the common parameters (D_A, D_B, C_A^*, $E_f^{\ominus}$ and k^0) remained the same using both BV and SMH theory. A reorganisation energy of 0.5 $\pm$ 0.1 eV was determined, and this is attributed to the anionic charge being strongly delocalised on the aromatic portion of the molecule, resulting in relatively small inner sphere contribution to the reorganisation energy.[6] The MSADs for both theories across the scan rates were comparable, suggesting that both theories are equally capable of parameterisation of the data. This contrasts with the previous chapter, detailing the one-electron reduction of oxygen in an ionic liquid. This difference is likely to be due to the differing transfer coefficients; in the reduction of oxygen the transfer coefficient is *ca.* 0.3, whilst for the reduction of 2-NT in $[P_{14,6,6,6}][FAP]$, the transfer coefficient is 0.5. This is consistent with studies conducted in molecular solvents, where deviation in the transfer coefficient from 0.5 results in a disparity in the relative abilities of BV and SMH theories to parameterise the experimental data.[7]

2.1.2 Reduction of 2-nitrotoluene in [Emim][NTf_2]

The next system to be examined is the reduction of 2-nitrotoluene (2-NT) in the imidazolium-based ionic liquid, [Emim][NTf_2]. This ionic liquid was chosen for its relatively low viscosity of 34 cP[8] and ease of purification. Its component ions are more equally sized than the previously examined RTIL, which allows us to examine

any possible size-disparity effects of the solvents.

CVs were performed on *ca.* 10 mM solutions of 2-NT in [Emim][NTf_2] over a range of scan rates (10 —4000 mV s^{-1}) at 298 K. The potential was swept from -0.90 V vs Ag, a value at which no Faradaic current flows, to the potential at which 2-NT is at a diffusion controlled rate, -1.16 V vs Ag, and back to -0.90 V vs Ag. At a scan rate of 200 mV s^{-1}, the reductive peak appeared on the forward scan at -1.08 V vs Ag with a peak current of -2.2 nA, whilst the peak corresponding to the reoxidation of the reduced species appeared on the reverse scan at -0.99 V vs Ag with a peak current of 0.54 nA. The limiting current was -2.2 nA, and the half peak potential was 1.035 V vs Ag wire. All CVs were baseline corrected prior to the simulations being carried out. Representative voltammograms are shown in Figure 2.5.

Having established the potential at which 2-NT is fully reduced in this solvent, double step chronoamperometry was carried out at 298 K in order to establish the precise concentration, C_A^*, and diffusion coefficients, D_A and D_B. The chronoamperogram was conducted by stepping the potential from -0.91 V vs Ag to -1.15 V vs Ag, a potential cathodic of the reduction of 2-nitrotoluene, for 2s, then a final 2s at -0.91 V vs Ag. Three chronoamperograms were recorded, and as they overlayed, the second experiment was selected arbitrarily for further analysis. The first step, corresponding to the reduction of 2-NT, was analysed with respect to the Shoup and Szabo equation (described in the Theory Section) to yield C_A^* and D_A. A fitting program (also described in the Theory Section) was run to establish the values for these parameters with the lowest possible error, in this case a concentration of 12.4 $\pm$ 0.2 mM and a D_A of 8.2 $\pm$ 0.1 $\times$ 10^{-11} m^2 s^{-1}, with an error of 0.27%. A chronoamperometry simulation program (described in the Theory Section) was then run, using the parameters derived above, to ascertain a starting point for the below BV simulations for D_B of 8.2 $\times$ 10^{-11} m^2 s^{-1}.

A simulation program using BV kinetics (described in the Theory Section) was used

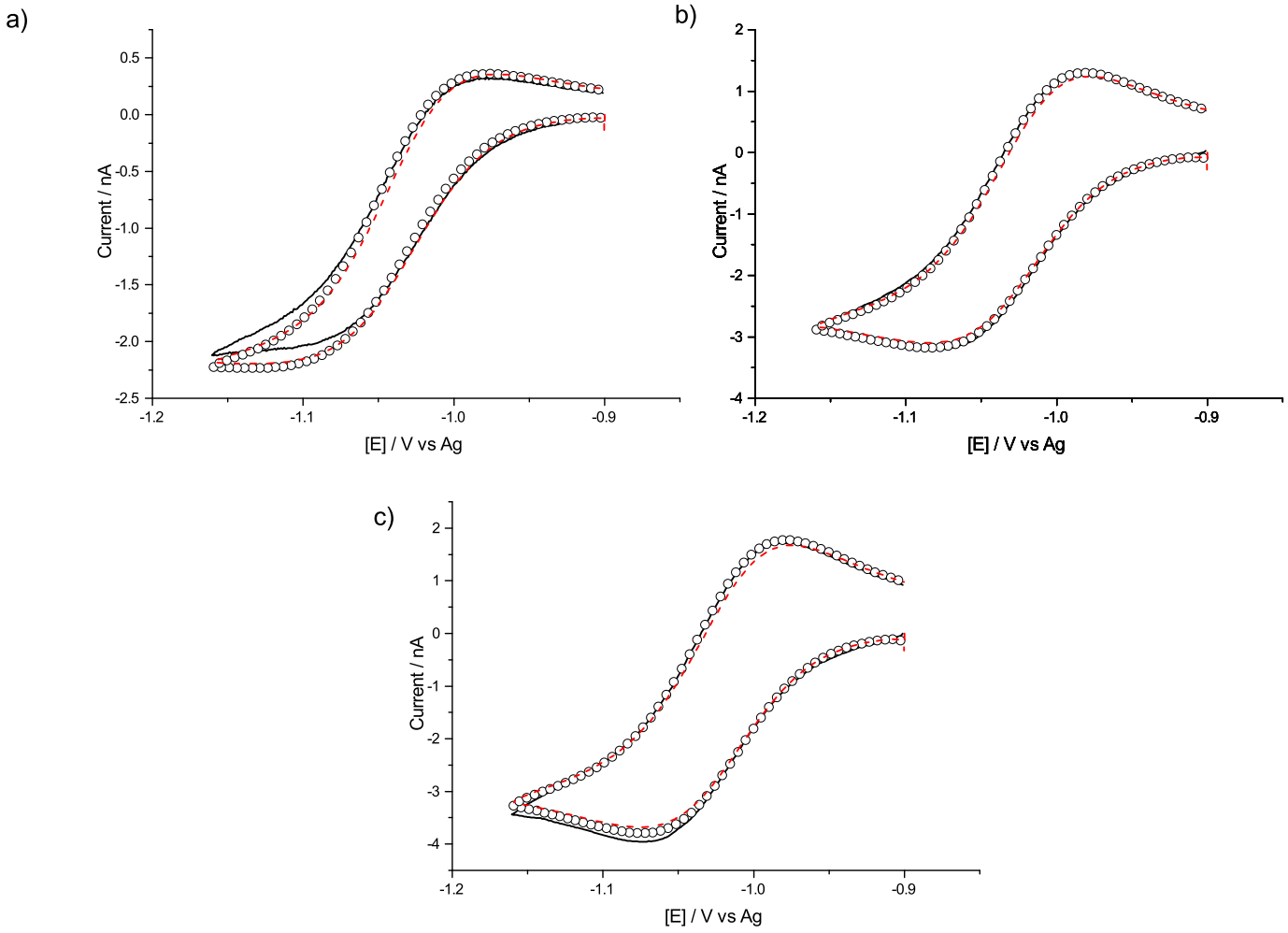


Figure 2.5: Experimental cyclic voltammetry of the reduction of 2-nitrotoluene in [Emim][NTf_2] on a μAu electrode (black solid line) at 298 $\pm$ 1 K, compared to Butler-Volmer Theory (red dashed line), and Symmetric Marcus-Hush Theory (circles) for a scan rate of a) 100 mV s^{-1}, b) 800 mV s^{-1} and c) 1500 mV s^{-1}.

to simulate the voltammograms, and they were then compared with the experimental data collected above (Figure 2.5). Values for C_A^*, D_A, and D_B were informed by chronoamperometry and simulations detailed immediately above, and the other parameters (α, $E_f^\ominus$ and k^0) were optimised to give the lowest possible calculated MSAD (see the Theory Section) across the scan rates.

Parameters	Butler-Volmer	Symmetric Marcus-Hush
D_A / m^2 s^{-1}	$8.2 \pm 0.1 \times 10^{-11}$	$8.2 \pm 0.1 \times 10^{-11}$
D_B / m^2 s^{-1}	$2.5 \pm 0.1 \times 10^{-11}$	$2.5 \pm 0.1 \times 10^{-11}$
Concentration / mM	12.2 ± 0.2	12.2 ± 0.2
k^0 / cm s^{-1}	0.022 ± 0.001	0.022 ± 0.001
$E_f^\ominus$ / V	-1.006 $\pm$ 0.004	-1.010 $\pm$ 0.006
α	0.45 ± 0.05	-
λ / eV	-	0.5 ± 0.1
MSAD (average) / %	7.12	6.24

Table 2.2: Simulation Results for the reduction of 2-nitrotoluene in [Emim][NTf_2] on a μAu electrode

The diffusion coefficients measured are of the same order of magnitude as each other, but differ in value, with D_A ($8.2 \pm 0.1 \times 10^{-11}$ m^2 s^{-1}) being over three times greater in magnitude than D_B ($2.5 \pm 0.1 \times 10^{-11}$ m^2 s^{-1}). Once again, this is attributable to the charged molecule experiencing a greater interaction with the charged solvent components, but to a lesser degree than seen in the phosphonium ionic liquid. This is likely due to the smaller sized imidazolium cation in Emim NTf_2, particularly the lack of multiple, long alkyl chains that are present in the phosphonium cation. The transfer coefficient, α, is 0.45, which suggests a slightly early transition state.

The heterogeneous rate constant, k^0, is $2.2 \pm 0.1 \times 10^{-2}$ cm s^{-1}, which is an order of magnitude faster than in the previously examined ionic liquid. As this system is also quasi-reversible, peak separation and wave-shape are sensitive to k^0, and so fitting to these features enabled the rate constant to be determined. A simulation program constructed with SMH kinetics (described in the Theory Section) was then run. As occurred previously, values for C_{A}^*, D_{A}, and D_{B} were informed by the chronoamperometry and associated chronoamperometric simulations, whilst the remaining parameters (λ, $E_f^{\ominus}$ and k^0) were established through optimisation of fit with experimental data, as reflected by calculated MSAD values. As in the previous section, the values for C_{A}^*, D_{A}, D_{B}, and k^0 were found to be the same as those established using BV theory. The reorganisation energy, λ, was determined to be 0.5 ± 0.1, which again suggests delocalisation of the charge on the aromatic molecule. In [Emim][NTf_2], both BV and SMH theories are able to parameterise the data well, with SMH performing slightly but not significantly better. A representative selection of experimental CVs with both BV and SMH theories overlayed appear in Figure 2.5.

2.1.3 Comparison of reduction of 2-nitrotoluene in [$P_{14,6,6,6}$][FAP] and [Emim][NTf_2]

The reduction of 2-NT was studied experimentally and by conducting simulations according to both BV and SMH theories in a phosphonium and an imidazolium based ionic liquid, as described in the previous sections. In [Emim][NTf_2], both diffusion coefficients increase relative to the phosphonium-based IL, however, D_{B} increases by an order of magnitude as the large phosphonium cation interacts much more strongly with the reduced species. This increased speed of diffusion is likely due to the difference in viscosities of the solvents, whereby [Emim][NTf_2] has a viscosity of 34 cP,[8] whilst [$P_{14,6,6,6}$][FAP] has a viscosity of 464 cP.[9] The value of k^0 also increases an order of magnitude in moving from the phosphonium based ionic liquid to the

imidazolium based ionic liquid. The transfer coefficient, α, in [Emim][NTf_2] is the same within uncertainty as the reduction in [$P_{14,6,6,6}$][FAP]. In both cases λ is 0.5 eV, suggesting that the primary contribution to reorganisational energy is inner sphere, or molecular, reorganisation.

2.2 Reduction of nitrocyclopentane and 1-nitrobutane in [$P_{14,6,6,6}$][FAP]

The following sub-sections detail the experimental CV of the reduction of nitrocyclopentane (NCP) and 1-nitrobutane (BuN) in [$P_{14,6,6,6}$][FAP], and the consequent comparison of the experimental data with BV and SMH theories. An experimental value for reorganisation energy will also be determined and described.

$$RNO_2 + e^- \rightleftharpoons RNO_2{}^{\bullet -};$$
$$R = n\text{-Butyl, cyclopentyl}$$

2.2.1 Nitrocyclopentane in [$P_{14,6,6,6}$][FAP]

Nitrocyclopentane (NCP) was selected as the next compound of interest, as its non-aromatic ring structure provides a good comparison with 2-NT (above) and BuN (below).

Cyclic voltammetry was performed on *ca.* 10 mM solutions of NCP in [$P_{14,6,6,6}$][FAP] over a range of scan rates (10 —2000 mV s^{-1}). The potential was swept from a potential at which no Faradaic current flows, -1.60 V vs Ag, to a potential at which NCP is at a diffusion limited rate, -1.95 V vs Ag, then back to -1.60 V vs Ag. At a scan rate of 200 mV s^{-1}, the peak corresponding to the reduction of NCP appeared on the forward scan at -1.88 V vs Ag, with a peak current of -0.58 nA, whilst a very small steady-state-like feature appeared on the reverse scan at -1.75 V vs Ag. The

limiting current was -0.51 nA, whilst the half-peak potential was -1.815 V vs Ag. Representative voltammograms are shown in Figure 2.6.

Double step chronoamperometry was then conducted in order to determine precise values for the concentration, C_{A}^{*}, and the diffusion coefficient, D_{A}. To undertake this, the potential was jumped from -1.65 V vs Ag, and held at -1.95 V vs Ag for 2s, then back to -1.65 V vs Ag for a further 2s. The chronoamperometry was conducted in triplicate, and a representative chronoamperogram was then analysed in accordance with the Shoup and Szabo equation, as described in the Theory Section, which generated values for C_{A}^{*} and D_{A}. A fitting program (described in the Theory Section) was used to find the values of C_{A}^{*} and D_{A} that have the lowest calculated MSAD, in this case, 15.0 mM and 1.04×10^{-11} m^2 s^{-1}, with an error of 1.22%. A simulation program (as described in the Theory Section) was used to obtain a starting point for the below BV simulations for D_{B}, using values for C_{A}^{*} and D_{A} that were obtained above. The diffusion coefficient of NCP, D_{A}, is of the same order of magnitude as that of 2-NT in this solvent, suggesting a comparable level of interaction of the molecule with the charged components of the solvent, particularly the cation. However, the larger D_{B} (relative to D_{A}) suggests that fast diffusion of the reduced species is occurring, as the anion is less strongly connected with the IL cation - this is probably partly a size effect.

CV simulations were then conducted with a program utilising BV kinetics (as described in the Theory Section), and the generated voltammograms were compared with the experimental CVs collected as described above (Figures 2.6). Values for C_{A}^{*}, D_{A} and D_{B} were taken from the chronoamperometric fitting program discussed above, and the remaining parameters (α, $E_f^{\ominus}$ and k^0) were optimised to the lowest possible calculated average MSAD values.

As this system did not have a discernible back peak, values for k^0 and $\mathrm{E}_f^{\ominus}$ were able to be obtained through fitting of the wave-shape. This is possible due to the

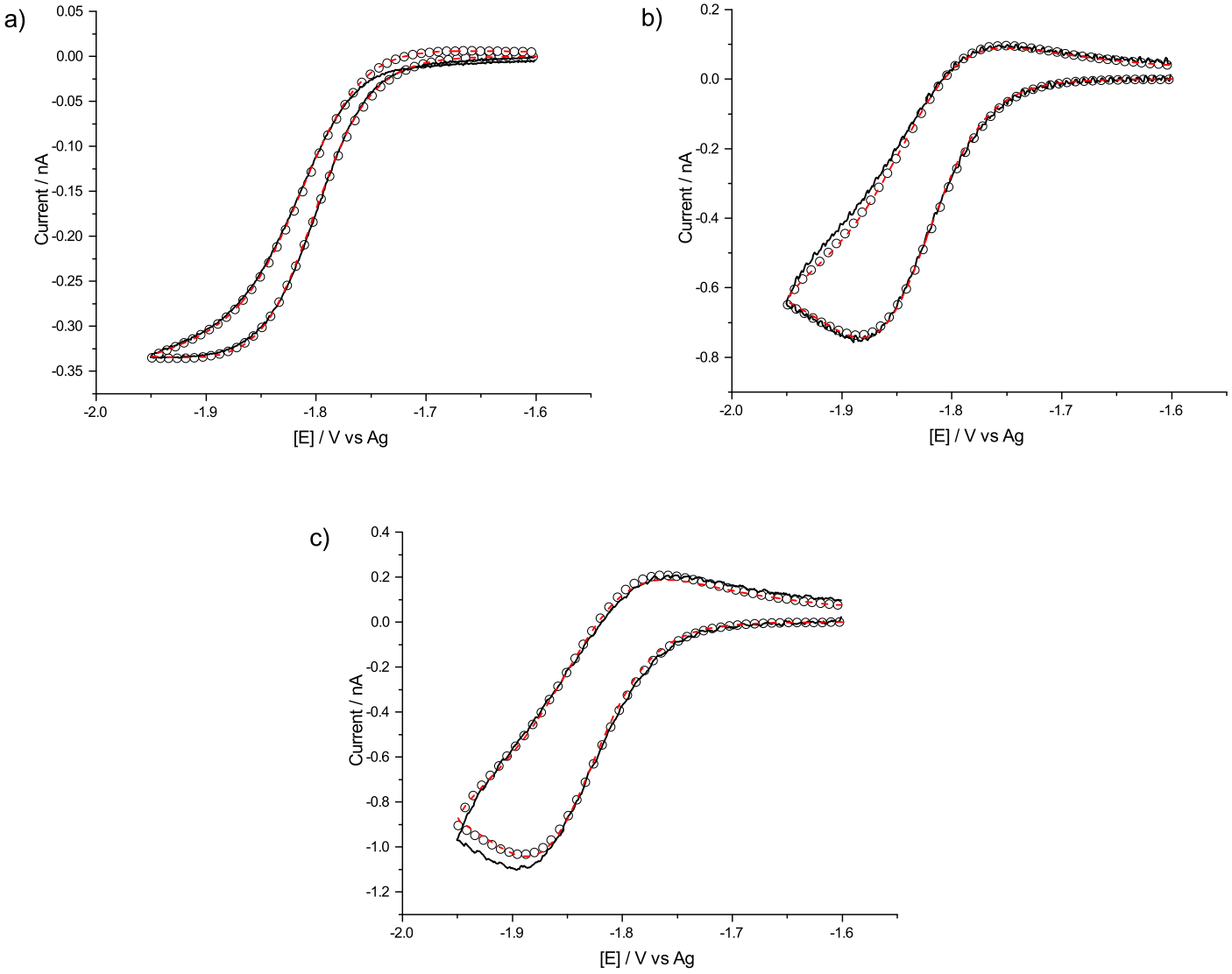


Figure 2.6: Experimental cyclic voltammetry of the reduction of nitrocyclopropane in $[P_{14,6,6,6}][FAP]$ on a μAu electrode (black solid line) at 298 $\pm$ 1 K, compared to Butler-Volmer Theory (red dashed line), and Symmetric Marcus-Hush Theory (circles) for a scan rate of a) 10 mV s^{-1}, b) 400 mV s^{-1} and c) 1000 mV s^{-1}.

Parameters	Butler-Volmer	Symmetric Marcus-Hush
D_A / m^2 s^{-1}	1.04 ± 0.1 × 10^{-11}	1.04 ± 0.1 × 10^{-11}
D_B / m^2 s^{-1}	8.0 ± 0.1 × 10^{-12}	8.0 ± 0.1 × 10^{-11}
Concentration / mM	15.0 ± 0.1	15.0 ± 0.1
k^0 / cm s^{-1}	0.004 ± 0.0005	0.0032 ± 0.0005
$E_f^{\ominus}$	-1.855 ± 0.006	-1.855 ± 0.006
α	0.65 ± 0.05	-
λ / eV	-	2 ± 0.1
MSAD (average) / %	7.60	7.11

Table 2.3: Simulation Results for the reduction of nitrocyclopropane in $[P_{14,6,6,6}][FAP]$ on a μAu electrode

quasi-reversible nature of the reduction, since the wave shape is sensitive to k^0, as outlined in Part I.

The transfer coefficient, at 0.65 ± 0.05, suggests a relatively "late" transition state, and contrasts the previously more symmetric transition states seen for 2-NT. The value for the rate constant, k^0, was established to be 0.004 ± 0.0005 cm s^{-1}, and is of the same order of magnitude as 2-NT.

Simulations were then carried out with a program utilising SMH kinetics (as described in the Theory Section). Similarly to above, values for C_A^*, D_A and D_B were taken from chronoamperometric simulations, with other parameters (λ, $E_f^{\ominus}$ and k^0) optimised through establishing the best fit to the experimental CVs, as quantified by calculated MSAD values. Once again, values for k^0 and $E_f^{\ominus}$ were able to be obtained despite the lack of back peak through fitting of the wave-shape. Experimental CVs from various scan rates are shown with simulated CVs from both BV and SMH theories in Figure

2.6. Values for diffusion coefficients and concentration were the same as established through the BV program, however in this case, the rate constant differed slightly, with SMH theory optimising a slightly smaller value for k^0, of 0.0032 ± 0.0005 cm s^{-1}. Reorganisation energy was optimised to 2.0 ± 0.1 eV, which suggests a much more significant reorganisation than that occurs with 2-NT, both in terms of inner and outer sphere reorganisation. With an average MSAD of *ca.* 7%, both BV and SMH theories were equally able to model the experimental CVs and parameterise the data.

2.2.2 Reduction of 1-nitrobutane in $[P_{14,6,6,6}][FAP]$

The final nitro-compound that was considered was 1-nitrobutane (BuN). This was chosen as it lacks the ring structure of the previous two compounds; it possesses an alkyl chain instead.

Experimental cyclic voltammetry was conducted on *ca.* 10 mM solutions of BuN at 297 K over a range of scan rates (100 —2000 mV s^{-1}). The potential was swept from -1.50 V vs Ag, a point at which no Faradaic current flows, to -1.85 V vs Ag, a potential cathodic of the reduction of BuN, then back to -1.50 V vs Ag. At a scan rate of 200 mV s^{-1}, a peak corresponding to the reduction of BuN appeared on the forward scan at -1.73 V vs Ag, with a peak current of -1.61 nA. On the reverse scan, a steady-state like feature appeared at -1.58 V vs Ag, and even at the highest scan rates, there was no discernible back peak. The limiting current was -1.46 nA, and the half-peak potential was -1.655 V vs Ag. Representative voltammograms are shown in Figure 2.7.

This voltammetry allowed the potential at which BuN is diffusion limited to be established, and following this double step chronoamperometry was undertaken to establish the precise concentration, and to elucidate the diffusion coefficients through further analysis. This was achieved by holding the potential at -1.55 V vs Ag, followed

by -1.85 V vs Ag for 2s, and back to -1.55 V vs Ag for a final 2s. The experimental chronoamperograms were analysed according to the Shoup and Szabo equation (as described in the Theory Section), to obtain values for C_{A}^{*} and D_{A}. A fitting program (as described in the Theory Section) was used to find values for C_{A}^{*} and D_{A} with the lowest possible error, in this case 18.21 mM and 2.23×10^{-11} m^2 s^{-1}, with an error of 0.62%. A simulation program, as outlined in the Theory Section, was then run, using the values for C_{A}^{*} and D_{A} determined above to establish a starting value for D_{B} of 1×10^{-9} m^2 s $^{-1}$. The value for D_{A} was in the same order of magnitude as the other nitro compounds. The concentration of BuN in was much higher than the other nitro compounds in this IL, indicating a higher solubility of BuN in this ionic liquid.

BV simulations were then undertaken, with the values for C_{A}^{*}, D_{A} and D_{B} from the above optimisation used as a starting point, and the other parameters (α, $E_f^{\ominus}$ and k^0) being determined by the generation of a simulation with the lowest calculated MSAD values. The lack of back peak, combined with the extremely large value for D_{B}, which is greater than D_{A} by two orders of magnitude, suggests that extremely fast diffusion of the reduced species is occurring (however, the possibility of follow-up chemistry cannot be excluded, as it is not easily possible under conditions of convergent or nearly convergent diffusion to distinguish between a simple E mechanism and an EC mechanism with the determined diffusion coefficients, where D_{B} is much larger than D_{A}). D_{B} taking a larger value than D_{A} is extremely unusual in RTILs. Providing the values simulated are correct, this could be due to the interaction and reorientation of alkyl chain of the charged nitrobutane anion relative to the alkylated components of the cation, enabling faster diffusion to occur. Despite the lack of back peak, both k^0 and $\mathrm{E}_f^{\ominus}$ were able to be extracted through fitting to the experimental wave-shape, since the wave-shape is sensitive to k^0 in this quasireversible regime, as discussed in Part I. All parameters were kept the same across scan rates, excepting $E_f^{\ominus}$, which was

Parameters	Butler-Volmer	Symmetric Marcus-Hush
D_A / m^2 s^{-1}	2.6 ± 0.1 × 10^{-11}	2.6 ± 0.1 × 10^{-11}
D_B / m^2 s^{-1}	1.00 ± 0.1 × 10^{-9}	1.00 ± 0.1 × 10^{-9}
Concentration / mM	21.5	21
k^0 / cm s^{-1}	0.011 ± 0.001	0.0095 ± 0.0005
$E_f^{\ominus}$	-1.735 ± 0.005	-1.735 ± 0.005
α	0.55 ± 0.05	-
λ / eV	-	5 ± 0.1
MSAD (average) / %	5.19	4.46

Table 2.4: Simulation Results for the reduction of 1-nitrobutane in $[P_{14,6,6,6}][FAP]$ on a μAu electrode

allowed to vary ± 0.005 V due to the use of pseudo-reference electrode. The value of the transfer coefficient, at 0.55 ± 0.05, is slightly product-like. k^0 is significantly larger than the rate constant calculated for the reduction of NCP.

A simulation program written with SMH kinetics (as described in the Theory Section) was used to generate voltammograms that were compared with the experimental data collected above. Data from the chronoamperometric simulations above was used as a starting point for values of C_A^*, D_A and D_B. In the case of SMH theory, the other parameters (λ, $E_f^{\ominus}$ and k^0) were optimised through fitting to the experimental data, as quantified by the lowest calculated MSAD values. As in BV theory, values for k^0 and $E_f^{\ominus}$ were able to be extracted through fitting of the wave-shape. All parameters were kept constant across the scan rates, excepting $E_f^{\ominus}$, which was allowed to vary by ± 0.005 V due to the use of a pseudo-reference electrode. The values for D_A and D_B established by SMH theory were consistent with the values elucidated from the BV

simulations, whilst the concentration varied slightly (0.5 mM). The value for k^0 was in the order of 0.0095 ± 0.0005 cm s^{-1}, and lies in between 2-NT and NCP. The value established for λ, of 5 ± 0.1 eV, is the largest value seen for any of the compounds discussed thus far, indicating that a significant reorganisation is occurring. SMH and BV theories were equally able to parameterise the data, with the average MSAD across scan rates being *ca.* 5%. Figure 2.7 shows representative experimental and simulated CVs across the scan rate range.

2.2.3 Discussion of the reduction of nitrocyclopentane and 1-nitrobutane in $[P_{14,6,6,6}][FAP]$

The reduction of NCP and BuN in $[P_{14,6,6,6}][FAP]$ was studied both experimentally, and by conducting simulations informed by BV theory and SMH theory. The concentration of BuN was much higher than NCP, by 5 mM. Both compounds had similar values of D_A, but D_B was two orders of magnitude larger for the reduced form of BuN than for the reduced form of NCP. k^0 was also an order of magnitude larger in the reduction of BuN than it was in the reduction of NCP. The transition state, α, gleaned through optimisation of parameters in BV theory, was more product-like, at 0.65, in the case of NCP, and closer to symmetric in the reduction of BuN, at 0.55. The value for reorganisation energy established through the use of SMH, λ, was more than twice as large in the case of BuN, at 5 eV, when compared to the reduction of NCP, at 2 eV, and an order of magnitude larger than the value extracted for 2-NT, of 0.5 eV. These differences are likely attributable to the difference in structure of the molecules. In the case of 2-NT, the lower reorganisation is attributable to the delocalisation of the charge in the aromatic portion of the molecule. In moving to aliphatic systems, NCP and BuN, the charge is localised on the nitro group itself, which interacts more stongly with the environment. The primary nitro-alkyl, BuN, experiences a much greater interaction with the other nitro molecules than the sec-

ondary nitro-alkyl, NCP. In both cases, BV theory and SMH theory were equally adept at parameterisation of the data.

This chapter has reported the use of BV and SMH theories to parameterise the reduction of 2-nitrotoluene in two ionic liquids ([Emim][NTf_2] and [$P_{14,6,6,6}$][FAP]), and nitrocyclopentane and 1-nitrobutane in [$P_{14,6,6,6}$][FAP]. In all cases, BV and SMH theories were equally capable of parameterisation of the data. The reorganisation energy, λ, from SMH theory, was determined to be 0.5 $\pm$ 0.1 eV for the reduction of 2-NT in [$P_{14,6,6,6}$][FAP] and [Emim][NTf_2], 2 $\pm$ 0.1 eV for the reduction of NCP in [$P_{14,6,6,6}$][FAP], and 5 $\pm$ 0.1 eV for the reduction of BuN in [$P_{14,6,6,6}$][FAP]. This increase in reorganisation energy reflects the change in localisation of the charge in moving from an aromatic molcule (2-NT), to a cyclic molecule (NCP), and finally an aliphatic molecule (1-BuN). The increased interaction with the environment of the BuN molecule as compared with NCP likely explains the increased reorganisation energy. The next chapter examines the application of Asymmetric Marcus-Hush theory to these systems, and to the reduction of oxygen, to establish asymmetry parameters (γ) for the first time in RTILs.

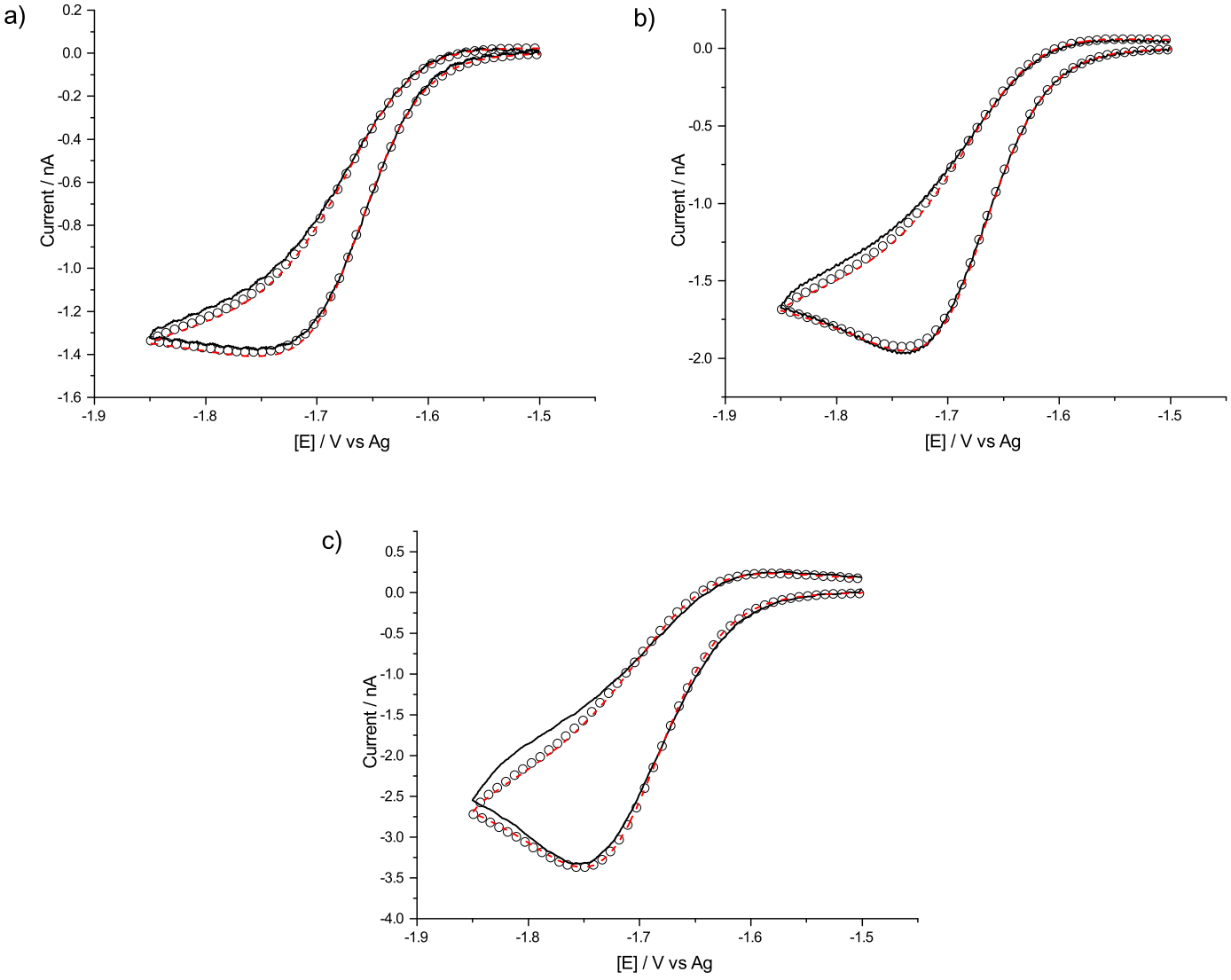


Figure 2.7: Experimental cyclic voltammetry of the reduction of 1-nitrobutane in $[P_{14,6,6,6}][FAP]$ on a μAu electrode (black solid line) at 298 $\pm$ 1 K, compared to Butler-Volmer Theory (red dashed line), and Symmetric Marcus-Hush Theory (circles) for a scan rate of a) 100 mV s^{-1}, b) 400 mV s^{-1} and c) 2000 mV s^{-1}.

References

[1] O'Mahony, A. M.; Silvester, D. S.; Aldous, L.; Hardacre, C.; Compton, R. G. *J. Chem. Eng. Data* **2008**, *53*, 2884–2891.

[2] Shoup, D.; Szabo, A. *J. Electroanal. Chem. Interfacial Electrochem.* **1982**, *140*, 237–245.

[3] Buzzeo, M. C.; Klymenko, O. V.; Wadhawan, J. D.; Hardacre, C.; Seddon, K. R.; Compton, R. G. *J. Phys. Chem. A* **2003**, *107*, 8872–8878.

[4] Laborda, E.; Wang, Y.; Henstridge, M. C.; Martínez-Ortiz, F.; Molina, A.; Compton, R. G. *Chem. Phys. Lett.* **2011**, *512*, 133–137.

[5] Henstridge, M. C.; Wang, Y.; Limon-Petersen, J. G.; Laborda, E.; Compton, R. G. *Chem. Phys. Let.* **2011**, *517*, 29–35.

[6] Bromley, S. T.; Illas, F.; Mas-Torrent, M. *Phys. Chem. Chem. Phys.* **2008**, *10*, 121–127.

[7] Suwatchara, D.; Henstridge, M. C.; Rees, N. V.; Compton, R. G. *J. Phys. Chem. C* **2011**, *115*, 14876–14882.

[8] Bonhote, P.; Dias, A. P.; Papageorgiou, N.; Kalyanasundaram, K.; Gratzel, M. *Inorg. Chem.* **1996**, *35*, 1168–1178.

[9] Barrosse-Antle, L. E.; Bond, A. M.; Compton, R. G.; O'Mahony, A. M.; Rogers, E. I.; Silvester, D. S. *Chem. Asian J.* **2010**, *5*, 202–30.

Chapter 3

The Application of Asymmetric Marcus-Hush Theory to Voltammetry in Room Temperature Ionic Liquids

The subsequent subsections detail the outcome of first experimental voltammetry and second simulations based on Asymmetric Marcus-Hush (AMH) theory of the reduction of oxygen in [Bmpyrr][NTf_2], and the reduction of 2-NT, NCP and BuN in [$P_{14,6,6,6}$][FAP].

3.1 Reduction of Oxygen in [Bmpyrr][NTf_2]

The first system to be studied was the reduction of oxygen in [Bmpyrr][NTf_2] at a μAu electrode at 298 K. Experimental CVs were recorded as documented in Chapter 1, along with simulations written according to Butler-Volmer and Symmetric Marcus-Hush theories. For comparison, these are included in Figure 3.1.

A program using Asymmetric Marcus-Hush (AMH) theory, as described in the Theory section, was used to simulate voltammograms using literature values[1–4] as starting points for the diffusion coefficient of oxygen (D_{A}), the diffusion coefficient of superoxide (D_{B}), and the concentration of oxygen (C_{A}^{*}). The parameters used (Table 3.1) were kept constant over scan rates, with the exception of $E_f^{\ominus}$, which was allowed to vary by ± 0.02 V due to the use of a pseudo reference electrode. Table 3.1 contains values from BV and SMH theories from the previous chapter for comparison. The values measured for AMH theory for D_{A}, D_{B}, C_{A}^{*}, k^0 and $E_f^{\ominus}$ are consistent with the values reported using SMH theory in Chapter 1. In particular, the value for λ of 0.4 eV, suggests a dominant inner-sphere contribution to the reorganization energy, with a negligible outer-sphere contribution, and is consistent with the previous chapter.

As established in the Introduction, where α is less than 0.5, γ takes a value less than 0. This suggests that the force constants in the reactant weaken as the oxygen is reduced to superoxide. This is not unexpected, given the molecule experiences weakening through the addition of the electron to the double bond. The additional electron fills one of the two degenerate molecular orbitals in the oxygen molecule, moving from a diradical species, with two unpaired electrons, to a charged species with one unpaired electron. It also worth noting that the value for the asymmetry parameter, γ, of -0.4, is consistent with the alpha value of 0.29 established in previous work.

AMH theory, with an average MSAD of 11.2 ± 1% was able to parameterize the data similarly well to BV theory (9.52 ± 1%), and better than SMH theory (13.9 ± 1%). This is demonstrated both through the calculated MSADs and the visual better fit, as shown in Figure 3.1. As indicated in the Introduction, this finding is consistent with previously published work in molecular solvents.

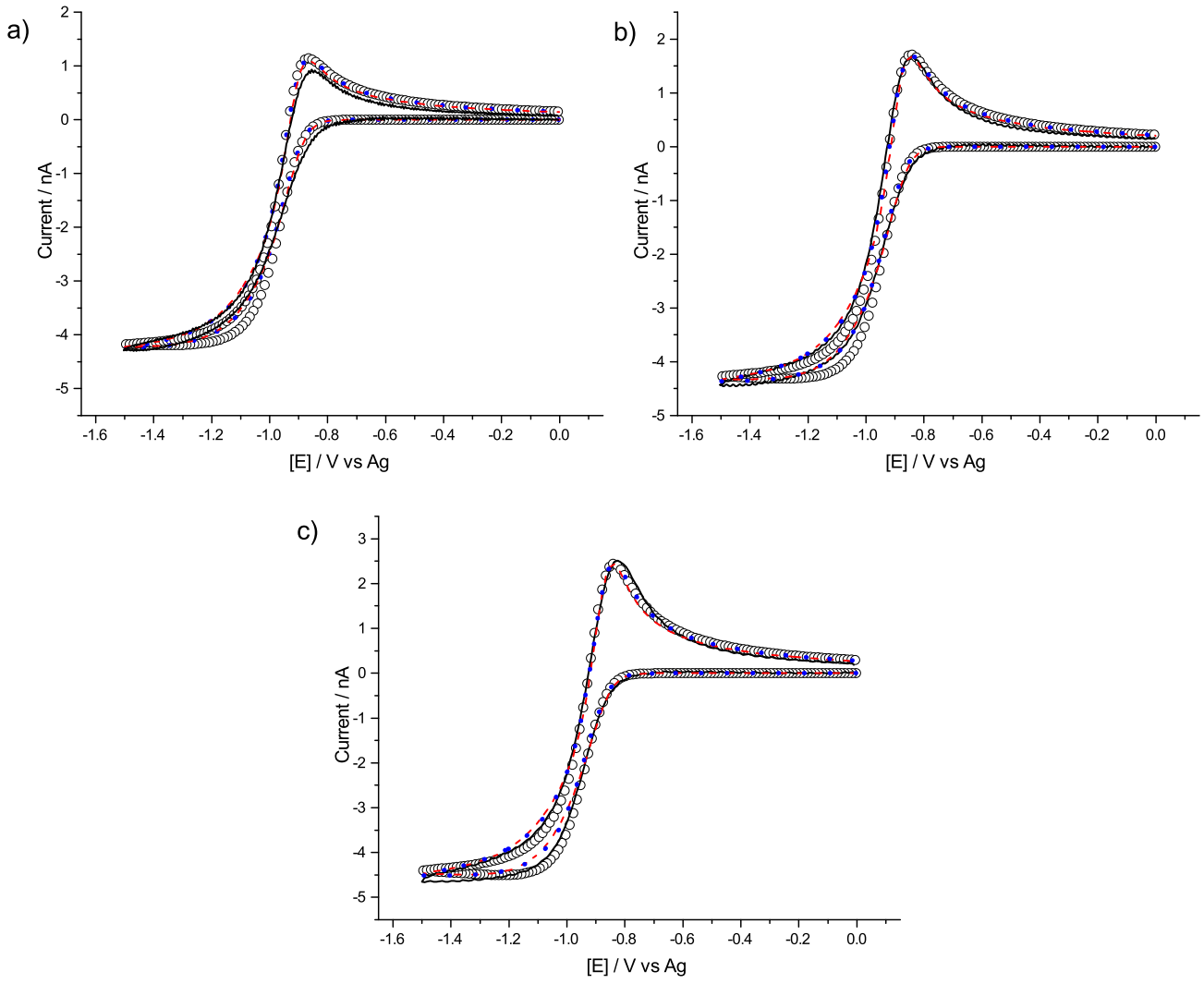


Figure 3.1: Experimental cyclic voltammetry of the reduction of Oxygen in [Bmpyrr][NTf_2] on a μAu electrode (black solid line, from Chapter 1) at 298 $\pm$ 1 K, compared to Butler-Volmer Theory (red dashed line, from Chapter 1), and Symmetric Marcus-Hush Theory (circles, from Chapter 1) and Asymmetric Marcus-Hush Theory (blue dot) for a scan rate of a) 100 mV s^{-1}, b) 200 mV s^{-1} and c) 400 mV s^{-1}.

Parameters	Butler-Volmer	Symmetric Marcus-Hush	Asymmetric Marcus-Hush
D_A / m^2 s^{-1}	$2.05 \pm 0.1 \times 10^{-10}$	$2.05 \pm 0.1 \times 10^{-10}$	$2.05 \pm \times 10^{-10}$
D_B / m^2 s^{-1}	$1.8 \pm 0.1 \times 10^{-11}$	$1.55 \pm 0.1 \times 10^{-11}$	$1.55 \pm 0.1 \times 10^{-11}$
Concentration / mM	10.0 ± 0.1	10.0 ± 0.1	10.0 ± 0.1
k^0 / cm s^{-1}	0.0023 ± 0.0005	0.0015 ± 0.0005	0.0015 ± 0.0005
$E_f^{\ominus}$ / V	-0.87 ± 0.02	-0.87 ± 0.02	-0.87 ± 0.02
α	0.29 ± 0.05	-	-
λ / eV	-	0.4 ± 0.1	0.4 ± 0.1
γ	-	-	-0.4 ± 0.1
MSAD (average) / %	9.52 ± 1	13.9 ± 1	11.2 ± 1

Table 3.1: Simulation Results for the Reduction of Oxygen in [Bmpyrr][NTf_2] on a μAu electrode. Parameters for Butler-Volmer and Symmetric Marcus-Hush Theories from Chapter 1 included for comparison.

3.2 Reduction of Nitro Compounds in $[P_{14,6,6,6}][FAP]$

The subsequent subsubsections examine the experimental voltammetry and application of AMH theory to the one electron reduction of 2-nitrotoluene (2-NT), nitrocyclopentane (NCP), and 1-nitrobutane (BuN).

$$RNO_2 + e^- \rightleftharpoons [RNO_2]^{\bullet -} \tag{3.1}$$

$$R = 2 - MeC_6H_4, n - Butyl, cyclopentyl \tag{3.2}$$

3.2.1 Reduction of 2-nitrotoluene in $[P_{14,6,6,6}][FAP]$

The first molecule under study is 2-nitrotoluene (2-NT) in $[P_{14,6,6,6}][FAP]$, studied at a μAu electrode at 298 $\pm$ 1 K.

Experimental cyclic voltammetry was conducted as documented in Chapter 2, along with simulations written according to Butler-Volmer and Symmetric Marcus-Hush theories, and are included for reference in Figure 3.2.

A program utilizing Asymmetric Marcus-Hush theory, as described in the Theory section, was run, using previously published values determined through the use of double-step potential chronoamperometry for the diffusion coefficient of 2-NT (D_A), the diffusion coefficient of the reduced species (D_B), and the concentration of 2-NT (C_A^*). Values for k^0, $E_f^{\ominus}$, λ, and γ were optimised to obtain the lowest possible MSAD value, as calculated as shown in the Theory section. A full list of optimised parameters, plus the values for BV and SMH theories, as established in the previous chapter, are shown in Table 3.2.

The values estimated for D_A, D_B, C_A^*, k^0, and $E_f^{\ominus}$ were the same within error of those established using BV and SMH theories. The value for λ of 0.5 eV reflects delocalization of the charge on the aromatic portion of the molecule, and this is consistent with the value established in the previous chapter using SMH theory.

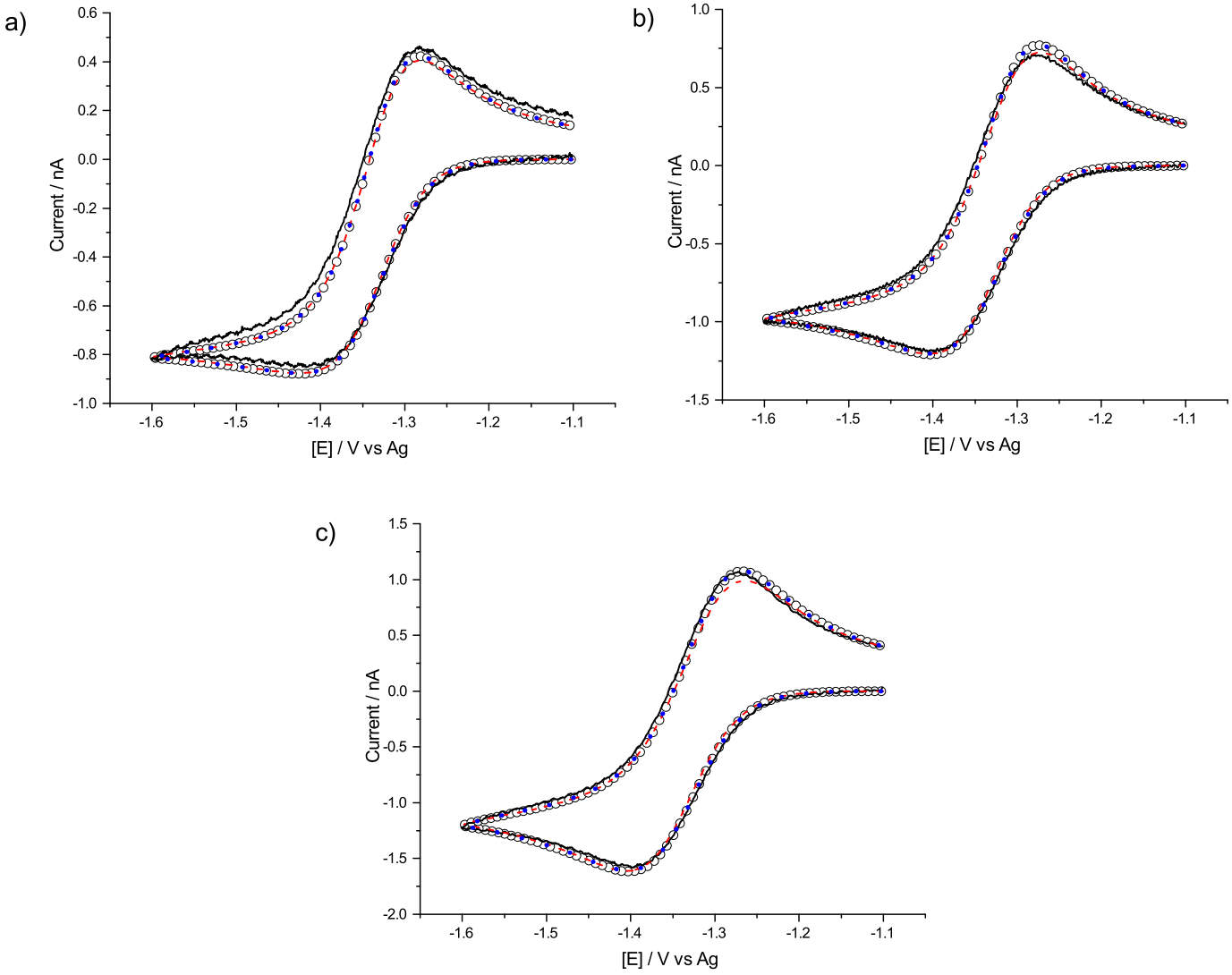


Figure 3.2: Experimental cyclic voltammetry of the reduction of 2-nitrotoluene in $[P_{14,6,6,6}][FAP]$ on a μAu electrode (black solid line, from Chapter 2) at 298 $\pm$ 1 K, compared to Butler-Volmer Theory (red dashed line, from Chapter 2), and Symmetric Marcus-Hush Theory (circles, from Chapter 2), and Asymmetric Marcus-Hush Theory (blue dot) for a scan rate of a) 100 mV s^{-1}, b) 400 mV s^{-1} and c) 1000 mV s^{-1}.

Parameters	Butler-Volmer	Symmetric Marcus-Hush	Asymmetric Marcus-Hush
D_A / m^2 s^{-1}	$2.2 \pm 0.1 \times 10^{-11}$	$2.2 \pm 0.1 \times 10^{-11}$	$2.16 \pm 0.1\ 10^{-11}$
D_B / m^2 s^{-1}	$4.3 \pm 0.1 \times 10^{-12}$	$4.3 \pm 0.1 \times 10^{-12}$	$4.3 \pm 0.1\ 10^{-11}$
Concentration / mM	16.3 ± 0.3	16.3 ± 0.3	16.0 ± 0.3
k^0 / cm s^{-1}	0.0014 ± 0.0005	0.0014 ± 0.0005	0.0014 ± 0.0005
$E_f^{\ominus}$ / V	-1.305 ± 0.003	-1.305 ± 0.003	-1.305 ± 0.007
α	0.5 ± 0.05	-	-
λ / eV	-	0.5 ± 0.1	0.5 ± 0.1
γ	-	-	-0.05 ± 0.1
MSAD (average) / %	8.89 ± 1	7.92 ± 1	7.84 ± 1‘

Table 3.2: Simulation Results for the reduction of 2-nitrotoluene in $[P_{14,6,6,6}][FAP]$ on a μAu electrode. Parameters for Butler-Volmer and Symmetric Marcus-Hush Theories from Chapter 2 included for comparison.

The γ value of -0.05 $\pm$ 0.1 indicate that the force constants in the reactants and products are not dissimilar, suggesting a symmetric transition state. This is congruent with the value for α, which was measured as 0.5. Given the symmetric nature of the transition state, the relationship between α and γ, and predictions from modelling in molecular solvents, as discussed in the Introduction, it is not unexpected that AMH theory does similarly well, with an average MSAD of 7.84 $\pm$ 1%, at parameterizing the experimental data as BV (8.89 $\pm$ 1%) and SMH (7.92 $\pm$ 1%) theories.

3.2.2 Reduction of Nitrocyclopentane in $[P_{14,6,6,6}][FAP]$

The second system under study is the reduction of nitrocyclopentane (NCP) in $[P_{14,6,6,6}][FAP]$ at a μAu electrode.

Experimental CVs were undertaken as described in Chapter 2, along with simulations written according to Butler-Volmer and Symmetric Marcus-Hush theories. These are shown for comparative purposes in Figure 3.3.

Asymmetric Marcus-Hush theory written into a simulation program, as described in the Theory section, was used to generate simulated voltammograms. Starting points for values for diffusion coefficients (D_A and D_B) and concentration of NCP (C_A^*) were taken from the previous chapter using double-step potential chronoamperometry. Values for the other parameters (k^0, $E_f^{\ominus}$, λ, and γ) were established through optimization, where the combination of values which resulted in simulated voltammogram with the lowest calculated MSAD values (as described in the Theory section) were used. All parameters were kept constant across scan rates, with the exception of $E_f^{\ominus}$, which was allowed to vary by $\pm$ 0.006 V. A representative selection of scan rates of simulated voltammograms overlayed with experimental voltammetry is shown in Figure 3.3. Table 3.3 contains values for all parameters found through AMH theory, as well as BV and SMH parameters from the previous chapter for reference.

Values for all parameters generated using AMH theory were consistent with those

Parameters	Butler-Volmer	Symmetric Marcus-Hush	Asymmetric Marcus-Hush
D_A / m^2 s^{-1}	$1.04 \pm 0.1 \times 10^{-11}$	$1.04 \pm 0.1 \times 10^{-11}$	$1.04 \pm 0.1 \times 10^{-11}$
D_B / m^2 s^{-1}	$8.0 \pm 0.1 \times 10^{-12}$	$8.0 \pm 0.1 \times 10^{-11}$	$8.0 \pm 0.1 \times 10^{-12}$
Concentration / mM	15.0 ± 0.1	15.0 ± 0.1	15.0 ± 0.1
k^0 / cm s^{-1}	0.004 ± 0.0005	0.0032 ± 0.0005	0.0032 ± 0.0005
$E_f^{\ominus}$	-1.855 ± 0.006	-1.855 ± 0.006	-1.855 ± 0.006
α	0.65 ± 0.05	-	-
λ / eV	-	2.0 ± 0.1	2.0 ± 0.1
γ	-	-	0.25 ± 0.05
MSAD (average) / %	7.60 ± 1	7.11 ± 1	6.99 ± 1

Table 3.3: Simulation Results for the reduction of nitrocyclopropane in $[P_{14,6,6,6}][FAP]$ on a μAu electrode. Parameters for Butler-Volmer and Symmetric Marcus-Hush Theories from Chapter 2 included for comparison.

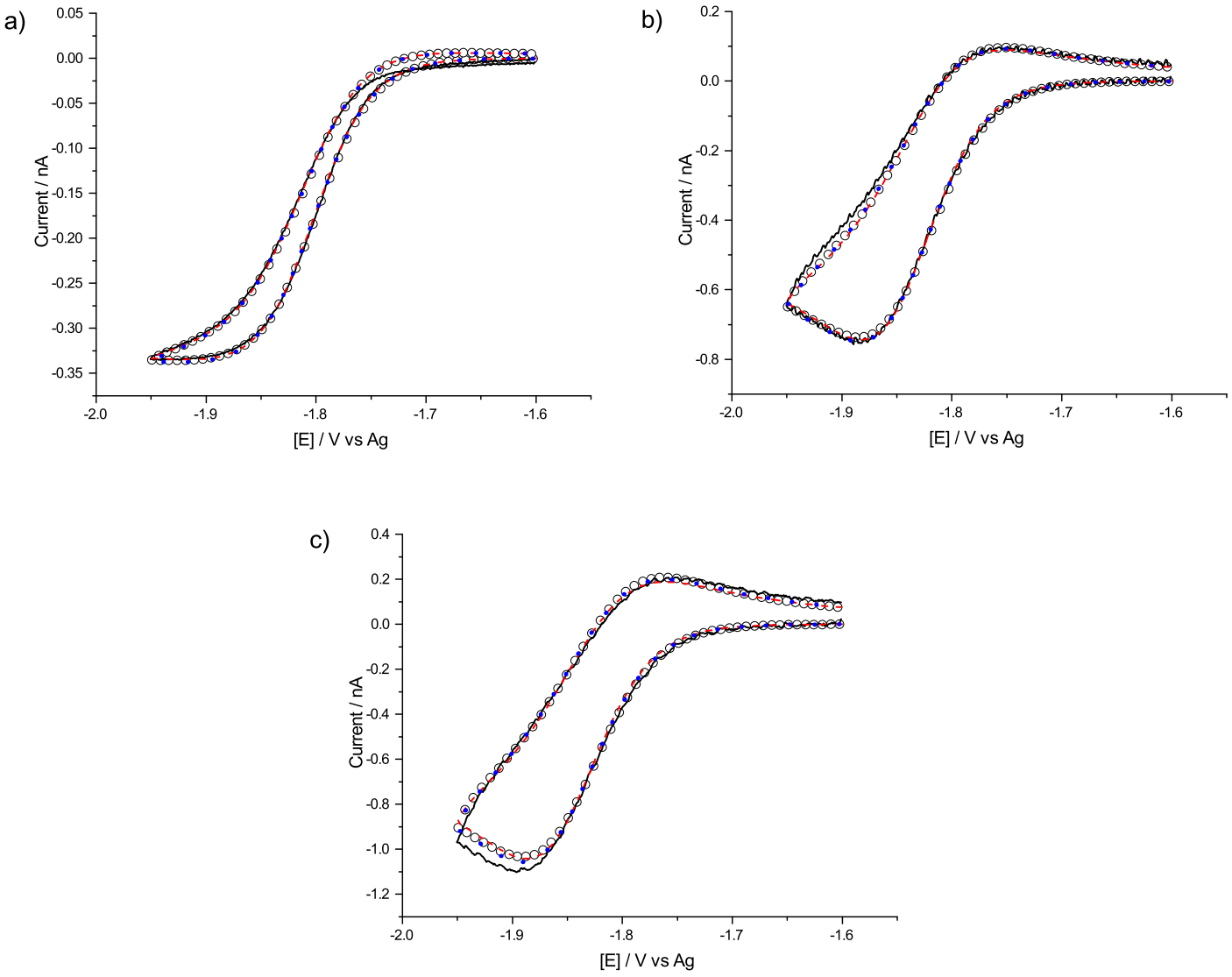


Figure 3.3: Experimental cyclic voltammetry of the reduction of nitrocyclopropane in $[P_{14,6,6,6}][FAP]$ on a μAu electrode (solid line, from Chapter 2) at 298 $\pm$ 1 K, compared to Butler-Volmer Theory (red dashed line, from Chapter 2), Symmetric Marcus-Hush Theory (circles, from Chapter 2) and Asymmetric Marcus-Hush Theory (blue dot) for a scan rate of a) 10 mV s^{-1}, b) 400 mV s^{-1} and c) 1000 mV s^{-1}.

estimated using BV and SMH theories. The value for λ, of 2.0 $\pm$ 0.1 eV, reflects localization of the charge on the nitro group, which results in increased interaction of the secondary nitro-alkyl with the charged components of the solvent. γ is measured

as 0.25 ± 0.05, which indicates that the force constants in the product are stronger than those in the reactant. This is consistent with the value previously measured for α of 0.65 ± 0.05 as explained in the Introduction, reflecting a transition state that is more product-like.

In this case, as with the previous nitro-compound, 2-NT, AMH theory, with an average MSAD of 6.99 ± 1 %, is similarly adept to both BV (7.60 ± 1 %) and SMH (7.11 ± 1 %) theories at parameterizing the data.

3.2.3 Reduction of 1-Nitrobutane in $[P_{14,6,6,6}][FAP]$

Experimental cyclic voltammetry was conducted as documented in Chapter 2, along with simulations written according to Butler-Volmer and Symmetric Marcus-Hush theories as shown in Figure 3.4.

A program designed to simulate voltammetry written by Dr Edward O Barnes, according to Asymmetric Marcus-Hush theory (as described in the Theory section), was used to produce simulations. Previous work, as detailed in the last chapter, on this system provided the starting points for values for D_A, D_B and C_A^* through double-step potential chronoamperometry, whilst values for the other parameters (k^0, $E_f^{\ominus}$, λ, and γ) were established through optimization of the voltammograms, as judged by their MSAD value (which is described in the Theory section). A full list of values, as determined by AMH theory, and from BV and SMH theories, taken from a previous chapter for comparison, are listed in Table 3.4, and a selection of voltammograms, showing experimental voltammetry, AMH theory, and BV and SMH theories for comparison are shown in Figure 3.4. The MSAD values represent an average across all scan rates.

The values for D_A, D_B, C_A^*, k^0, $E_f^{\ominus}$, and λ, for SMH theory, were the same within error across all theories. The value measured for λ, of 5.0 ± 0.5 eV, reflects increasing localization of charge on the nitro group resulting in an increased interaction with

Parameters	Butler-Volmer	Symmetric Marcus-Hush	Asymmetric Marcus-Hush
D_A / m^2 s^{-1}	$2.6 \pm 0.1 \times 10^{-11}$	$2.6 \pm 0.1 \times 10^{-11}$	$2.55 \pm 0.1 \times 10^{-11}$
D_B / m^2 s^{-1}	$1.00 \pm 0.1 \times 10^{-9}$	$1.00 \pm 0.1 \times 10^{-9}$	$1.00 \pm 0.1 \times 10^{-9}$
Concentration / mM	21.5	21.0	21.0
k^0 / cm s^{-1}	0.011 ± 0.001	0.0095 ± 0.0005	0.011 ± 0.001
$E_f^{\ominus}$	-1.735 ± 0.005	-1.735 ± 0.005	-1.735 ± 0.005
α	0.55 ± 0.05	-	-
λ / eV	-	5.0 ± 0.1	5.0 ± 0.1
γ	-	-	0
MSAD (average) / %	5.19 ± 1	4.46 ± 1	4.46 ± 1

Table 3.4: Simulation Results for the reduction of 1-nitrobutane in $[P_{14,6,6,6}][FAP]$ on a μAu electrode. Parameters for Butler-Volmer and Symmetric Marcus-Hush Theories from Chapter 2 included for comparison.

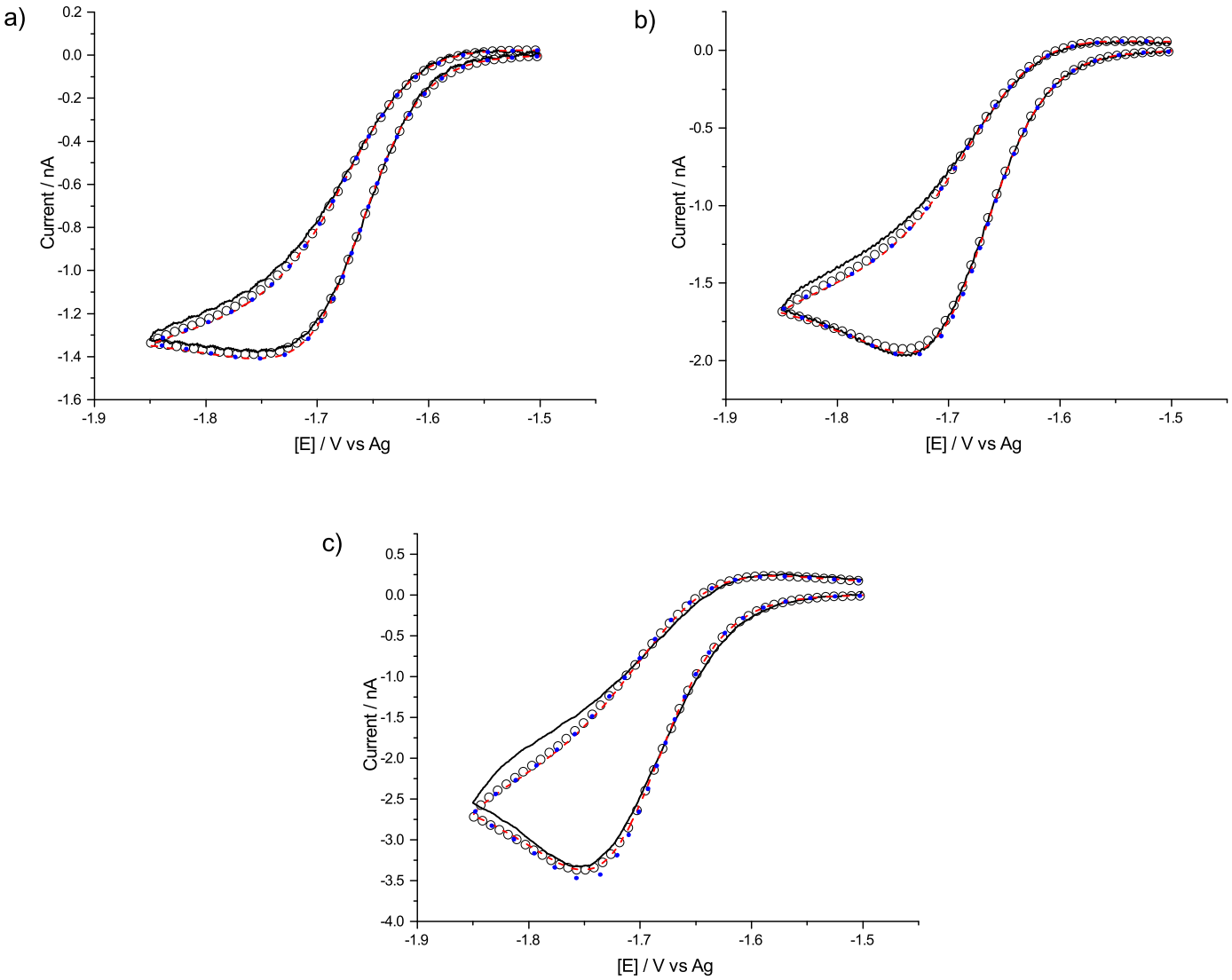


Figure 3.4: Experimental cyclic voltammetry of the reduction of 1-nitrobutane in $[P_{14,6,6,6}][FAP]$ on a μAu electrode (black solid line, from Chapter 2) at 298 $\pm$ 1 K, compared to Butler-Volmer Theory (red dashed line, from Chapter 2), Symmetric Marcus-Hush Theory (circles, from Chapter 2) and Asymmetric Marcus-Hush Theory (blue dot) for a scan rate of a) 100 mV s^{-1}, b) 400 mV s^{-1} and c) 2000 mV s^{-1}.

the charged components of the ionic solvent as the molecule moves from a secondary nitro-alkyl, as seen in NCP with a lower value for reorganization energy, to a primary nitro-alkyl, as seen with BuN. The value estimated for γ of 0 $\pm$ 0.05 suggests that

the force constants of the reactants and products are similar. This is consistent with previously measured α values, as discussed in the Introduction. In this system, as with both the 2-NT and NCP, AMH, BV and SMH theories were similarly able to parameterise the experimental data, with average MSAD values of 4.46, 5.19 and 4.46 $\pm$ 1 % respectively.

This Chapter outlined the application of AMH to a series of reductions in RTILs. This enabled values for the asymmetry parameter, γ, to be produced in each case. For the reduction of oxygen in [Bmpyrr][NTf_2], an asymmetry parameter of -0.4 was estimated, which suggests the force constants in oxygen are larger than those in superoxide, and is consistent with an α value of 0.29. For the reductions of 2-NT, NCP, and BuN in [$P_{14,6,6,6}$][FAP], γ = -0.05, 0.25, and 0 $\pm$ 0.05 respectively. This reflects the equal force constants for both 2-NT and BuN, and is consistent with the symmetric transition state predicted by the measured α of 0.5 in the previous chapter. In the case of NCP, the value for γ of 0.25 $\pm$ 0.05 reflects force constants that are stronger in the reduced species than the oxidised species. This is also consistent with an α of 0.65.

3.3 Part III Conclusions

Part III critically compared the ability of Butler-Volmer theory, Symmetric Marcus-Hush theory, and Asymmetric Marcus-Hush theory to parameterise and provide physical insight to reduction processes in RTILs. The model systems chosen were the reduction of oxygen and the reductions of 2-nitrotoluene, nitrocyclopentane, and 1-nitrobutane.

The first chapter focused on modelling the experimental voltammetry of oxygen reduction in [Bmpyrr][NTf_2]. BV theory was more adept at fitting the data than SMH theory. α, a phenomenological parameter describing the transition state, was deter-

mined to be 0.29, whilst λ was found to take a value of 0.4 $\pm$ 0.1 eV. This corresponds to a predominately inner-sphere process.

The second chapter examined the reduction of three nitro compounds. The first, 2-NT, was investigated in two RTILs - [Emim][NTf_2] and [$P_{14,6,6,6}$][FAP]. In both solvents, α was 0.50 $\pm$ 0.05 and λ was 0.5 $\pm$ 0.1 eV. Next, the reductions of NCP and BuN were investigated in [$P_{14,6,6,6}$][FAP]. In the case of NCP, fitting of the experimental voltammetry yielded α of 0.65 $\pm$ 0.05 from BV theory and λ of 2 $\pm$ 0.1 eV from SMH theory, whilst in BuN, $\alpha = 0.55 \pm 0.05$ and $\lambda = 5 \pm 0.1$ eV. In all cases in the second chapter, BV and SMH theory were equally adept at parameterising the data. The increasing reorganisation energy was attributed to the increased localisation of charge as the molecules change from aromatic (2-NT) to aliphatic (NCP, BuN).

Chapter 3 applied AMH theory to the reduction of oxygen in [Bmpyrr][NTf_2], and the reductions of 2-NT, NCP, and BuN in [$P_{14,6,6,6}$][FAP]. Asymmetry parameters were obtained for all systems, with γ = -0.4 in the case of oxygen reduction, and -0.05, 0.25, and 0 $\pm$ 0.05 for 2-NT, NCP, and BuN respectively. This is consistent with an early transition state in the case of the oxygen, symmetric transition states in the case of 2-NT and BuN, and a late transition state for NCP. This Part has established that AMH theory is particularly useful at providing physical insight when the transition coefficient, α, varies significantly from 0.5, indicating an asymmetric transition state.

References

[1] Katayama, Y.; Sekiguchi, K.; Yamagata, M.; Miura, T. *J. Electrochem. Soc.* **2005**, *152*, E247.

[2] Evans, R. G.; Klymenko, O. V.; Saddoughi, S.; Hardacre, C.; Compton, R. G. *J. Phys. Chem. B* **2004**, *108*, 7878–7886.

[3] Yuan, X.-Z.; Alzate, V.; Xie, Z.; Ivey, D. G.; Qu, W. *J. Electrochem. Soc.* **2014**, *161*, A451–A457.

[4] Monaco, S.; Arangio, A. M.; Soavi, F.; Mastragostino, M.; Paillard, E.; Passerini, S. *Electrochim. Acta* **2012**, *83*, 94–104.

Part IV

Silver Nanoparticle Oxidation in Room Temperature Ionic Liquids

This Part documents, for the first time, consideration of the oxidation of silver nanoparticles in Room Temperature Ionic Liquids. It begins with an Introduction to the nano-impact method, the capping agents and RTIL used, then continues with an Experimental section. Three chapters are contained in this Part that report the polymer-gated oxidation of silver nanoparticles, the role of chloride in direct detection of NPs, and the role of the capping agent respectively.

3.4 Introduction

As documented in Part I, the increased interest in nanoparticles had led to a range of techniques being developed to characterise them, the most recent being the 'nano-impact' method of analysis, which allows a fast, easy characterisation of nanoparticles, especially compared with *ex situ* sizing techniques, such as Transmission Electron Microscopy, Scanning Electron Microscopy, and Dynamic Light Scattering, which require expensive equipment and highly trained technicians for operation. A brief history of the nano-impact method and its reported applications is undertaken in the following section.

Reports of electrochemistry of particle suspensions were first made in 1995 by Heyrovsky in the study of colloidal semiconductors.[1–4] Heyrovsky deduced that the voltammetric response represented the sum of many individual NPs, (but this did not extend to the electrochemistry of individual NPs) which generated two observations that enabled the detection of individual particles. First, that the particles can be observed if the NP is able to catalyse a redox reaction of a species present in solution, and second that a NP can be directly oxidised or reduced as it comes into contact with the electrode. Early experimental work based on these principles was undertaken by Scholz[5–7] and Compton.[8–11] The work of Scholz *et. al* primarily focused on the detection of adhered particles from a suspension on mercury electrodes,[5–7] whilst

Compton used the above methods, often in conjunction with sonoelectrochemistry, to characterise micro-sized particles and measure the potential of zero charge for several solid electrodes.[8–11]

Metallic particles were first investigated by Korshunov and Heyrovsky[12] in their work on ultrafine metallic powders. They characterised copper, iron, nickel, molybdenum, and tungsten powders on a hanging mercury drop electrode in an aqueous solution. It was noted that the particles moved *via* Brownian motion to within a tunnelling distance of the electrode surface, and exchanged electrons with the electrode (providing that it was held at a sufficient potential to drive the reaction). From here, reports of the use of nano-impact methods to detect and characterise metallic particles grew considerably, and can be broadly grouped into three categories: indirect detection, direct detection, and capacitative impacts.

The indirect detection of metallic nanoparticles, whereby the presence of the catalytic nanoparticle enables the monitoring of a redox process on an otherwise inert electrode, was first reported by Xiao and Bard.[13] They detected platinum nanoparticles by monitoring the current-time transient for signals corresponding to the reduction of protons. Where the NPs adsorb to the electrode surface, 'staircase' signals are observed.[14] Since then, a number of other metal NPs have been indirectly detected.* Iridium oxide NPs were detected through monitoring the electrocatalytic oxidation of water,[16] whilst platinum NPs were detected by monitoring the reduction of hydrazine.[17] Ag NPs have also been indirectly detected through the electrocatalytic reduction of hydrogen peroxide,[18] whilst gold NPs promote the electrooxidation of hydrazine.[19] More recently, carbon nanotubes coated with palladium nanoparticles were characterised by detecting hydrogen oxidation.[20]

Kahk and coworkers[21] investigated the electron transfer kinetics of gold and silver nanoparticles (*via* proton reduction), and concluded that whilst silver NPs exhibit

*For a full list of electrocatalytic processes *via* nano-impact up to 2014, see the review by Cheng and Compton.[15]

a kinetic nano effect, gold NPs do not. Zhou *et. al*[22] extended this to nickel NPs, determining that the size effect was not the largest contributor to the rate of electron transfer, rather the presence of surface oxide layers controlled the kinetics. The study of nanoparticle kinetics was extended in a recent paper by Jiao *et. al*,[23] who report the kinetics of electrocatalytic oxidation of hydrogen on platinum NPs. Pumera reports transition metal dichalcogenides being capable of indirect detection (by measuring hydrogen evolution) and direct oxidative detection.[24]

Direct detection of metallic nanoparticles, through diffusion-driven contact of a NP with a charged electrode resulting in a 'spike' in the current-time transient (compared with the staircase signals observed with indirect detection, discussed above), is an extremely powerful technique, pioneered by Compton,[25] to characterise individual nanoparticles. The direct detection method provides a straight forward sizing method for spherical nanoparticles through the process outlined in Equation 3.3:

$$\frac{V_{NP}}{V_{Ag,molar}} = \frac{Q}{nF} = \text{no. of moles} \tag{3.3}$$

where Q is the charge under the spike in current, V_{NP} is the volume of the nanoparticle, $V_{Ag,molar}$ is the moles of silver per nanoparticle, F is the Faraday constant, and n is the number of electrons.

This has been undertaken for silver,[25] gold,[26] copper,[27] nickel,[18] and iron oxides.[28,29] Aside from sizing, concentration can be estimated through the frequency of the signals, and this has been achieved in complex media, including optically opaque solutions.[30,31] The concentrations of nanoparticle mixtures, where the concentrations of each species were also discerned, in this case silver and nickel NPs, have also been quantified.[18] Other properties, such as the electrostatics,[32] and estimates and analysis of aggregation,[33–35] and agglomeration[36] have also been reported. Recently, use of this method has enabled the detection of silver NP-decorated viruses, illustrating

the broad range of potential applications of this electrochemical technique.[37]

Capacitative impacts, reported by Poon *et. al*,[38] have been documented to characterise graphene nanoplatelets, whereby the impacting nanoplatelets remove charge from the electode-electrolyte interface. This was evidenced by the elongated shape and duration of the spikes, (where Faradaic spikes show sharp on/off behaviour of *ca.* 10 ms in duration), and a change in the polarity of the spikes as the current is stepped reductively to oxidatively. This application of the method enables a much broader range of carbon-based materials to be analysed.

However, to date, nano-impact methods of any of the above varieties have not been demonstrated in ionic solvents, something this Part achieves for the first time with silver nanoparticles.

The silver nanoparticles used throughout this Part are capped with either citrate and polyethylene glycol (PEG), as shown in Figure 3.5. Recall from Part I that the citrate capping stabilises the nanoparticles through charge, whilst PEG stablises the NPs sterically, making it a much more suitable capping agent for use in high ionic strength environments.

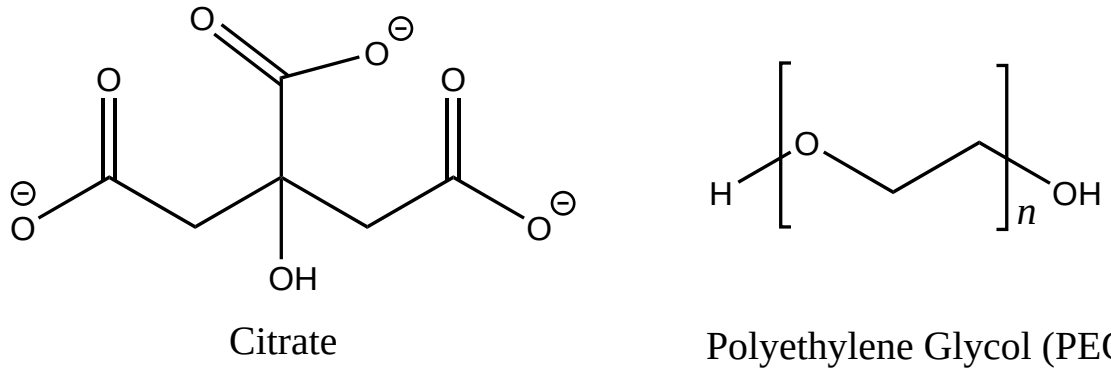


Figure 3.5: Capping agents examined in this study: citrate and polyethylene glycol (PEG).

Interest in Room Temperature Ionic Liquids (RTILs) and nanoparticles has grown with their frequent use in the synthesisis of nanoparticles,[39–41] and the modification

of electrodes,[42–44] particularly to act as catalysts when they are immobilised onto the electrode surface.[45–47] Nanoparticles in RTILs have also been reported as catalysts for hydrogenolysis,[48] in the case of palladium NPs immobilised on carbon nanotubes in [Emim][NTf_2], and selective hydrogenation, albeit not electrochemically.[49]

The RTIL used throughout this Part is 1-butyl-3-methylimizolium tetrafluoroborate ([Bmim][BF_4], Figure 3.6). It was selected for its water miscibility, to allow phase transfer of the nanoparticles into the RTIL, low viscosity, and ease of synthesis.

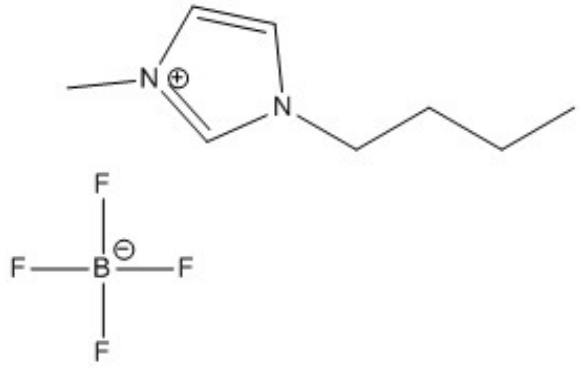


Figure 3.6: The RTIL used in this study: 1-butyl-3-methylimizolium tetrafluoroborate ([Bmim][BF_4]).

This Part of the thesis aims to examine the oxidation of Ag NPs in [Bmim][BF_4], including the effect of the capping agent and the presence of chloride on the observed mechanism.

3.5 Experimental

3.5.1 Nanoparticle Modification and Sample Preparation

The silver nanoparticles, capped with both citrate and PEG, were sourced from NanoComposix, San Diego, USA, and used as received in Chapters 4 and 5. To make PEG capped Ag NPs of varying chain lengths for Chapter 6, a small amount of solid thiolated PEG (2.2 mg) was dissolved in 1 mL of water. 10 μL of the thiolated

PEG stock solution was combined with 490 μL of the citrate capped Ag nanoparticles, shaken, and left undisturbed for 30 mins, during which time the solution turned from a light into an intense yellow colour. For Chapter 4, solutions were prepared by mixing 8μL of silver nanoparticle solution as received with 20 μL of RTIL. For Chapter 5, 2μL of the modified silver nanoparticle solution was combined with 30 μL of RTIL to produce an eventual concentration of 6.5 $\times$ 10^{-6} mol m^{-3} Ag NPs. The [Bmim][Cl] solution was prepared by dissolving 4.7 mg of the solid in 100 μL of [Bmim][BF_4]. It was then placed under a 0.2 mbar vacuum for 72 hours prior to use. For Chapter 6, 2μL of the modified silver nanoparticle solution was combined with 30 μL of RTIL. This produced a final concentration of 4.6 $\times$ 10^{-7} mol m^{-3} Ag NPs. In each case, the solution was then placed under a 0.2 mbar vacuum overnight to remove residual water prior to experimental use.

3.5.2 TEM

To confirm the silver particle sizes, experiments were carried out using a JEOL 2010 analytical transmission electron microscope (TEM; Herts, UK), which comprises a LaB_6 electron gun and can be operated at accelerating voltages of between 80 and 200 kV. The TEM samples were prepared by depositing a drop of the silver nanoparticle suspension (as received from the supplier) on a carbon-coated copper TEM grid and left to dry at room temperature for several hours before examination in the TEM. Figure 4.1 shows the TEM images of the spherical silver nanoparticles as an inset. ImageJ software developed at the National Institutes of Health, USA was used to size the Ag citrate and Ag PEG capped nanoparticles recorded on the TEM images. Size distributions for the citrate and PEG capped NPs are found in Figure 3.7.[50]

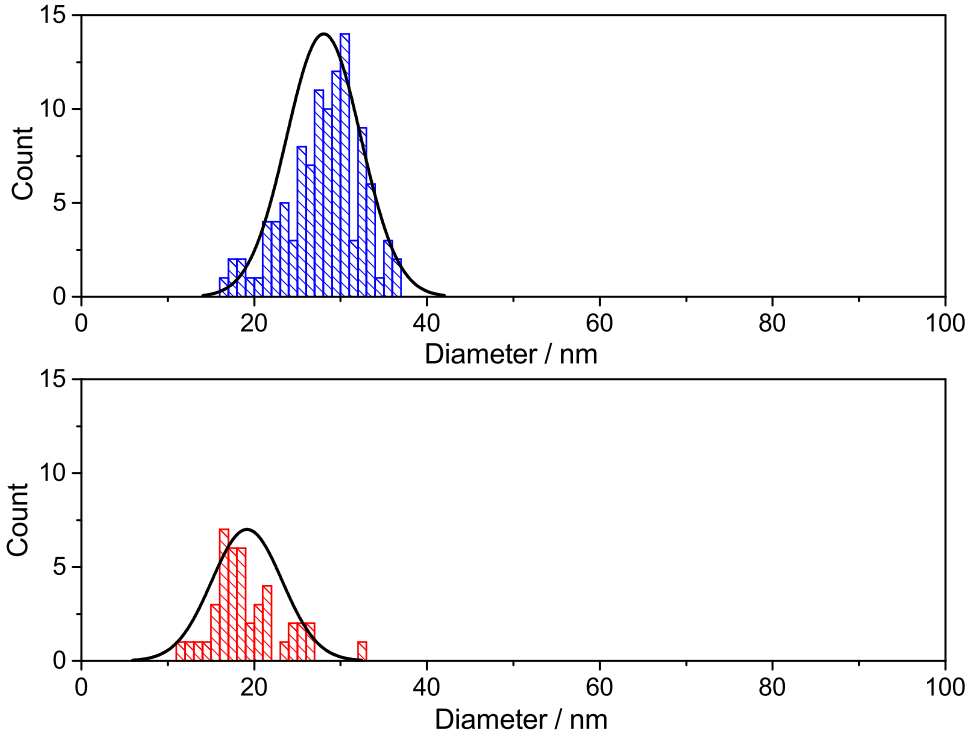


Figure 3.7: Histogram from TEM sizing of citrate capped silver nanoparticles (28.0 ± 4.3 nm, n = 109) blue, and PEG capped silver nanoparticles (19.2 ± 4.3 nm, n = 43), red.

3.5.3 Dynamic Light Scattering

Dynamic Light Scattering (DLS) measurements were performed using a Malvern Zetasizer Nano ZS instrument to measure the hydrodynamic radius of the nanoparticles (capped with citrate, and 2000, 6000 and 10,000 MW PEG). Each sample was diluted (50 μL of nanoparticle solution in 1 mL of water) and filtered, using a sterile Whatman 0.2 μm filter to remove any dust particles or other large contaminants, before being placed in a disposable solvent-resistant micro cuvette. Before any measurements were taken, the sample was equilibrated at 25 °C inside the DLS instrument for two minutes. Three sets of twelve light scattering measurements were then taken using 570nm light, and averaged to give three size distributions for the nanoparticles.

3.5.4 UV-Vis Spectroscopy

UV-Vis spectrophotometry was recorded on a Shimadzu UV-1800 using 50 μL High Precision Quartz Cells (Hellma Analytics, Germany). In all cases, a baseline correction was performed with empty cells inside the instrument prior to measurement, and the absorbance was recorded from 1100 – 250 nm. For the experiments conducted in water, each sample was diluted prior to analysis by combining 10 μL of the nanoparticle solution with 210 μL of water, and water was used as the reference solvent. For the experiments undertaken in RTIL, 10 μL of the nanoparticle solution was combined with 70 μL [Bmim][BF_4], and placed under vacuum overnight. An additional 70 μL aliquot of neat RTIL was placed under vacuum, and this sample was used in the reference cell.

3.5.5 Transfer into Glovebox and Experimental Assembly

All experiments were carried out in an acrylic MBRAUN glovebox (GB-2202-P-VAC) under an inert Argon atmosphere, as detailed in Part II (General Experimental Details). Once all of the samples had been brought into the glovebox, a solution containing 10 μL of the NP in RTIL stock solution (plus an aliquot of the chloride containing RTIL, if appropriate) was placed in a plastic collar fixed on top of the working electrode, and a T-cell was used for structural stability, as described previously.[51]

3.5.6 Electrochemical Apparatus

Electrochemical experiments (cyclic voltammetry and chronoamperometry) were conducted using a low noise potentiostat that was built in-house and detailed in Part II (General Experimental Details), with a working carbon microdisc electrode and a silver wire (counter and a quasi-reference electrode).

References

[1] Heyrovský, M.; Jirkovsky, J. *Langmuir* **1995**, *11*, 4288–4292.

[2] Heyrovský, M.; Jirkovsky, J.; Mueller, B. R. *Langmuir* **1995**, *11*, 4293–4299.

[3] Heyrovský, M.; Jirkovsky, J.; Struplova-Bartackova, M. *Langmuir* **1995**, *11*, 4300–4308.

[4] Heyrovský, M.; Jirkovsky, J.; Struplova-Bartackova, M. *Langmuir* **1995**, *11*, 4309–4312.

[5] Hellberg, D.; Scholz, F.; Schauer, F.; Weitschies, W. *Electrochem. Commun.* **2002**, *4*, 305 – 309.

[6] Scholz, F.; Hellberg, D.; Harnisch, F.; Hummel, A.; Hasse, U. *Electrochem. Commun.* **2004**, *6*, 929 – 933.

[7] Hellberg, D.; Scholz, F.; Schubert, F.; Lovrić, M.; Omanović, D.; Hernández, V. A.; Thede, R. *J. Phys. Chem. B* **2005**, *109*, 14715–14726.

[8] Rees, N. V.; Banks, C. E.; Compton, R. G. *J. Phys. Chem. B* **2004**, *108*, 18391–18394.

[9] Banks, C. E.; Rees, N. V.; Compton, R. G. *J. Phys. Chem. B* **2002**, *106*, 5810–5813.

[10] Banks, C. E.; Rees, N. V.; Compton, R. G. *J. Electroanal. Chem.* **2002**, *535*, 41–47.

[11] Clegg, A. D.; Rees, N. V.; Banks, C. E.; Compton, R. G. *ChemPhysChem* **2006**, *7*, 807–811.

[12] Korshunov, A.; Heyrovský, M. *Electroanal.* **2006**, *18*, 423–426.

[13] Xiao, X.; Bard, A. J. *J. Am. Chem. Soc.* **2007**, *129*, 9610–9612.

[14] Zhou, H.; Park, J. H.; Fan, F.-R. F.; Bard, A. J. *J. Am. Chem. Soc.* **2012**, *134*, 13212–13215.

[15] Cheng, W.; Compton, R. G. *Trend. Anal. Chem.* **2014**, *58*, 79 – 89.

[16] Kwon, S. J.; Fan, F.-R. F.; Bard, A. J. *J. Am. Chem. Soc.* **2010**, *132*, 13165–13167.

[17] Guo, Z.; Percival, S. J.; Zhang, B. *J. Am. Chem. Soc.* **2014**, *136*, 8879–8882.

[18] Stuart, E. J. E.; Zhou, Y.-G.; Rees, N. V.; Compton, R. G. *RSC Adv.* **2012**, *2*, 6879–6884.

[19] Kleijn, S. E. F.; Lai, S. C. S.; Miller, T. S.; Yanson, A. I.; Koper, M. T. M.; Unwin, P. R. *J. Am. Chem. Soc.* **2012**, *134*, 18558–18561.

[20] Li, X.; Batchelor-McAuley, C.; Whitby, S. A. I.; Tschulik, K.; Shao, L.; Compton, R. G. *Angew. Chem. Int. Ed.* **2016**, *55*, 4296–4299.

[21] Kahk, J. M.; Rees, N. V.; Pillay, J.; Tshikhudo, R.; Vilakazi, S.; Compton, R. G. *Nano Today* **2012**, *7*, 174 – 179.

[22] Zhou, Y.-G.; Rees, N. V.; Compton, R. G. *Phys. Chem. Chem. Phys.* **2013**, *15*, 761–763.

[23] Jiao, X.; Lin, C.; Young, N. P.; Batchelor-McAuley, C.; Compton, R. G. *J. Phys. Chem. C* **2016**, *120*, 13148–13158.

[24] Lim, C. S.; Tan, S. M.; Sofer, Z.; Pumera, M. *ACS Nano* **2015**, *9*, 8474–8483.

[25] Zhou, Y.-G.; Rees, N. V.; Compton, R. G. *Angew. Chem. Int. Ed.* **2011**, *50*, 4219–4221.

[26] Zhou, Y.-G.; Rees, N. V.; Pillay, J.; Tshikhudo, R.; Vilakazi, S.; Compton, R. G. *Chem. Commun.* **2012**, *48*, 224–226.

[27] Haddou, B.; Rees, N. V.; Compton, R. G. *Phys. Chem. Chem. Phys.* **2012**, *14*, 13612–13617.

[28] Tschulik, K.; Haddou, B.; Omanović, D.; Rees, N. V.; Compton, R. G. *Nano Research* **2013**, *6*, 836–841.

[29] Shimizu, K.; Tschulik, K.; Compton, R. G. *Chem. Sci.* **2016**, *7*, 1408–1414.

[30] Stuart, E. J. E.; Rees, N. V.; Cullen, J. T.; Compton, R. G. *Nanoscale* **2013**, *5*, 174–177.

[31] Toh, H. S.; Compton, R. G. *ChemistryOpen* **2015**, *4*, 261–263.

[32] Tschulik, K.; Cheng, W.; Batchelor-McAuley, C.; Murphy, S.; Omanovic, D.; Compton, R. G. *Chem. Electro. Chem.* **2015**, *2*, 112–118.

[33] Rees, N. V.; Zhou, Y.-G.; Compton, R. G. *Chem. Phys. Chem.* **2011**, *12*, 1645–1647.

[34] Sokolov, S. V.; Tschulik, K.; Batchelor-McAuley, C.; Jurkschat, K.; Compton, R. G. *Anal. Chem.* **2015**, *87*, 10033–10039.

[35] Ellison, J.; Tschulik, K.; Stuart, E. J. E.; Jurkschat, K.; Omanovi, D.; Uhlemann, M.; Crossley, A.; Compton, R. G. *ChemistryOpen* **2013**, *2*, 69–75.

[36] Sokolov, S. V.; Kätelhön, E.; Compton, R. G. *J. Phys. Chem. C* **2015**, *119*, 25093–25099.

[37] Sepunaru, L.; Plowman, B. J.; Sokolov, S. V.; Young, N. P.; Compton, R. G. *Chem. Sci.* **2016**, *7*, 3892–3899.

[38] Poon, J.; Batchelor-McAuley, C.; Tschulik, K.; Compton, R. G. *Chem. Sci.* **2015**, *6*, 2869–2876.

[39] Li, Y.; Qiang, Q.; Zheng, X.; Wang, Z. *Electrochem. Commun.* **2015**, *58*, 41–45.

[40] Neiva, E. G. C.; Souza, V. H. R.; Huang, K.; Pénicaud, A.; Zarbin, A. J. G. *J. Colloid Interface Sci.* **2015**, *453*, 28–35.

[41] Absalan, G.; Akhond, M.; Ershadifar, H.; Rezaei, M. A. *Colloids Surf., A* **2015**, *486*, 192–202.

[42] Hu, X.; Dou, W.; Zhao, G. *J. Electroanal. Chem.* **2015**, *756*, 43–48.

[43] Momeni, S.; Nabipour, I. *Appl. Biochem. Biotech.* **2015**, *176*, 1937–1949.

[44] Fouladgar, M.; Karimi-Maleh, H.; Gupta, V. K. *J. Mol. Liq.* **2015**, *208*, 78–83.

[45] Shi, F.; Xi, J.; Hou, F.; Han, L.; Li, G.; Gong, S.; Chen, C.; Sun, W. *Mater. Sci. Eng., C* **2016**, *58*, 450–457.

[46] Sadeghzadeh, S. M. *Catal. Commun.* **2015**, *72*, 91–96.

[47] Liu, W.; Wang, D.; Duan, Y.; Zhang, Y.; Bian, F. *Tetrahedron Lett.* **2015**, *56*, 1784–1789.

[48] Meng, Y.; Aldous, L.; Pilgrim, B. S.; Donohoe, T. J.; Compton, R. G. *New J. Chem.* **2011**, *35*, 1369–1375.

[49] Scholten, J. D.; Leal, B. C.; Dupont, J. *ACS Catal.* **2012**, *2*, 184–200.

[50] Toh, H. S.; Jurkschat, K.; Compton, R. G. *Chem. Eur. J.* **2015**, *21*, 2998–3004.

[51] Rogers, E. I.; Silvester, D. S.; Aldous, L.; Hardacre, C.; Compton, R. G. *J. Phys. Chem. B* **2008**, *112*, 6551–6557.

Chapter 4

Polymer Gated Single Nanoparticle Oxidation

In this chapter, we first analyse nanoparticles with two different capping agents, citrate and PEG, of the same nominal core size, and establish reactivity differences of each with acid using UV-Vis spectrophotometry. The NPs are then electrochemically assessed and an ionic liquid is used to explore ensembles of NPs - using both dropcast and in situ modification methods. It is found that PEG coated NPs show, never seen before, stochastic stripping of individual NPs even from a surface immobilised NP ensemble. A polymer-gated mechanism, unobserved in the citrate capped case is proposed, to explain the oxidation of the silver PEG nanoparticles.

Initially, physical characterisation of the commercially sourced nominally 30 nm diameter sized nanoparticles (NPs), in the form of TEM and DLS analysis, and stability experiments, using UV-Vis spectrophotometry, were performed on silver nanoparticles capped with both citrate and polyethylene glycol (PEG) in an aqueous solution. Transfer of both citrate and PEG capped NPs into a RTIL from an aqueous stock was attempted and subsequently, electrochemical analysis of the successfully transferred PEG-capped silver nanoparticles using voltammetry and chronoamperometry

was performed.

4.1 Sizing

Transmission Electron Microscopy (TEM) was first used to size the silver core of the nanoparticles and returned values of 29.2 ± 4.2 nm for the citrate-capped NPs (109 particles analysed) and 19.2 ± 4.0 nm for the PEG-capped NPs (43 particles analysed).* The TEM sizing thus confirms that the silver cores of the NPs are of similar sizes. Due to the low atomic number, and hence the low TEM contrast of the capping agent, the size of the capping agent cannot be properly resolved by TEM. Thus, to establish the extent of the capping agent layer surrounding the core, Dynamic Light Scattering (DLS) was undertaken to measure the hydrodynamic diameter of the particles (their overall size). This analysis revealed that the hydrodynamic diameter of the NPs differed significantly, with the size of the citrate-capped nanoparticles calculated as *ca.* 35 (+ 40, – 20) nm, and the PEG-capped nanoparticles as *ca.* 70 (+ 80, – 33) nm. Figure 4.1 visually displays a two times larger hydrodynamic diameter of the PEG capped nanoparticles (red) compared with the citrate capped NPs (black), revealing the much increased thickness of the PEG over the citrate capping layer. The TEM images (inset in Figure 4.1) corroborate this, with the distance between the nanoparticles being twice as great in the case of the PEG capped NPs.

4.2 Reactivity Towards Oxidative Dissolution

To establish the relative NP reactivities for the different capping agents, an acid reactivity test, whereby the NPs react with protons in the presence of oxygen to produce hydrogen peroxide as elucidated in the Introduction, was undertaken and monitored by UV-Vis spectrophotometry. UV-Vis Absorption spectrophotometry was chosen as

*Histograms can be found in the Section 3.5.2

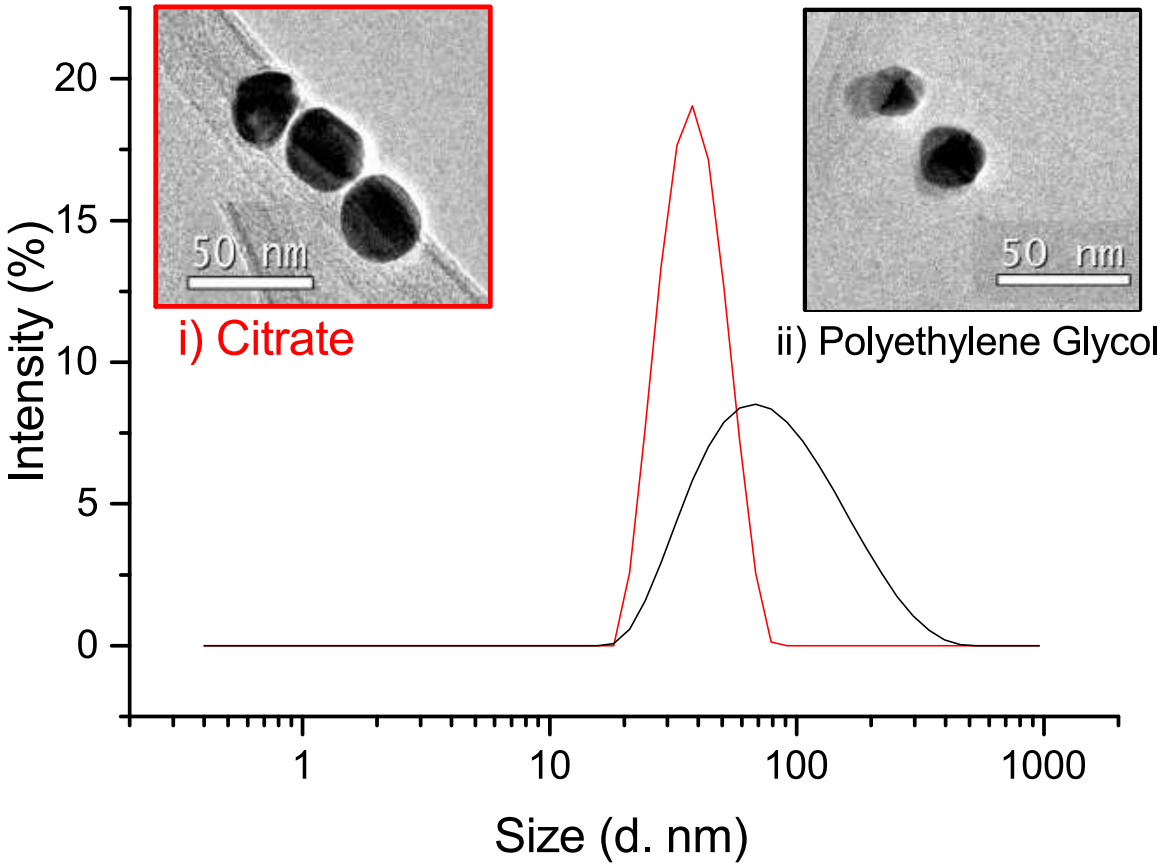


Figure 4.1: Dynamic Light Scattering analysis of citrate capped silver nanoparticles (red) with polyethylene glycol (PEG) capped silver nanoparticles (black) used in this study. Insets TEM images of citrate and PEG capped NPs.

the preferred method for this time-dependent analysis due to the presence of a surface plasmon resonance absorption peak that appears at *ca.* 400 nm for the silver NP size range under study. Changes in the size of this peak enable monitoring of changes in the population of nanoparticles relative to the control sample in the absence of acid. Nitric acid, to a 20 mM concentration, was added to two samples of citrate and PEG capped Ag NPs. The maximum absorption over time was then monitored, and the normalised[†] and the baseline corrected maximum absorbance over time is shown in Figure 4.2, alongside examples of the plasmon peak in the absence of acid of both the citrate and PEG capped NPs, which was found to be unaltered over the experimental

[†]This was calculated by dividing the experimental absorption by the maximum absorption in the absence of acid.

time scales used. In the 20 mM nitric acid solution, the citrate capped nanoparticles

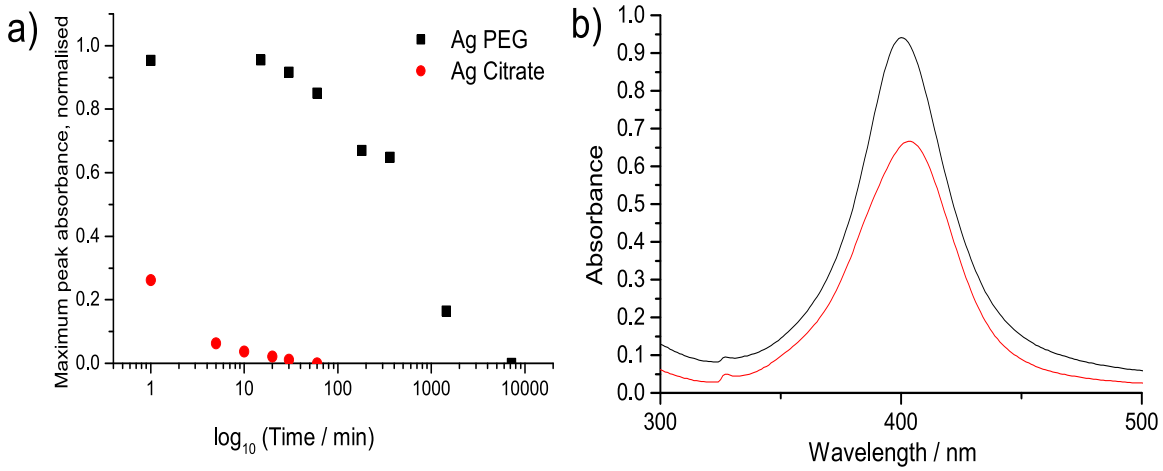


Figure 4.2: a) Normalised maximum peak absorbance with time for citrate-capped silver nanoparticles with 20 mM nitric acid (red diamonds) and PEG-capped silver nanoparticles with 20 mM nitric acid (black squares). b) Plasmon peaks of citrate (red) and PEG (black) capped NPs in the absence of acid.

degrade very quickly, with a two-thirds loss of absorption signal after five minutes, and a near-complete loss after 60 min, indicating the NP dissolution. In contrast, the signal corresponding to the PEG capped NPs showed very slow degradation, decaying an equivalent amount only after 24 hours. Complete disappearance of the absorption peak at 400 nm for the PEG capped NPs occurred after 5 days, representing a dissolution rate *ca.* 100 times slower than that seen in the citrate capped NPs. To ensure the degradation observed with the citrate-capped NPs was not an ionic strength induced agglomeration or aggregation, an equivalent timed experiment was performed with 20 mM sodium nitrate (Figure 4.3), where the peak observed at 400 nm remained present after 60 mins, demonstrating that the degradation of the signal is a result of higher reactivity, that is NP dissolution, and unrelated to the stability of the NP.

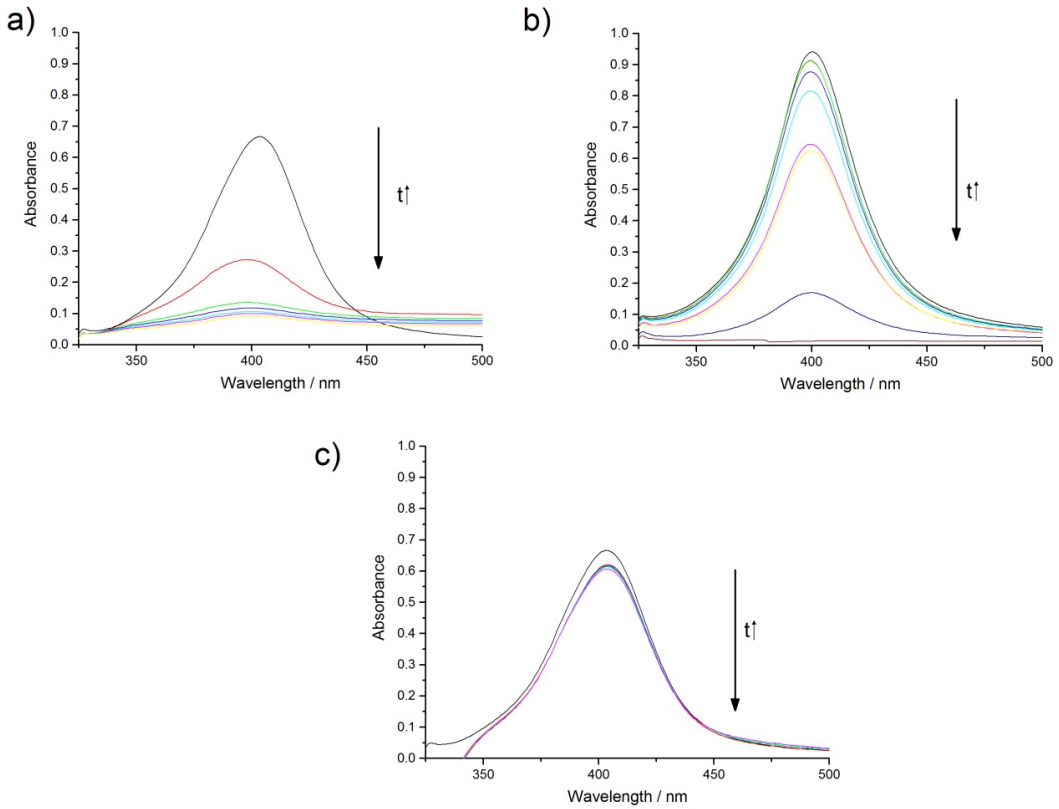


Figure 4.3: UV-Vis spectra of a) citrate capped Ag NPs in 20 mM nitric acid (black is the absence of acid, red is 5 minutes post acid addition, green 10 mins, navy is 20, cyan is 30 minutes and yellow is 60 minutes post addition) b) PEG capped Ag NPs in 20 mM nitric acid (black is in the absence of acid, red is 15 minutes post addition [obscured by the black line], green 30 mins, navy is 60, nyan is 180 minutes, navy is after 24 hours and brown is 5 days) and c) citrate capped Ag NPs in 20 mM sodium nitrate (black is in the absence of acid, red is 10 minutes post addition, green 20 mins, navy is 30 and nyan is 60 minutes).

Note in this context 'stability' means that the NPs are resistant to aggregation and agglomeration, whilst 'reactivity' relates to their proton and oxygen driven chemical dissolution to hydrogen peroxide (see Equation 4.1).

$$O_2 + 2H^+(aq) + 2Ag(s) \leftrightharpoons H_2O_2(aq) + 2Ag^+(aq) \tag{4.1}$$

Further evidence for the decrease of the absorbance being due to dissolution of the

Ag NPs instead of their association is that the baseline of the scan did not increase over time (as would be observed for large NP aggregates due to light scattering). This experiment thus suggests that in the 20 mM nitric acid, the citrate capped NPs are approximately two orders of magnitude more reactive than the PEG capped NPs. This lack of reactivity in the case of the PEG capped NPs might have major implications in its persistence in various liquid media and it is hence illuminating to study the PEG capped nanoparticles in a different medium to better understand the role of this capping agent in terms of solvent-particle interaction. RTILs are ideal solvents to examine the effects of the capping agent on a microscopic and nanoscale, as they allow new insights to be gained into how a solvent with charged components interacts with the capping agent material, and allow verification that NPs can be studied electrochemically in an ionic solvent.

4.3 Reactivity Differences in Ionic Liquids

Electrochemical NP studies performed previously in water provided limited insight into the effect of PEG coating on the reactivity of Ag NPs.[1] Therefore, electrochemical analysis was undertaken in [Bmim][BF_4] in order to explore whether PEG-related reactivity differences can be studied in a suitable alternative solvent. Initially, PEG coated Ag NPs were dropcast on a glassy carbon electrode, submerged in [Bmim][BF_4] and a Cyclic Voltammogram (CV) was measured from 0 to 1.5 V vs a silver wire (blue line, Figure 4.5). The CV shows two features, the first, at *ca.* 0.1 V, is most likely trace chloride in the RTIL reacting with Ag to form AgCl,[2] and the second feature at 0.65 V is attributed to the oxidation of Ag to Ag^+(aq). A subsequent second scan showed a significantly smaller stripping peak (see Figure 4.4).

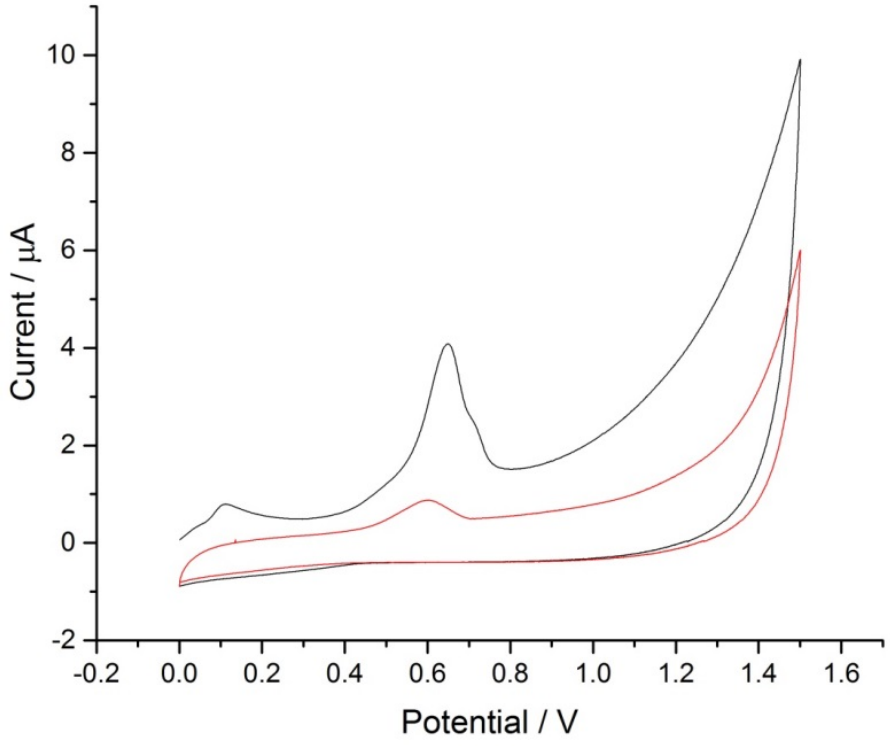


Figure 4.4: CV of Ag PEG NPs dropcast on a glassy carbon electrode in RTIL: first scan (black) and second scan (red).

Dropcasting the capping agent material alone gave voltammetry without any stripping features, indicating the electrochemical inertness of polyethylene glycol under the experimental conditions. This evidences the first successful electrochemical stripping of dropcast Ag NPs in RTIL (Figure 4.5, shown in blue). However, as this ex situ NP immobilisation technique is known to cause significant alteration of NPs upon evaporation of the solvent,[3,4] and the effect of this drying on the capping agent is unknown, an in situ surface modification of NPs on the electrode is preferred. The successful use of this has been reported in aqueous media[5,6] and is herein adapted for RTILs.

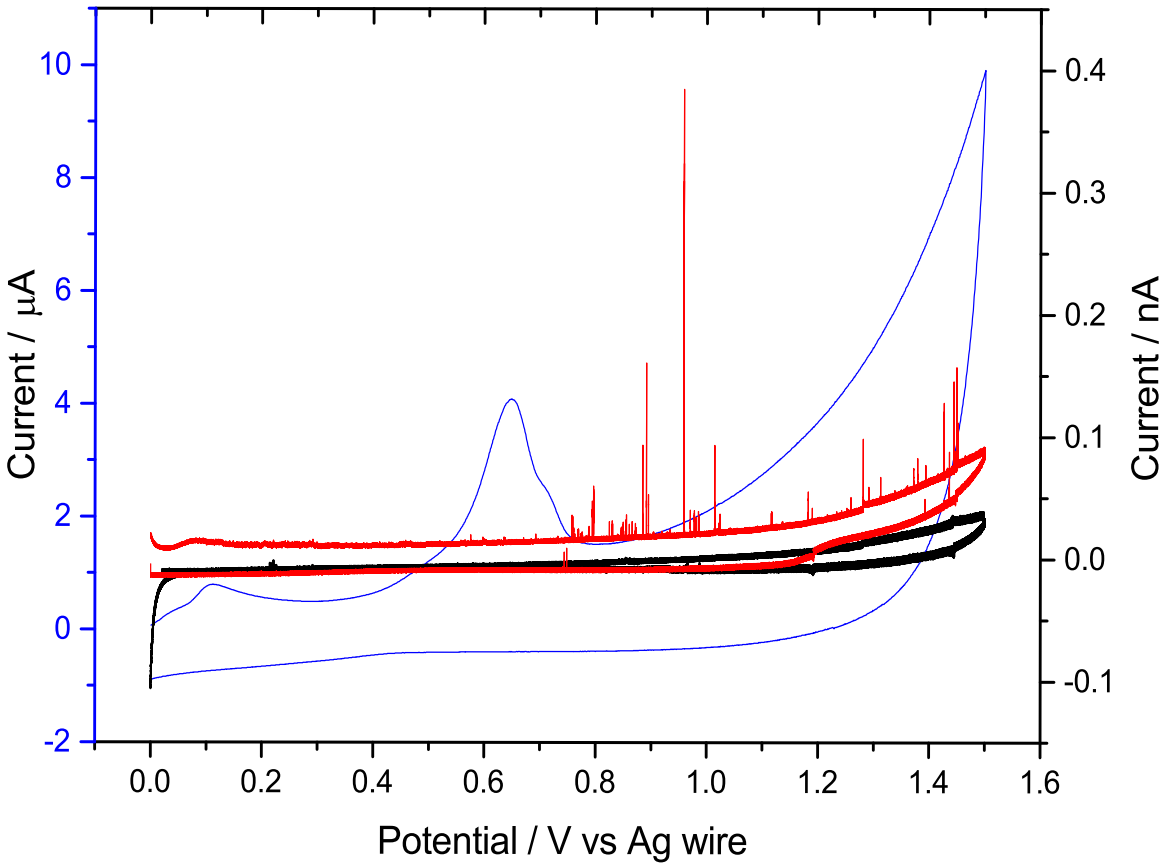


Figure 4.5: Cyclic Voltammetry: Dropcast NPs on a glassy carbon (blue), and in situ modification (20 min immersion time) both in the absence of NPs (black) and with PEG capped silver NPs in [Bmim][BF_4] (red) on a carbon fibre microelectrode.

4.3.1 Transfer into Ionic Liquid

In order to undertake reactivity studies of NPs in RTILs, transfer of the NPs into the new solvent needs to be achieved; a protocol hitherto unreported in the literature. To this end, the transfer of NPs capped in both citrate and PEG into a RTIL was attempted. The method chosen for NP transfer was adapted from a commonly used method[7] for transferring materials into RTILs, whereby the material of interest, dissolved in a volatile solvent, is mixed thoroughly with an RTIL that is highly miscible with that solvent, then exposed to vacuum overnight to remove the volatile solvent. Both samples of Ag NPs were originally solvated in water, hence, the ionic liquid chosen was 1-butyl-3-methylimidazolium tetrafluoroborate ([Bmim][BF_4]), selected for its

ease of synthesis and high water miscibility. UV-Vis analysis was performed on samples of both citrate and PEG capped silver nanoparticles solvated in [Bmim][BF_4] to verify the successful transfer. The absence of a clear plasmon peak associated with the Ag nanoparticles in Figure 4.6, and the overall increase in the background, suggesting that agglomeration has occurred, demonstrates that this transfer method was unsuccessful in the case of the citrate capped NPs. DLVO theory, named after Boris Derjaguin and Lev Landau, Evert Verwey and Theodoor Overbeek, describes the aggregation of dispersions as being controlled by the balance of Van der Waals (attractive) and coulombic (repulsive) forces. The instability of the citrate capped NPs is consistent with DVLO theory, where the expected screening of the ligand charge in high ionic strength solvents leads to aggregation. In contrast, the expected Ag plasmon peak at *ca.* 400 nm, as shown in Figure 4.6, is seen in the case of the PEG capped NPs, illustrating that the vacuum transfer method was successful, and possibly emphasising steric over electrostatic stabilisation in a high ionic strength environment.

Based on this, in situ modification studies with PEG-coated Ag nanoparticles were undertaken for the first time in RTILs.

4.3.2 In-situ Modification

Initially, to confirm that any electrochemical observations are due to the presence of NPs, an electrode was immersed in a blank aliquot of [Bmim][BF_4] for 10 minutes and a CV was recorded, sweeping the potential from 0 to 1.5 V (vs a silver wire). As the voltammetry of Figure 4.5 shows in black, in the blank RTIL, no cyclic voltammetric features were observed. In contrast, after 10 minutes immersion of the electrode in a RTIL at open circuit potential with silver nanoparticles suspended in the RTIL (red), sharp spikes in current were observed once a potential of 1 V was applied. These features were only detected at potentials more positive than 0.6 V on both the forward

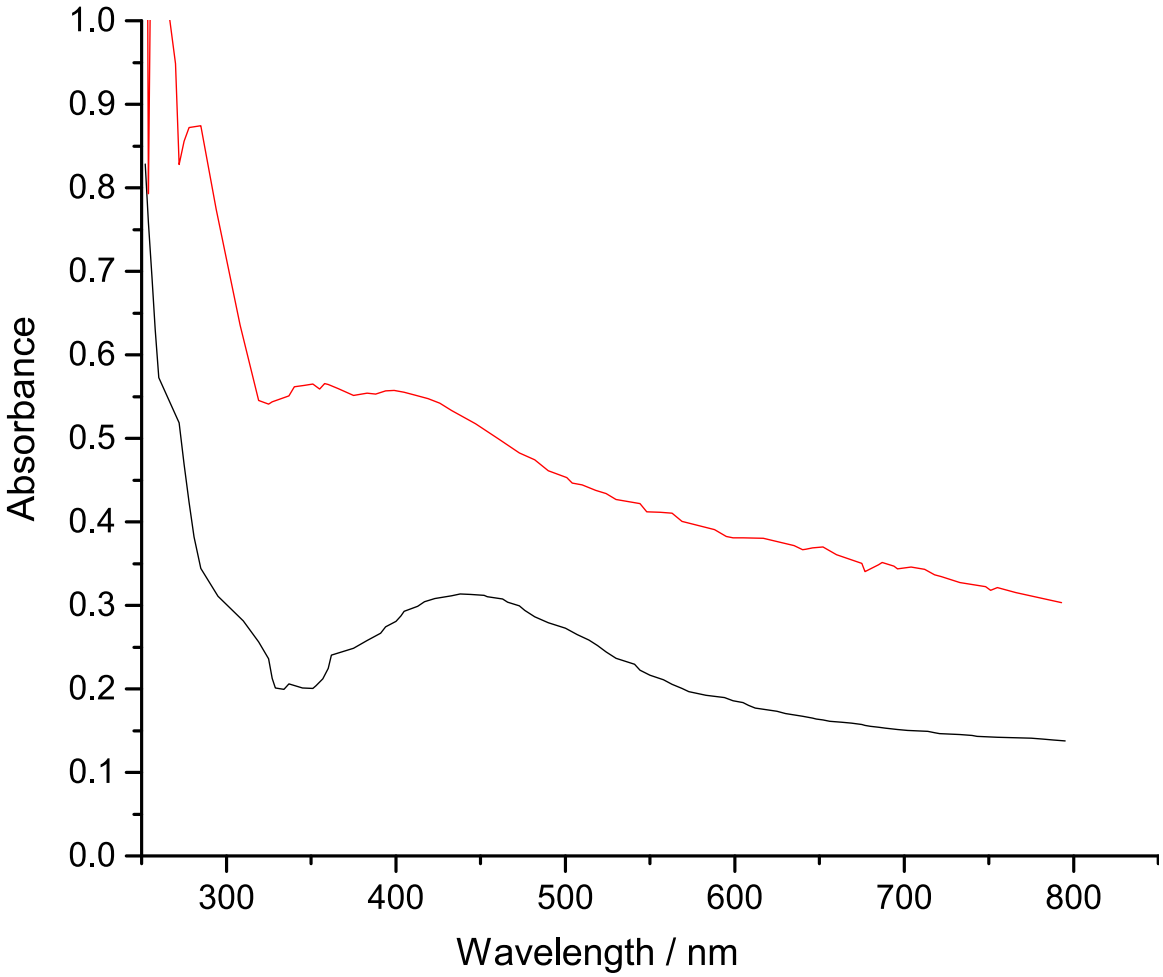


Figure 4.6: UV-Vis spectrum of citrate-capped silver nanoparticles (red) and PEG-capped silver nanoparticles (black) solvated in [Bmim][BF_4].

and reverse scan. These observations allow us to surmise, firstly, that the features observed are the result of the presence of nanoparticles in the solution. Secondly, the switching on and off of the features in a potential-dependent way evidences that the 'jumps' in current are related to a Faradaic reaction due to the oxidation of the Ag NPs. Thirdly, the non-continuous spike-like current features, herein referred to as 'stochastic stripping', with durations of the order of 10 ms, are distinct from the continuous, smooth and singular, stripping peak observed in aqueous solvents[8] or from dropcast PEG Ag NPs in RTIL, suggesting a more complex stripping mechanism of PEG capped NPs in RTILs. There are at least two possible options for the

origin of this stochastic stripping. The first is a 'nano-impact'[9,10] process whereby nanoparticles diffuse to the surface of the electrode, then immediately undergo a redox reaction when they arrive at the electrode. The second is a stochastic stripping whereby NPs diffuse to and adsorb at the electrode forming an ensemble, with each individual nanoparticle undergoing a redox reaction once a sufficiently high potential is applied. To distinguish between the two, the time between successive oxidative scans can be altered. In the former case, there is no trend expected, whereas in the latter case, an increased number of oxidative features with increased waiting time between scans is expected.

To explore which mechanism may have led to the 'stochastic' stripping features seen in Figure 4.5 time dependent chronoamperometry was performed by holding the potential at 1 V (vs a silver wire) for 50 s. Following this, the length of in situ modification was systematically varied, before applying a potential of 1 V. Herein modification time denotes the duration the electrode was immersed in the NP suspension under open circuit conditions before stripping.

4.4 Time Dependency

Figure 4.7 shows the number of individual spikes in current observed experimentally with different in situ modification times. It shows that with increased time between scans, the number of oxidative events also increased, demonstrating that the process is time dependent, indicating that the first mechanism proposed above, so called nano-impacts, is unlikely to be responsible for the results shown, suggesting that there is an assembly of NPs arranged at the electrode surface that are stripped stochastically upon applying a sufficiently oxidative potential. If each 'spike' in current is assumed to be the result of one complete NP undergoing oxidation (*vide infra*), the frequency of spikes with varied in situ modification time establishes if the NPs are adsorbing.

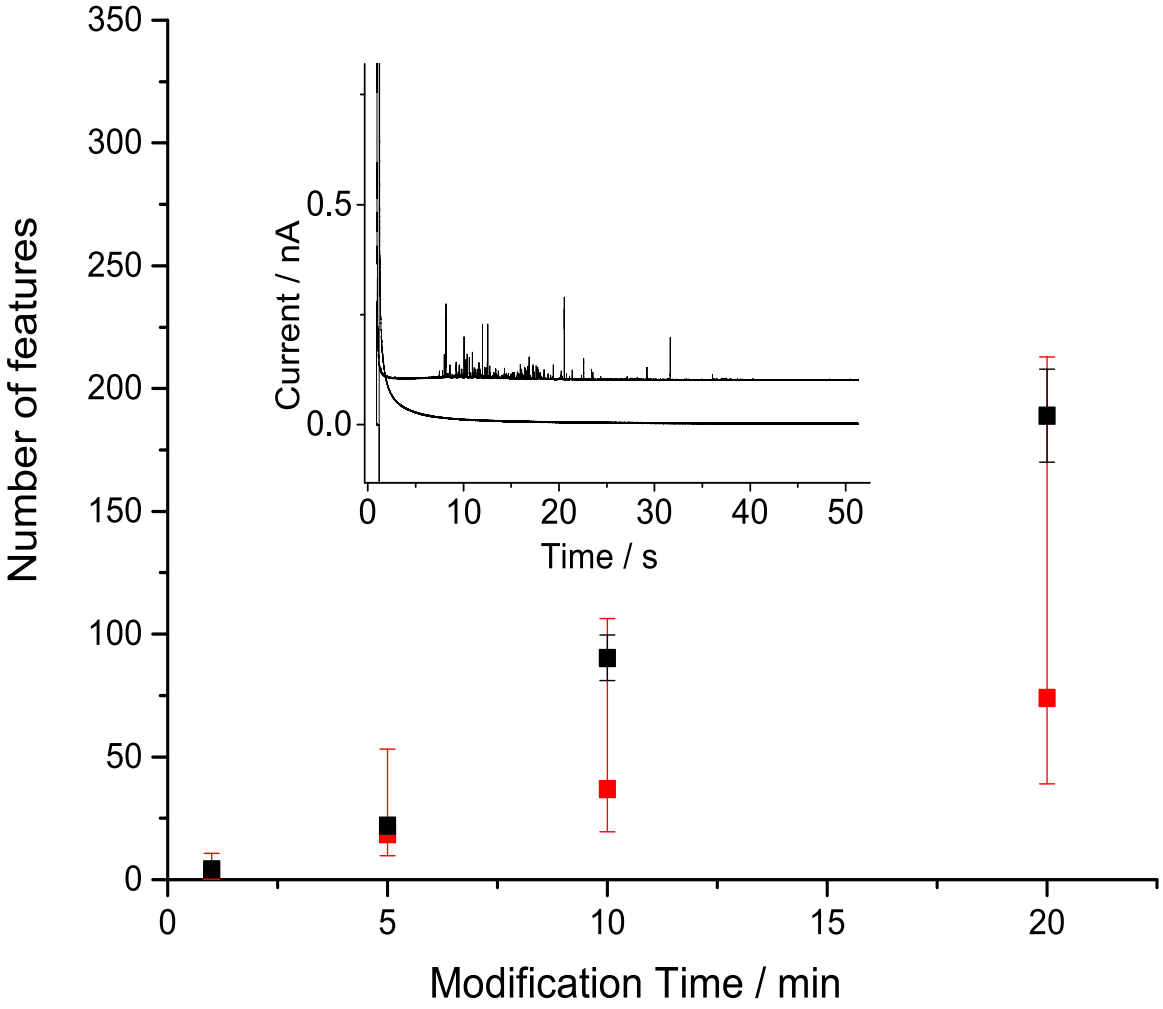


Figure 4.7: Frequency of impacts versus time at open circuit in between scans (black squares) and predicted cumulative number of impacts according to a steady-state approximation (red). Inset shows a representative chronoamperogram, both with no nanoparticles present, and with nanoparticles present after a ten minute wait, offset by 0.1 nA.

Taking a given size for the radius of the nanoparticles from DLS sizing above (36 nm), the diffusion coefficient can be estimated from the Stokes-Einstein equation,[11] giving a value of 6.6×10^{-14} m^2 s^{-1}, which then allows the estimation of the theoretical cumulative number of impacts per minute (red squares, Figure 4.7), using a steady-state approximation, which is an approximation of flux to a disc surface,[12] shown in Equation 4.2, where N is the number of impacts, N_A is the Avogadro constant, D is the diffusion coefficient as calculated above, $C_N P$ is the NP bulk con-

centration (*ca.* 80 pM), r is the radius of the electrode, and t is the time elapsed in seconds.

$$N = 4N_A DC_N Prt \tag{4.2}$$

An uncertainty was estimated in the theoretical value from calculation of the number of impacts expected within the mean $\pm$ 1σ standard deviation of the DLS sizing, with 19 nm representing the lower boundary (resulting in a diffusion coefficient of 1.25 $\times$ 10^{-13} m^2 s^{-1} and *ca.* 7 impacts min^{-1}) and 75 nm representing the upper boundary (giving a diffusion coefficient of 3.2 $\times$ 10^{-14} m^2 s^{-1} and *ca.* 4 impacts min^{-1} are predicted). The experimental error is given by the standard deviation of the mean, calculated for both the ten and one minute time points, which was extrapolated as a percentage across the other time points. The close agreement of the experimental number of oxidative features per scan with the predicted cumulative number indicates that diffusion-limited NP adsorption occurs throughout the waiting time with a sticking coefficient of *ca.* 1, [‡] causing an in situ modification of the electrode with NPs at open circuit potential. A typical adsorption-stripping mechanism, whereby a pre-accumulation with waiting time and a simultaneous reaction once a potential is applied, is inconsistent with the appearance of spikes in current in the chronoamperogram (as shown in the inset of Figure 4.7, at ten minutes at open circuit) as we would expect the oxidation of silver to occur rapidly after the application of a sufficiently positive potential. However, this observation can be understood in light of a capping-agent gated NP stripping, evidencing the crucial effect of the PEG ligand to NP stripping as will be described below. To explore any possible thermodynamic effect of the capping agent on the oxidation, and to further confirm that the features are due to the oxidation of silver, a study considering the relationship between the charge (obtained by integrating each current feature over time) with the potential

[‡]The sticking coefficient is herein defined as the proportion of particles that are immobilised at the surface with respect to the number that arrive at the electrode surface.

was undertaken.

4.5 Potential Dependency

Chronoamperograms at 12 potentials within the range of 0 — 1.1 V were measured, and a time of 10 mins fixed as in-situ modification time prior to each scan. The same characteristic spike features as before were observed at all potentials greater than 0.6 V. Figure 4.8 displays the average charge of every current feature at varying potentials from 0 — 1.1 V. The charge per feature is negligible at potentials close to 0 V, increasing to a maximum at potentials greater than or equal to 0.6 V. These observations are consistent with a dynamic process, involving a partial unwrapping and wrapping of the polymer coating, prior to the oxidation of the silver core as elucidated below.

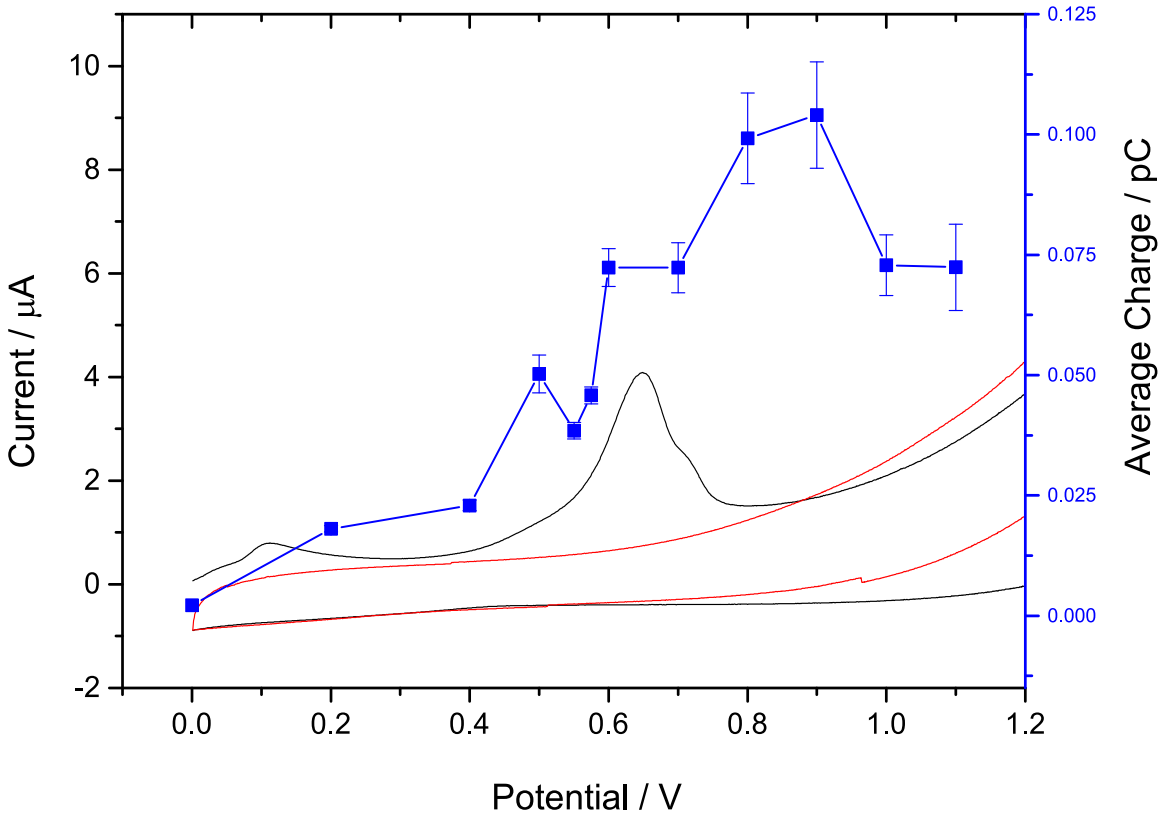


Figure 4.8: The average charge of individual oxidative current features at different potentials (blue) compared with a CV of Ag PEG NPs dropcast on a glassy carbon electrode (black), blank RTIL with a bare GC (red).

However, first, to further confirm that it is the complete oxidation of *individual* silver NPs that is being seen in the chronoamperometry, the charge measured per feature was converted into a radius.

4.6 Sizing of nanoparticles

Each spike was charge integrated and, applying Faraday's 1st Law to provide the number of atoms, assuming the exchange of one electron per silver atom, knowing the density of silver, and, finally, assuming that the particles are spherical (an assumption that holds on the basis of the TEM images) converting the charge to a radius.[1] All features from 0.8 — 1.1 V were included in the electrochemical sizing method, due to

their equivalence in average charge, as illustrated in Figure 4.8. Figure 4.9 shows a sizing histogram of the electrochemical sizing, in red, compared with the sizing from TEM, in black. The histograms are in excellent agreement with one another. The average radius of the impacts is calculated from impacts as 22.0 ± 9.2 nm, which is the same within uncertainty with the average radius from TEM sizing of 19.2 ± 4.0 nm. This close agreement strongly suggests that each feature represents a complete oxidation of a single silver NP. Note that this is the first experiment to demonstrate the ability to accurately size nanoparticles in an ionic liquid using an electrochemical sizing method.

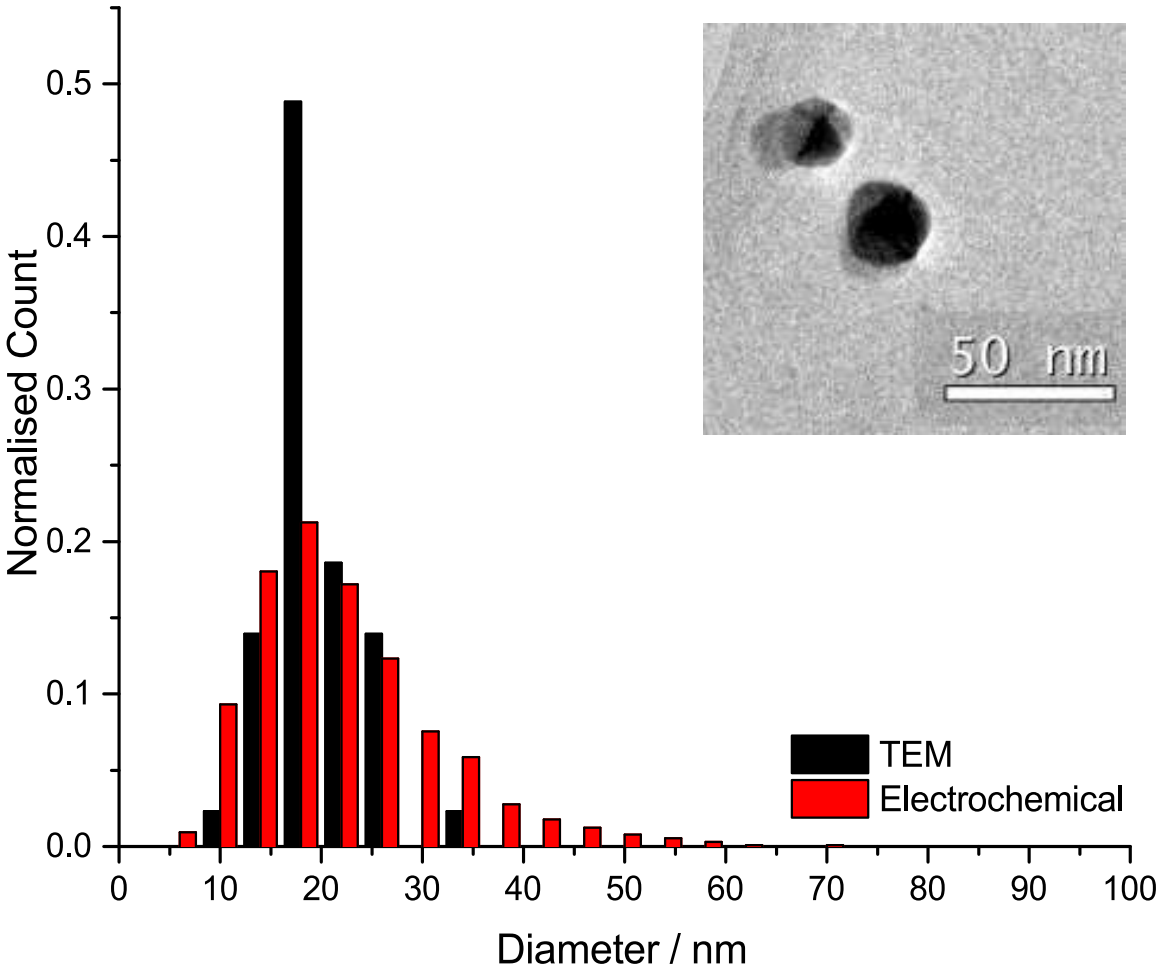


Figure 4.9: Sizing histogram of the electrochemical sizing method (red) compared with TEM Sizing (black); inset is an image from TEM sizing.

4.7 Proposed Mechanism for Stochastic Stripping

In previous experiments conducted in aqueous media, stochastic features, that allowed sizing of individual nanoparticles, were only observed during individual *diffusional* nanoparticle impacts at microelectrodes. During 'nano-impact' experiments in aqueous media, individual nanoparticles move *via* Brownian motion, and as they make contact with the electrode surface, they react almost instantaneously, undergoing electron transfer. In contrast, the stochastic features observed in both the chronoamperogram and the voltammogram in RTIL do not require that individual NPs arrive at the electrode at any given time, but out of an ensemble of NPs immobilised on the electrode surface, individual NPs can become electroactive, and following this, undergo a redox reaction. The following mechanism is suggested to describe this observation.

$$NP_{inactive} \underset{k_d}{\overset{k_a}{\rightleftarrows}} NP_{active} \xrightarrow{k_{ox}} NP_{ox} \tag{4.3}$$

The above polymer-gated mechanism may involve a reversible partial unwrapping process to activate the nanoparticle, followed by an irreversible oxidation of the activated nanoparticle. This relationship supports the notion that the polymer capping agent gates the redox reaction occurring at the nanoparticle. If the capping agent were involved in a change in the *thermodynamics* of the process, it would be expected that this 'switching on' potential would be altered relative to the dropcast CV seen in Figure 4.8, shifting it closer to zero whereby the process is made thermodynamically more favourable than silver alone, or shifting it to a higher potential where this process is made more burdensome due to the increased overpotential as the energy barrier to undergo the oxidation becomes higher. However, what is seen is that the average charge increased to a maximum at 0.6 V, the same maximum observed in the dropcasting CV, suggesting that the capping agent effect is not thermodynamic, but

is consistent with the 'polymer gated' mechanism proposed above.

To assist with further validation of this mechanism, a count of features was performed with an equal number of NPs on the electrode (this was attempted through using equal immersion times, but cannot be proven numerically due to capacitative charging at short times) at various potentials to see whether there is a relationship between the presence of spikes in current and the stage (beginning, middle or end) of the 50 s chronoamperogram. The recorded current-time responses are shown in Figure 4.10. The number of features according to potential were then analysed, with a lower (blue), moderate (red), and higher potential (green) chosen (see inset, Figure 4.10). With increasing potential, the number of features decrease and tend towards occurring at shorter times after applying a potential in the chronoamperogram. The representative chronoamperograms shown in Figure 4.10 at each potential reveal that the high count in the lower potentials is due to smaller features, corresponding to incomplete oxidation (in agreement with the charge per spike as shown in Figure 4.8). These results tentatively support the hypothesis of a polymer gated mechanism, involving an unwrapping activation of the nanoparticle being in competition with the electron transfer process, as elucidated in Equation 4.3. The presence of features less than 0.025 pC in size at potentials lower than 0.6 V suggests that there is insufficient overpotential to ensure complete oxidation within the lifetime of the activated (unwrapped) species. At potentials higher than 0.6 V, a constant stripping charge is observed, in agreement with the full oxidation of particles once they are unwrapped. This process is therefore limited by the activation of the particle, as evidenced in the oxidation occurring within shorter times after the potential step.

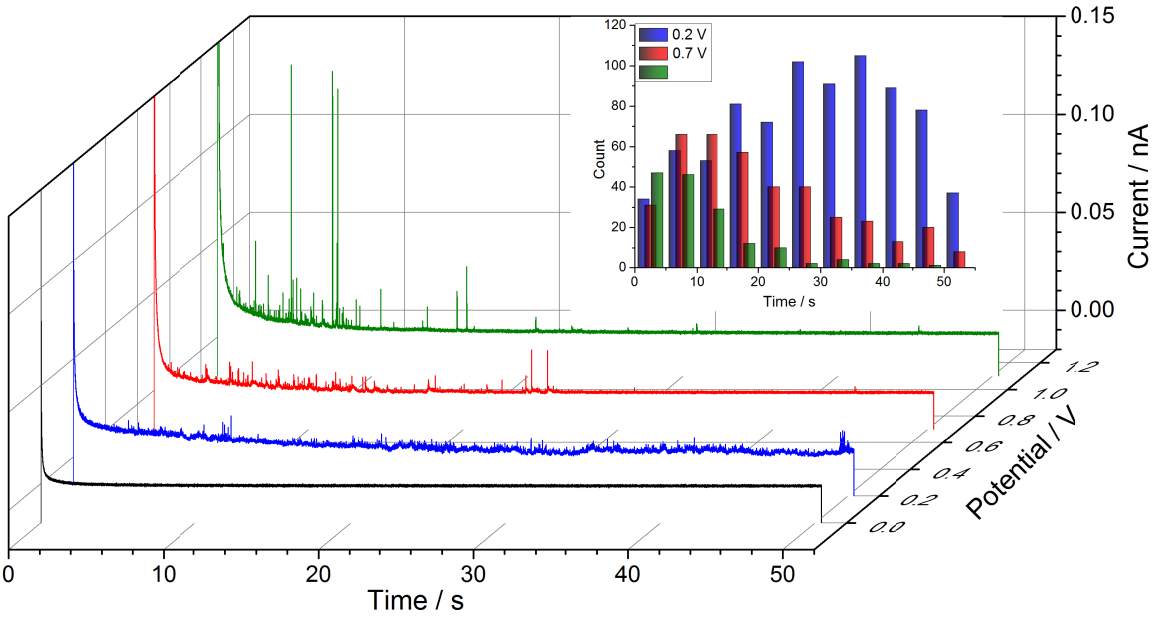


Figure 4.10: Chronoamperograms recorded after 10 mins in situ modification time; 0 V (black), 0.2 V (blue), 0.7 V (red) and 1.1 V (green). Inset is number of features with time of experiments undertaken at increasing potentials; 0.2 V (blue), 0.7 V (red), and 1.1 V (green).

4.8 Conclusions

This chapter detailed the oxidation of an individual silver nanoparticle, which was detected *via* sharp individual current spikes and explained by a polymer gated redox mechanism. This mechanism involves the dynamic equilibrium between a wrapped and unwrapped nanoparticle, allowing charge transfer to the nanoparticle to occur only in the latter, activated state. This first observation of stochastic stripping of individual nanoparticles from a surface immobilized ensemble is demonstrated to allow for up until now inaccessible insights into the effect of nanoparticle capping agents on electron transfer dynamics. The following chapter explores the effect of chloride on the mechanism of oxidation.

References

[1] Toh, H. S.; Jurkschat, K.; Compton, R. G. *Chem. Eur. J.* **2015**, *21*, 2998–3004.

[2] Toh, H. S.; Batchelor-McAuley, C.; Tschulik, K.; Compton, R. G. *Analyst* **2013**, *138*, 4292–4297.

[3] Toh, H. S.; Batchelor-McAuley, C.; Tschulik, K.; Uhlemann, M.; Crossley, A.; Compton, R. G. *Nanoscale* **2013**, *5*, 4884–4893.

[4] Cloake, S. J.; Toh, H. S.; Lee, P. T.; Salter, C.; Johnston, C.; Compton, R. G. *Chemistry Open* **2015**, *4*, 22–26.

[5] Stuart, E. J. E.; Tschulik, K.; Ellison, J.; Compton, R. G. *Electroanal.* **2014**, *26*, 285–291.

[6] Tschulik, K.; Batchelor-McAuley, C.; Toh, H.-S.; Stuart, E. J. E.; Compton, R. G. *Phys. Chem. Chem. Phys.* **2014**, *16*, 616–623.

[7] Silvester, D. S.; Wain, A. J.; Aldous, L.; Hardacre, C.; Compton, R. G. *J. Electroanal. Chem.* **2006**, *596*, 131 – 140.

[8] Zhou, Y.-G.; Rees, N. V.; Compton, R. G. *Chem. Phys. Lett.* **2011**, *514*, 291 – 293.

[9] Cheng, W.; Compton, R. G. *Trend. Anal. Chem.* **2014**, *58*, 79 – 89.

[10] Rees, N. V. *Electrochem. Comm.* **2014**, *43*, 83 – 86.

[11] Miller, C. C. *Proc. R. Soc. A* **1924**, *106*, 724–749.

[12] Yukio, S. *Rev. Polarog.* **1968**, *15*, 177–187.

Chapter 5

Nano-impacts in Room Temperature Ionic Liquids - the role of chloride

To date, the study of nanoparticles *via* the nano-impact methodology has not been reported in RTILs. Theoretical works[1,2] have explored the microscopic interactions of RTILs and nanoparticles, and this Chapter extends this understanding through *experimental* electrochemistry. Additionally, consideration must be given to halide impurities, which are commonly present in RTILs as residual starting materials from the synthetic process, and are known to affect the properties of the ionic liquid, such as density, electrochemical window and viscosity,[3] and, importantly, are also known to alter reaction outcomes.[4–6]

This work demonstrates first how individual nanoparticles can be studied in an ionic liquid environment and second evidences the dominant role of chloride upon the electrochemical response of silver NPs.

This chapter outlines the results of voltammetry of the oxidation of silver nanoparticles in a RTIL with added chloride, in particular the presence of a silver stripping

peak, its growth with time between scans, and the role of chloride on its size. Following this, chronoamperometry is undertaken, and the observed spikes in the current are integrated and sized, and this is contrasted with immobilised silver nanoparticles in ILs.

5.1 Silver Stripping

A carbon microelectrode was immersed into a solution containing [Bmim][BF_4] and 100 mM chloride. A voltammogram was recorded by sweeping the potential from 0 V (vs a silver wire) to 0.5 V at a scan rate of 1000 mV s^{-1}. PEG capped silver nanoparticles (Ag NPs, 2.7×10^{-7} mM) were then added to the solution and another cyclic voltammogram was recorded as above, with a ten minute wait time imposed. Figure 5.1 shows the voltammograms in the absence (black) and presence (red) of the silver nanoparticles. There are no voltammetric features at this potential in the presence of nanoparticles with no chloride in solution.[7] In the presence of the Ag NPs, a peak appears in the forward scan of the voltammogram at *ca.* 0.25 V. The shape is indicative of adsorbed material being oxidised which suggests that the nanoparticles in solution move *via* Brownian motion, arrive at the electrode and adsorb on the surface over time. Upon application of a sufficiently positive potential, the silver nanoparticle ensemble undergoes oxidation to silver chloride, resulting in the presence of a silver stripping peak on the voltammogram. The smooth, continuous nature of the peak indicates that it is an ensemble of NPs undergoing oxidation as opposed to individual NPs. Equation 5.1 shows this reaction pathway, beginning with the oxidation of the silver nanoparticles which then react with the chloride in the solution to form silver chloride.

$$Ag(s) + Cl^- \rightleftharpoons AgCl(s) + e^- \tag{5.1}$$

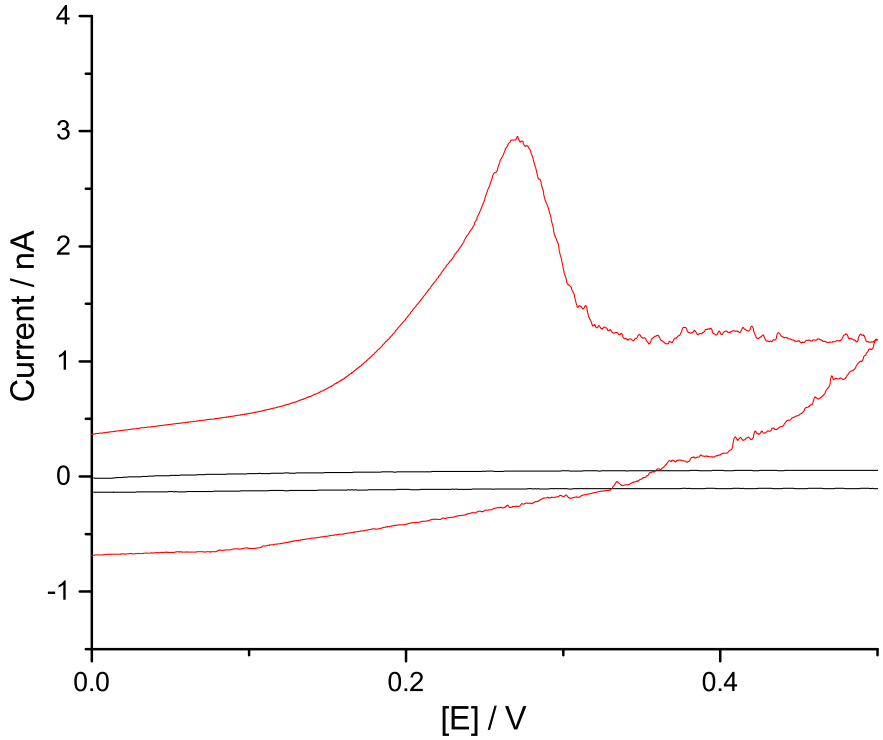


Figure 5.1: Voltammogram of [Bmim][BF_4] and 100 mM chloride in the absence (black) and presence (red) of silver nanoparticles, recorded at 1 V s^{-1} vs a silver wire.

$$AgCl(s) + xCl^- \longrightarrow AgCl_{1+x}^{-x} \tag{5.2}$$

Having electrochemically formed AgCl, the material may react further, resulting in the dissolution of the silver from the surface.[8] Equation 5.2 outlines the dissolution process of the solid silver chloride to higher halides, facilitated by an excess of chloride present in solution.[9] A second scan performed immediately after the first, which shows no peak in the voltammogram in this potential window, evidences this complete dissolution process.

5.2 Time Dependency

To verify that the peak at 0.25 V (vs Ag wire) is as a result of the silver nanoparticles accumulating at the electrode surface, a time dependency study was undertaken. The time between the voltammetric scans was varied to investigate if nanoparticle arrivals affected the size of the peak. Cyclic voltammograms were recorded in a solution of Ag NPs in RTIL containing 100 mM chloride by sweeping the potential from -0.1 V to 0.3 V (vs a silver wire) at a scan rate of 1000 mV s^{-1}. The time between each scan was increased, beginning with 1 min and increasing steadily up to 60 minutes between scans. Figure 5.2 shows the appearance of a peak at 0.24 V that increases with time between scans. The inset in Figure 5.2 shows the analysis of this data, whereby the area under the peak at 0.2 V is integrated to provide a charge that is then converted into a number of nanoparticles. This was achieved through the process outlined in Equations 5.3 and 5.4 (assuming the particles are spherical, with a density (ρ) of 10.5 $\times$ 10 ^{6} gm^{-3}, molar mass (M_R) of 107.9 g mol^{-1} and a radius (r_{NP}) of 10 nm):

$$\frac{\frac{4}{3}\pi r_{NP}^3 \times \rho}{M_R} = \text{mol (NP)} \tag{5.3}$$

$$\text{Number of NPs} = \frac{C_{NP}}{\text{mol (NP)}} \tag{5.4}$$

The curvature in this plot is attributed to aggregation of the silver nanoparticles. Toh *et. al*[10] have shown that aggregation of nanoparticles results in incomplete stripping, which returns a lower current than expected.

The size of the peak (and therefore the number of nanoparticles) increases with time between scans and is a good indication that the oxidative feature corresponds to the accumulation and subsequent stripping of the silver nanoparticles. The close agreement with the expected frequency of nanoparticle arrivals (0.77 Hz), as calculated from a diffusion limited flux, with the number calculated from the total stripping

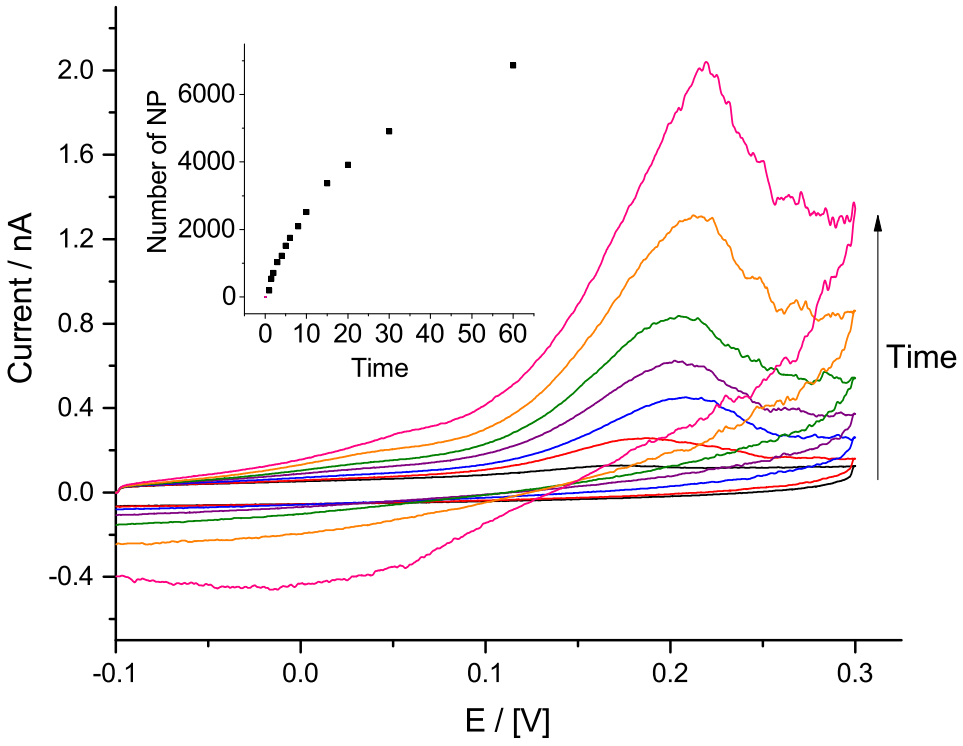


Figure 5.2: Cyclic voltammogram of Ag NPs (2.7×10^{-7} mM) in RTIL with 100 mM chloride, at a scan rate of 1000 mV s^{-1}. Black is 1 min resting between scans at open circuit potential, whilst red is 2 min, blue is 4 mins, purple is 6 mins, green is 10 mins, orange is 20 mins and pink is 60 mins. The inset shows the analysis of this data, with each peak integrated to provide a charge, which is then converted into a number of nanoparticles vs time in minutes.

charge (1.3 Hz) evidences oxidation of the entire nanoparticle, rather than a surface layer oxidation, such that with increasing time, more nanoparticles arrive and adsorb at the surface, and upon the application of a sufficiently positive potential, they undergo oxidation to silver chloride.

5.3 Chloride Concentration Effects

To further evidence the dependence of the electrochemical response on the chloride concentration, the concentration of chloride in solution was decreased and size of the stripping peak was monitored. A carbon microelectrode was immersed in a solution containing silver nanoparticles (2.4×10^{-7} mM) and 125 mM chloride in [Bmim][BF_4]. A cyclic voltammogram was then recorded by sweeping the potential from 0 V (vs a silver wire) to 1.5 V at a scan rate of 10 mV s^{-1}. Two peaks were observed - a small peak at 0.05 V, and a large peak at +0.8 V, as shown in Figure 5.3. The peak corresponding to the stripping of the silver nanoparticles shifts with scan rate, due to the slow kinetics of the Ag/Ag^+ couple in RTILs.[11] The use of silver wire, acting as a pseudo reference electrode, may also result in a small amount of variation of potential. The large peak at +0.8 V is attributed to the oxidation of chloride. This reaction has been previously documented in this ionic liquid on a carbon-based electrode.[12]

Four samples were prepared with varying volumes of chloride added to the IL (6 μL [105 mM], 4 μL [80 mM], 2 μL [47 mM], and a sample with no added chloride). Cyclic voltammograms were recorded, and the peak at 0.05 V was monitored, as shown in Figure 5.4. The peak remained the same size at a concentration of 100 mM chloride or above, but scaled in size as the volume of chloride added was reduced. In the solution with no added chloride, there was no discernible peak at 0.05 V, as is consistent with previous literature.[7] The inflection in the sample with no added chloride is due to existing chloride impurities (estimated from the steady state current to be approximately 10 mM), where the oxidation is limited by the insufficient concentration of chloride. Due to the synthetic method,[13] chloride impurities are omnipresent,[3,12,14,15] and each batch prepared will naturally vary in the amount of chloride present. In particular, chloride impurities tend to be higher in hydrophilic ionic liquids, such as [Bmim][BF_4], due to the less effective washing with dichloromethane compared with water.[16] Figure 5.3 shows the plot from 0 V to 1.5 V, whilst Figure 5.4 focuses on

the peak at 0.05 V.

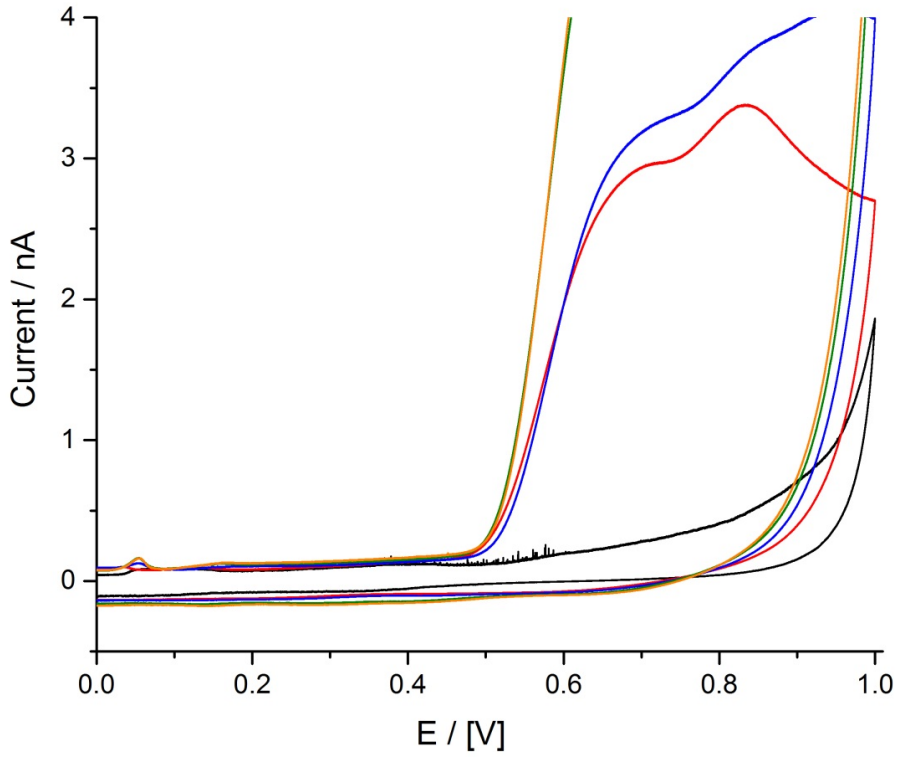


Figure 5.3: Cyclic voltammograms of Ag NPs in [Bmim][BF4], recorded at 10 mV s^{-1}. Black is in the absence of chloride, red 2 μL, blue 4 μL, green 6 μL, and orange 8 μL.

The peak reaching a maximum at 100 mM chloride concentration suggests that the process driving the appearance of the peak is limited by the presence of the silver nanoparticles.

5.4 Electrochemical Sizing

Having evidenced the ability to electrochemically detect the presence of the silver nanoparticles in the IL by adsorption and stripping of the silver material in the

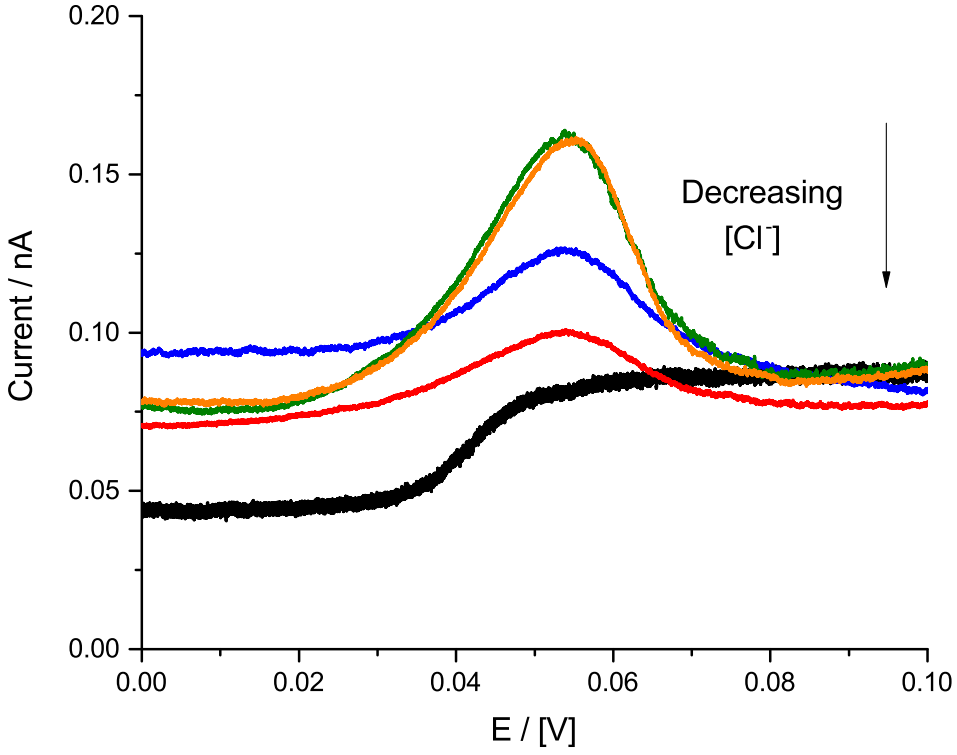


Figure 5.4: Cyclic voltammogram, recorded at 10 mV s^{-1}, of Ag NPs in RTIL with decreasing chloride concentration, whereby the black line is with no added chloride, and red 2 μL (47 mM), blue 4 μL (80 mM), green 6 μL (105 mM), and orange 8 μL (125 mM).

presence of chloride, the work now turns to investigating the stochastic detection of individual silver nanoparticles impacting upon the electrode. In order to fully understand the possible mechanism operating, the CV was recorded to a slightly more positive potential (0.5 V) at a slow scan rate. The potential was thus swept from 0 V to 0.5 V vs a silver wire at 10 mV s^{-1}. Figure 5.5 shows a CV with a stripping wave, which appears at 0.1 V, and spikes in current, which appear after the onset of the continuous wave, at ca. 0.15 V, and disappear on the reverse scan at 0.15 V. The stripping wave at 0.1 V is attributed to the electrochemical ensemble response of the silver nanoparticles that have absorbed to the electrode surface, and are oxidised

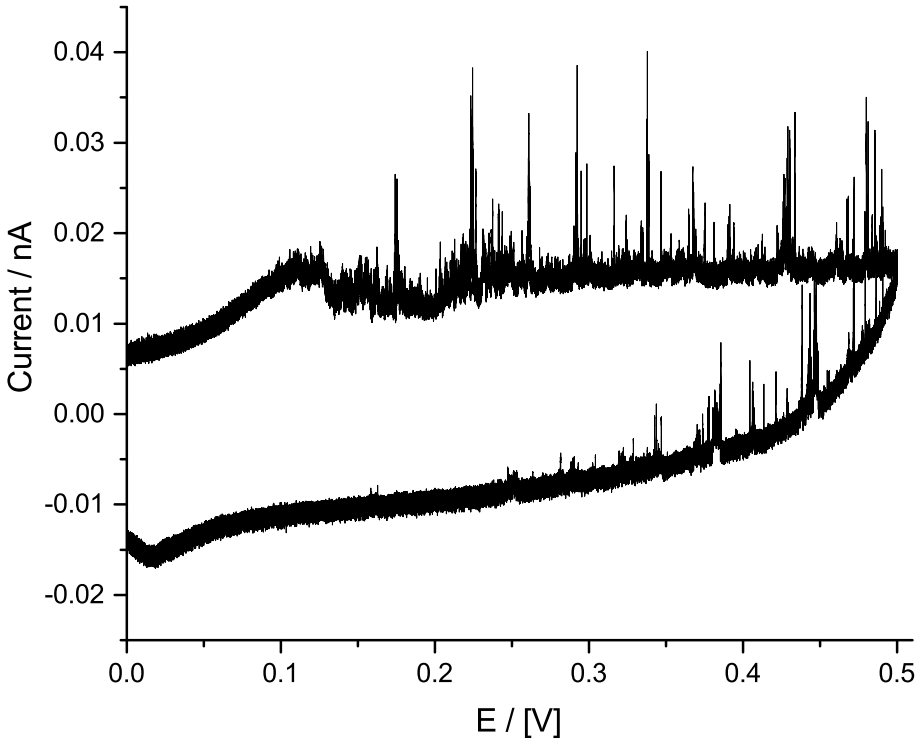


Figure 5.5: Cyclic voltammogram of silver nanoparticles in [Bmim][BF_4] with 100 mM chloride at a scan rate of 10 mV s^{-1}.

simultaneously. In contrast, the individual spikes in current arising after the stripping wave may relate to individual nanoparticles arriving at the electrode and undergoing oxidation. To confirm that the spikes in current represent individual nanoparticles, a series of chronoamperograms were performed by holding the potential at 0.4 V vs a silver wire for 120s. A representative chronoamperogram is shown in Figure 5.6, with two of the features highlighted. By integrating the area underneath the spike in current to yield the charge, this can be converted to calculate the size of the NP (by assuming that the nanoparticles are spherical and by using Faraday's first law). From converting the charge to radii from 267 features across 18 chronoamperograms, the nanoparticles were calculated to be 7.6 $\pm$ 3.7 nm in radius. This is consistent with

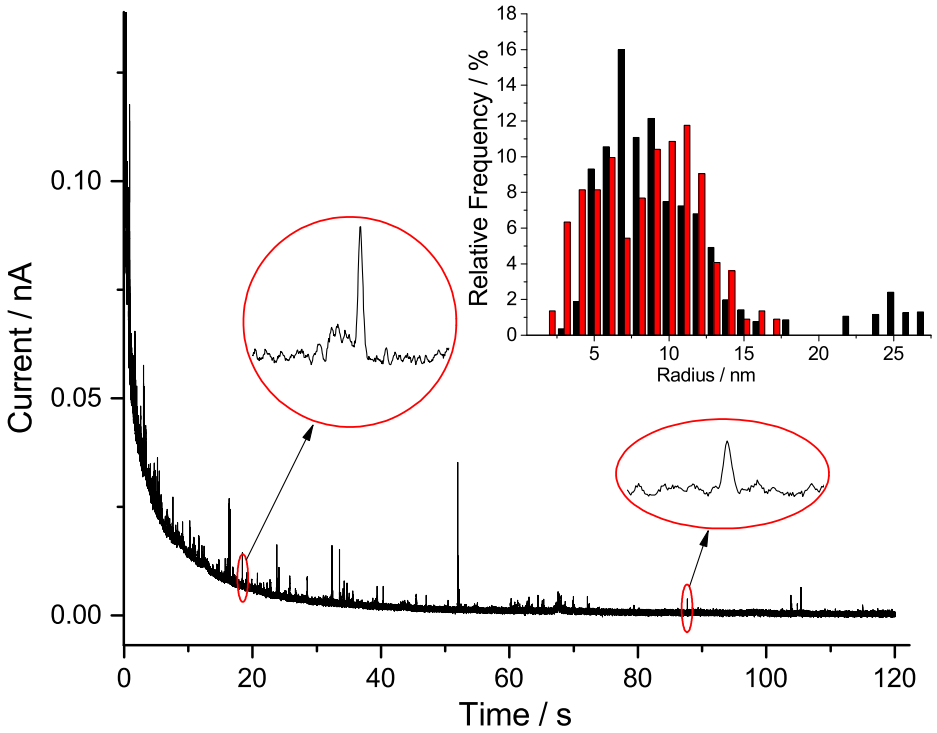


Figure 5.6: A representative chronoamperogram recorded at 0.4 V for 120 s, with two features highlighted. Inset is a sizing histogram of the electrochemical sizing method (black) compared with SEM Sizing[17] (red).

other sizing techniques (SEM) previously reported[17] on this batch of nanoparticles, which gave 8.5 ± 3.5 nm as the radii.

The inset of Figure 4.9 shows a sizing histogram with the diffusion-weighted[18] sizes from impacts being shown in black, and SEM sizing[17] shown in red. The size distribution histograms are in good agreement, suggesting that electrochemical sizing of silver nanoparticles in the ionic liquid has been successful.

5.5 Mechanism

To establish the nature of the impacts witnessed in this study, the time between scans was varied. Chronoamperograms were recorded by holding the potential at 0.4

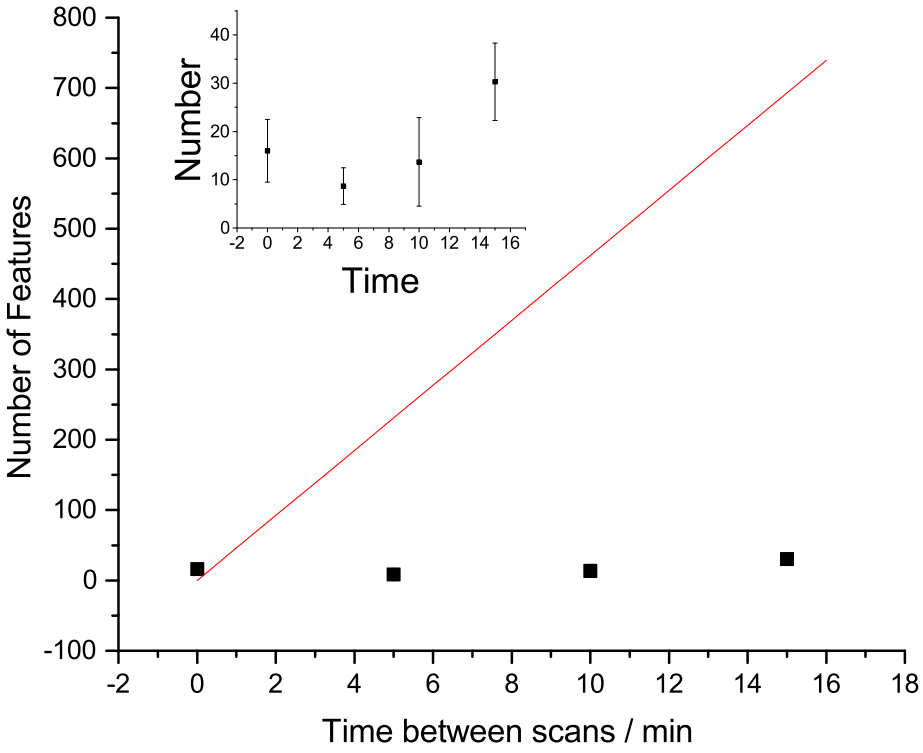


Figure 5.7: Average number of impacts observed after a stated modification time at open circuit potential (black squares, average of 7 features observed in a 120 s time period) and an expected frequency from a steady-state approximation (red line). Inset is the experimental data close-up.

V for 120 s. The time in between each scan was varied at random, and each time point was repeated at minimum in triplicate. The number of impacts with respect to modification time is shown in Figure 5.7. The red line represents the expected theoretical number of features for the situation in which the NPs are accumulating on the electrode surface from a steady-state approximation, as shown in Equation 5.5. This generates the expected number of nanoparticles, if we assume that the nanoparticle's

arrival is determined by the diffusion coefficient and the concentration, and that every nanoparticle that arrives undergoes oxidation. N_A is the Avogadro constant, D is the diffusion coefficient of the nanoparticle (calculated through the Stokes-Einstein equation: 2.4×10^{-13} m^2 s^{-1}), C_{NP} is the concentration of the nanoparticles (2.7×10^{-7} mM), r is the radius of the electrode, and t is time in seconds.

$$N = 4N_A D C_{NP} r t \tag{5.5}$$

In the previous chapter, in the absence of chloride, time modification dependence was one of the key pieces of evidence towards a polymer-gated mechanism, whereby surface immobilised PEG capped Ag NPs underwent a reversible 'unwrapping' phase before undergoing an irreversible oxidation. In the presence of chloride, the observed spike frequency is time-independent, evidencing that the impacts observed herein are not the result of a polymer-gated oxidation mechanism. Rather, the spikes in the current appear to be a result of a mechanism that is akin to that seen in aqueous solvents - the nanoparticle diffuses to the electrode *via* Brownian motion, and undergoes electron transfer as it makes tunnelling contact with the electrode surface, providing the latter is held at a sufficient potential to allow the electrochemical process to occur. This switch in mechanism results from the addition of chloride, which allows bypassing of the polymer rearrangement process that is necessary in the absence of chloride. Figure 5.8 shows the mechanism in the presence of chloride. The reaction of the oxidised silver to silver chloride occurs at a lower overpotential than the dissolution of Ag^+, and this process occurs without the need for the polyethylene glycol molecules to rearrange to allow access to the silver core.

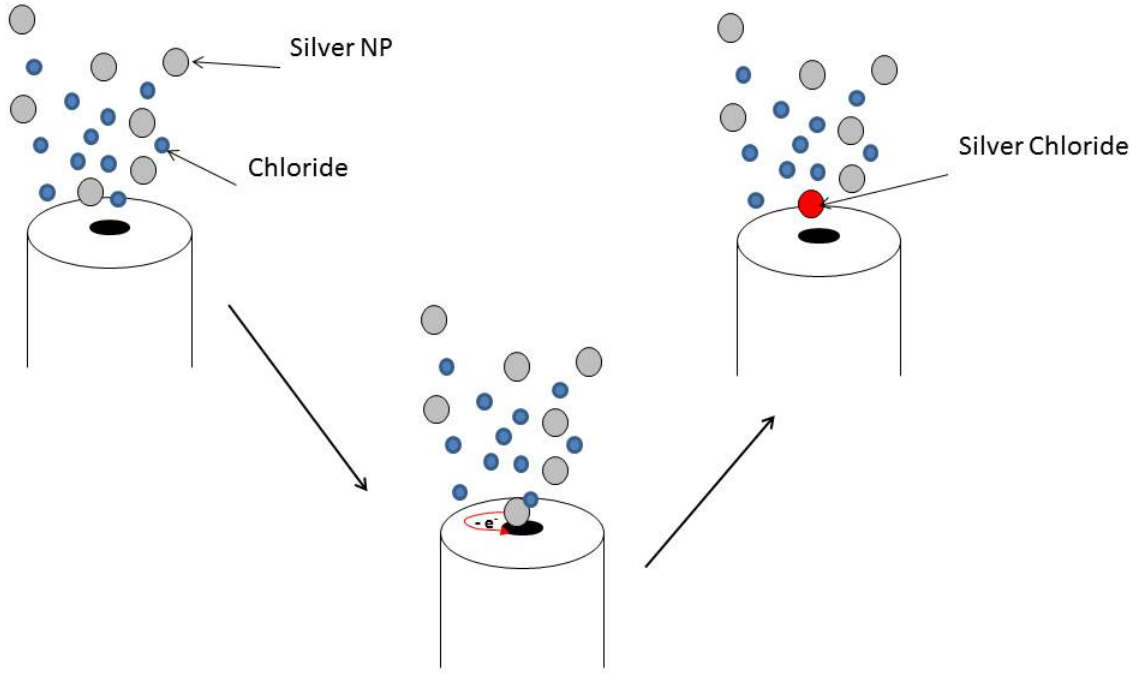


Figure 5.8: Schematic outlining the oxidation of silver nanoparticles to silver chloride, first with nanoparticles arriving at the electrode *via* Brownian motion, second undergoing electron transfer, and lastly forming silver chloride.

5.6 Conclusions

This chapter has evidenced that the observation of direct oxidation of silver nanoparticles via 'nano-impacts' has been shown for the first time in a RTIL. The presence of chloride facilitates this oxidation, allowing the polymer rearrangement required in the absence of chloride through the oxidation of the silver to silver chloride. This study was the first to extend the nano-impact methodology to an ionic solvent, extending nanoparticle analysis to RTILs and exploring the dominant role of chloride in affecting reaction mechanisms. The following chapter explores the role of the capping agent in affecting the mechanism of oxidation of Ag NPs.

References

[1] Cheng, P.; Liu, C.; Yang, Y.; Huang, S. *Chem. Phys.* **2015**, *452*, 1–8.

[2] He, Z.; Alexandridis, P. *Phys. Chem. Chem. Phys.* **2015**, *17*, 18238–18261.

[3] Seddon, K. R.; Stark, A.; Torres, M. J. *Pure Appl. Chem.* **2000**, *72*, 2275–2287.

[4] J. Dyson, P.; J. Ellis, D.; Welton, T.; G. Parker, D. *Chem. Commun.* **1999**, 25–26.

[5] Anderson, K.; Goodrich, P.; Hardacre, C.; Rooney, D. W. *Green Chem.* **2003**, *5*, 448–453.

[6] Hu, S.; Wang, Z.; Qu, F.; Chu, T.; Wang, X. *J. Phys. Chem. A* **2011**, *115*, 13452–13466.

[7] Tanner, E. E. L.; Tschulik, K.; Tahany, R.; Jurkschat, K.; Batchelor-McAuley, C.; Compton, R. G. *J. Phys. Chem. C* **2015**, *119*, 18808–18815.

[8] Levard, C.; Mitra, S.; Yang, T.; Jew, A. D.; Badireddy, A. R.; Lowry, G. V.; Brown, G. E. *Environ. Sci. Technol.* **2013**, *47*, 5738–5745.

[9] Chambers, B. A.; Afrooz, A. R. M. N.; Bae, S.; Aich, N.; Katz, L.; Saleh, N. B.; Kirisits, M. J. *Environ. Sci. Technol.* **2014**, *48*, 761–769.

[10] Toh, H. S.; Batchelor-McAuley, C.; Tschulik, K.; Uhlemann, M.; Crossley, A.; Compton, R. G. *Nanoscale* **2013**, *5*, 4884–4893.

[11] Rogers, E. I.; Silvester, D. S.; Jones, S. E. W.; Aldous, L.; Hardacre, C.; Russell, A.; Davies, S. G.; Compton, R. G. *J. Phys. Chem. C* **2007**, *111*, 13957–13966.

[12] Villagrán, C.; Banks, C. E.; Hardacre, C.; Compton, R. G. *Anal. Chem.* **2004**, *76*, 1998–2003.

[13] Bonhote, P.; Dias, A. P.; Papageorgiou, N.; Kalyanasundaram, K.; Gratzel, M. *Inorg. Chem.* **1996**, *35*, 1168–1178.

[14] Tsuda, T.; Hussey, C. L. *Modern Aspects of Electrochemistry, No. 45*; Springer, 2009; pp 63–174.

[15] Peter Wasserscheid, T. W. In *Ionic Liquids in Synthesis*; Peter Wasserscheid, T. W., Ed.; Wiley-VCH: Weinheim, 2003; Chapter 53.

[16] Wasserscheid, P., Welton, T., Eds. *Ionic Liquids in Synthesis*; Wiley-VCH Verlag GmbH: Hoboken, 2014.

[17] Lees, J. C.; Ellison, J.; Batchelor-McAuley, C.; Tschulik, K.; Damm, C.; Omanović, D.; Compton, R. G. *Chem. Phys. Chem.* **2013**, *14*, 3895–3897.

[18] Sokolov, S. V.; Batchelor-McAuley, C.; Tschulik, K.; Fletcher, S.; Compton, R. G. *Chem. Eur. J.* **2015**, *21*, 10741–10746.

Chapter 6

Capping Agent Controlled Electron Transfer Dynamics

Of particular interest to understanding the microscopic interactions of the NP with the solvent is the effect of the capping agent. The capping agent is used to partially stabilise the nanoparticle, and can alter its properties and behaviour.[1] Gold NPs have been shown to display different interactions with a gelatine substrate based on their capping agents,[2] whilst the catalytic effect of nano-Pt has been reported to be affected by the capping agent.[3]

As outlined in Part I, there are multiple ways that the capping agent can stabilise the NP, and poly(ethylene) glycol (PEG), is used as a capping agent because of the steric hindrance it provides. Steric stability enables the NP to survive in high ionic strength environments, and so PEG is the capping agent of choice in a wide range of applications.[4] In the medical field, the length of the PEG chain has been manipulated in a range of studies,[5–7] and for example can affect nanoparticle uptake into cells, and reduce macrophage interception.[8] The molecular weight of the PEG capping has also been shown to strongly influence plasma protein adsorption, and therefore how long nanoparticles are able to persist in the bloodstream.[9]

A number of studies have been undertaken in aqueous solvents to attempt to gain a deeper understanding of changes in dynamics as a result of a change in the capping agent.[1,10] Given that it is likely modification of the capping agent will result in a change in dynamics, undertaking a systemic study of the affects of modifying the PEG capping agent will allow insight into the microscopic and nanoscopic interactions, and provide more information about the polymer-gating mechanism previously proposed. This chapter provides an experimental investigation into the role of the capping agent in affecting the dynamics of electron transfer of Ag NPs in a RTIL demonstrating the critical role the capping agent plays in the mechanism of electron transfer. The previous two chapters have outlined work with 5000 MW PEG capped Ag NPs - this chapter extends this work in a systematic way. This is achieved through modification and subsequent characterisation of silver nanoparticles in water using Dynamic Light Scattering (DLS) and UV-Vis spectrophotometry. This is followed by transfer of the PEG capped NPs (2000, 6000, and 10,000 MW) into [Bmim][BF_4], which was also characterised using UV-Vis spectrometry. Finally, electrochemistry is undertaken in the form of chronoamperometry on the samples, the outcome of which is sizing of the nanoparticles, and insight into the mechanism of oxidation.

6.1 Modification of nanoparticles

The silver nanoparticles capped with citrate were recapped with poly(ethylene) glycol of increasing molecular weights (2000, 6000, 10,000) before any analysis was undertaken. This was achieved by combining dissolved samples of thiolated PEG in water with citrate capped nanoparticles, mixing the samples thoroughly, and allowing the capping agent replacement to occur over the period of 30 minutes. Two analysis techniques were undertaken to monitor this modification, which will be outlined below. UV-Vis was also used to monitor the transfer of modified nanoparticles from water

into a RTIL so that electrochemical analysis could be undertaken.

6.1.1 Dynamic Light Scattering

DLS was used to track the recapping of the nanoparticles with the variously weighted PEG molecules by monitoring the size of the nanoparticles' hydrodynamic radii. The analysis, shown in Figure 6.1, returned hydrodynamic radii (Z-averages) of 29.3 ± 0.1 nm for the unmodified, citrate capped nanoparticles, 29.7 ± 0.4 nm for the nanoparticles recapped with 2000 MW PEG, 37.3 ± 0.4 nm for the 6000 MW recapped sample, and 51.7 ± 0.1 nm for the 10,000 MW PEG Ag NPs. The Polydispersity Index (PdI) for all measurements was ≤ 0.2, indicating that the sample was monodispersed. The

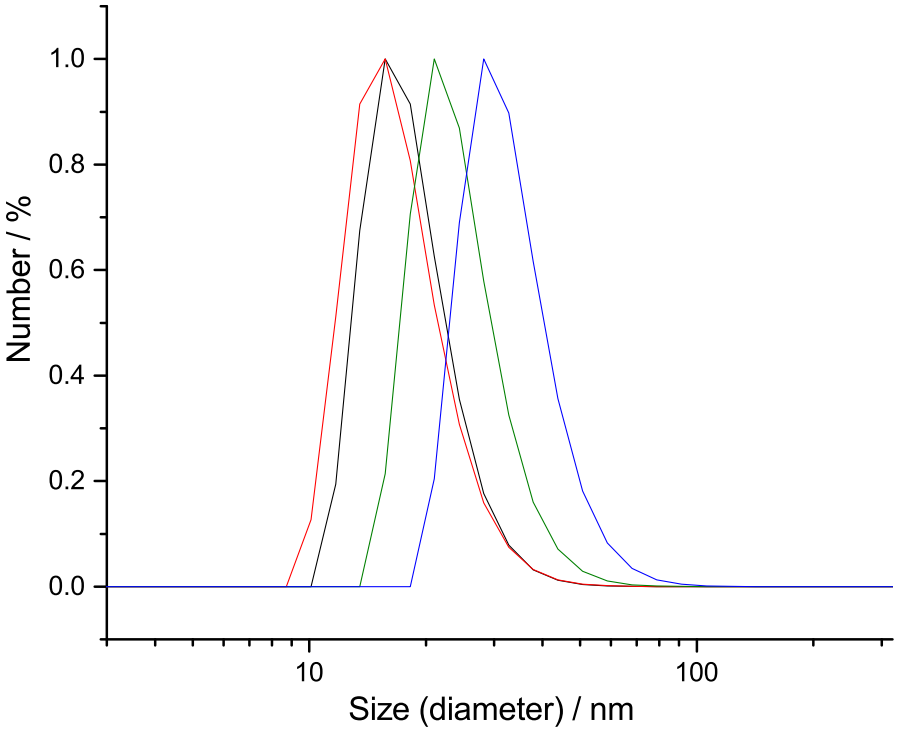


Figure 6.1: Normalised Dynamic Light Scattering (DLS) analysis of citrate capped Ag NPs, 2000 MW PEG capped Ag NPs, 6000 MW PEG capped Ag NPs, and 10,000 MW PEG capped Ag NPs.

hydrodynamic radii provide a measurement of the combined thickness of the capping agent layer and the core size. As the molecular weight of the PEG molecule increases, there is a significant increase in the observed size of the nanoparticle. This suggests that the modification was successful, and that the PEG chains are not simply binding more tightly in the case of the larger molecular weights, allowing insight into the affect of a thicker capping agent layer on the electron transfer kinetics.

6.1.2 UV-Vis Spectrometry

UV-Vis spectrophotometry was used to examine the plasmon peak resonance of the silver nanoparticles, which was reported to be at 400 nm for PEG capped silver nanoparticles in water in Chapter 4. A shift or absence of the plasmon peak can indicate that aggregation or dissolution has occurred, and so UV-Vis spectrometry is a reliable method of establishing that nanoparticles remain in solution. In water, the citrate capped nanoparticles reach their maximum absorption at 392 nm, whilst all three of the PEG capped nanoparticles absorb maximally at 396 nm, as shown in Figure 6.2. Although small, this nevertheless clear shift further evidences the successful recapping of the nanoparticles.

In ionic liquid, the plasmon becomes much broader than the plasmon observed in water, and the maximum absorbance occurs at 412 nm. The existence of a plasmon peak in the IL evidences the successful recapping and transfer into RTIL. In contrast, the UV-Vis spectrometry of citrate capped Ag nanoparticles, or lack thereof, which was reported in Chapter 4, demonstrates that the citrate capped NPs are not stable in an ionic liquid environment.

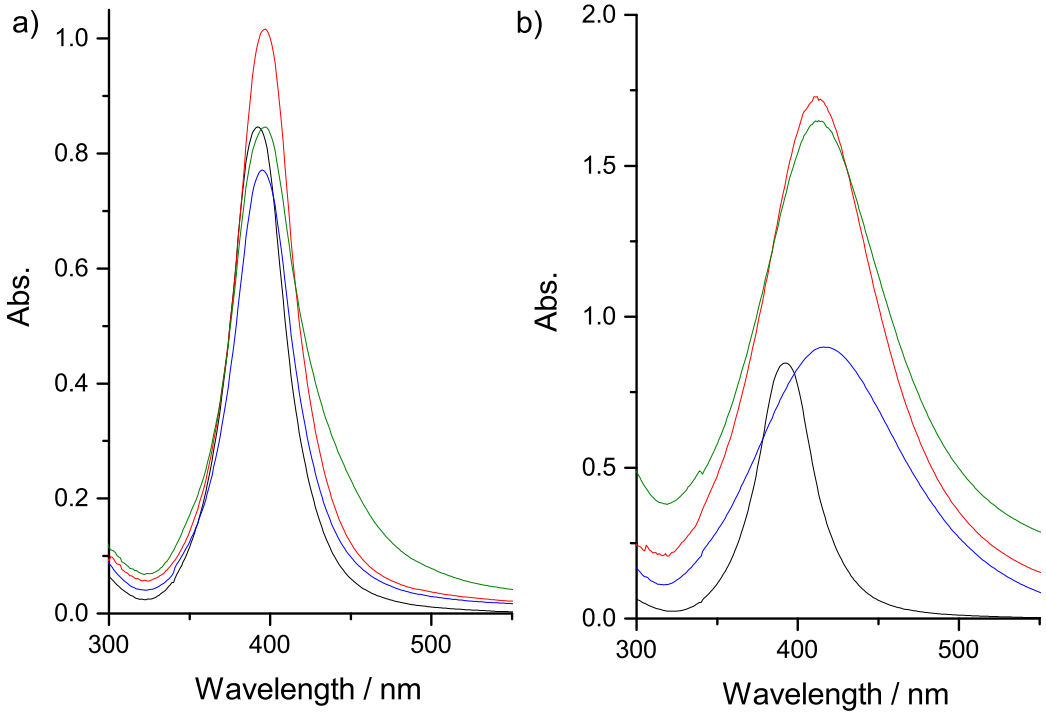


Figure 6.2: UV-Vis spectra of a) citrate, 2000 MW PEG (red), 6000 MW PEG (green), and 10,000 MW PEG (blue) capped silver nanoparticles in water, at a concentration of 3.0 $\times$ 10^{-7} mol m^{-3} and b) citrate capped in water for comparison with 2000 MW PEG, 6000 MW PEG, and 10,000 MW PEG capped silver nanoparticles in [Bmim][BF_4] at a concentration of 9.3 $\times$ 10^{-7} mol m^{-3}.

6.2 Electrochemistry

The nanoparticles solvated in the ionic liquid, still under vacuum, were transferred into a glovebox, and an aliquot (10 μL) of 2000 MW PEG in RTIL was placed onto a microcarbon working electrode (of radius 3.55 μm), with a silver wire (as a counter and pseudo reference electrode) also immersed. The use of a pseudo-reference electrode may result in a variation in potential necessary to observe oxidation, and the potential was varied ($\pm$ 0.1 V) in the subsequent experiments to reflect this possibility. Chronoamperometry was then performed by holding the potential at 1.7 V for 50 s. Upon application of a sufficiently positive potential, spikes in the current appear

during the course of the chronoamperogram. A series of chronoamperograms were recorded in order to obtain a sufficient number of spikes for analysis. This procedure was repeated with the nanoparticles capped with 6000 MW PEG and 10,000 MW PEG, holding the potential at 1.7 V for 300 s and at 1.6 V for 600 s respectively. Figure 6.3 shows representative chronoamperograms of each molecular weight.

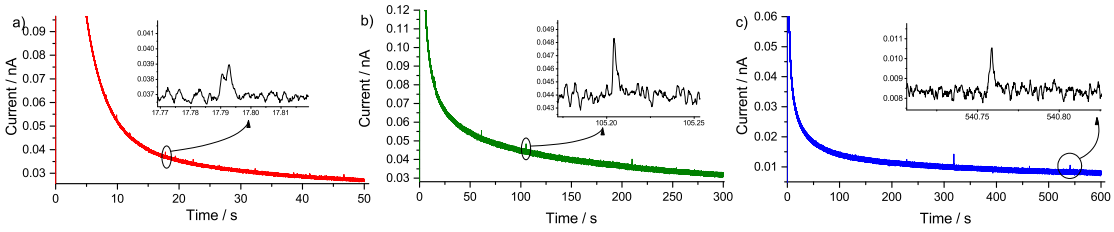


Figure 6.3: Representative chronoamperograms of silver nanoparticles capped with a) 2000 MW PEG, recorded at 1.7 V for 50s, b) 6000 MW PEG recorded at 1.7 V for 300 s, and c) 10,0000 MW PEG, recorded at 1.6 V for 600 s. Each inset is one highlighted feature from the given chronoamperogram.

6.2.1 Electrochemical Sizing

The spikes in the current observed in the chronoamperograms were integrated, and the charge converted to an equivalent radius (by applying Faraday's first law, and by assuming the particles to be spherical). The 2000 MW nanoparticles had a mean radius of 7.8 ± 1.3 nm (where the uncertainty is taken from the standard deviation of radii), whilst the 6000 MW NPs are sized at 7.9 ± 3.3 nm, and the 10,000 MW particles are 8.78 ± 4 nm. This is in excellent agreement with previous SEM sizing of this batch of nanoparticles,[11] which provided a radius of 8.5 ± 3.5 nm. Figure 6.4 shows the distribution of sizes in each sample as measured electrochemically, which are in excellent agreement with one another and are over a small range of values. This indicates that the electrochemical sizing of the nanoparticles is not influenced by capping with variously weighted PEG, and that each spike corresponds to a single nanoparticle silver core undergoing full oxidation. However, the frequency

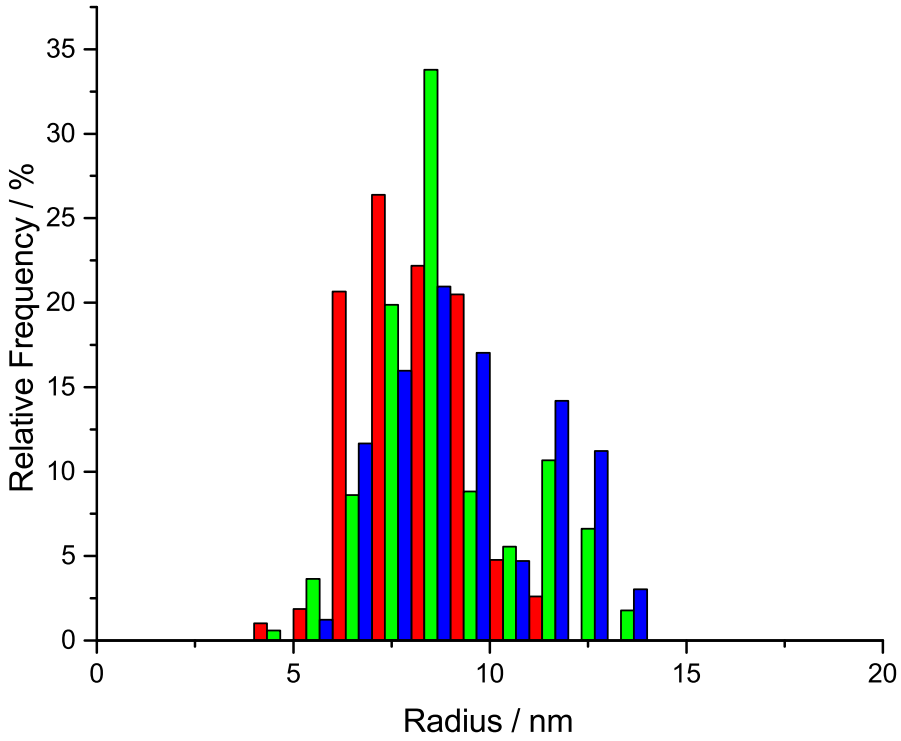


Figure 6.4: Sizing histogram displaying the relative frequencies of silver nanoparticles capped with 2000 MW PEG (n = 112), 6000 MW PEG (n = 112), and 10,000 MW PEG (n = 90).

of the impacts differed across samples of the same concentration of nanoparticles with different molecular weights. The implications of the variable frequency and the existence or absence of a time dependency is next discussed.

6.2.2 Time Dependency and Frequency

To establish if the 2000 MW PEG NPs are accumulating at the electrode surface, and therefore could be said to demonstrate the same modification time dependency as observed in Chapter 4 in the case of the 6000 MW PEG capped NPs, the time at open circuit potential between scans was systematically varied from 5 to 30 minutes.

For consistency, this was also repeated using the 6000 MW PEG. The 10,000 MW PEG returned such a low frequency of impacts that the presence or absence of a time dependency is unclear. In contrast, Figure 6.5 shows the average number of spikes observed per second over three chronoamperograms recorded at 1.7 V with the stated modification time in place between scans. The 6000 MW PEG, as previously

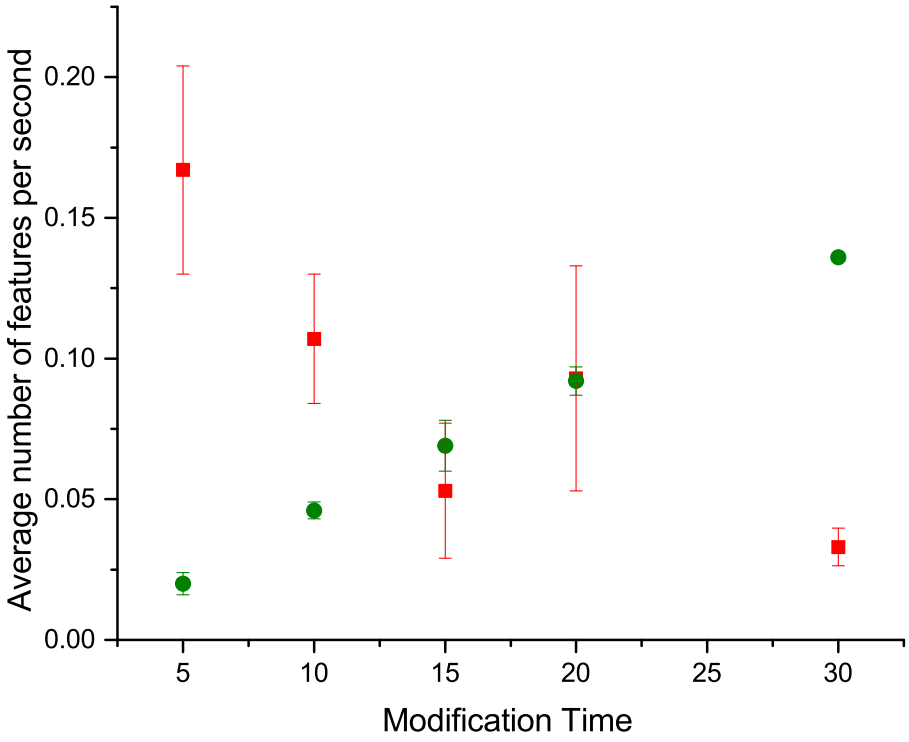


Figure 6.5: Average number of impacts observed per second after a stated modification time at open circuit potential of 2000 MW PEG Ag NPs (square), and 6000 MW PEG (circle). Errors shown are Standard Error of the Mean.

reported in Chapter 4, show a linear relationship between the number of features and the modification time, reflecting accumulation of material at the electrode surface. In contrast, the 2000 MW PEG display a random distribution of the number of features per second with modification time, suggesting that there is no accumulation of the 2000 MW PEG NPs at the electrode. To establish the frequency of impacts,

beginning with the 2000 MW NPs, the number of features observed per second of chronoamperogram was averaged across all scans. This gave a frequency of impacts of 0.07 s^{-1}. In the calculation of the frequency of both the 6000 MW and 10,000 MW PEG NPs, the modification time imposed was taken into account, returning frequencies of 0.02 s^{-1} and 0.007 s^{-1} respectively. The increase in the Stokes radius of the nanoparticle will result in a smaller diffusion coefficient, and thus it is not inconsistent with the observed decrease in frequency with increasing molecular weight of the capping agent. However, the differing time dependencies of the 2000 and 6000 MW NPs suggests that the capping agent is differently implicated in its role in the electron transfer process.

6.3 Mechanism

The modification time dependency observed in the frequency of features of the 6000 MW PEG Ag NPs is consistent with a polymer-gating mechanism, as previously established for experiments using PEG NPs in Chapter 4. This mechanism involves an accumulation period, whereby nanoparticles diffuse to and arrive at the electrode. Once adsorbed the the electrode, the NPs then undergo a reversible partial 'unwrapping' process, where the polymer capping the nanoparticle partly uncoils. Once the large polymer has unwrapped sufficiently so it no longer prohibits electrical contact with the silver core, electron transfer can occur, resulting in an irreversible oxidation of the silver core to Ag^+. The key piece of evidence for this mechanism is the modification time dependency, which reflects accumulation of nanoparticles at the electrode surface, where the number of oxidative features observed correlates to the length of time the electrode submerged in the solution is held at open circuit potential, allowing the nanoparticles to 'unwrap' at the electrode surface. Moreover, if the polymer did not inhibit the electrochemical process, then any pre-adsorbed nanoparticles should

be oxidised within the first 10s of milliseconds after application of an anodic potential to the working electrode. As can be seen from Figure 6.3, the oxidative features corresponding to the NP oxidation are found to occur stochastically on the timescale of seconds to minutes after the start of the chronoamperogram. The accumulation of the nanoparticles is critical to this mechanism, as this demonstrates the role of the capping agent in 'gating' the electron transfer process.

In the case of the 2000 MW nanoparticles, no such time dependency is observed. This suggests that in the case of NPs with lower weight capping agents, the PEG does not appreciably hinder electron transfer. This is supported by the DLS results, which show that the 2000 MW NPs are equivalently sized to the citrate capped NPs, but smaller than the higher-weighted PEG NPs. The oxidation observed in this case is comparable to a 'nano-impact' mechanism, previously observed in aqueous systems, where the capping agent does not play a significant role in the oxidation.[12] This mechanism involves diffusion of the NP to the electrode (*via* Brownian motion), followed by the NP making contact with the electrode held at a sufficiently positive potential, and finally, oxidation of the NP to Ag^+. 'Nano-impacts' are characterised by a random frequency of spikes at each modification time, as there is no preaccumulation time.[13,14] This lack of nanoparticle accumulation is further evidenced by the absence of a stripping wave in a cyclic voltammogram after a waiting period of 15 minutes (see Figure 6.6). Figure 6.7 is a schematic illustrating the two proposed mechanisms.

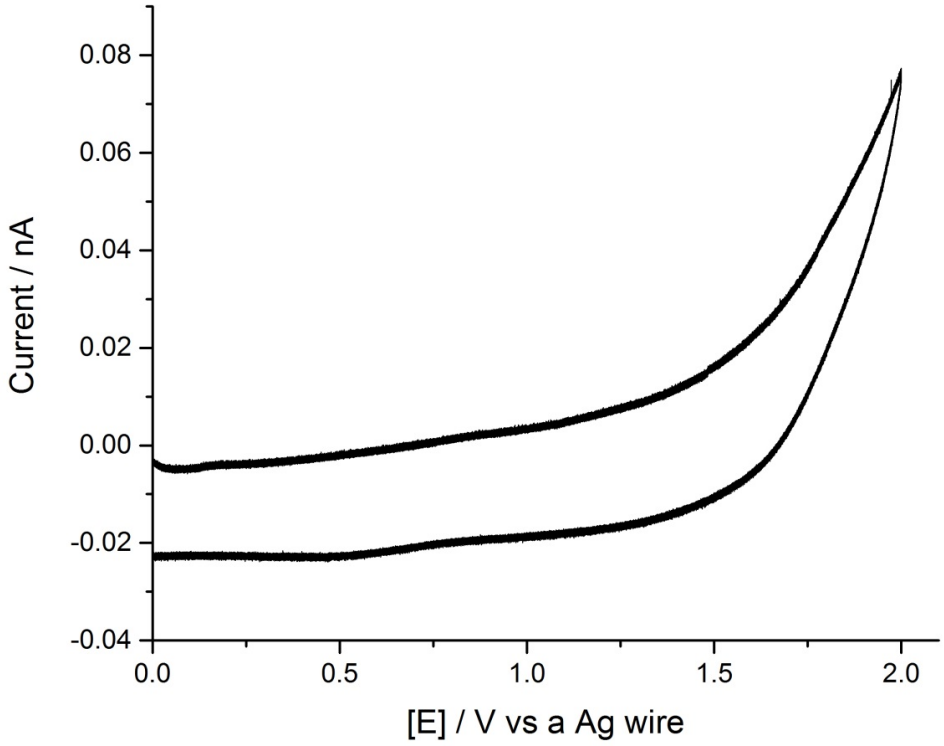


Figure 6.6: A Cyclic Voltammogram of 2000 MW PEG Ag NPs after a 10 min wait period measured at 10 mV s^{-1} on a microcarbon electrode with a silver wire (pseudo-reference and counter electrode).

The 10,000 MW PEG capped nanoparticles experience such a low frequency of oxidation such that it is not possible to conclusively discern the operative electrochemical mechanism. However, it is clear that the very large capping agent component blocks electron transfer with the silver core, such that a large proportion of the nanoparticles are rendered electrochemically inactive. This, combined with the larger Stokes radius of the molecule, results in a very low observed frequency. This differentiation evidences that the composition of the capping agent may be manipulated to control the mechanism by which the NP undergo electron transfer, and corroborates the role of the capping agent in 'gating' the reaction in the case of the higher weight PEG capping agents. This chapter has demonstrated that the manipulation of the cap-

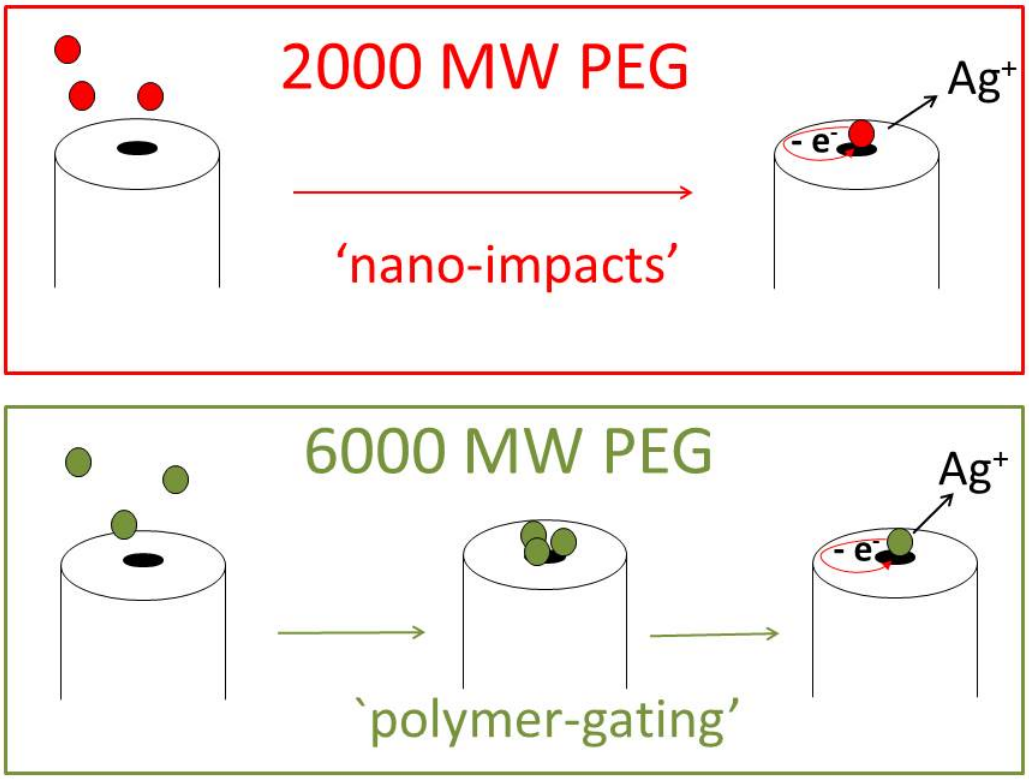


Figure 6.7: Schematic outlining the two proposed mechanisms of oxidation of silver nanoparticles to Ag^+, with the 2000 MW PEG oxidation progressing unhindered by the polymer (nano-impacts) and the 6000 MW PEG undergoing a polymer-gated oxidation.

ping agent characteristics, in this case, the molecular weight of poly(ethylene) glycol molecules, facilitates a controlled shift in mechanism of electron transfer of nanoparticles in RTILs. It has been shown that the capping agent plays a large role in electron transfer dynamics, and that the nanoparticles' electrochemical behaviour can shift with relatively minor changes made to the capping agent.

6.4 Conclusions

This chapter demonstrated that the frequency of nanoparticle oxidation is limited as the molecular weight of the PEG chains is increased, from 0.07 s^{-1} for the 2000 MW NPs, to 0.02 s^{-1} and 0.007 s^{-1} for the 6000 and 10,000 MW NPs respectively, as is consistent with an increase in the Stokes radius, and a shift from 'nano-impact' to 'polymer-gating' mechanisms is observed moving from 2000 MW to 6000 MW PEG Ag NPs.

6.5 Part IV Conclusions

Part IV detailed the exploration of nanoparticle oxidation in RTILs, by examining the oxidation of silver nanoparticles in [Bmim][BF_4]. The polymer-gated oxidation of the silver nanoparticles was elucidated in Chapter 4. This mechanism was evidenced by the presence of a time dependency, suggesting that the polymer coating needs time to 'unwrap' before the silver core is accessible for electron transfer with the electrode. This chapter reported the novel stochastic oxidation of Ag NPs from an assembly, and demonstrated the use of preconcentration of the electrode at OCP prior to applying a potential to see increased numbers of features. Considering the role of chloride, Chapter 5 reported direct nano-impacts to be observed for the first time in RTILs. The presence of the chloride shifts the potential at which the silver oxidation is observed, and is attributed to the oxidation of silver to silver chloride in lieu of Ag^+. To examine the effect of the polyethylene glycol capping agent on the oxidation process, Chapter 6 examined Ag NPs capped with 2000, 6000, and 10,000 MW PEG. The frequency of oxidative features decreased with the weight of the capping agents, with frequencies of 0.07 s^{-1}, 0.02 s^{-1}, and 0.007 s^{-1} reported for the 2000, 6000, and 10,000 MW respectively. A shift of mechanism was observed in moving from the 2000MW PEG to the 6000MW PEG, with nano-impacts being replaced by polymer-

gating as the molecular weight increases.

This Part has served to give an account of the first studies of Ag NPs in a RTIL, and detail the mechanism of oxidation, the role certain impurities can play, and the impact of the capping agent. It was found that the presence of chloride and the length of the capping agent can affect the mechanism of oxidation, with two possible mechanisms - nano-impacts and polymer-gated oxidation - being discussed. More broadly, this work serves to open the possibilities of the use of RTILs and NPs in combination, which may prove more powerful than use of one material alone. In particular, their use in combination when considering catalysis of industrially or environmentally important materials, such as the reduction of carbon dioxide, could serve to greatly enhance the electrochemical response.

References

[1] Tejamaya, M.; Römer, I.; Merrifield, R. C.; Lead, J. R. *Environ. Sci. Technol.* **2012**, *46*, 7011–7017.

[2] Bhattacharya, S.; Srivastava, A.; Pal, A. *Angew. Chem.* **2006**, *118*, 3000–3003.

[3] Kuhn, J. N.; Tsung, C.-K.; Huang, W.; Somorjai, G. A. *J. Catal.* **2009**, *265*, 209 – 215.

[4] Patsula, V.; Moskvin, M.; Dutz, S.; Horák, D. *J. Phys. Chem. Solids* **2016**, *88*, 24 – 30.

[5] Kingshott, P.; Thissen, H.; Griesser, H. J. *Biomaterials* **2002**, *23*, 2043 – 2056.

[6] Mosqueira, V.; Legrand, P.; Morgat, J.-L.; Vert, M.; Mysiakine, E.; Gref, R.; Devissaguet, J.-P.; Barratt, G. *Pharm. Res.* **2001**, *18*, 1411–1419.

[7] Maldiney, T.; Richard, C.; Seguin, J.; Wattier, N.; Bessodes, M.; Scherman, D. *ACS Nano* **2011**, *5*, 854–862.

[8] Pozzi, D.; Colapicchioni, V.; Caracciolo, G.; Piovesana, S.; Capriotti, A. L.; Palchetti, S.; De Grossi, S.; Riccioli, A.; Amenitsch, H.; Lagana, A. *Nanoscale* **2014**, *6*, 2782–2792.

[9] Gref, R.; Lück, M.; Quellec, P.; Marchand, M.; Dellacherie, E.; Harnisch, S.; Blunk, T.; Müller, R. *Colloids Surf., B* **2000**, *18*, 301 – 313.

[10] Dror-Ehre, A.; Mamane, H.; Belenkova, T.; Markovich, G.; Adin, A. *J. Colloid Interface Sci.* **2009**, *339*, 521 – 526.

[11] Lees, J. C.; Ellison, J.; Batchelor-McAuley, C.; Tschulik, K.; Damm, C.; Omanović, D.; Compton, R. G. *ChemPhysChem* **2013**, *14*, 3895–3897.

[12] Toh, H. S.; Jurkschat, K.; Compton, R. G. *Chem. Eur. J.* **2015**, *21*, 2998–3004.

[13] Zhou, Y.-G.; Rees, N. V.; Compton, R. G. *Chem. Phys. Lett.* **2011**, *514*, 291 – 293.

[14] Cheng, W.; Compton, R. G. *Trend. Anal. Chem.* **2014**, *58*, 79 – 89.

Part V

Conclusions

Part III explored the use of Butler-Volmer, Symmetric Marcus-Hush and Asymmetric Marcus-Hush theories in quantitatively describing one-electron transfer in Room Temperature Ionic Liquids. Chapter 1 studied the reduction of oxygen at a microdisc electrode in [Bmpyrr][NTf_2] using cyclic voltammetry. Butler-Volmer theory and SMH theory were used to create simulation programs, and the simulated voltammograms were compared with experimental data. BV theory, although empirical, provided voltammograms with lower MSAD values than those generated using SMH theory. A reorganisation energy, from the SMH program, was determined to be 0.4 ± 0.1 eV. This low value likely corresponds to a dominant inner sphere reorganisation, and limited solvent reorganisation.

Chapter 2 explored the reduction of 2-nitrotoluene at a gold microdisc electrode in two ionic liquids ([$P_{14,6,6,6}$][FAP] and [Emim][NTf_2]) *via* cyclic voltammetry at 298 K. This was followed by the reduction of nitrocyclopentane and 1-nitrobutane at a gold microdisc electrode in the ionic liquid [$P_{14,6,6,6}$][FAP]. BV and SMH theories were used to create a program to simulate voltammograms, which were then compared with the experimental voltammetry obtained above. In all cases, BV and SMH theories were equally capable of parameterisation of the data. The Marcusian parameter, λ, from SMH theory, was determined to be 0.5 ± 0.1 eV for the reduction of 2-NT in [$P_{14,6,6,6}$][FAP] and [Emim][NTf_2], 2 ± 0.1 eV for the reduction of NCP in [$P_{14,6,6,6}$][FAP], and 5 ± 0.1 eV for the reduction of BuN in [$P_{14,6,6,6}$][FAP]. This increase in reorganisation energy likely corresponds to the charge being delocalised on the aromatic portion of the molecule in the case of 2-NT, to the localisation on the nitro group itself in the case of NCP and BuN. The increased interaction with the environment of the BuN molecule as compared with NCP likely explains the increased reorganisation energy.

Chapter 3 examined the application of Asymmetric Marcus-Hush theory, first with respect to the reduction of oxygen in [Bmpyrr][NTf_2], and it was found that AMH

theory was similarly adept at parameterization of the data as BV theory, and generally superior to SMH theory. A λ value was measured, of 0.5 eV, which once again suggests a predominantly inner-sphere contribution to the reorganization energy. An asymmetry parameter of -0.4 was estimated, which is consistent with the force constants in oxygen being larger than those in superoxide, and is consistent with an α value of 0.29. AMH theory was also used to study the one electron reduction of 2-NT, NCP and BuN in $[P_{14,6,6,6}][FAP]$. AMH theory performed similarly well to both BV and SMH theories in terms of ability to parameterize experimental data. λ was measured as 0.5, 2, and 5 $\pm$ 0.5 eV for 2-NT, NCP, and BuN, reflecting the increased interaction with the environment that accompanied the localization of charge on the nitro group. Values for the asymmetry parameter, γ, of -0.05, 0.25, and 0 $\pm$ 0.05 for 2-NT, NCP, and BuN, were estimated. This reflects the equal force constants for both 2-NT and BuN, and are consistent with the symmetric transition state predicted by the measured α of 0.5. In the case of NCP, the value for γ of 0.25 $\pm$ 0.05 reflects force constants that are stronger in the reduced species than the oxidised species. This is also consistent with the value measured for α of 0.65. Broadly, it appears that in these cases, reductions carried out in ionic liquids conform to the findings in molecular solvents, with AMH theory outperforming SMH theory in cases where the transfer coefficient, α, estimated through BV theory deviates significantly from 0.5.

Part IV focused on the redox chemistry of silver nanoparticles in a RTIL. In Chapter 4, the oxidation of silver nanoparticles coated with polyethylene glycol was observed in a Room Temperature Ionic Liquid for the first time. An adsorbed assembly of NPs underwent individual stochastic oxidation, which is consistent with a polymer gated mechanism, in which a dynamic activation process precedes the electron transfer. This stochastic stripping allowed the convenient analysis and sizing of individual particles from an ensemble alongside mechanistic insights into nanoparticle redox reactivity.

In Chapter 5, direct oxidation of silver nanoparticles via 'nano-impacts' has been observed for the first time in a RTIL. The presence of chloride facilitates this oxidation, allowing the polymer rearrangement required in the absence of chloride through the oxidation of the silver to silver chloride. This study was the first to extend the nano-impact methodology to an ionic solvent, extending nanoparticle analysis to RTILs and exploring the dominant role of chloride in affecting reaction mechanisms.

Chapter 6 revealed that manipulation of the capping agent characteristics, in this case, the molecular weight of poly(ethylene) glycol molecules, facilitated a controlled shift in mechanism of electron transfer of nanoparticles in RTILs. It was shown that the capping agent plays a large role in electron transfer dynamics, and that the nanoparticles' electrochemical behaviour can shift with relatively minor changes made to the capping agent. To this end, it has been demonstrated that the frequency of nanoparticle oxidation is limited as the molecular weight of the PEG chains is increased, from 0.07 s^{-1} for the 2000 MW NPs, to 0.02 s^{-1} and 0.007 s^{-1} for the 6000 and 10,000 MW NPs respectively, as is consistent with an increase in the Stokes radius, and a shift from 'nano-impact' to 'polymer-gating' mechanisms is observed moving from 2000 MW to 6000 MW PEG Ag NPs.

The thesis offers insights into the electrochemistry of nanoparticles in high-ionic strength environments, and has illustrated the possible effects of changing the capping agent on the mechanism of oxidation. This fundamental knowledge may facilitate greater control over the reaction outcomes when choosing the NP substrate. This work opens the possibilities of the use of RTILs and NPs in combination, and may be particularly valuable in future work in catalysis, energy storage, and medical applications of NPs, and other applications where high ionic strength environments predominate.

Appendix A

Derivation of the Butler-Volmer Equation

Part III: Derivation of the Butler-Volmer equation.

Consider a one electron transfer:

$$\mathrm{A} + \mathrm{e}^- \rightleftharpoons \mathrm{B} \tag{A.1}$$

where A to B is described by the rate constant k_c (cathodic), and B to A k_a (anodic).

The flux is related to the current by:

$$I = FAj \tag{A.2}$$

where F is the Faraday constant, and A is the electrode area.

The rate of flux is described by:

$$j = k(n)[reactant]_0^n \tag{A.3}$$

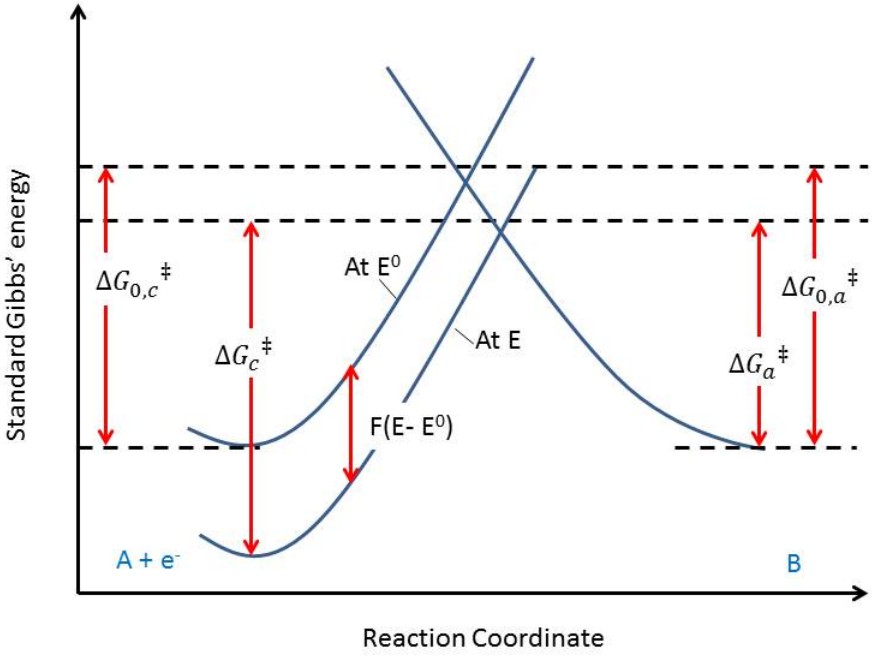


Figure A.1: The effect of a potential change on the standard Gibbs' energies of activation for oxidation and reduction.

where n is the order of the reactant, k(n) is the nth order rate constant, and the subscript denotes that it is the surface concentration of reactant. n is usually assumed to be 1, denoting a single order rate constant.

To describe the overall flux, rate constants for both the reactant and product must be considered:

$$j = k_a[A]_0 - k_c[B]_0 \tag{A.4}$$

where $[A]_0$ and $[B]_0$ are the surface concentrations of the reactants and products respectively, and n = 1.

Using the Arrhenius Equation to relate the rate constants to the Gibbs energy of

activation yields:

$$k_c = A_c exp \frac{-\Delta G_c^{\ddagger}}{RT} \tag{A.5}$$

$$k_a = A_a exp \frac{-\Delta G_a^{\ddagger}}{RT} \tag{A.6}$$

where A is the frequency factor and $\Delta G_c^{\ddagger}$ and $\Delta G_a^{\ddagger}$ are the forward and reverse free activation energies.

Figure A.1 is a schematic of a Gibbs' energy-reaction coordinate diagram. The upper reactant curve corresponds to an electrode potential of $E_f^{\ominus}$), with activation energies of $\Delta G_0^{\ddagger} c$ and $\Delta G_0^{\ddagger} a$. The lower reactant curve shows the effect of changing the potential to a new value, E, in which the relative energy of the electrode changes by $-F\Delta E = -F(E - E_f^{\ominus})$. If ΔE is positive, the barrier for oxidation ($\Delta G_a^{\ddagger}$) becomes smaller than $\Delta G_0^{\ddagger} a$ by a fraction of the overall charge. This fraction is defined as the transfer coefficient (α), where $0 < \alpha < 1$ and $\alpha + \beta = 1$. Thus the free activation energies of the reactant and product can be described as:

$$\Delta G_c^{\ddagger} = \Delta G_0^{\ddagger} c + \alpha F(E - E_f^{\ominus}) \tag{A.7}$$

$$\Delta G_a^{\ddagger} = \Delta G_0^{\ddagger} a + \beta F(E - E_f^{\ominus}) \tag{A.8}$$

Substitution of Equations A.7 and A.8 into Equations A.5 and A.6 gives:

$$k_c = A_c exp\left(\frac{\Delta G_0^{\ddagger} c}{RT}\right) exp\left[\frac{-\alpha}{RT}(E - E_f^{\ominus})\right] \tag{A.9}$$

$$k_a = A_a exp\left(\frac{\Delta G_0^{\ddagger} a}{RT}\right) exp\left[\frac{\beta}{RT}(E - E_f^{\ominus})\right] \tag{A.10}$$

When the interface is at equilibrium, $[A]_0 = [B]_0$, $E = E_f^{\ominus}$, and $k_a[A]_0 = k_b[B]_0$, meaning that $E_f^{\ominus}$ is the potential at which the rate constants take the same value,

and simplifies to the Nernst Equation:

$$E = E_f^{\ominus} + \frac{RT}{F} ln \frac{[A]}{[B]} \tag{A.11}$$

This can described by the standard rate constant, k^0. k_a and k_c are related to k^0 by:

$$k_c = k^0 exp\left[\frac{-\alpha}{RT}(E - E_f^{\ominus})\right] \tag{A.12}$$

$$k_a = k^0 exp\left[\frac{\beta}{RT}(E - E_f^{\ominus})\right] \tag{A.13}$$

Substituting Equations A.12 and A.13 into Equation A.4 gives an expression for the Butler-Volmer equation:

$$i = FAk^0\left[[A]_0 exp\left[\frac{-\alpha}{RT}(E - E_f^{\ominus})\right] - [B]_0 exp\left[\frac{\beta}{RT}(E - E_f^{\ominus})\right]\right] \tag{A.14}$$